Synthese et characterization de nanoplaquette bi emittrice

Corentin Dabard

Thèse de doctorat de Sorbonne Université

Spécialité : Chimie des matériaux

Ecole doctorale 397 : Physique et Chimie des Matériaux

réalisée

à l'Institut des Nanosciences de Paris (Sorbonne Université)
et au Laboratoire de Physique et d'étude des Matériaux (ESPCI Paris)

présentée par

Corentin DABARD

pour obtenir le grade de :

Docteur de Sorbonne Université

Sujet de thèse :

Synthesis and characterization of bi-emitting nanoplatelets

Présentation et soutenance le 24 octobre 2023

Devant un jury composé de :

M. Alberto BRAMATI (LKB, Paris)	Président du jury
Mme Lise-Marie LACROIX (INSA, Toulouse)	Rapportrice
M. Damien BOYER (ICCF, Clermont-Ferrand)	Rapporteur
M. Philippe GOLDNER (ENSCP, Paris)	Examinateur
M. Jean Yves PIQUEMAL (U. Paris Cité, Paris)	Examinateur
M. Emmanuel LHUILLIER (INSP, Paris)	Directeur de thèse
Mme Sandrine ITHURRIA (ESPCI, Paris)	Invitée

Content

Notations and abbreviations

Abbreviations:

Abbreviation	*Signification*
CE	Cation Exchange
CIE	Comission Internationale de l'Eclairage
CT	Charge Transfer
c-ALD	Colloidal Atomic Layer Deposition
ETL, HTL	Electron Transport Layer, Hole Transport Layer
EQE	External Quantum Efficiency
FOM	Figure-of-merit
FRET	Förster Resonant Energy Transfer
FWHM	Full Width at Half Maximum
HOMO, LUMO	Highest Occupied, Lowest Unoccupied Molecular Orbital
LCD, QD-LCD	Liquid Crystal Display, Quantum Dot-Liquid Cristal Displays
LED, LEDs	Light Emitting Diode, Light Emitting Diodes
O-LED, QD-LED	Organic-, Quantum Dot-Light Emitting Diode
MBE	Molecular Beam Epitaxy
ML, MLs	Monolayer, Monolayers
NC, NCs	Nanocrystal, Nanocrystals
NIR, SWIR	Near-Infrared, Short-Wave Infrared
NP, NPs	Nanoparticle, Nanoparticles
NPL, NPLs	Nanoplatelet, Nanoplatelets
QD, QDs	Quantum Dot, Quantum Dots
SPV	Surface Photovoltage
ZB	Zinc-Blend

Notations:

Abbreviation	*Signification*
BE, KE	Binding Energy, Kinetic Energy
CB, VB	Conduction Band, Valence Band
E_F, E_g	Fermi Energy, Band Gap Energy
lh, hh, SO	Light Hole, Heavy Hole, Spin Orbit
T	Temperature
k	Boltzmann Constant
b	Bowing Factor
ΔV_{CB}, ΔV_{VB}	Conduction Band Offset, Valence Band Offset
I_{DS}, V_{GS}	Drain-Source Current, Gate-Source Bias
η_{PL}, η_{charge}, $\eta_{geometry}$	Photoluminescence, Charge Injection, Geometric Efficiency Factor

Characterization techniques:

Abbreviation	*Signification*
ASE	Amplified Stimulated Emission
EDX	Energy Dispersive X-ray spectroscopy
EL	Electroluminescence
FET	Field Effect Transistor
FTIR	Fourier Transform Infrared spectroscopy
HAADF-STEM	High-angle annular dark-field Scanning TEM
PL, TRPL	Photoluminescence, Tim-Resolved Photoluminescence
PLE	Photoluminescence Excitation
QY, PLQY	Quantum Yield, Photoluminescence Quantum Yield
TA	Transient Absorption
TEM	Transmission Electron Microscopy
UPS, XPS, PES	UV-, X-ray Photoelectron Spectroscopy
XRD	X-Ray Diffraction

Chemicals:

Abbreviation	*Signification*
Alq_3	Tris(8-hydroxyquinolinato)aluminum
CBZ	Chlorobenzene
$Cd(ac)_2$, $Hg(ac)_2$	Cadmium, Mercury Acetate
$Cd(deca)_2$	Cadmium Decanoate
$Cd(prop)_2$	Cadmium Propionate
$Cd(myr)_2$	Cadmium Myristate
$Cd(OA)_2$, $NaOA$, $Hg(OA)_2$	Cadmium, Sodium, Mercury Oleate
DCM	Dichloromethane
CHF	Chloroform
EDT, DDT	Ethanedithiol, Dodecanthiol
EtOH, MeOH	Ethanol, Methanol
OA, OLAm	Oleic Acid, Oleylamine
ODE	Octadecene
IPA	Isopropanol
ITO	Indium Tin Oxide
PEDOT:PSS	poly(3,4-ethylenedioxythiophene) polystyrene sulfonate
pTPD	Poly(N,N'-bis-4-butylphenyl-N,N'-bisphenyl)benzidine
Pvk	Polyvinylcarbazole
PMMA	Polymethylmethacrylate
TCE	Tetrachloroethylene
TCO	Transparent Conductive Oxide
TBP, TOP	Tributyl, Trioctyl Phosphine

Introduction

The historical invention of the light-emitting diode (LED) is often attributed to Oleg Losev in 1927 when he observed light emission when a bias was applied to silicon carbide[2]. However, the efficiency was low, and it didn't receive much attention. In the late 1930s, Guillaume Destriau's pioneering work on electroluminescence from zinc sulfide crystals laid the foundation for future advancements[1]. The field took a significant turn in 1962 when Nick Holonyak Jr. created the first practical visible-spectrum LED using gallium arsenide phosphide, revolutionizing the lighting industry with a more energy-efficient and longer-lasting alternative to incandescent bulbs. Subsequent advancements in LED technology have expanded the range of colors and increased efficiency, making them essential for display technology and various applications.

The emissive material is a crucial component of an LED, and it has continuously evolved based on research on electroluminescent materials. From the early use of silicon carbide by Losev to the current Ce:YAG coating found in common displays, advancements have been made. Modern LED fabrication involves epitaxy methods like metal-organic chemical vapor deposition or molecular beam epitaxy, which create the active region responsible for light emission. The process starts with a growth substrate, such as sapphire or silicon carbide, onto which precise layers of semiconductor materials like gallium nitride or indium gallium nitride are grown. These engineered epitaxial layers possess varying bandgaps, enabling the emission of different colors of light.

To reduce high cost of epitaxial deposition, colloidal II-VI semiconductors have brought a particular interest regarding their cost-effective and scalable synthesis. Such bulk materials have always brought interest for their optical properties. For example, a color gamut is based on the color of CdS to CdSe and has been used is the tainting of the New York taxis cab or even in the yellow sunflowers of Van Gogh.

The first syntheses of II-VI semiconductor colloidal and low-polydisperse nanocrystals were performed by Bawendi's team in 1993. When reducing the size of semiconductors to the nanoscale range, a wider range of properties can be achieved, depending on their shape and compositions. Among the various morphologies, 2D geometry has garnered significant interest in recent years. The first synthesis of zinc-blend 2D CdSe particles is credited to Ithurria et al. in 2009. This synthesis enabled the production of a monodispersed population of nanocrystals, resulting in extremely narrow optical features. Due to their anisotropic shape, these particles can form complex heterostructures to enhance their optical properties and self-assemble on a substrate to generate oriented emission. Consequently, these particles hold promise as materials for improving color quality, power efficiency, and reducing the cost of current visible LEDs.

In the realm of near-infrared technologies, the current state-of-the-art is characterized by high costs and limited applications, primarily within defense and space domains. By combining the small band gap energies of Hg-based compounds with the narrow emission features of the 2D geometry, the potential range of uses for near-infrared devices can be expanded. These materials are promising candidates for various everyday applications, including infrared detection in autonomous cars, trash sorting, and ceramic glasses.

In this context, I worked on the synthesis of II-VI semiconductor nanoplatelets. At ESPCI under the supervision of S. Ithurria, I synthesized the material, from core-only particles to complex

heterostructures. The nanoplatelets fabricated there have always been designed with both the aim of improving the optical properties toward their incorporation into LED devices. Subsequently, in the team of E. Lhuillier at INSP in Sorbonne Université, I characterized the electronic band structure of the material using X-ray photoemission spectroscopy at synchrotron SOLEIL in collaboration with M. Silly, and fabricated the optoelectronic devices discussed throughout this manuscript, which will be divided into four chapters.

In the first chapter, I will introduce the concept of nanoplatelets (NPLs) and elucidate their main differences from their spherical counterparts, quantum dots (QDs). To accomplish this, I will initially present their synthesis process and then delve into their optical properties and specifically designed NPL heterostructures. This chapter will also introduce the different characterization techniques that will be employed throughout this manuscript to uncover the distinctive properties of NPLs.

Moving on to the second chapter, I will discuss the development of a single bi-emitting NPL based on a core-multi-crown structure, from its design to its synthesis, including the investigation of the mechanism behind this peculiar behavior. Ultimately, we will construct a LED utilizing these particles as the active layer and demonstrate bicolor electroluminescence.

In the third chapter, the focus will be on optimizing the cation exchange procedure used for synthesizing a new class of material, the $HgSe_xTe_{1-x}$ 3 ML NPLs. I will demonstrate tunable near-infrared photoluminescence. Additionally, we will establish the band diagram alignment based on the alloy composition and confirm it using an uncommon technique called time-resolved X-ray photoemission spectroscopy.

Lastly, in the fourth chapter, I will attempt to optimize the photoluminescence of a HgTe 3 ML NPLs film, particularly concerning the degradation of its optical features. To achieve this, I will investigate the mechanisms underlying this degradation and propose a post-synthetic treatment to enhance the photoluminescence of the film. Armed with this strengthened photoluminescence, we will report the first-ever electroluminescence from Hg-based NPLs and demonstrate oriented emission within an HgTe NPLs film using a metallic nanostructure.

Chapter 1: Synthesis and optical properties of Nanoplatelets

During my Ph.D. studies, I focused on II-VI semiconductor 2D nanocrystals, also known as nanoplatelets (NPLs). Research on these particles has mainly focused on their unique optical properties. Due to their distinctive shape, these 2D particles serve as interesting starting building blocks for the formation of more complex heterostructures. Those heterostructures have garnered significant interest, particularly regarding their integration into optoelectronic devices. The exceptional photoluminescent properties of NPLs make them ideal candidates as down-converters in displays or as electroluminescent materials in Light Emitting Diodes (LEDs). Therefore, in this first chapter, the reader will be introduced to NPLs, their optical properties, and their synthesis methods. An overview of the characterization techniques available in our toolbox to investigate the NPLs properties will also be provided. Additionally, the operational principles of LEDs will be described to highlight the advantages of using NPLs for such applications.

The first part will be dedicated to **quantum confinement** and its effect on the optical properties of NPLs. In particular, the absorption spectrum and the emission dynamics will be investigated and compared with spherical quantum dots.

In the second part, I will focus on **the synthesis of NPLs**. After presenting the initial synthesis of NPLs, we will address the formation of heterostructure, including core-shell and core-crown NPLs. To complete this synthesis-oriented sub-chapter, the cation exchange procedure will be introduced.

In the third part, I will discuss various characterization tools, including time-resolved optical measurements, photoemission, and field-effect-transistor, that will be used to investigate the structure of the NPLs and **probe the dynamic of charge carriers** after their formation within a material. Different strategies to **unveil the electronic structure** of NPLs will also be addressed, with a particular focus on X-ray photoemission spectroscopy.

All of these investigations will lead to the fourth part of this chapter which is dedicated to the incorporation of **NPLs in optoelectronic devices,** particularly LEDs. After introducing the challenges in this field and the potential of NPLs as emitters in TV screen displays, I will present an overview of quantum dot-based LEDs, from their fabrication to their characterization.

Publication associated:

- Diroll, B. T.; Guzelturk, B.; Po, H.; **Dabard, C.**; Fu, N.; Makke, L.; Lhuillier, E.; Ithurria, S. 2D II–VI Semiconductor Nanoplatelets: From Material Synthesis to Optoelectronic Integration. *Chem. Rev.*, 123, 3543 (2023)

Content

Since its development in the 1970s, Molecular Beam Epitaxy (MBE) has been the classical method for forming epitaxial quantum wells. However, this technique requires a large amount of material and energy. Another drawback of MBE is the requirement for a small lattice mismatch between the substrate and the material, which limits the formation of complex quantum well heterostructures.

Over the last decade, the development of nanocrystal colloidal syntheses has opened new perspectives in semiconductor applications. Colloidal syntheses address the lattice parameter requirement by allowing the growth of nanocrystals (NCs) in solution without the need for a substrate, while maintaining a high level of precision comparable to MBE. Additionally, solution-based growth pathways enable the formation of complex architectures, facilitating the creation of more refined structures. Research on such materials has gained interest following the pioneer works of Bawendi's team in 1993, where they reported the first low-polydisperse syntheses of CdE (E: S, Se, Te) quantum dots (QDs)[4].

Colloidal NCs differ from epitaxially grown structures in several aspects. For instance, they possess an additional layer of ligands on top of the inorganic core to ensure their colloidal stability and electroneutrality. Controlling the size of NCs remains challenging, unlike the precise control achieved at the atomic layer for MBE deposition. However, since the late 2000s, a new class of colloidal semiconductor NCs, known as 2D-nanoplatelets[5–8], has been developed allowing control of the thickness.

In this manuscript, my focus will primarily be on II-VI semiconductors based on Cd or Hg as the metal, and S, Se, and Te as the chalcogen. Although other materials, such as lead-based NPLs (PbS, PbSe …)[9] and transition metal dichalcogenides predominantly based on Mo and W chalcogenides[10], have been synthesized in the same shape, they will not be studied here.

1. Quantum confinement in NCs.

A semiconductor is a material with a valence band (VB) full of electrons and an empty conduction band (CB). In a bulk material, the difference in energy between the lowest accessible state of the CB and the higher occupied state of the VB is named the band gap (E_g) and depends on the considered material.

In a semiconductor, an incoming photon can be absorbed when its energy is higher than E_g. Through an interband transition, an electron is then promoted from the VB to the CB, leaving a positively charged electron vacancy inside the VB, called a hole. The electron and hole have opposite charges and are located in a very small area. In this sense, they are often compared to the electron-

proton pair that constitutes a hydrogen atom. Consequently, the two charges interact together through attractive Coulombic forces. Being surrounded by a myriad of other electrons, repulsive forces balance this attractive force leading to an equilibrium between these forces. An electron-hole pair, also called an exciton, is created. This energy, however, remains small in comparison to the energy brought by the quantum confinement.

To be considered as a NC, an object needs to have at least one of its dimensions lower than 100 nm. At this scale, the Newtonian mechanics or the Maxwell electromagnetic theories fail to completely explain the physical properties of the material. A new approach is required: quantum mechanics, introduced by Max Planck and others at the beginning of the 20th century. In this new approach, the notions of particle and wave are intriguing and a physical object can exhibit both corpuscular and wave properties.

The first colloidally synthesis of NCs has been carried out by Rossetti *et al.* in 1983[11] where they obtained spherical quantum dots (QDs). However, the first quantum confinement observed in NCs was reported by Ekimov in 1981[12]. Using the spherical equations developed by Efros *et al.* in 1981[13], they mathematically described this phenomenon three years later[14]. In this chapter, we will follow their pioneering works to unveil the quantum confinement in NCs.

a. From bulk to 3D quantum confinement.

When a charge is confined in a semiconductor QDs surrounded by a dielectric medium, the behavior of the system can be conceptualized as a charge enclosed within a sphere with a similar radius "*a*". The wavefunctions that describe the distribution of the charge inside the QD are determined by solving the Schrödinger equation in spherical coordinates:

$$\psi_{n,L,M}(r,\theta,\phi) = Y_{L,M}(\theta,\phi)\frac{\sqrt{2}}{a\sqrt{r}}\frac{J_L\left(\varphi_{n,L}\frac{r}{a}\right)}{J_{L+1}(\varphi_{n,L})}$$

where $Y_{L,M}$ correspond to the normalized spherical wavefunctions, *n* corresponds to the principal quantum number usually denoted as {n = 1, 2, 3 …}, *L* corresponds to the angular quantum number usually denoted as {S, P, D …}, M corresponds to the momentum projection, J_L corresponds to the Bessel function of L order and $\varphi_{n,L}$ the nth root of this Bessel function. The discrete energies associated with these wavefunctions are as follows:

$$E_{n,L} = \frac{\hbar^2}{2m^* a^2}\,\varphi_{n,L}^2 = \frac{\hbar^2}{2m^*}k_{n,L}^2$$

where m^* is the effective mass of the charge. The projection of the angular momentum induces the formation of several different energetic states that are degenerate in perfect spherical geometry. Each of them can be associated to a wave vector $k_{n,L}$.

The obtained equation can be used for both electrons in the CB and holes in the VB. Consequently, the energetic state diagram of QDs follows the general trend exhibited in **Figure 1**. Due to the higher effective mass of the holes, the energetic states located in the VB are usually less energetically spread. The orthogonality of the wavefunctions then leads to the following well-known selection rules: Δn = 0 and ΔL = 0. As a result, the authorized transitions observed in QDs are $1S_e$ -> $1S_h$, and $1P_e$ -> $1P_h$ … Those transitions are represented by black arrows in **Figure 1**. Taking the first one as an example, we can write the interband energy transition as:

$$E_{1,0;1,0} = E_g + \frac{\hbar^2}{2m_e^* a^2}\,\varphi_{1,0,}^2 + \frac{\hbar^2}{2m_h^* a^2}\,\varphi_{1,0}^2 = E_g + \frac{\hbar^2\pi^2}{2\mu a^2}$$

with m_e^* and m_h^* the effective masses of the electron and the hole, μ the reduced effective mass of the electron-hole pair and E_g the bulk band gap of the material.

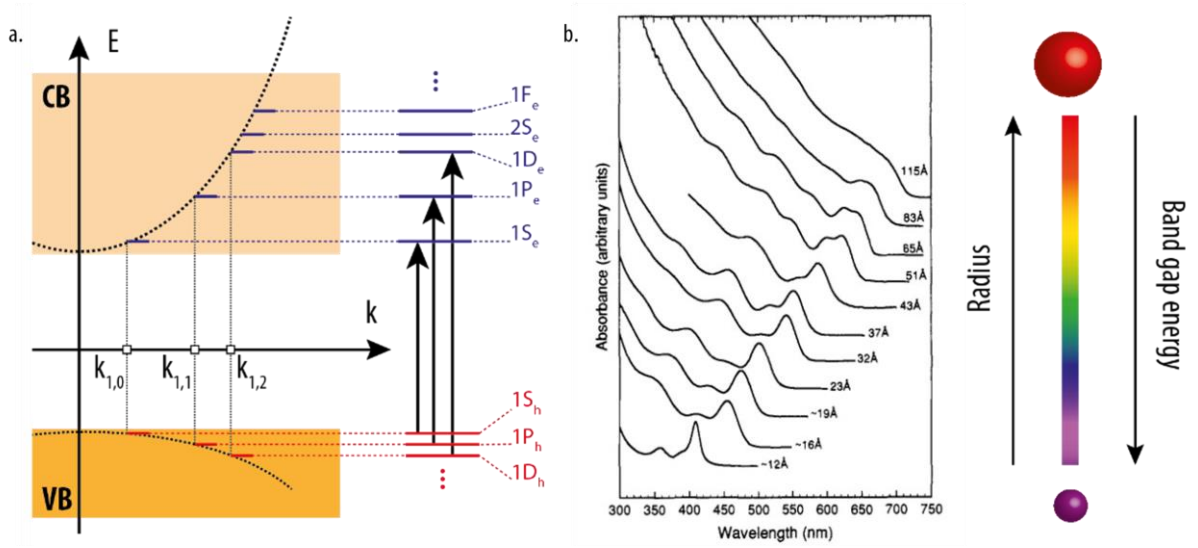

Figure 1: *Optical transitions in QDs. a. Energetic states of the VB (red) and CB (blue), the notes on the right correspond to their label. The black arrows correspond to the autorized transition. b. Evolution of the absorption spectrum of CdSe QDs according to their radius. The color scale on the right enhance the redshift of the optical properties with the radius increase. The absorption spectra are taken from ref [8].*

In this initial attempt to describe the energetic states in a sphere, we made the approximation that the charges are no interacting. However, to successfully describe the absorption spectrum of a semiconductor particle, it is necessary to consider the Coulombic interaction between the hole and the electron. This interaction introduces a term into the Schrödinger equations, which makes them difficult to solve using analytical expressions. Nevertheless, a good approximation has been obtained computationally, and the associated energy can be expressed as follows:

$$E_{e-h} = -\frac{1.8e^2}{\epsilon a}$$

where e represents the elemental charge and ε denotes the relative permittivity of the material[15]. Finally, the energy of the lowest transition observed between $1S_e$ and $1S_h$ states can be expressed as:

$$E_{1,0;1,0} = E_g + E_{conf} + E_{e-h} = E_g + \frac{\hbar^2\pi^2}{2\mu a^2} - \frac{1.8e^2}{\epsilon a}$$

This expression is obtained when considering parabolic bands. However, exceptions exist, primarily due to non-parabolicity such as in HgTe NCs where more complex dependencies are observed[16]. Nonetheless, in general, the significance of each contribution strongly depends on the size of the particle. In the case of quantum confinement, the dependence in radius follows an inverse-square (a^{-2}) relationship, while for Coulombic interaction, it follows an inverse (a^{-1}) one. Consequently, for sufficiently small systems, the Coulombic interaction only serves as a correction to the quantum confinement. This transition from one regime to the other is linked to the Bohr radius of the material.

The higher the Bohr radius, the greater the influence of quantum confinement on low-dimensional QDs. **Table 1** provides examples of II-VI semiconductor Bohr radii. For small Cd-based NCs (a few nm in size), quantum confinement effects are therefore expected. It is worth mentioning that HgSe and HgTe are semimetals as they lack a band gap. Consequently, the diverse range of optical properties observed for Hg-based NCs is solely associated with quantum confinement effects[17].

Table 1: *General parameters for different II-VI semiconductors. Except mentioned data are taken from ref[18].*

	ZnS	*CdS*	*CdSe*	*CdTe*	*HgSe*	*HgTe*
Band gap (eV)	3.71	2.46	1.68	1.51	0	0
Bohr radius (nm)	1.5[19]	2.6[19]	5.3[20]	6.5	17[21]	40[22]
Lattice parameter (Å)	5.41	5.83	6.08	6.48	6.09	6.46
Electron effective mass (in m_0)	0.26	0.21	0.12	0.09	0.04	0.03
Light hole effective mass (in m_0)	0.36	0.15	0.11	0.12	0.03	0.01[16]
Heavy hole effective mass (in m_0)	1.42	0.68	0.57	0.82	0.67[23]	0.33[16]

b. Structure of NPLs optical properties.

As the understanding of II-VI semiconductors improved, researchers have successfully synthesized nanocrystals with new shapes. For instance, using CdSe, nanospheres[4,24], nanorods[25,26], nanoplatelets[5,27,28] (NPLs), and even more exotic shapes can be obtained[26]. The previously derived 3D equations can be extended to other geometries, including 1D materials (with a 2D confinement) and 2D materials (with a 1D confinement). The calculated density of states varies depending on the considered geometry, which explains the difference observed in the absorption spectra of these materials, see **Figure 3a-b**.

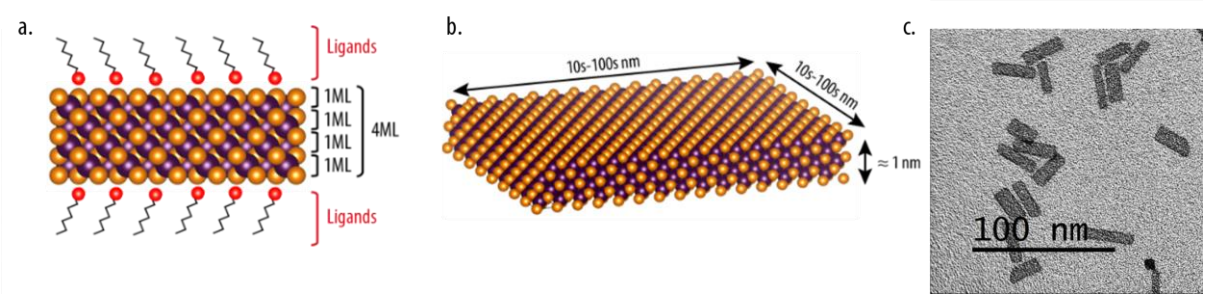

Figure 2: *Quantum confinement in NPLs. a. Sketch of CdSe 4 ML NPLs on the side. A monolayer (ML) is defined as the association of a plan of cadmium (orange) and a plan of chalcogen (purple). An additional layer of organic ligands is covering all the facets. b. Sketch of an NPL tilted. The lateral dimensions are large in comparison to the thickness. This induces quantum confinement in 1D. c. TEM picture of CdSe 4 ML NPLs.*

Among these NCs, NPLs of II-VI semiconductors have garnered significant attention due to their unique optical characteristics and the availability of more advanced synthetic procedures. These NPLs can be synthesized in two distinct crystalline structures: wurtzite and zinc blend (ZB). In this manuscript, we primarily focus on ZB NPLs. ZB NPLs are considered 2D materials due to their thickness which range from a few nm, and their substantial lateral dimensions that can be extend up to hundreds of nanometers (see **Figure 2b** and TEM picture **Figure 2c**).Within their thickness, NPLs are comprised of alternating cation and chalcogen planes, with each combination of planes referred to as a monolayer (ML). For instance, **Figure 2a** depicts NPLs consisting in 4 MLs. The two outermost planes are composed

of cations resulting in a positively charged structure. An additional layer of ligands is incorporated to achieve electroneutrality and provide and colloidal stability in common non-polar solvents such as hexane and toluene.

In the subsequent paragraphs, we will delve into the analysis of the absorption and emission properties of these NPLs to gain a comprehensive understanding on their increasing significance.

c. Analysis of nanoplatelets absorption.

The density of states in 2D materials is expected to exhibit steps-like features, resembling a continuum (**Figure 3a**). While this description can explain the general aspects of the absorption spectrum, it fails to capture the distinct characteristics observed in the NPLs (see **Figure 3b**). To obtain a more accurate understanding of the involved transitions (i.e. the promotion of an electron from the VB to the CB), an additional factor need to be considered; the complexity of the VB.

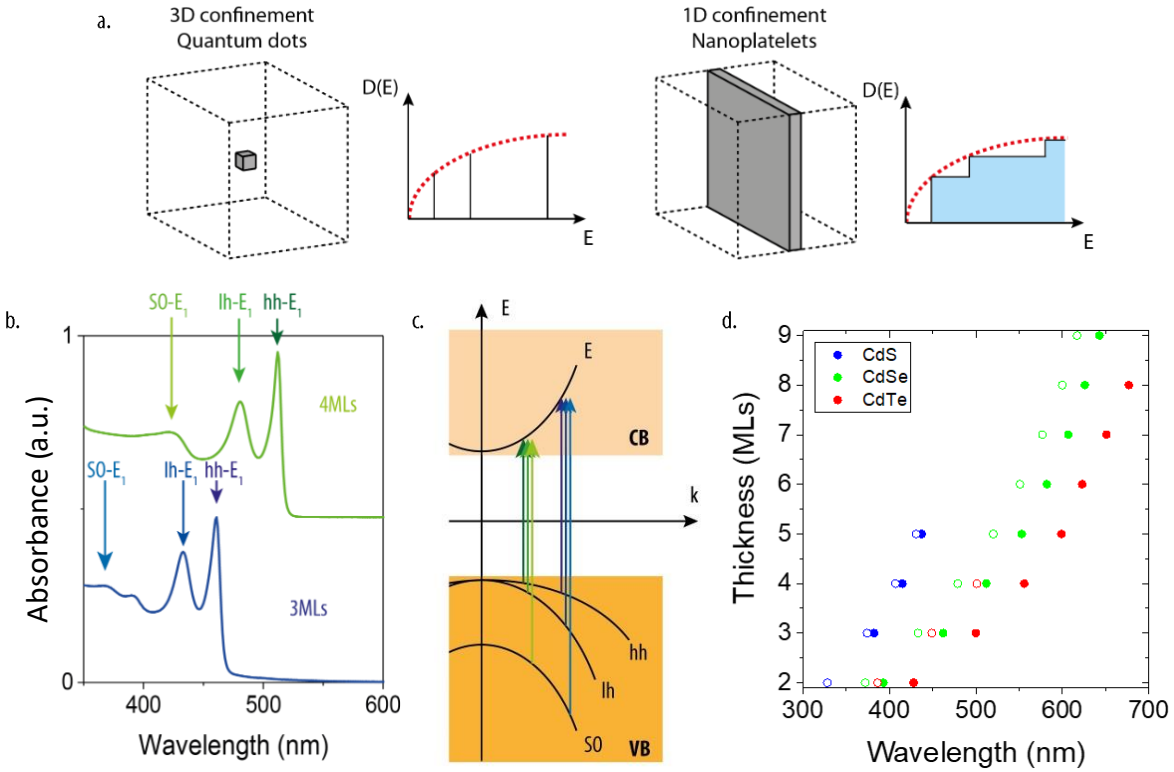

Figure 3: *Structure of the absorption spectrum in NPLs. a. Density of states according to the energy for QDs and NPLs. The red dashed lines correspond to the density of states inside the bulk material. b. Evolution of the absorption spectrum of NPLs according to the thickness. The green spectrum corresponds to 4 ML NPLs while the blue one to 3 ML NPLs. The transitions are labeled and shown by arrows. c. Sketch in the energy of the different transitions observed according to the wave vector k=π/a with the thickness of the NPLs. the groups of colored arrows correspond to the features labeled in b. d. Position of the first (solid dot) and second (empty dots) excitonic peaks according to the material and the thickness of the NPLs (expressed in MLs).*

In ZB II-VI semiconductors, such as CdSe, the VB is comprised of two s orbital from the metal and six p orbitals from the chalcogen. These orbitals contribute a total two and four valence electrons, respectively. Consequently, the CB and VB of CdSe are primarily compose of two vacant s orbitals from the Cd and six filled p orbitals from the chalcogen.

At the gamma point of the crystal (k=0 in **Figure 3c**), the spin-orbit (SO) coupling partially splits the six degenerated states of the VB, introducing a new quantum number called the angular

momentum J. This quantum number can take two values: 3/2 and ½, resulting in to the formation of two bands. The band associated with J=1/2 are doubly degenerated and referred to as spin-orbit band (SO), while the bands associated with J=3/2 are fourfold degenerated. As the size of the material decreases (k≠0), further splitting occurs based on the projection of the angular momentum, J_z, resulting in two subbands within the J=3/2 band: these subband are twofold degenerated when J_z=±3/2, and known as the heavy hole band (hh), and twofold degenerated when J_z=±1/2, referred to as light hole band (lh)). The hh and lh bands exhibit different curvatures in the band structure diagram due to the difference in the effective mass of the holes, with the lh band having a lower effective and thus a higher curvature (see values in **Table 1**).

Based on this information, Ithurria et al. unveiled in 2011, the band structure of the CdSe[29] (see **Figure 3**). At the nanoscale (k≠0), three types of transitions from the SO, lh, and hh states to the CB band state (referred to as E) are expected in absorption spectrum. When considering the step-like continuum associated with the 2D shape of the NPLs, the complete absorption spectrum can be described. For example, in the case of CdSe 4 ML NPLs, the hh-E transition is responsible for the first excitonic peak at 510 nm, the lh-E transition for the second excitonic peak at 460 nm, and the SO-E transition to the hill localized at 422 nm (as depicted in **Figure 3d**).

As previously mentioned, the quantum confinement in NPLs occurs only along the thickness direction. Thus, by varying the number of MLs in the NPLs, we can control the degree of quantum confinement. For instance, **Figure 3c** displays the absorption spectra of CdSe 3 and 4 ML NPLs, where the first excitonic peak shifts from 460 nm to 510 nm with increasing MLs. Modulation of the absorption band edge can also be achieved by altering the material's band gap. It is worth noting that smaller chalcogen atoms lead to bluer optical features (refer to band gap values in **Table 1**). Therefore, a wide range of band gap energies can be obtained by adjusting the composition and thickness of the NPLs (as shown in **Figure 3c**, presenting the energies of the first (solid dots) and second (empty dots) excitonic peaks based on the material and NPL thickness given in MLs).

The synthesis of NPLs allows atomic-scale precision of the thickness. The absence of roughness on the wide facets induces no inhomogeneous broadening contributing to very narrow absorption and emission features, in contrast with QDs. Their large volume reduces non-radiative Auger recombination[30], that are at the origin of the large lasing threshold observed in those spherical NPs[31]. Additionally, each transition in NPLs is associated with a large cross-section, which enhances the absorption efficiency[29]. These factors drive the research interest in NPLs, particularly in applications such as light harvesting[32], with the potential to outperform thin-film CdTe materials deposited through techniques like sputtering[33].

d. Photoluminescence form nanoplatelets.

Emission features.

Once excited, the hole (or electron) within an exciton undergoes relaxation towards the band edge state. Specifically, for the hole, this state corresponds to the hh state. The relaxation process toward the lowest energy state occurs rapidly, even before any recombination processes take place (within picosecond)[34]. Once the charge carriers reach these states, the exciton can undergo several relaxation mechanisms, including radiative recombination through fluorescence or phosphorescence involving intermediate emissive states, as well as non-radiative relaxation (as depicted in **Figure 4b**). In direct band gap semiconductors, the primary pathway for radiative relaxation is direct recombination through the E-hh transition, which is referred to as band edge recombination.

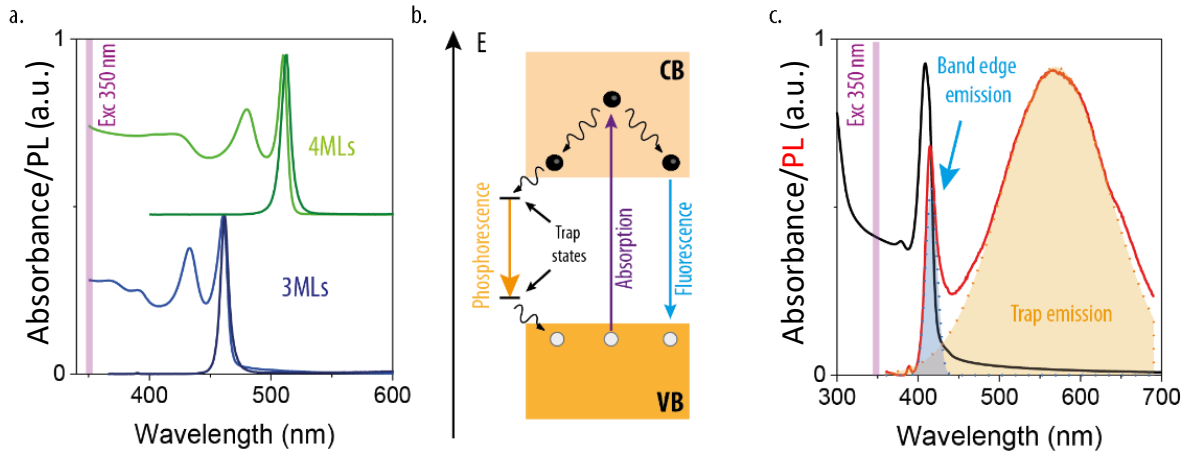

Figure 4: *Photoluminescence process in NPLs. a. Absorption (light color) and emission (dark color) of CdSe 3 ML (blue) and 4 ML (green) NPLs. The wavelength of excitation is at 350 nm. b. Sketch of the different radiative deexcitation pathways in NPLs. c. Emission features of CdS 4 ML NPLs. The band-edge emission (blue) corresponds to the fluorescence process while the phosphorescence (orange) involves trap emission leading to red-shifted emission. The wavelength of excitation is 350 nm.*

Therefore, the emission spectrum of NPLs consists of a single emission peak. For instance, **Figure 4a** displays the band edge emission of CdSe 3 and 4 ML NPLs following the absorption of a photon at 350 nm. Similar to the absorption properties, the emission is influenced by the material composition and the thickness of NPLs. This allows for cover the visible range (CdSe and CdTe)[29,35], ranging from ultraviolet (ZnE, CdS)[36,37] to the NIR domain (HgE)[38,39].

As mentioned previously, the synthesis of NPLs allows for precise control of their thickness at the atomic layer level, resulting in a smooth surface without roughness. Consequently, all NPLs have the same thickness, and their ensemble emission corresponds to the emission of a single particle[40]. In contrast, QD syntheses typically result in polydisperse size distribution, leading to intrinsic broadening of optical features. It leads to broad emission spectra with a full width at half maximum (FWHM) of several tens of meV, as shown in **Figure 5a**. The absence of inhomogeneous broadening in NPLs explains their narrow emission and enhanced their attractiveness. For instance, in the case of CdTe 3 ML NPLs, a FWHM of 7 nm (35 meV) is observed, which corresponds to approximately 2kT (with k the Boltzmann constant and T the temperature) at room temperature[41]. The similarity between measurements of single particle emission and ensemble measurements confirms that the observed FWHM is not caused by inhomogeneous broadening[40]. Additionally, compared to QDs, NPLs exhibit a weak Stokes shift (i.e. energetic difference between the maximums of both the absorption and emission peaks). As a result, NPLs are valuable for applications involving interparticle Förster resonant energy transfer (FRET) in dense films[42]. However, it is worth noting that NPLs may also be more susceptible to reabsorption process.

Emission efficiency.

We further characterized the NCs by determining their fluorescence quantum yield (QY), which is defined as the ratio of emitted photons to absorbed photons. This QY can be calculated using the following expression:

$$QY = \frac{N_{emitted\ photon}}{N_{absorbed\ photon}} = \frac{k_{rad}}{\sum_i k_i}$$

where $\sum_i k_i$ and k_{rad} correspond to the sum of all the relaxation recombination rates and the radiative recombination rate, respectively. Experimentally, when using an integrating sphere, this corresponds to the integration of the emitted signal divided by the difference of absorption between the excitation peak with and without the NPLs (see **Figure 5c**). In NPLs, the QY primarily depends on the surface chemistry[43], ligand coverage[44], and density of defects. Defects present in NPLs can lead to the formation of deep trap states that may exhibit either emissive or non-emissive behavior. Emissive trap states result in subband gap emission in addition to the band edge emission (as observed in the example of CdS 4 ML NPLs in **Figure 4c**). The origin of these traps can be attributed to various factors, including dangling bonds on the surface due to poor ligand passivation, defects within the NPLs (such as atoms vacancies), and dopants[45]. As the number of defects increases in the crystal, the probability for an exciton to localize on a deep trap state also increases… Additionally, larger NPLs have a higher probability of hosting defects. Consequently, larger NPLs generally exhibit lower QY ranging from a few tens of percent for small NPLs to less than 1 % for larger ones.

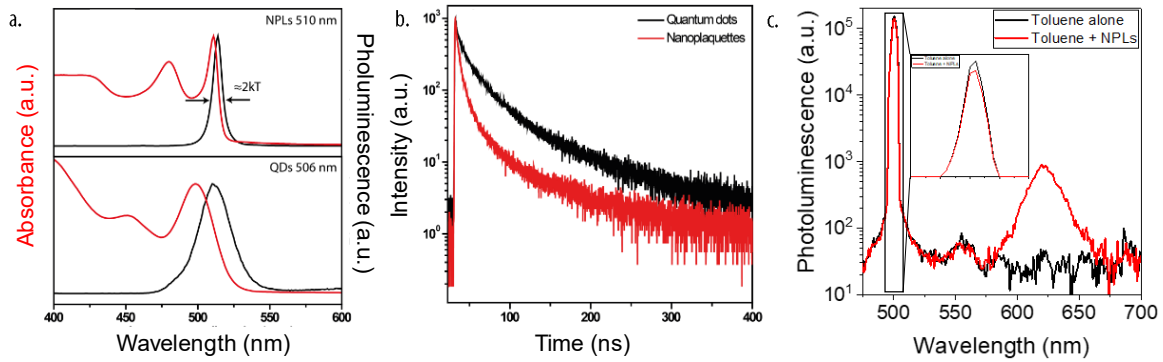

Figure 5: *NPLs as efficient emitters. a. Absorption (red) and emission (black) spectra for CdSe 4 ML NPLs (top panel) and CdSe QDs (bottom panel). b. Photoluminescence intensity decay at maximum of emission for QDs (black) and NPLs (red). The excitation is conducted at 376 nm. c. Quantum yield measurement. Emission spectra of a solution without (black) and with (red) NPLs. The small panel is a zoom on the difference of absorption of the excitation peak.* ***Figure a and b*** *have reproduced with modification from E. Izquierdo thesis.*

Emission dynamics.

Band edge and trap emissions can be distinguished based on their relaxation dynamics. The band edge emission, associated with the first excitonic transition, occurs rapidly with lifetimes on the order of a few nanoseconds. On the other hand, the emission induced by traps has significantly longer lifetime, typically in the range of several hundreds of nanoseconds[46]. In comparison to QDs, NPLs exhibit faster recombination processes[29,40] with lifetimes in the few nanoseconds range for NPLs and tens of nanoseconds for QDs (see **Figure 5b**). This difference arises from the higher binding energy of excitons in NPLs. In this sense, 2D NPLs behave intermediately between 0D QD for which binding energy of few tens meV have been reported[47], and transition metal dichalcogenides for which binding energies up to 0.9 eV have been reported[48].

To enhance the quality of the PL, the growth of NPLs heterostructures has been developed and will be discussed in the subsequent section.

2. Colloidal synthesis: from core to nanoplatelets heterostructures.

a. Nanoplatelets s as starting building blocks.

QDs VS NPLs synthesis.

In the previous section, we discussed the sensitivity of the optical properties to the size dispersion of the nanoparticles (NPs). The first syntheses of highly monodisperse NCs of cadmium chalcogenides have been developed by Bawendi *et al.*[4]. Building upon Victor LaMer's research on the nucleation and growth of colloidal NPs, they proposed a synthesis method based on the high-temperature injection of precursors, resulting in the formation of NCs with low polydispersity (<5%). Their synthesis is approach involved the addition of a highly reactive cadmium precursor, dimethyl cadmium, into a coordinating solvent (tri-octyl phosphine oxide) at elevated temperatures. By controlling this parameter, the authors were able to regulate the Ostwald ripening process, which governs the growth of the NCs. This process enabled the production of NCs with narrow size distributions.

Despite the significant progress made in achieving monodisperse NCs, a major limitation of the early syntheses (i.e. before 2000s) was the use of highly pyrophoric cadmium precursors, which are not suitable for large-scale production. To address this issue, alternative synthesis methods were developed to minimize the reliance on these organometallic compounds [49–52] or to avoid the formation of NCs through rapid injection [49,53]. These developments allowed to establish general rules for growing high-quality NCs: the precursor reactivities need to be reduced at a temperature under the growth temperature but high enough to induce the nucleation; the temperature of the reaction needs to be high to induce the crystal growth but low enough to avoid erratic growth leading to large size dispersity.

In 2005, Cao's team introduced a new synthesis approach based on these concepts[24]. They utilized selenium powder and cadmium myristate ($Cd(CH_3(CH_2)_{12}COOH)_2$, $Cd(myr)_2$) as precursors, in a non-polar and non-coordinating solvent called octadecene ($CH_2=CH(CH_2)_{15}CH_3$, ODE, T_{eb}=315 °C). To prevent oxidation, the mixture was degassed and placed under argon (see **Figure 6a** for a sketch of the setup). The temperature was set at 240 °C. During the temperature increase, the active species of selenium formed in situ through complexation with ODE, resulting in a yellowish solution at 170 °C. At around 200 °C, the $Cd(myr)_2$ starts to decompose, triggering homogeneous nucleation. CdSe nuclei formed, and the suspension gradually turned orangish. At this stage, the precursors were reactive, allowing further particle growth either by monomer attachment or by Ostwald ripening at 240 °C. This process allowed the control of the size of the particle and their optical properties. Using similar conditions, CdTe and CdS QDs were also synthesized using TBPTe[24] and sulfur[54], respectively.

A few years later, syntheses of NPLs were developed. Son *et al.*[27] obtained wurtzite CdSe whereas Ithurria *et al.*[5] synthesized ZB CdSe NPLs. In Ithurria's work, the synthesis strategy is adapted from the synthesis by Cao *et al.* with slight modifications. After the nucleation, if the reaction continues, the nuclei will undergo isotropic growth, resulting in the formation of QDs. To obtain NPLs, a symmetry break is required to induce anisotropic growth. Ithurria *et al.* proposed the introduction of a second cadmium precursor, cadmium acetate ($Cd(CH_2COO)_2$, $Cd(ac)_2$), to promote lateral extension. This $Cd(ac)_2$ is added when the color of the solution turns bright orange. The timing of this addition is critical: if the nuclei are too small (resp. too large) (i.e. addition at too low temperature

(resp. high temperature)) thinner (resp. thicker) NPLs will be formed. It is worth mentioning that during the lateral extension of the nuclei, not all of them successfully extend, which leads to the formation of QDs as a side product of CdSe 4 ML NPLs.

The introduction of carboxylate side chains with different sizes plays a crucial role in breaking the symmetry during the growth mechanism. The addition of acetates was found to be a key parameter, as other metal acetates also lead to the formation of NPLs[5]. However, the exact mechanism of symmetry breaking and anisotropic growth is still under debate. Various theories, including successive attachments of precursors[55–57], oriented attachments[9,58], templated growth[59], or dissolution recrystallization processes[60–62], have been proposed, but none of them can fully explain all experimental observations.

Regarding the lateral extension of NPLs, Norris group's research suggested that once anisotropic growth is triggered, the precursors preferentially crystallize on the lateral facets rather than on the wider ones[60–62]. Therefore, the NPLs lateral extension can be controlled by adjusting the annealing time at 240°C, or through the further injection of precursors, like in the growth of QDs. Finally, as the lateral extension is completed, the temperature is lowered to room temperature. Around 160°C, oleic acid (OA) is added to fully cover the NPLs surfaces with ligands.

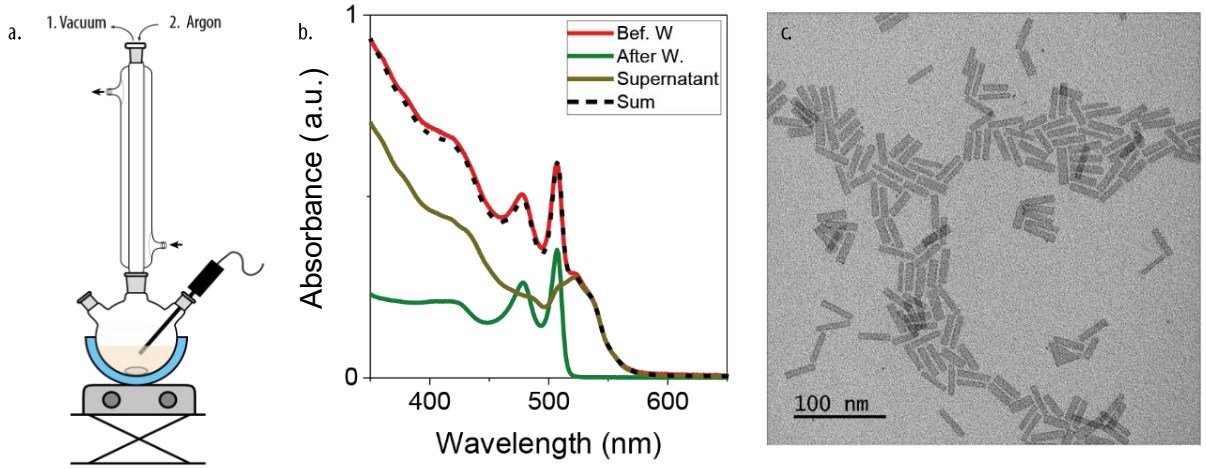

Figure 6: *Synthesis of CdSe 4 ML NPLs. a. Sketch of the setup. b. Absorption before (red) and after (green) the washing steps. The absorption spectrum of the supernatant, containing side products is shown in khaki green. The sum of the supernatant and final NPLs is plotted (dashed black) showing exact overlap with the spectrum before washing. c. TEM picture of the obtained CdSe 4 ML NPLs.*

The absorption spectrum of the final mixture is presented in red **Figure 6b**. It is a mix of NPLs and QDs with their first excitonic peaks at respectively 510 and around 540 nm. These two populations can be separated by size selective precipitation. Due to their large lateral extension, the NPLs are less colloidally stable than the QDs. So, the addition of non-solvent (ethanol, EtOH) induces their precipitation and enables their separation from QDs by centrifugation. The absorption spectra of the QD in the supernatant (dark green) and of the remaining NPLs in the pellets redispersed in hexane (light green) are shown in **Figure 6b**. After the precipitation-redispersion step, no shoulders are visible at longer wavelengths anymore on the absorption spectra of NPLs, a sign of pure population NPLs.

The as obtained CdSe 4 ML NPLs exhibit a first excitonic peak at 513 nm and a second one at 481 nm. These particles have a bright green emission presenting a very small Stokes shift of 2 nm. The QY can reach 40 % but is decreasing with the washing steps as ligands get ripped off the surface.

Transmission Electron Microscopy (TEM) is a relevant method to investigate the shape of the particle obtained and is used as a routine characterization technic. In this case, NPLs exhibit small lateral extensions (typically 30nm x 10nm, see **Figure 6c**). A continuous precursor addition, either after the formation of the small nuclei or as a second post-synthesizing step, is leading to a further lateral extension. A careful choice of the synthesis parameters can lead to NPLs with various lateral extensions. For example, CdSe 3ML NPLs from small 15 x 15 nm² squares[63] to large rectangular nanosheets of few µm²[55,57] can be obtained. The shape of the particles can be tuned by the choice of precursors. For example, the amount of acetate and its "humidity", has a drastic influence on the final aspect ratio of the CdSe 4 ML NPLs obtained using the synthesis depicted above[64]. Rectangles (resp. squares) are obtained when small (resp. large) amounts of dried acetates (resp. wet) are used. In general, the surface chemistry during the growth is driving the shape of the final particles.

The synthesis developed by Ithurria *et al.* has been later optimized to obtained thicker NPLs[5]. During symmetry breaking, the balance between the energy per surface area and the energy per volume unit is crucial to determine the thickness of the final NPLs. By tuning this ratio, NPLs of different thicknesses can be obtained. For example, the groups of Eychmüller[65], Talapin[66], and Moreels[67] have demonstrated the direct synthesis of CdSe NPLs up to 9 MLs using halide cadmium to reduce the energy per surface unit.

The growth of NPLs has been extended to other chalcogens and syntheses of CdTe[29,41] and CdS[29,37] have been developed. In these syntheses, the growth mechanism is however slightly different from the one first established for CdSe 4ML NPLs. Each population of NPLs is first extended before being transformed into a thicker population through an inter-NPLs Ostwald ripening process depicted by Norris' group[60,61]. It is worth mentioning that the shape of CdS NPLs is more erratic with the obtention of disks while CdTe syntheses lead to regular rectangles.

Alloyed NPLs.

Since their first synthesis, NPLs have been widely investigated. Various shapes, lateral extensions, and compositions can now be obtained. One of the main drawbacks remains the lake of optical features modulation. The NPLs are defined at the atomic layer scale which induces discrete values for their band gap energy. To overpass this limitation, several strategies have been implemented including tuning the surface chemistry and formation of alloys. For example, Sargent's group demonstrated the first synthesis of alloyed CdS_xSe_{1-x} 4 ML NPLs[68]. Later, in 2016, Tenne *et al.*[69]. performed the first synthesis of $CdSe_xTe_{1-x}$ 3 ML NPLs and a continuous tuning of the optical properties was obtained according to the composition (see **Figure 7a**). The band gap does not vary linearly with the composition of this alloy. In fact, the band gap energy of alloys rich in Te ($x < 0.5$) is smaller than those of CdTe and CdSe taken separately. This is a direct consequence of the bowing effect observed in alloys that postulate the following dependence for the band gap energy:

$$E_{CdSe_xTe_{1-x}} = xE_{CdSe} + (1-x)E_{CdTe} - bx(1-x)$$

with b the bowing parameter, E_{CdSe} (resp. E_{CdTe}) the band gap energy of CdSe (resp. CdTe). The experimental value of b is 0. 76 eV value[69] which is similar to the bowing parameter found for the bulk (0.75 eV[70]), see **Figure 7b**. This bowing parameter is only depending on the nature of the chalcogens.

Therefore, the emission energy of the $CdSe_xTe_{1-x}$ can also be below the band gap energy of CdSe and CdTe (**Figure 7c**). Nevertheless, the emission maximum is not following this trend and is continuously red-shifting. In addition, the higher the ratio in the small chalcogen (i.e. Se), the broader the emission. This observation can be explained by a transition between isolated clusters of CdTe and a homogeneous alloying inside the material[69]. This alloying strategy has also been implemented to $CdSe_xS_{1-x}$ NPLs that enabled to blue-shift the optical properties of CdSe NPLs[68,71].

We have seen here the first syntheses of Cd-based NPLs. We also unveiled their limitations regarding wavelength tunability and QY efficiency. Similar, to what is done for QDs, more complex heterostructures can be grown starting from these core NPLs to modulate and/or improve their optical properties.

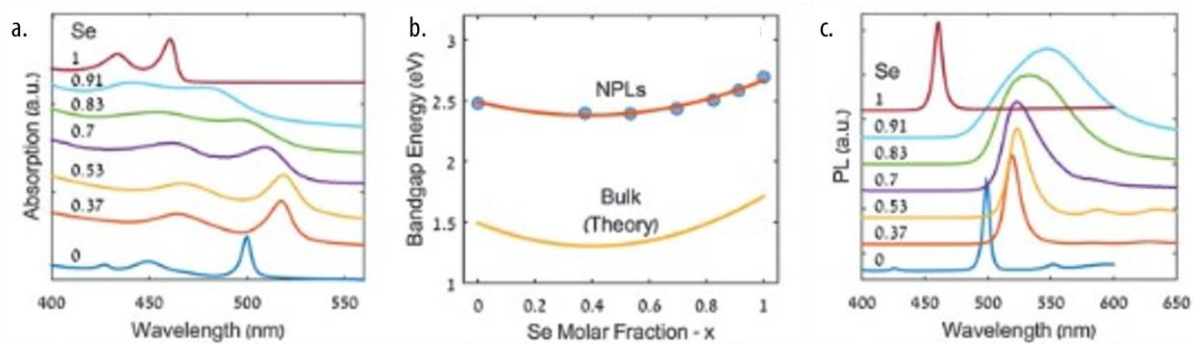

Figure 7: *Optical properties of $CdSe_xTe_{1-x}$ NPLs. a. Absorption spectra of $CdSe_xTe_{1-x}$ 3 ML NPLs for various compositions in Se. b. Band gap energy of the same NPLs according to their composition. The orange fit corresponds to the band bending fitting giving b = 0.76 eV. The yellow curves correspond to the calculated evolution of the band gap according to the composition in Se for b = 0.76 eV. c. Emission spectra of $CdSe_xTe_{1-x}$ 3 ML NPLs for the same compositions. All the figures have been taken from ref [69].*

b. Heterostructures of NPLs.

The optical properties of 2D materials are strongly dependent on the quality of the surface. A missing atom or a non-passivated dangling bond on the surface are creating traps where an exciton can recombine non-radiatively. Thus, chemist has implemented core-shell heterostructures from spherical particles to NPLs. When it comes to 2D anisotropic structure, the growth of a second material on NPLs can occur in two different directions (see **Figure 8**). This leads to the formation of two types of heterostructures. First, core-shell is obtained when the second material is added isotropically around the NPLs. The shell can be made of the same material as the core leading to thicker NPLs[35,72,73] or with a second material leading to core-shell heterostructures[72,74–76]. Besides, core-crown heterostructures can be grown while adding a semiconductor perpendicularly to the confined direction[32,77–79].

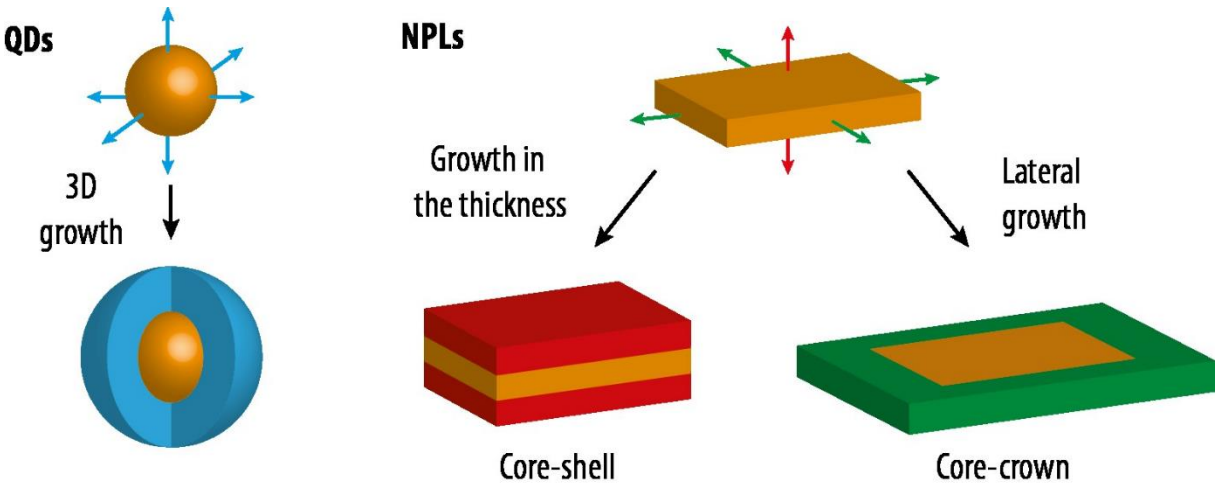

Figure 8: *Heterostructure growth. Sketch of the different types of heterostructure that can be obtained either in QDs (blue) or in NPLs (red and green). A growth in thickness leads to core-shell heterostructures (red) and a lateral growth leads to core-crown heterostructures (green).*

Band alignment in heterostructures.

Up to now, we have seen that the optical properties of NPLs could be tuned mainly through quantum confinement. In heterostructures, the electron and hole wavefunction localization depends on the band alignment between the two semiconductors (see **Figure 9a**). When an exciton is formed, the electrons (resp. the hole) will localize in the material with the lowest CB (resp. the highest VB). This is especially the case when the CB offset (ΔV_{CB}) and the VB offset (ΔV_{VB}) are high. This leads to the formation of three types of heterostructures (see **Figure 9**).

- Type I: This case is typically obtained when the band gap difference between the two materials is large (e.g., a ZnS shell-crown on top of/around a CdSe core). The highest VB and the lowest CB are located in the same material and so are the charges due to high ΔV_{CB} and ΔV_{VB} (**Figure 9a**). In this case, the optical properties, are mostly driven by the material where are localized the two charge carriers. Usually, this material of lowest band gap is localize inside the heterostructure, but inverted type I band alignment can also be found where the smallest band gap material is localize outside (e.g. a shell of HgS on top of CdSe[80]).

- Type II: In type II band alignment, the lowest VB and the highest CB are in two different materials. The band offset ΔV_{CB} or ΔV_{VB} is large enough to overpass the binding energy of the exciton and dissociate the two charges into the two materials (e.g., a CdTe shell on top of a CdSe core[81]) (**Figure 9c**). Due to Coulomb interactions, the charge carriers will preferentially be located at the interface between the two materials. Thus, while the absorption properties are determined by the two materials, the emission is governed by the interface.

- Quasi-type I band alignment: In this case, the two VB (or CB) are nearly degenerated. Therefore, one of the charge carriers is located inside the material with the smallest band gap while the second one is delocalized over the whole heterostructure (e.g., a CdS shell on top of a CdSe core) (**Figure 9b**). The optical features are closed to those observed for a type I band alignment.

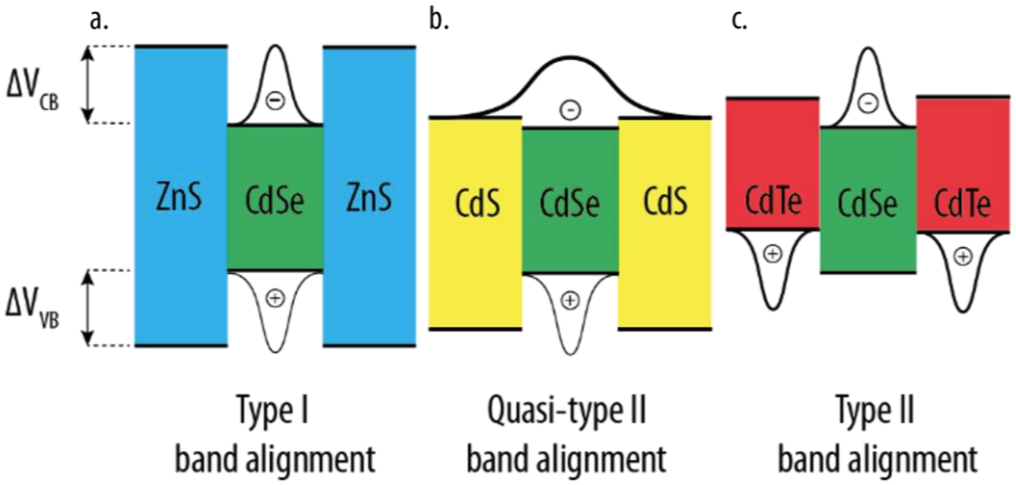

Figure 9: *Charge carriers' localization in different band alignments. a. Type I band alignment in the case of a core of CdSe and a shell of ZnS. The two charge carriers are located inside the CdSe. b. Quasi-type I band alignment in the case of a core of CdSe and a shell of CdS. Holes are located inside CdSe and electrons are delocalized over the whole NPLs. c. Type II band alignment in the case of a core of CdSe and a shell of CdTe. Holes and electrons are localized respectively in CdSe and CdTe but remain close to the interface due to Coulombic interactions.*

According to the band alignment considered, the carrier's localization can be tuned and so the optical properties of the particle. In the case of NPLs, the type of heterostructure grown (core-shell or core-crown) and the final lateral extension of the particle have also a critical effect on the optical properties.

Isotropic growth: core-shell NPLs

In NPLs, the surface-to-volume ratio is large, an efficient passivation is required to improve their optical properties in particular their QY. This passivation can be done through the use of a specific surface chemistry like using a mix of bromide and oleylamine[43,82]. It, however, leads to poor results when NPLs are deposited on films. Similar to QDs, a shell can be grown on the top and bottom facets of 2D nanoparticles to increase the PL QY in the case of a type I band alignment. Being localized in the center of the heterostructure, the active material is protected by the shell from the external environment. As a consequence, the core-shell structures tend to be more robust in comparison to core-only NPL especially when deposited on a film.

The first core-shell structures on colloidal NPs have been obtained by P. Guyot Sionnest's group at the University of Chicago in 1996[83]. At that time, they demonstrated the growth of a ZnS shell around a CdSe core, enhancing the emission properties of the core. In their work, high temperature conditions have been used which were not compatible with NPLs. In this context, in 2011, two low-temperature procedures have been developed by Ithurria *et al.*[72] and by Mahler *et al.*[74] to grow a shell on top of 2D materials using a colloidal atomic layer deposition (c-ALD). This general procedure enables the successive deposition of anion and cation layers on both wide facets (see **Figure 10a-b**). It leads to an increase in the thickness by two layers on each step. Starting from CdSe 4 ML NPLs, they obtained thicker core-shell NPLs of CdSe@CdZnS owning a type I band alignment that localized the charge carriers in CdSe. This strategy is now well understood and widely used by the community to grow complex core-shell structures with atomic layer control. However, this process involves the use of none stable precursors especially in the case of Se and Te sources.

In order to grow CdSe and CdTe shells, our team developed an alternative method to grow NPLs in thickness[35]. It is based on the activation of the wide facets. As we explained earlier, the growth in thickness is deactivated due to the bulky carboxylate ligands that passivate the surface. When performing a ligand exchange toward halides, one can nevertheless activate this surface[67]. The further addition of a growth solution leads to the crystallization of precursors on top of the wide facets. To avoid erratic growth, an additional cadmium acetate precursor is added after the completion of ≈ 1 ML to quench the reaction through a deactivation of the surface. This process induces a discrete growth in thickness with an atomic layer control of the thickness (see **Figure 10c**). This method can be applied to form thicker NPLs of CdS, CdSe, and CdTe but also to form heterostructures like CdSe-CdTe or CdSe-ZnSe which are challenging using the c-ALD method.

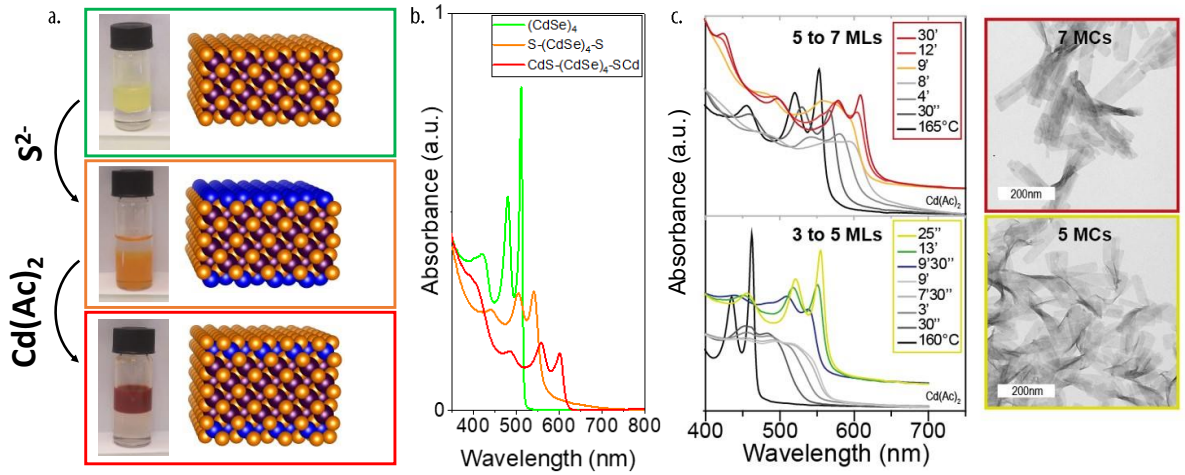

Figure 10: *Atomically controlled shell growth. a. Sketch of the c-ALD process with the growth of a layer of CdS on top and bottom facets of a 4 ML NPLs. This process involves a phase transfer from hexane to NMF (resp. on the top and on the bottom of the vial). b. Absorption spectra during the two steps of the c-ALD. c. Absorption spectra taken during the direct growth of an additional layer on top of CdSe 3 ML (bottom) and CdSe 5 ML (top) with the TEM pictures of their respective final NPLs. The colored lines correspond to the absorption spectra taken after the quenching of the reaction by $Cd(Ac)_2$ addition (adapted from ref [35]).*

Those two methods enable to control the particle's thickness at the atomic layer scale but suffer from a major drawback which is the limited quantum efficiency.

To tackle this drawback, another strategy has been proposed relying on the slow injection of the shell precursors at high temperatures (around 300°C). For example, by adding a mix of cadmium and zinc oleate, and dodecanthiol (DDT) as sulfur precursor to a mix of CdSe 4 ML NPLs dispersed in trioctylamine (TOA) at 300°C we can grow a shell of CdZnS on top of the CdSe core[75,76,84]. The growth conditions of the shell deposition are in this case harsh and the stability of the core NPLs needs to be considered. This particular point explains the current lake's inefficient growth of shells on top of CdTe-based NPLs.

To limit that, a strategy consists in introducing the NPLs at high temperatures once the shell precursors have begun to be injected. To preferentially induces the growth in thickness rather than a secondary nucleation, OA is also added before the growth. A small amount of oleylamine (OLAm) is also added in order to optimize the passivation during the shell growth of the NPLs[75,76]. At the end of the growth, no reduction of the lateral extension of the NPLs is observed. The increase in thickness can

be monitored by elemental analysis (like Energy Dispersive X-ray analysis (EDX)) and/or by TEM analysis when the NPLs successfully lay on the edge (see **Figure 11b**).

During the shell growth, the emission of the solution is shifted to the red as the shell grows thicker and thicker (see **Figure 11a**). The native ligands owning low dielectric constants are replaced by the growing semiconductor that presents a higher dielectric constant. Therefore, the approximated infinite initial quantum well will be transformed into a finite one only enabling a partial delocalization of the wavefunctions inside the shell material (see sketch **Figure 11c**). To limit this, material presenting higher band offsets can be used to confine the charge carriers in the active material. However, it often comes with a higher lattice mismatch between the two materials. When the strains become too high, the stress at the interface can create defects and hence decrease the QY.

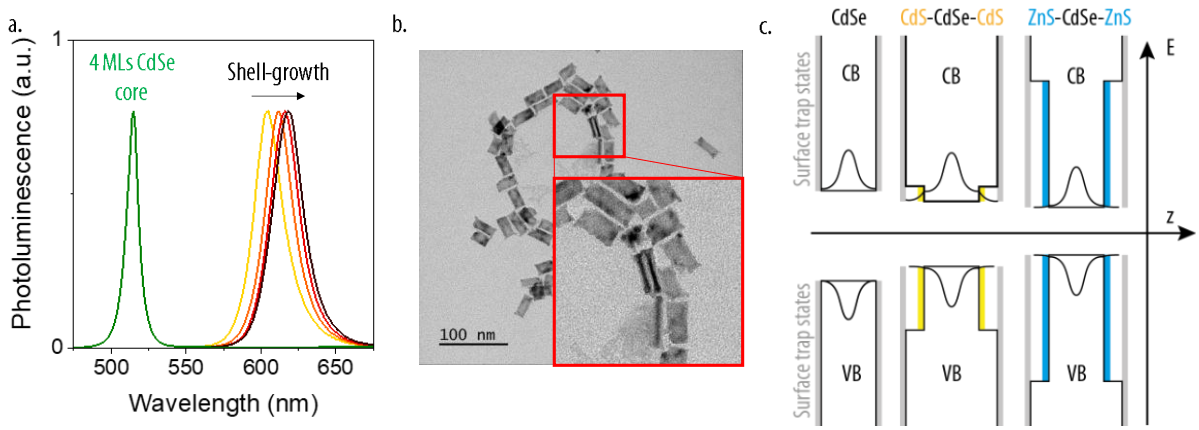

Figure 11: *Core-shell growth. a. Evolution of the photoluminescence according to the time during the growth of $Cd_{0.05}Zn_{0.95}S$ a shell on top of CdSe 4 ML NPLs. The green spectrum corresponds to the emission of the core. The spectra have been normalized for clarity. b. TEM picture of the core-shell CdSe@CdZnS. c. Sketch of the evolution of the delocalization of the charge carriers wavefunction inside the shell for three different situations: without shell, with a shell of CdS and with a shell of ZnS. In the first case, the wavefunctions can visit the surface states, in the second one, only the electron can be trapped on the surface and in the last one, all the charge carriers are localized inside the core material.*

Finally, the growth of a shell on core NPLs is leading to a large improvement in their optical properties. NPLs presenting nearly 100% PL QY[75] can now be obtained and incorporated into devices including LEDs[75,85] and lasers[86–89]. Few drawbacks might nevertheless appear: the increase in the thickness induces an indissociable redshift of the optical properties (see **Figure 11a**). A thick shell might also come with a more difficult charge injection inside the active material decreasing the efficiency of the optoelectronic device. A balance is then required between PL efficiency and charge mobility in film.

In conclusion, type I core-shell NPLs have attracted the most interest due to their high QY efficiency which can reach close to 100 % in the 600 to 660 nm range. However, core-crown NPLs ae, in a sense, more original and enable a wide tunability of the in-plane wavefunction localization leading to a large palette of optical properties.

Lateral extension: core-crown NPLs.

The first syntheses of core-crown NPLs have been developed in 2013 by Prudnikau *et al.* and Tessier *et al.* The heterostructures were made of a core of CdSe and a crown of CdS[90,91] (noted CdSe-CdS). Using similar procedures, several heterostructures have then been developed including CdSe-CdTe[32,78,79], inverted CdTe-CdSe[79], and inverted CdS-CdSe[92]. A mix of chalcogen can also be injected leading to an alloyed crown with reports on the synthesis of $CdSe\text{-}CdSe_xTe_{1-x}$ [93,94] and $CdSe\text{-}CdS_xSe_{1-x}$[71] NPLs heterostructures. In addition, the growth is not limited to only one material, instead, several

crowns can be grown successively leading to more complex heterostructures like the CdSe-CdS-CdTe core-crown-crown heterostructure developed by the Moreels' group[77]. It is worth mentioning that this method can also be implemented using the same material for both the core and the crown leading to NPLs with large lateral extensions (for CdSe[56] or CdTe[57] for example).

As for the growth of the core CdSe NPLs, the lateral extension requires the presence of both cadmium acetate and oleic acid to ensure the dispersion of the NPLs during the lateral extension. After an initial step of degassing, the chalcogens precursor (S, Se, or Te) is slowly added to the solution to limit the secondary nucleation and induce a homogeneous growth of the crown. For the same reasons, the injection speed and the temperature are chosen according to the introduced chalcogen and the thickness of the initial NPLs. Consistently with the model developed by Norris' team, the completion of the lateral facets is far more favorable than the wide ones[60]. As a result, the extension will only occur laterally. Following this same model, this process becomes tougher as the thickness increases explaining the higher temperatures used during the lateral extension of thicker NPLs[90].

When two different materials are used, elemental analysis of the chalcogenide ratio through EDX can give insights into the lateral extension increase. However, it doesn't enable localizing the position of the core inside the final particle. Elemental mapping using TEM coupled with EDX is usually used to investigate the geometric parameters of core-crown NPLs[78].

When a lateral extension is carried out, the thickness of the material added remains the same as the core. This enables perfect control of the crown thickness. The quantum confinement and the dielectric environment remain the same for the core material, and the absorption properties of the core material are usually left unaffected. For example, **Figure 12** is following the absorption of the reaction during the growth of a CdS crown around CdSe 4 ML NPLs core. Initially, the features at 510 nm and 480 nm correspond only to the CdSe 4 ML NPLs (green arrow). As the growth is occurring, another contribution appears around 405 nm (blue arrow). This absorption corresponds to the excitonic features of CdS 4 ML NPLs. This peak becomes stronger and stronger testifying to the lateral extension of the crown.

Thus, the absorption spectrum of the core-crown heterostructure results from the addition of the absorption features of the core and the crown. Therefore, we can monitor the growth of the crown through the evolution of the associated absorption features. This is especially the case when the excitonic peaks of the core and the crown are not overlapping. For example, in **Figure 12b** is monitored the growth of a crown of $CdSe_{0,5}Te_{0,5}$ around a core of CdSe. The alloy owning a narrower band gap as CdSe, its first excitonic peak is localized at higher wavelengths. As the crown is getting larger and larger, the optical properties of the $CdSe_{0.5}Te_{0.5}$ crown are slowly increasing while red-shifting. This behavior had already been observed during the synthesis of CdSe-CdTe core-crown[78] and had been attributed to lateral quantum confinement that occurs when the crown is thin. This has even been used as a way to tune the color of a particle in the case of CdS-CdSe core-crown[92].

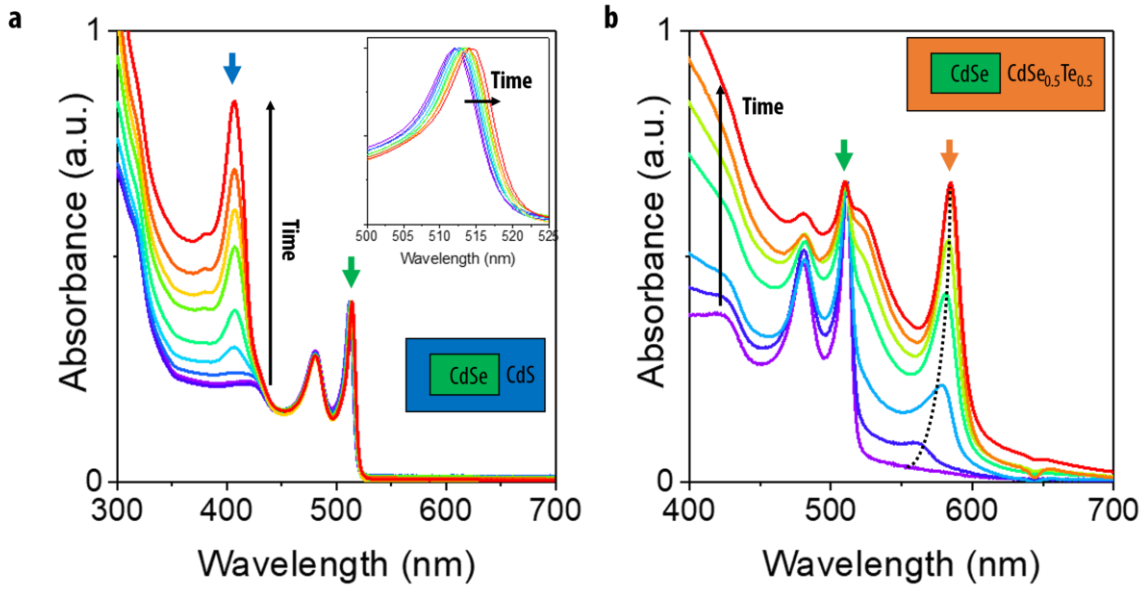

Figure 12: *Lateral confinement in core-crown NPLs. a. Absorption spectra according to the time of injection during the growth of a CdS crown around a CdSe 4 ML core. The blue and green arrows correspond respectively to the first excitonic peak feature of CdS and CdSe. The small panel shows a zoom on the first excitonic peak of the CdSe core. b. Absorption spectra according to the time of injection during the growth of a $CdSe_{0.5}Te_{0.5}$ crown around a CdSe 4 ML core. The green and orange arrows correspond respectively to the first excitonic peak feature of CdSe and $CdSe_{0.5}Te_{0.5}$.*

When a semiconductor absorbs a photon, an electron is promoted from the VB to the CB leaving a hole in the first one. This newly created electron-hole pair can then recombine and emit a new photon. This recombination is possible only if the electron and hole wavefunctions overlaps. As a consequence, and contrarily to the absorption properties, the emission features in a core-crown heterostructure will mainly depend on the localization of this electron-hole pair rather than on quantum confinement alone. And this localization depends on the band alignment.

- *Quasi-type I heterostructure like CdSe-CdS:*

In CdSe-CdS 4 ML NPLs, a quasi-type I band alignment is obtained. Both electron and hole wavefunction are localized in CdSe and the emission is similar to the core only NPLs (see **Figure 13c**). Indeed, the VB is large leading inducing the presence of the hole in the CdSe. Despite a small ΔV_{CB}, the exciton binding energy is such that the electron will also remain in CdSe (see **Figure 13a-b**). In addition, by growing a lateral crown of CdS, the dangling bonds on the edges of the NPLs will be passivated, decreasing the number of surface trap states. This will reduce the non-radiative deexcitation channels leading to an increase of PL QY. In the case of CdSe-CdS NPLs, stable QY up to 90% can be obtained[44,95].

Excitons can also be created in the CdS crown. Due to the large ΔV_{VB}, it will diffuse toward the CdSe core. Therefore, the CdS is also playing the role of exciton concentrator, enhancing at the same time the absorption cross-section of the particle. This can easily be observed using photoluminescence excitation (PLE) measurements on two populations of core-crown NPLs presenting different CdS crown sizes (see **Figure 13d**). The PLE spectra conducted on the diluted solutions are perfectly matching their respective absorption spectrum: confirming the concentrator effect of the CdS crown. When the size of the CdS is drastically increasing, the probability for the exciton to encounter trap-states during their diffusion toward the core increases. Thus, this induces a decrease in the QY.

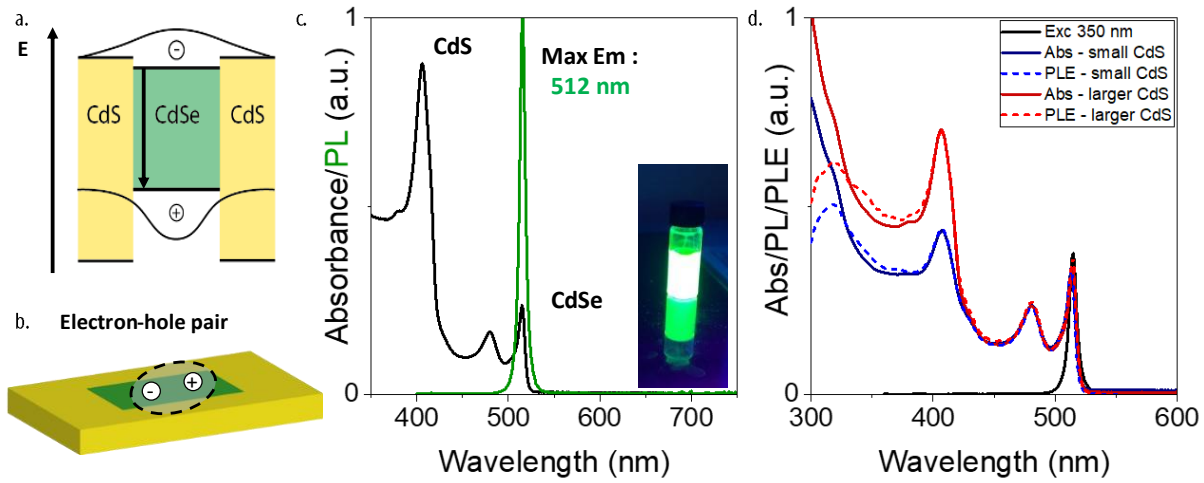

Figure 13: *Quasi-type I core-crown heterostructure. a. Band diagram of CdSe-CdS core crown. b. Sketch of the core-crown NPLs with the localization of a formed exciton inside the NPLs. c. Absorption (black) and emission (green) spectra of CdSe-CdS core-crown NPLs. The picture shows shows a vial containing those particle exited by a UV lamp at 385 nm. d. Absorption (colored solid), emission (black, exc 350nm) and PLE measurement (em 518 nm) for two different size of CdS crown.*

In conclussion, type I or quasi-type I band alignment in core-crown heterostructures like CdSe-CdS enables to increase the QY, like in a core-shell structure, but without changing the wavelength of emission. Those particles are very bright in solution but lakes the robustness brought by the shell in core-shell structures. Consequently, their uses in optoelectronics remain limited with only few reports on LEDs[96,97] or laser[98].

- *Type II heterostructure like CdSe-CdTe:*

In the case of a type II band alignment like CdSe-CdTe, when a photon is absorbed in the CdSe part (resp. CdTe), the driving force ΔV_{VB} (resp. ΔV_{CB}) will drag the hole (resp. the electron) toward the CdTe crown (resp. the CdSe core). Thus, the charge carriers are localized in the two different materials. Nevertheless, due to the Coulombic interactions, the two charges will be mostly localized at the interface between the two materials (see **Figure 14a-b**). When coupled with phonons, electrons, and holes can recombine through this interface. This leads to the emission of a photon that owns a smaller energy in comparison to the two materials taken separately, offering an interesting alternative to quantum confinement for the design of emission properties. For example, in the case of the CdSe-CdTe 4 ML core-crown, the first excitonic peaks of CdSe and CdTe are localized respectively at 512 nm (2.42 eV) and 555 nm (2.23 eV) while the interfacial recombination is centered at 655nm (1.89 eV) (see **Figure 14c**). So, this interface does not forbid the exciton recombination, but only separates the two charge carriers, limiting the overlap of their wavefunction. As a consequence, the emission dynamic is usually slower (up to several hundred ns)[79] than at the band edge.

This interfacial recombination is also broader than the band edge emission of the two pristine materials. Here, the FWHM of CdSe and CdTe emissions are respectively 9 and 7 nm[41] while the FWHM of the interfacial recombination is around 60 nm (170 meV). This difference arises from different reasons: the nature of the recombination that is induced by a phonon coupling which will enlarge the resulting emission[99]; the local composition and strains at the interface that induces inhomogeneous band alignment along the interface; the presence of defects at the interface due to the nature of the lateral growth (lower temperature growth than for core-shell leading to poorer crystallinity). Nevertheless, due to the high driving force ΔV_{CB} and ΔV_{VB} in type II band alignment, it becomes more

interesting for the charges to be localized at the interface rather than in shallow surface trap states. As a consequence, this specific emission presents also a higher QY (up to 50%). The possibility for the exciton to be formed in both materials enables also a large absorption cross-section for those materials.

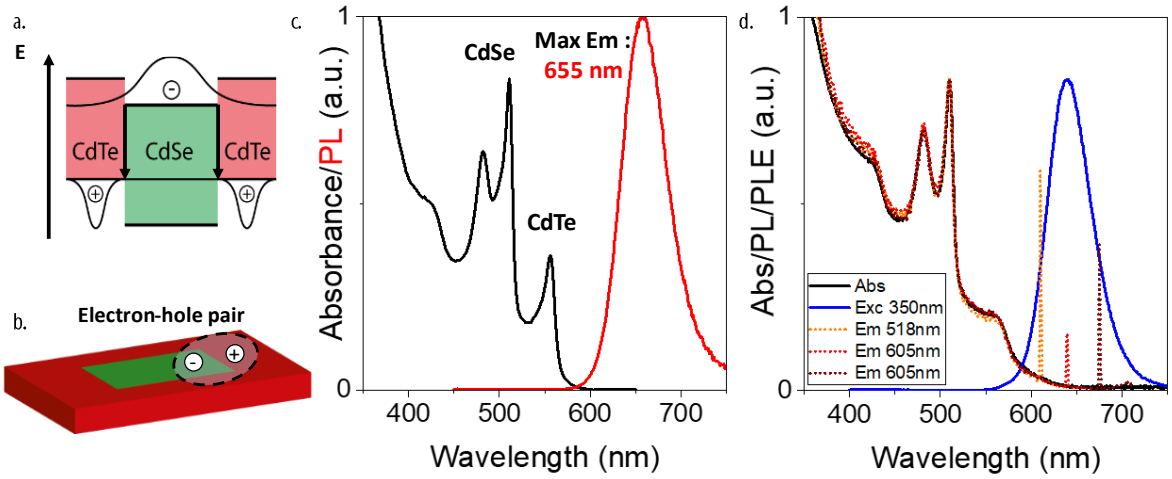

Figure 14: *Type II core-crown heterostructure. a. Band diagram of CdSe-CdTe core crown. b. Sketch of the core-crown NPLs with the localization of a formed exciton inside the NPLs. c. Absorption (black) and emission (red) spectra of core-crown CdSe-CdTe. d. Absorption (black), emission (blue, exc 350nm) and PLE measurement (dot lines, at different wavelength).*

The band offsets ΔV_{CB} and ΔV_{VB} between the two materials considered drive the optical properties of the final particle. It is however possible to tune their value using a crown made of alloys. Kelestemur *et al.* and Dufour *et al.* investigated CdSe-CdSe$_x$Te$_{1-x}$ core-crown NPLs and unveiled more complex behavior according to the Se/Te ratio in the crown[93,94]. Especially, bicolor emitting particles were obtained using a 4/6 Se:Te ratio in the external crown[93].

Through those few examples, we saw the large possibility enabled by the core-crown heterostructures in NPLs. Contrary to type II QDs[81,100,101], NPLs own the advantage of controlling the quantum confinement with extreme precision, even during the growth of the crown.

Up to now, I have discussed the formation of cadmium-based NPLs. However, other colloidal II-VI 2D materials have also been successfully synthesized like Pb-based NPLs[9,102], Zn-based NPLs (mostly wurtzite)[36,103], and Hg-based NPLs[38,39,80]. In this last case, direct syntheses have nevertheless not been developed yet.

c. Cation exchange.

We have shown that Cd-based NPLs are synthesized using hot injection procedures. At high temperatures, the exchange equilibrium between the nanocrystals and the solution is dynamic due to the large thermal energy available in the system. Consequently, those hot injection syntheses are working well for relatively stable particles but fail in producing metastable particles. To overpass these limitations, chemists proposed a cation exchange (CE) on already synthesized NPLs.

In bulk materials, the solid-state[104] exchange is usually limited by the diffusion length of the atoms inside the material. To increase their mobility, high-temperature treatments are usually conducted. A famous example is the doping of Si with dopant species that are conducted at 850 to 1150°C[105]. In comparison, less severe procedures can be used in NCs due to their high surface-to-

volume ratio, enabling exchange down to room temperature. Thus, Schoos *et al.* implemented the first CE procedure on NCs in 1994. In their work, they mixed at room temperature, CdS QDs with a Hg^{2+} precursor[106]. In this first attempt, only the top layers of CdS have been exchanged and a CdS-HgS core-shell was formed. This opened the path for numerous possibilities in creating new NCs structures.

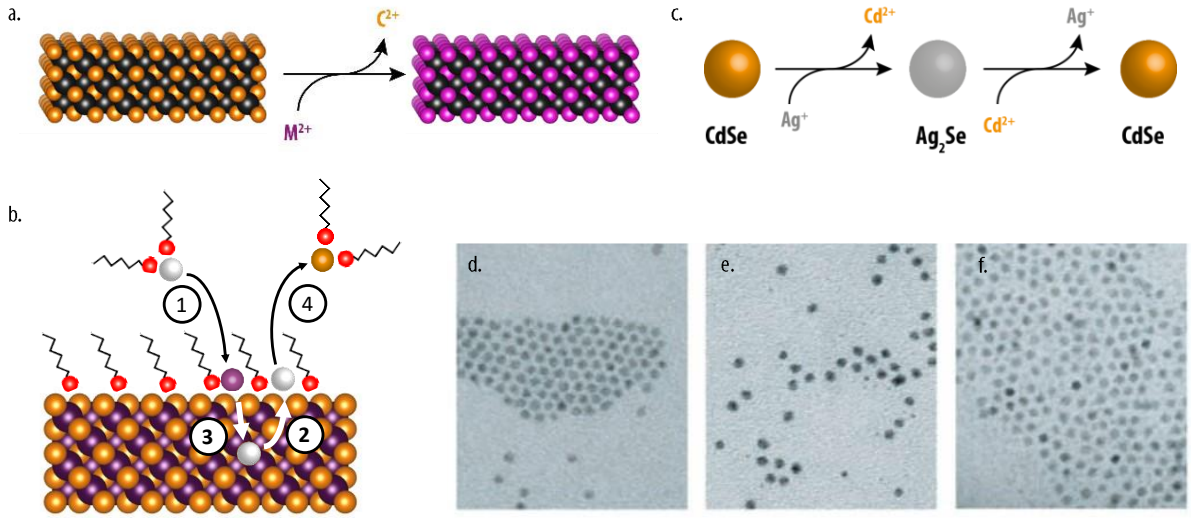

Figure 15: *Cation exchange. a. Sketch of the topotactic sum up of the cation exchange for a ZB NPLs. The incoming cation is in purple and the host cation is in orange. b. Sketch of the detailed steps of the cation exchange. The white sphere corresponds to the initial position of the pointed cation. c. Sum up of the first cation exchange and retro-exchange performed by Son et al. on CdSe QDs. d-f. Associated TEM pictures with respectively the initial QDs, the Ag_2Se QDs and the retro-exchanged CdSe QDs.* ***Figure 10c-f*** *are reproduced from ref [111].*

In II-VI semiconductors, two different exchanges can be expected: anion and cation exchanges. Due to their large ion radii, anion exchange often owns low mobility and is then less efficient as opposed to the case of halide perovskite in which anion exchange is easier[107]. On the other hand, the small cations can be easily replaced by another cation[108,109]. These CE procedures are all based on the same idea: replacing a host cation with another cation without changing the anion framework. To do so, the NCs are put in the presence of a dissolved ionic crystal with an incoming action that would lead to the topotactic CE (see **Figure 15a**). This can be summed up by the following equation where M, C, and A correspond respectively to the incoming cation, the host cation, and the anion:

$$mM^{n+}_{(solvated)} + nC - A_{(solid)} = nC^{m+}_{(solvated)} + mM - A_{(solid)}$$

As mentioned by the n and m ratio in the sum equation, the CE can involve cations owning similar (Cd^{2+}, Pb^{2+}, Hg^{2+}…) or different (Ag^{+}, Cu^{+} …) oxidation states. This process, in solution, can be divided into several steps[108,110]. All those steps are critical during the exchange as all the sub-products are the reactants of the next steps. In consequence, acting on one step of the reaction will affect the whole process (see **Figure 15b**). The steps mentioned include:

- 1. Migration toward the surface and desolvation of the incoming action. This step strongly depends on the surface chemistry of the NPLs as well as the ligands that surround the precursor.
- 2. Diffusion of the host cation outside the NPLs. This step strongly depends on the lattice parameter and the ionic radius of this cation.

- 3. Diffusion of the incoming cation through the anion lattice. This step strongly depends on the lattice parameter and the ionic radius of this cation.
- 4. Migration away from the surface and solvation of the host cation. This step strongly depends on the surface chemistry of the NPLs and the available ligands in the solution.

The activation energy of the diffusion is generally high. At room temperature, this diffusion usually limits the depth of the process to a few layers. Thus, while considering those different steps, the CE will be possible only if some conditions are fulfilled:

- The ionic radii of the cation need to be small enough to inter-diffuse in the anion framework.
- The lattice parameters of the initial and final crystal structure need to be similar to avoid the apparition of high lattice constrains.
- The crystal energy of the initial crystal needs to be higher or at least equal to the final crystal one to limit the retro exchange.
- The solubility of the host cation in the solution needs to be higher or at least equal to the incoming cation's one to favor the extraction of the host cation.

As a consequence, valuables chemical parameters such as the hardness of the ligand/cations, the solubility, and association/dissociation energies … are relevant to optimize a CE[108]. While the structural parameters are intrinsic to the cation exchange, the chemist can play on the other parameters to modulate it. Using Pearson's HSAB (Hard-Soft Acid-Base) theory, one can modulate the affinity of the cation with the present ligands and thus stabilize the system in the wanted composition. For example, in 2004, Son *et al.* observed the first full CE in NCs by introducing an Ag^+ precursor dissolved in methanol in the presence of CdSe NCs[111] (see **Figure 15c-f**). The presence of this hard basis solvent is dragging out the hard acid Cd^{2+} cations and Ag^+ , as a soft acid, enables the formation of Ag_2Se particles. The retro-exchange (i.e. back to CdSe) has also been successfully implemented through the addition of trioctylphosphine. This last soft basis is dragging out the soft acid Ag^+ cation leading to the reformation of the CdSe NCs.

During this exchange, they also observed a reorganization of the surface that led to the modification of the shape of the initial particle (from rods to QDs). This unveils one of the key challenges of the CE process in NPLs: preserving the shape of the particle. In fact, due to their high surface-to-volume ratio, these are metastable materials. When the cation exchange is too fast, the anion framework can be disturbed leading to the formation of particles that minimize this surface-to-volume ratio, in other words, spherical particles[111]. A difference in the diffusion rate of the host and incoming cations respectively outside and inside the particle (i.e., Kirkenhall effect) can also lead to a disaggregation of the particle during the process[112].

According to the conditions implemented and the involved material, partial or complete CE can be performed (see **Figure 16**). A full CE can lead to the obtention of new nanoparticles like Hg-based NPLs as described later in this manuscript. By tuning the quantity of the incoming cations, alloyed or doped particles with controlled compositions like $Zn_xCd_{1-x}Se$ QDs[113] or Ag^+, Cu^+ CdSe[114–116] 4 ML can be synthesized. Small domains inside a matrix can also be obtained like $Cd_xHg_{1-x}Se$ domains inside a CdSe matrix[117]. HgS@CdS QDs[106] or ZnSe@ZnS NPLs[118] can also be obtained, thanks to both the non-mixing of the two materials during the CE and to the limited diffusion length of this process.

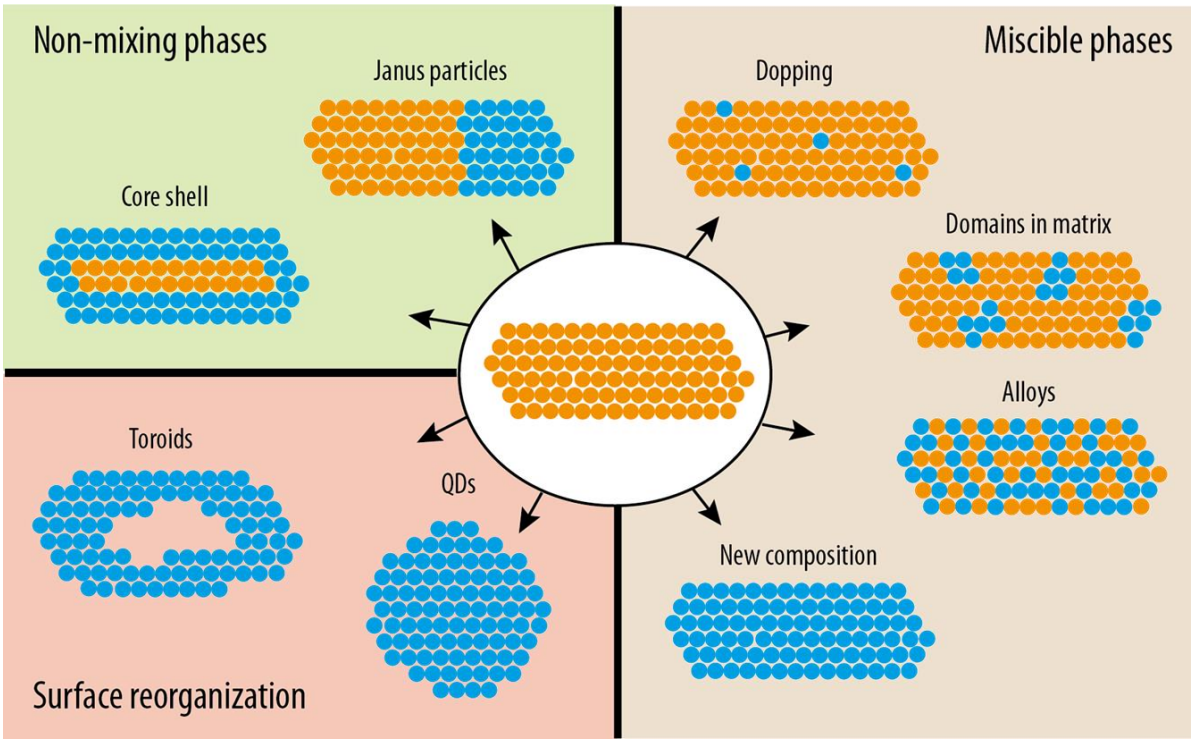

Figure 16: *Sketch of the variety of new materials that can be obtained from cation exchanges. Inspired by ref [108].*

Using surface reorganization as a tool, new shapes can be achieved like toroids[112], or a change from rods to QDs can be performed[111]. Finally, this procedure is not limited to II-VI semiconductors but can be implemented in other materials including III-V[119,120], I-VI[118,121,122], and IV-VI[118,123–125] semiconductors with various shapes. This large variety of new materials is obtained from a new pool of advanced materials for further applications.

3. Unveiling the electronic structure and charge dynamics in NPLs.

The synthesis of new materials, and especially new heterostructures, requires to understand the photo physic behind the processes that occur inside the particles. Classic absorption spectrometer to complex pump-probe setups are used according to the process investigated. During my Ph.D., I got the chance to visit and conduct on the time-resolved photoluminescence and transient absorption setups of Dr. B.T. Diroll at the Argonne National Laboratory optical measurements. I also get the opportunity to conduct photoemission measurements on the TEMPO beamline of SOLEIL under the supervision of Dr. M.G. Silly. Thus, in the following section, I will introduce those setups, their use and the information that can be extracted from the measurements.

a. Optical spectroscopy to monitor the charge carrier dynamics.

During the absorption process, an electron located in the VB is promoted in the CB creating an exciton. After its formation, this exciton can encounter different relaxation processes (see **Figure 17**):

- *Intraband cooling:* Through intraband cooling, the system will decrease in energy as the charge carriers will localize in the top and bottom levels of the VB and CB. This process is fast (ps).

- *Trap-de-trapping:* The exciton can be relocated in traps. A de-trapping process can occur to free the exciton but the overall process will induce a delay in the exciton's relaxation. In some cases, *trap recombinations* can occur leading to a non-radiative relaxation.
- *Auger recombination:* when a multiexciton regime is obtained, an exciton can recombine non-radiatively to promote an electron of a second exciton to higher energetic states.
- *Photoluminescence:* the exciton can recombine radiatively either through direct recombination *(fluorescence)* or through intermediate-state radiative transitions (*phosphorescence*).
- *Stimulated emission:* Under an incident light, the interaction with an incoming photon can induce the emission of an identic photon with the same energy, the same direction of propagation, and the same polarization.
- *Inter-particular process*: When NCs are close to each other, energy transfers can occur by Förster Resonance Energy Transfer (*FRET*), or *charge transport* between NCs can occur.

To disentangle all these different processes, the dynamics of the photoluminescence can be investigated through Time-Resolved Photoluminescence (TR PL) or the relaxation of the excited states through Transient Absorption (TA).

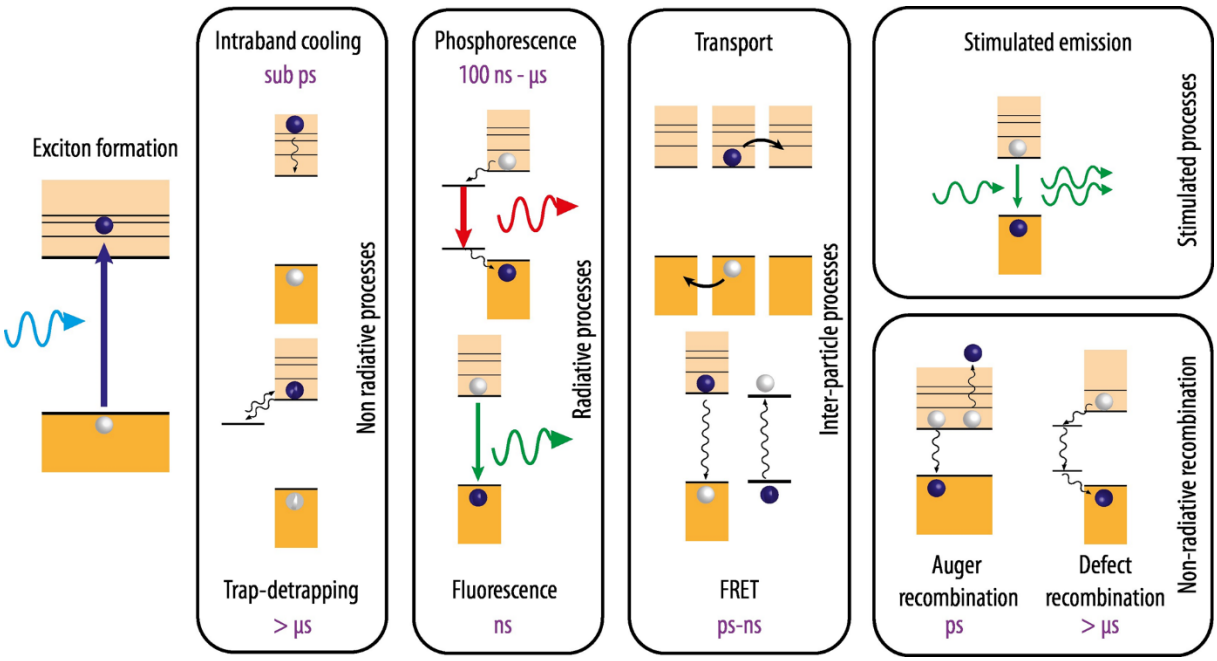

Figure 17: *Exciton dynamic processes. Sketch of the main different processes that can encounter an exciton after its formation. In purple is given an approximation of the timescale of each process.*

Time-resolved photoluminescence.

The TR PL involves the excitation of a particle using a pulsed laser (typically 376 nm with a 70 ps pulsed width in our setup) and the collection according to the time of the emitted photons. The repetition rate of the laser is set for the PL dynamic to come back to zero before the next pulse. A sketch of the experiment is shown in **Figure 18a**. This method only enables a time resolution limited by the detector answer (down to tens of ps for the state-of-the-art Microchannel-plates Photomultiplier Tubes (MCP-PMT)[126]). This resolution perfectly matches the relaxation dynamics of band edge emission and slower processes (trap-emission, interface emission …). However, TR-PL gives only insights into radiative relaxations and fails in probing the non-radiative processes. In addition,

photoluminescence is often associated with several simultaneous processes leading to multiexponential decay. It is difficult to disentangle the different contributions.

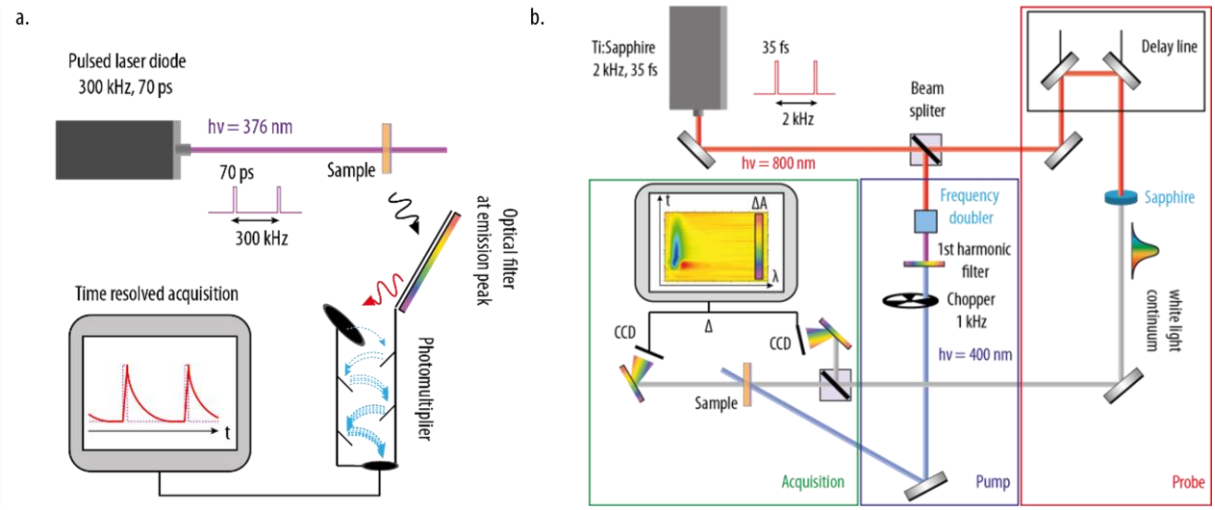

Figure 18: *Studying the dynamic inside NPLs. a. Sketch of the time-resolved photoluminescence setup. The source is a pump laser at 375 nm with a 300 kHz repetition for a 70 ps pulse width. b. Sketch of transient absorption setup. The laser source is a Ti: Sapphire at 800 nm. In the pump section (in blue) the laser is doubled and filtered to obtain a source at 400 nm. In the probe section, a sapphire disk is excited to obtain a white continuum. In the acquisition section, the absorption is measured by subtracting a reference white light spectrum from the spectrum measured after the sample. The ΔA is then obtained by subtracting an absorption spectrum taken without laser excitation.*

Transient absorption.

On the contrary, TA experiments enable monitoring the filling and emptying of the excited states. This method consists in using a synchronized pump (laser at 400 nm) and probe (white light continuum) to monitor the absorption evolution inside the solution. During the short times following the absorption of a photon, fast processes like the intraband cooling down of the charge carriers and their migrations can happen. Classical MCP-PMT detectors cannot reach the sub ps time resolution required here for such phenomena[34].

To tackle this issue, the pump and the probe can be obtained using a pulsed laser source. For example, an 800 nm laser with a short pulse of a few tens of fs can typically be used. The resolution is yet decreased down to the width of the pulse. To synchronize the pump and the probe, a unique pulsed source equipped with a beam splitter is used. A delay line is then added to induce a difference in the optical path of the two pulses. In most cases, the energy of a source at 800 nm is not sufficient to excite the studied NCs. So, the pump beam is doubled using nonlinear crystal materials to produce a pump source at 400 nm. The white light continuum used to probe the absorption is obtained by the excitation of a sapphire substrate using the 800 nm probe beam. Finally, the pump and the probe are aligned to overlap on the sample and the absorption signal is obtained using a CCD detector. A sketch of the used setup is shown in **Figure 18b**.

During TA experiment, the absorption before the pulse and after the excitation pulse are compared (ΔA):

$$\Delta A(t) = A_{after\ pulse}\ (t) - A_{bef\ pulse}$$

the probe intensity is generally reduced to approximate $A_{bef\ pulse}$ to the absorption of the ground state. The analysis of ΔA will give insights into the process occurring during the relaxation time of the excited state.

First, excitons are generated by the pump source. After the pulse, the excited states are populated with charge carriers. As a consequence, fewer electrons can be promoted from the VB. This induces a bleach of the associated absorption features (ΔA<0) and is called ground-state bleach. Through emission, trap-detrapping, delocalization, or intraband cooling of the exciton, the excited state will relax either to an intermediate or to the ground-state (ΔA is coming back to 0). By monitoring the bleach time evolution, one can probe the dynamic of this relaxation. A probing photon can also induce stimulated emission of an electron leading to an increase of the light received by the detector. As a consequence, a ΔA<0 is observed, red-shifted in comparison to the ground-state bleach. It is sometimes difficult to detangle those two phenomena.

In the case of heterostructures, selective excitation can be performed to induce the formation of exciton in a unique material. The migration of charge carriers can then be monitored through the post-pulse bleach increase of other optical features leading to a ΔA<0; these phenomena are called charge transfers.

Other features can be observed like excited-state absorption, enabling to monitor intraband transitions, Stark effect, and sub-product formation … Overall, TA measurements are interesting to probe non-radiative processes and investigate the dark and deep-trap states. When transport occurs in an NCs array, other measurements are used to investigate it.

b. Field effect transistor to probe majority carriers.

Transport in an NCs array.

In NCs arrays, the wavefunctions are localized inside the particles and the transport of charges only occurs through tunnel events between particles. This process is called hopping transport and has to be opposed to the band transport that happens in bulk semiconductors where the wavefunctions are delocalized over the volume. This thermally activated process explains the associated low charge carriers mobilities measured[127,128] (commonly 1 $cm^2.V^{-1}s^{-1}$ whereas the mobility in undoped silicon[129] reaches 1000 $cm^2.V^{-1}.s^{-1}$). To flow in an NCs channel, charge carriers will encounter successive tunnel events through a percolation path inside the film (**Figure 19a**). In a classical device, the electrodes are separated by several µm. To reach high performances, good charge mobilities are crucial. Some NPLs syntheses are now enabling the obtention of large laterally extended NPLs that would reduce the number of hopping events to cross the channel. In addition, the hopping transport is sensitive to quantum confinement changes, including deep trap states but also NCs size inhomogeneities (see **Figure 19a**). The controlled synthesis of NPLs leads to no broadening of the thickness in NPLs in comparison to QDs. As a consequence, these particles are good candidates to reach large mobility at the film scale.

Due to its tunnel nature, this mobility is also sensitive to the inter-particular distance[127,128]: the closer the NCs, the higher the mobility. Thus, the surface chemistry of the particle is an important parameter to consider. The native bulky ligands, originated from the colloidal synthesis, will create large insulating shells around the NCs leading to a low probability of inter-particular hopping (see **Figure 19b**). Total removal of the ligands is here not considered as it would induce surface dangling bonds and trap states formations on the particle. Ligand exchange toward short ligands has proven its

efficiency. Short bidentate organic (ethanedithiol (EDT)[130], short amines …) or inorganic (sulfide anion[130], zintl ions[131], …) ligands can be used to increase the particles packing and decrease the inter-particular distance. In addition, sulfide anions induce a decrease in the activation energy required for a hopping event, increasing the mobility of the charges (see **Figure 19b**).

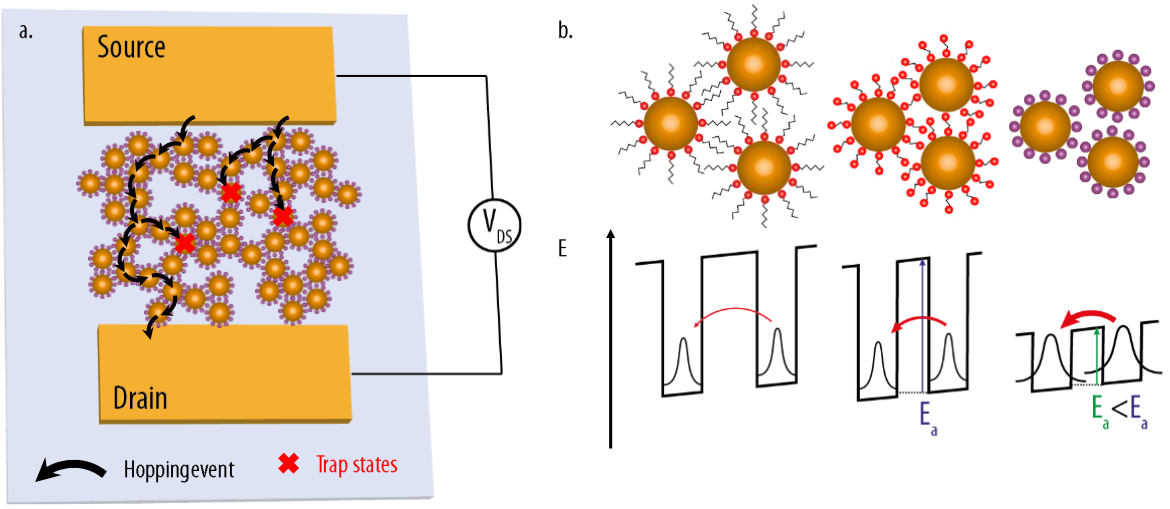

Figure 19: *Hopping transport in NCs arrays. a. Sketch of the percolation path that enables conduction through a NCs channel through hopping event. The Ncs are deposited between two electrodes and a bias is applied. The cross in red are representing traps that prevent the conduction due to immobilized charges. b. Sketch of the potential landscape of a film of NCs with different surface chemistry. The panel on the left represents long alkyl chains, the panel in the middle can be attributed to EDT ligands and the panel on the right to sulfide anions. The size of the red arrow is proportional to the probability of a tunnel event.*

Depending on the targeted the final ligands, several approaches can be considered for the ligand exchange:

- *Ligand exchange in solution:*

This process is similar to the successive layer deposition conducted in c-ALD[72] and is generally used for anion-capping ligands . The anions are first dissolved in a polar solvent like N-methylformamide or dimethylformamide. The NPLs suspension in non-polar solvent is then added and a biphasic mixture is formed. The ligand exchange induces a phase transfer of the NPLs in the polar solvent. This process is similar to the one used when doing colloidal atomic layer deposition. The obtained suspension is usually called an “ink” and is attractive for its user-friendly processability.

- *Ligand exchange on film:*

In other cases, the ligand exchange is performed directly on a film of NCs capped with long aliphatic chains. It is used when ligand exchanges in solution leads to the aggregation of NCs. After the deposition of the NCs arrays, the films are dipped into a solution where an excess of incoming ligands is present. The diffusion of the ligand inside and outside is nevertheless limiting the thickness of the films that can be exchanged.

Ligand exchange with short ligands, conducted on film, induces a shrinking of the film volume which leads to cracks. Several successive thin depositions can be performed to obtain homogeneous

film through the filling of the cracks. These multiple steps are crucial, especially for optoelectronic applications where the quality of a film is critic for transport properties.

Field-effect-transistors.

A common strategy to probe the charge mobility in a film of NCs consists in designing a Field-Effect-Transistor (FET). It is composed of the nanoparticles layer, a dielectric, and three contacts: source, drain, and gate (see **Figure 20a**). This device enables the injection of charge carriers inside the studied film. In this geometry, the current I_{DS} flowing through the film, can be monitored by applying a bias, V_{DS}, between the drain and the source. Through the gate-source channel, a bias V_{GS} can be applied to inject charges in the semiconductor: the higher the bias, the larger the carrier density injected, this is the gate effect. For example, a negative V_{GS} will fill the gate with electrons. To counterbalance the excess charge, holes will be supplied in the semiconductor channel. Therefore, monitoring the current flowing through the drain-source, I_{DS}, according to the V_{GS} bias, will unveil the majority carrier nature inside the semiconductor as:

- If the conductance increases for a positive $V_{GS,}$ the majority carriers are electrons, it is a n-type semiconductor.
- If the conductance increases for a negative $V_{GS,}$ the majority carriers are holes, it is a p-type semiconductor.
- If the conductance increases for both a positive and a negative V_{GS}, the semiconductor is “ambipolar”.

Sketches of transfer curves are presented in **Figure 20c**. They present a specific threshold value linked to the relative localization of the Fermi level in the gap of the semiconductor: the closer it is from a band, the smaller will be $|V_{GS,thr}|$. Consequently, FET measurements enable us to determine the Fermi energy inside a semiconductor, see **Figure 20d**. This information is crucial for further incorporation of the material inside optoelectronic devices.

First, to make a FET, gold interdigitated electrodes (20 µm spacing) are designed using optical lithography on a Si/SiO_2 substrate. NCs are then deposited on top of the interdigitated electrode pattern. To enhance the coupling between the neighbors and ease the hopping transport, a post-deposition ligand exchange using ethanedithiol (EDT) has been performed. These new ligands have the double advantages to present two anchoring groups and a small carbon chain which is ideal to achieve cross-linking.

Then, several types of dielectrics can be used to form an FET. Here, instead of a conventional dielectric, we used an electrolytic matrix of polyethylene glycol containing lithium perchlorate $LiClO_4$ topped with a copper grid used as the top gate electrode[132]. The mobility of the Li^+ inside the gel forms a capacitor in the electrolyte through the accumulation of Li^+ cations near or far from the grid, inducing the gate effect. This ion-gel strategy is interesting as:

- It enables measurements in the air.
- It enables high gate capacitance inducing the injection of a large number of charges (up to several carriers per NCs).
- Thick films can be gated thanks to Li ions percolation within the film of particles.

This last point is particularly advantageous for the design of phototransistors where thick films are desired to enhance the light-matter interaction.

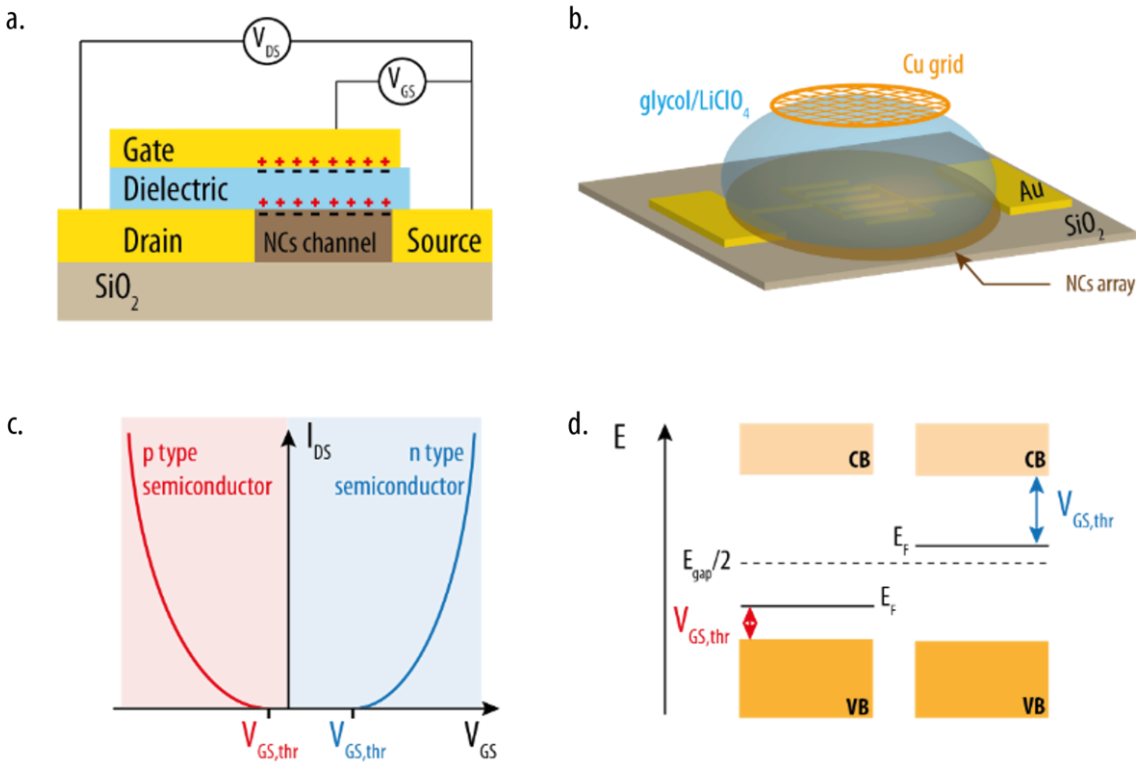

Figure 20: *Field effect transistor to measure charge mobility inside an NCs array. a. Sketch of the field effect transistor working process. b. Sketch of the used FET based on polyethylene glycol/$LiClO_4$ gel as dielectric. c. Sketch of the transfer curves (drain intensity according to the gate bias) for a p-type semiconductor (in red) and for a n-type semiconductor. d. Sketch representing the relative Fermi level position according to the measured transfer curves. The dash line corresponds to the position of half the band gap energy. The black lines mentioned E_F corresponds to the Fermi levels.*

One of the major drawbacks of such a device is its time response which is slow due to the diffusion of ions in the gel matrix. Consequently, this investigation will mostly aim at determining the majority carrier nature. The deposition of the gel has been carried out in a glovebox and the copper grid is finally deposited on top of the electrolyte. The final device is presented in **Figure 20b**.

c. XPS to unveil band alignment.

A classical method used to unveil the band alignment of the material is photoelectron spectroscopy (PES). This analytical technic is based on the photoelectric effect. When a material is exposed to an incoming source of photons with a high enough energy, electrons located in the different orbitals (core levels) composing the material can be ejected from the material. By measuring the kinetic energy (KE) of the electrons coming out of the material, we can determine the binding energy (BE) of the orbitals of the different atoms from the material. Thus, it gives an overview of the elements composing the material as well as an idea of their chemical states (i.e. chemical environment, oxidation state…).

From kinetic to binding energy.

PES is divided into two large families of experiments based on the range of energy of the photons used. Ultraviolet photoelectron spectroscopy (UPS) uses photons with relatively low energies (up to 40 eV) and is widely used to investigate molecules' electronic structures. X-ray photoelectron spectroscopy (XPS) is using photons of higher energies (keV) enabling to probe the electrons from the core levels of its constituting elements. This explains why this scale of energy is widely used during the

elemental characterization of materials. Due to the limited mean free path of the electrons in a material, XPS remains mostly a surface technic with a penetration depth of up to a few nms.

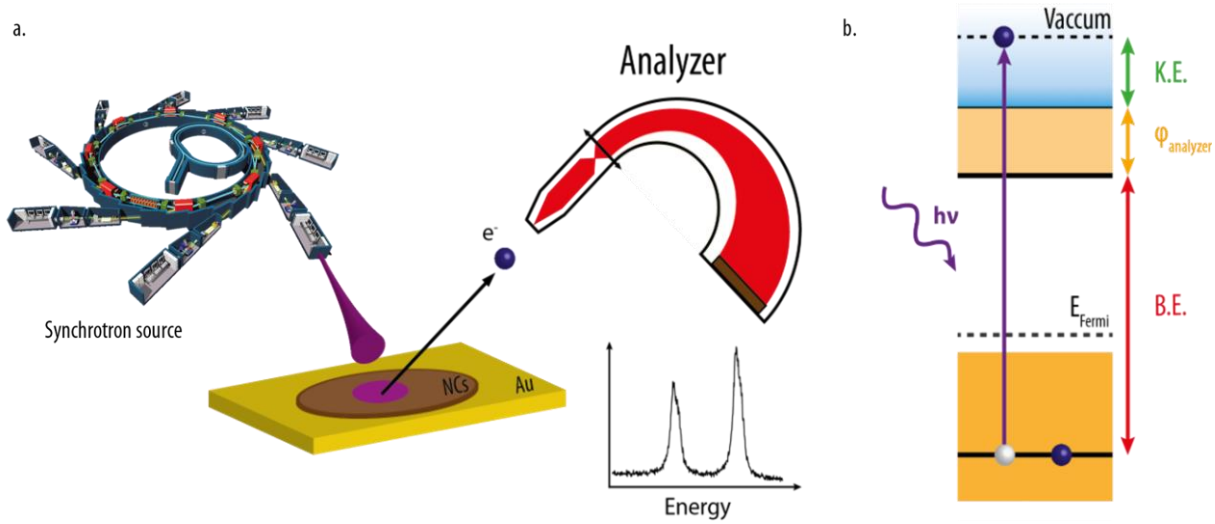

Figure 21: *X-ray photoemission spectroscopy. a. Sketch of the set up used on the TEMPO beamline in SOLEIL. b. Sketch summing up the data treatment from raw kinetic energies to binding energies.*

X-ray sources might be very different, from elemental lamps (like He, Mg, or Al lamps) to synchrotron beamlines. When the first allows to have precise photon energies (that correspond to core-level energy of the used element) for a cost-effective measurement, the synchrotron beamline allows a large flexibility of the X-ray energy used alongside with a high incoming irradiance (e.g. for the TEMPO beamline at SOLEIL, energies from 40 eV to 1500 eV can be chosen[133]). The modulation and the selection of the wavelength are obtained thanks to the introduction of a grating in the optical path. As the photon energy increases, the electrons get more chance to escape the sample. This modulation also enables tuning the probing depth and so the type of electrons analyzed (valence band or core levels).

When illuminated by high enough photon energies, the electrons emitted through the photoelectric effect can escape the material and be collected by an analyzer, see **Figure 21a**. In our case, the detector used is a hemispherical electron energy analyzer. In the first part, the incoming electrons are accelerated in the analyzer. Then, two hemispherical electrodes are spreading the electrons according to their kinetic energy (KE): the trajectory of the electron with the lower KE will be more affected, leading to a smaller radius of curvature in the hemisphere. The electron will finally end their travel on a microchannel plate detector that sorts and counts the electrons according to their curvature (and so their initial KE). The associated binding energy (BE) of the electron in the material, is determined from the expression of the energy conservation:

$$h\nu = \phi_{analyzer} + KE + BE$$

where KE is the kinetic energy, BE the binding energy, hν the photon energy and $\phi_{analyzer}$ the work function of the analyzer that can be measured using a reference sample for which the BE is well-known, **Figure 21b**. In our case, the calibration of the work function of the analyzer has been realized using the Fermi level of gold and by fitting it with a Fermi-Dirac repartition function.

As mentioned earlier in the discussion, the photon energy is obtained through the use of a grating. At "high" photon energies (around 600 eV), the error between the implemented and effective photon energies on the TEMPO beamline can be up to 1 eV which is critical regarding the band gap energy of the material considered. Additional calibration is required to determine the exact value of this incoming energy. To do so, we compare the KE of the electrons coming from the same core level but excited by the first and second orders of the monochromator, the difference in energy being then equal to the exact energy of the incoming photon. Despite requiring this additional measurement for the photon energy calibration, the high brightness of the synchrotron source provides a high photon flux that enables the obtention of well-defined spectra in a limited amount of time with a precision higher than the usual commercial devices. Additionally, synchrotron radiation provides a white source that enables to tune the escape depth of the photoelectrons.

Unveiling band alignment.

During an XPS experiment, electrons are ejected from the sample leaving a charge vacancy. The lack of an electron will make it more costly in energy to eject a second electron. If the process keeps happening, the slow charging of the sample will induce a rigid shift in the energy of all the electrons in the material. To avoid such behavior, the samples are first deposited on a gold conductive substrate to refill the photo holes created with electrons. In the case of high band gap material, this gold film might not be efficient enough. Thus, an additional ligand exchange from native ligands toward ethanedithiol (EDT) is performed to ensure a better conductivity of the film and optimized the charge reinjection. This last treatment is similar to the one conducted on the film made for FET measurements. The samples are then placed in an ultrahigh vacuum (down to 10^{-9}-10^{-10} mbar) to avoid interactions with gas molecules.

An overview of the XPS spectrum leads to the obtention of three particular regions in energy. Each of them is carrying valuable information:

- *At intermediate kinetic energies: the core-level spectrum.*

The electrons are extracted from the core levels of the element constituting the sample (the material, but also the ligands, the substrate …), each element owning specific number of lines in XPS. For a given core level, the states present one to two peaks according to their angular orbital momentum: an s state will give a singlet while p, d, f … states will give doublets of peaks. This splitting in two is due to the spin-orbit coupling and is intrinsic for each element. The peak's relative intensities are given by the degeneracy of the two states, the one owning the higher total angular orbital momentum (J) being localized at lower binding energy. For example, the spin-orbit coupling creates two states for Hg 4f states (see **Figure 22b**): J=5/2 and J=7/2 presenting a spin-orbit splitting of 4 eV, with relative intensities of 6:8.

Put together, those information enables to identify the elements present in a sample. For example, **Figure 22a** exhibits the XPS overview spectrum of the electron core-level energies in a HgTe 3 ML NPLs film. Here, several groups of peaks can be observed. In agreement with the composition of the NPLs, the doublets of peaks localized at 100 and 40 eV correspond respectively to Hg 4f and Te 4d core-level peaks. The presence of those groups confirms the NPLs composition. On another side, the peaks located around 84 eV corresponds to Au 4f core levels that are coming from apparent substrates areas under the NPLs array. In addition, S 2p features are also observed around 225 eV. This sulfur is not coming from the inorganic core of the particles but rather from the ligands (EDT) used to make a

conductive film. The two groups around 284 and 532 eV correspond to the C1s and O1s core-level peaks from the surface ligands or from other chemical pollutions. Overall, XPS is a precise technic and can detect the presence of elements down to a few ppm.

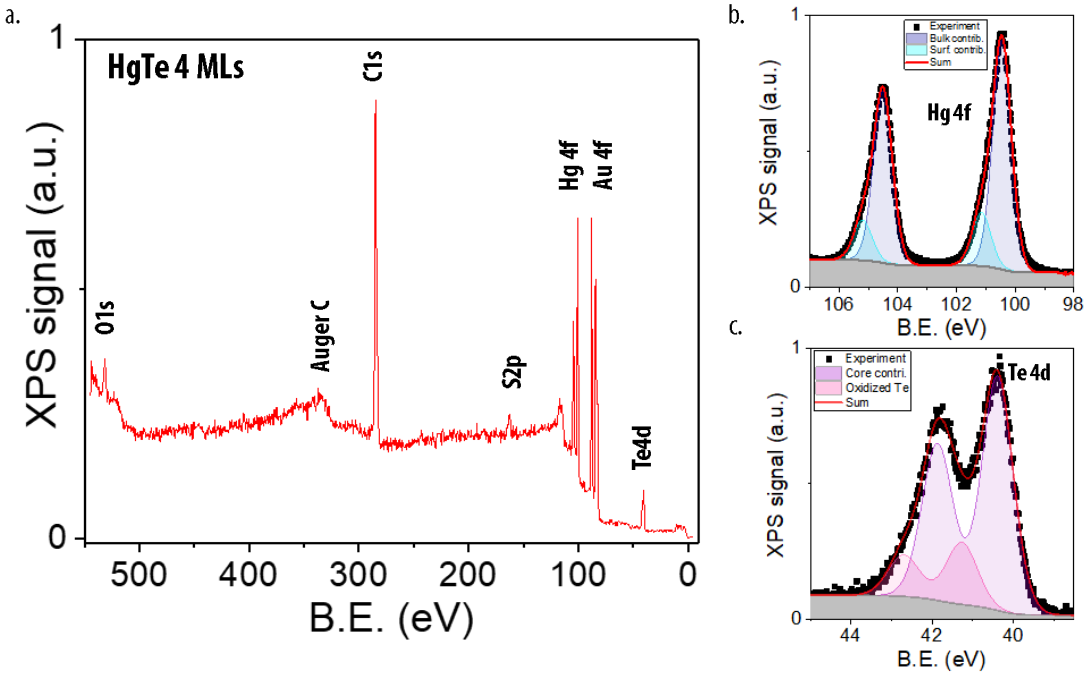

Figure 22: *XPS core-levels of HgTe 3 ML NPLs. a. Overview XPS spectrum. b. Focus on the Hg 4f states. c. Focus on the Te 4d states. For all the core levels, the photon energy used was 600 eV.*

In addition to the elemental analysis, XPS measurements also give insights into chemical environments. The energy of the core level is strongly affected by the oxidation state, the nature of the neighboring atoms, and their bonding hybridization. For example, in the case of the Hg 4f states, two contributions for each peak are usually observed and correspond to two different groups of Hg atoms: the atoms inside the particle that are coordinated to four chalcogenides atoms and those from the surface that are only bond to two of them while their dangling bonds are passivated by ligands. The sulfur atoms present on the surface being more electronegative, the binding energy of the electrons from the surface Hg will be higher than the one from the Hg in the NPLs (see the two contributions **Figure 22b**).

- *At low kinetic energies (i.e. high binding energies): the cut off of secondary electrons.*

The extracted electrons correspond to the secondary electrons: when a photoelectron is created, it has to migrate through the sample toward the surface before being detected by the analyzer. During their trip toward the surface, the electrons can lose energy through inelastic scattering or collisions. Those electrons constitute the major part of the secondary tail observed in photoelectron emission spectra (i.e. the background observed in XPS measurements, similar to the Bremsstrahlung observed in an X-ray source for XRD). Thus, the electrons detected by the analyzer correspond to the one that has been successfully extracted from the sample. The edge measurement of the electron detected with the lowest energy will give the value of the work function of the material. For example, the cut-off measurement for HgTe 3 ML NPLs is presented in **Figure 23a** and exhibits a clear edge at 4 eV.

- *At high kinetic energies (i.e. low binding energies): the valence band.*

The electrons collected are the closest to the Fermi level which is localized at the top of the VB. Thus, with the measurement of the edge of the VB, XPS signal enables to get access to the energetic difference between the Fermi level and the position of the top of the valence band. For example, the VB measurement for HgTe 3 ML NPLs is presented in **Figure 23b** and exhibits a clear edge at 0.3 eV.

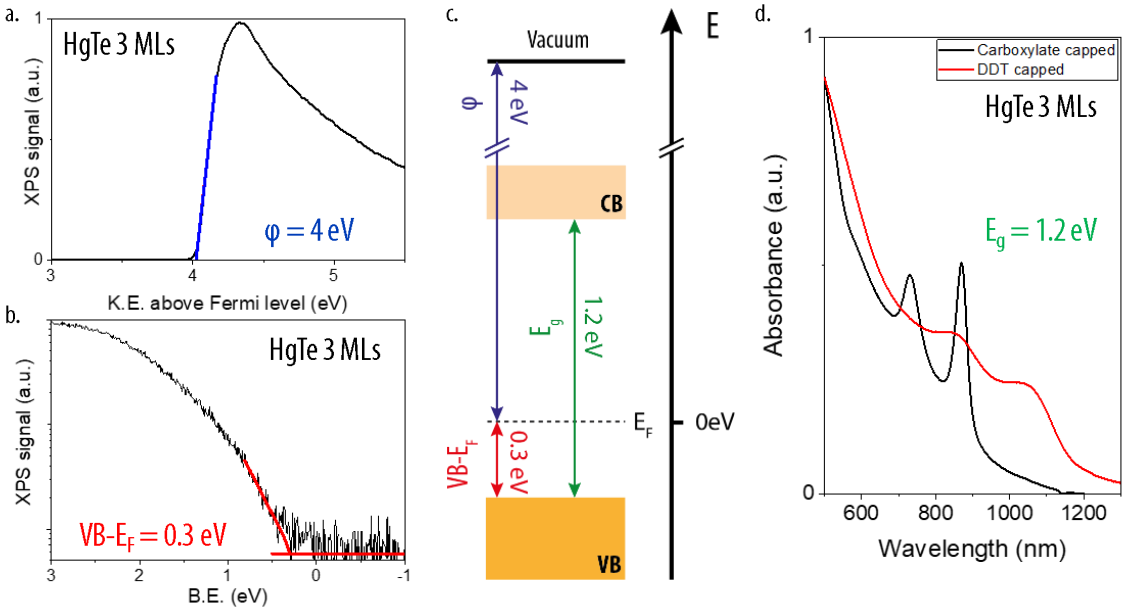

Figure 23: *Establishment of band diagram using photoemission. a. Secondary electron measurement for work-function determination in the case of HgTe 3 ML NPLs. In blue, is the fitting curve used to determine the work function. b. Lowest bound electron measurement for VB-E_F determination in the case of HgTe 3 ML NPLs. In red, are the fitting curves used to determine the VB-E_F value. c. Sketch the establishment of the band diagram using VB-E_F, the work function, and the band gap value in the case of HgTe 3 ML NPLs. d. Absorption spectra of HgTe 3 ML NPLs as a function of the surface chemistry (in black, NPLs capped with carboxylate, in red, with dodecanthiol (DDT)).*

To fully establish the band alignment diagram, information on the CB is missing. As XPS is a technic that only enables us to get access to the populated states, we coupled it with absorption measurements with the right surface chemistry. Indeed, the native ligands have been exchanged with EDT ligands for charge extraction, and similar surface chemistry should be considered when measuring the band gap energy. For example, the band gap energy of HgTe 3 ML NPLs capped with thiol has been measured to be 1.2 eV (see **Figure 23d**).

Finally, this method enables to determine the band alignment of the HgTe 3 ML NPLs. Those NPLs exhibit a Fermi level close to the VB which unveils a p-type behavior. This result is consistent with the previous works made on HgTe NPLs[130]. This method remains the most common and easiest way to unveil the electronic structure of semiconductor NCs. Other technics are existing based on electrochemistry[134] or STM[135]. Overall, XPS is also a complementary technic to EDX for elemental mapping on thicker films.

4. Optoelectronic device based on NPLs.

Due to their singularities, NPLs have been raised as promising materials for various applications. Their large absorption cross-section and long exciton lifetime in type II core-crown heterostructures are interesting for light energy harvesting. In addition, due to the low Amplified

Stimulated Emission (ASE) threshold, NPLs might also raise as good candidates for laser design. Here, we will focus on emission properties of NPLs for LED incorporation.

a. Working process of a display.

White light obtention.

Among different applications, the design of displays based on NPLs remains the most appealing. Despite the numerous different technologies that exist in this domain, the general working process remains the same: producing a white light that will be further filtered to obtain three red, green, and blue pixels. According to the technology considered, this white light is obtained differently:

- In plasma displays, that are no longer commercialized, the white light was obtained through the excitation of phosphorus emitters using a plasma. Electrodes are implanted inside each coated cell. The color balance was then obtained by modulating the ion formation in the plasma of each cell (by changing the applied bias).
- In LCD (Liquid Crystals Displays), the white light is obtained through the excitation of downconverters (Ce: YAG coating, QDs, organic molecules) by an epitaxially grown InGaN blue LED. The radiative relaxation then enables the obtention of a cold white light that passes through the polarizer. The association of liquid crystals and a second polarizer modulates the light intensity to match the required amount of color in the sub-pixel (see **Figure 24a**).
- In LED-based displays (Light Emitting Diode), the white light is obtained using a set of colored LEDs. An electrical current is applied between the two electrodes that sandwiched the emissive material (see **Figure 24b**). A radiative relaxation is induced by populating the excited states through charge injection. The color balance is then obtained by modulating the current flow in each LED. Different emitters can be used: organic molecules for OLEDs or quantum dots for QD-LEDs.

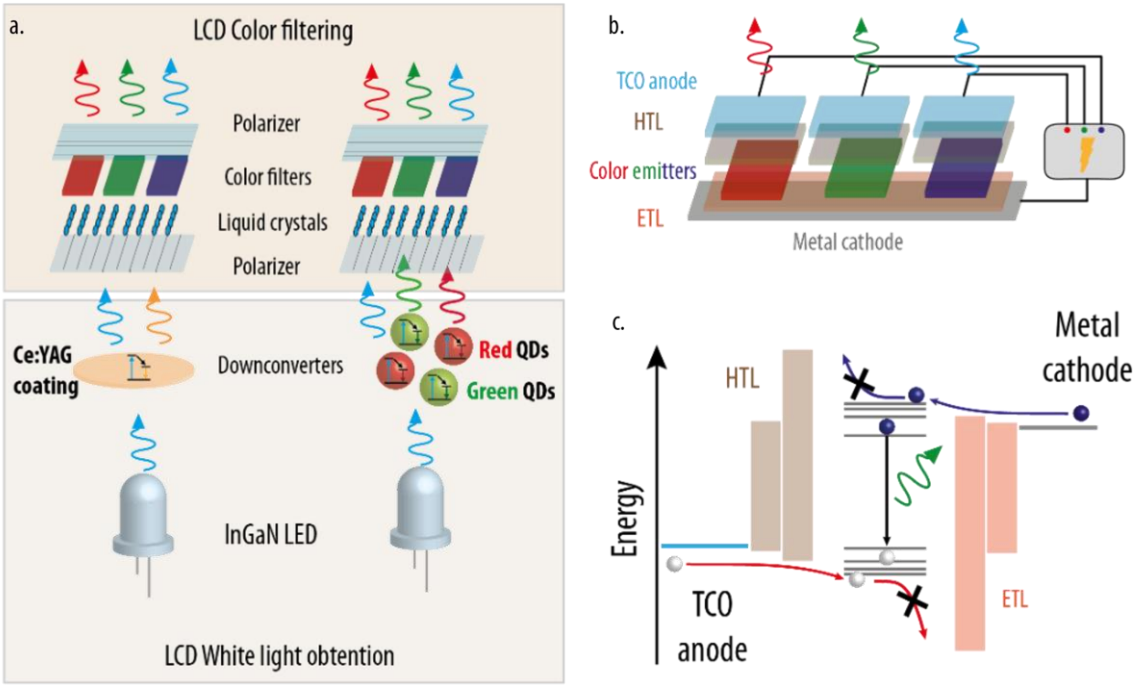

Figure 24: *Different display screens working process. a. Sketch of the working process of LCD based screens. The part on the left corresponds to the classic LCD displays using Ce:YAG as downconverter while the second one corresponds to QD assisted LCD displays. b. Sketch of the working process of an LED based display. c. Photoluminescent spectra of various green emitters.*

Like the cathode-ray tube that where common in the 2000s, plasma displays have quickly been supplanted by LCD displays due to their low production cost and reduced energy consumption. More recently, the first displays based on LEDs have been commercialized. Currently using organics as emitters, the next generation will most likely incorporate electrically excited QDs instead.

LCD displays.

In LCD displays, the downconverters are generally rare-earth doped phosphorus coatings like Ce: YAG that owns a broad yellow emission (see **Figure 25c**). As a consequence, filters are required to obtain green and red lights. This induces huge power losses and broad colors. QDs have been raised as good candidates to supplant Ce:YAG due to their narrow emission (see **Figure 25c**) and their cost-effective synthesis. Their incorporation avoids the use of color filters while improving the color gamut. The development of highly efficient downconverters nanoparticles has enabled the fabrication of QD-based LCD displays (QD-LCDs). All put together, this constitutes the first QDs-based technology to reach the mass market.

In such QD-LCD displays, the white light is obtained through the excitation of a blend of two downconverter NCs emitting the green and red ranges. Those two downconverters are embedded in a polymeric matrix to ensure their stability and extract the heat generated during the downconversion process. For each population, surface chemistry engineering is required. In the second chapter of this manuscript, we will demonstrate the design of a single particle that would enable the obtention of a bicolor emission in the green and the red.

Nevertheless, a lot of energy is lost during the downconversion process due to the relaxation of the excited particle toward the emissive state. In addition, due to this continuous need for a backlight, the white light can never be completely erased inducing limited contrasts. In this context, LED-based displays have been developed to achieve better color quality.

LED displays.

Since the late 2000s, O-LED (Organic-LED) displays have reached the mass market and are now commercialized. This technology uses polymers or small molecules as emitters and has enabled a large improvement in the color quality of the common displays. It also enables to turn on/off individually each pixel limiting the power consumption due to the need of a back light. Even more recently, QD-LED (Quantum Dot LED) displays prototypes have been developed by firms like Samsung and are seen as the future generation of displays. In this case, electroluminescence from QDs is used for the color obtention. Those two families of emitters enable easy processability and large flexibility opening the fields of possibilities (water compatibility, flexible screens[136], …). In comparison to the previous LCD displays, those architectures are also lighter as no liquid crystal cells are required in the display. Despite the more maturity of the O-LED TV screens, they still suffer from major drawbacks, that a switch to QD-LED could address:

- In comparison to inorganic QDs, the organics emitters are generally more sensitive to intense photo-irradiation and heating. It leads to a lower lifetime of the device. It is especially the case for the blue diode which leads to poor color balance and a drastic drop of the luminance.
- Organic dyes are also more sensitive to oxidation. As a consequence, careful encapsulation is required.
- The maximum luminance of the O-LED TV is weaker than the QD-LED TV limiting their use in bright environments.

- The cost of such a device is still high (see **Table 2**)

Table 2: *Sum up on few properties of the current commercialized TV displays (the power consumption is set at 100% for LCD displays).*

	LCD	*O-LED*	*QD-LED*
Lifespan	60 000 h	20 000 h	Expected >20 000 h
Max. luminance	4 000 cd/m²	1 000 cd/m²	>1 000 cd/m²
Power consumption	100%	40% (average)	30-50%
Lowest price	< 100 euros	≈1000 euros	Prototype

b. Color gamut of a display

CIE color diagram

When designing a display, industrials need to consider another crucial aspect: color perception. In particular, the shades of greens observed by the human eye are usually poorly transcript on a TV screen. To understand this challenge, we should first come back to the operation of human vision. When the light goes inside the eye, it is focalized on the retina which is covered by millions of photodetectors called rods. Those detectors are divided in three groups: the blue-, green- and red rods. Each kind owns its response toward a light stimulus. **Figure 25a** is showing the sensitivity of each population according to the incoming wavelength. By processing those electric signals, the brain is then able to reconstruct the picture.

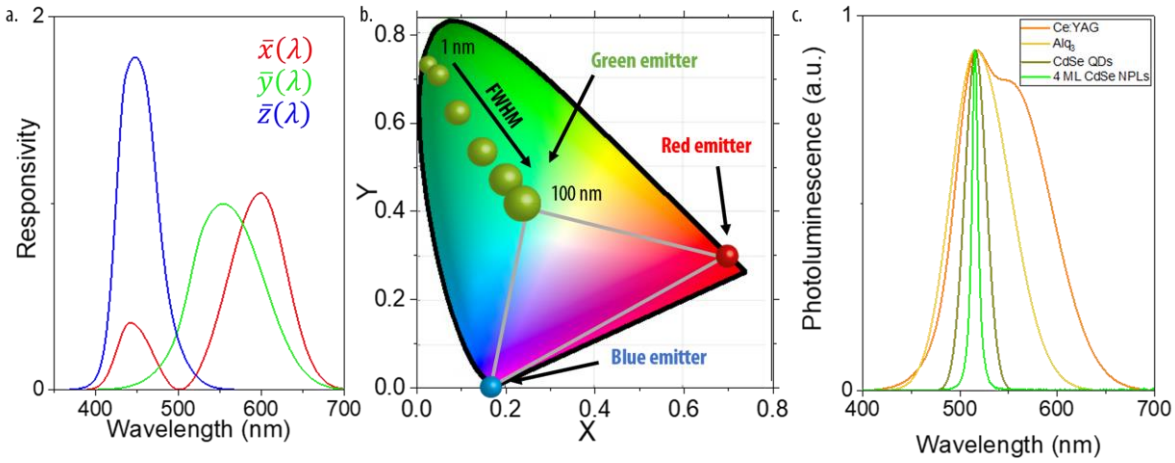

Figure 25: *Human perception of colors. a. Graph representing the responsivity of the three kinds of cone locate din the retina. b. CIE diagramm representing the colors that can be seen by the human eye. The black line corresponds to monochromatic colors. The green dots correspond to Gaussian emission spectra centered at 510 nm with increasing FWHM (from 1 to 100 nm). The grey triangle delimits the colors that can be obtained using emitters located at the submit of it. c. Emission spectra of different green emitters (PL spectrum of Alq_3 is taken from ref [138])*

To map all the shades percept by the human eyes, color maps are usually plotted to link the physiologic perception to the emission spectrum of an emitter. For example, in 1931 the *"Commission Internationale de l'éclairage"* (CIE) defined the CIE color space to help scale this color quality (see **Figure 25b**). In this graph, the emission signature (S(λ)) of an emitter is correlated with eye sensitivity and is associated with a point. These coordinates are calculated using the following equations:

$$X = \int_0^\infty S(\lambda)\bar{x}(\lambda)d\lambda \quad \text{and} \quad Y = \int_0^\infty S(\lambda)\bar{y}(\lambda)d\lambda \quad \text{and} \quad Z = \int_0^\infty S(\lambda)\bar{z}(\lambda)d\lambda$$

with $\bar{x}(\lambda)$, $\bar{y}(\lambda)$, and $\bar{z}(\lambda)$, the red, green, and blue responsivities as shown in **Figure 25a**. The position inside the color gamut is then given by the coordinates:

$$x = \frac{X}{X+Y+Z} \quad \text{and} \quad y = \frac{Y}{X+Y+Z}$$

Therefore, monochromatic colors are localized on the edges of this graph (black line) (see **Figure 25b**). The broader is the emission, the closer to the center is located the associated point. For example, the point positions of Gaussian emissions centered at 510 nm with increasing FWHM (from 1 to 100 nm) are shown in **Figure 25b** (green dots).

Extending the color gamut

Inside a pixel, colors are obtained by mixing contributions from the red, green, and blue sub-pixels. Each of them is associated with a point inside the CIE diagram. The colors that can then be obtained are all localized inside a triangle (also called color gamut) by the three associated points in the CIE diagram (see grey triangle in **Figure 25b**). Therefore, the FWHM has a crucial role to reduce the extension of this triangle. This is especially the case in the green range where the eye is the most sensitive. Consequently, narrow emitters are required to maximize the extension of the color gamut.

Regarding color purity, the switch from Ce:YAG to organic dyes has already largely improved the color gamut. Nevertheless, the best organic fluorophores remain limited by their large Huang Rhys factor (electron-phonon coupling) that induces a strong broadening of the emission features due to multiple vibrational states involved[137]. For example, the emission spectrum of the Alq_3 (tris(8-hydroxyquinolinato)aluminum), a classical green organic emitter used in OLED[138], is shown in **Figure 25c**. Considering this major limitation, NPLs, with their narrow optical features, are more promising candidates for color purity improvement. For example, in the green range, CdSe 4 ML NPLs present a narrow emission at 512 nm which is promising for further color gamut improvement. Thus, in chapter two, in parallel to the obtention of a bicolor emitting NPLs, I will demonstrate an extension of the color gamut in comparison to currently used QDs technology.

c. Design of a QD-based LED.

Structure of a QLED.

Since the development of the first QD-LED by Colvin *et al*. in 1994[139], strong improvements have been carried out in this domain. To improve their efficiency, the PL QY of the material itself can be first improved, for example, we have seen that by growing core-shell structures. One can also improve the charge injection. Electroluminescence (EL) can be obtained when putting directly the NCs film in contact with the electrodes. However, without further improvements, charges could just go through the device inducing large leakages. To induce the localization of the charge recombination inside the emissive array, additional layers are added: the electron and hole transfer layers (resp. ETL and HTL) (see **Figure 24c**). Then, the global structure remains the same:

- A first anode consisting of a transparent conductive oxide (TCO) is used for hole injection. The most common one is tin oxide doped with indium (ITO).
- One to several HTL to ease the hole injection inside the active material and/or block the electrons from going through the active layer. Usually, small organic molecules or conjugated polymeric films are used. To improve the performances of the device, the choice of the polymer is critic regarding its low hole conductivity.
- A NCs array as active layer where charges are radiatively recombining.

- One to several electron transfer layers (ETL) to ease the electron injection inside the active material and/or block the holes from going through the active layer. Generally, ZnO or TiO_2 particles are used for their deep VB and their CB nearly degenerated with the Fermi level of the metallic cathode (see **Figure 24c**).
- A metallic cathode that enables electron injection and backside reflexion. The commonly used metals include Ag, Al, and Au.

A clever engineering of the band alignment inside an LED structure induces a balance in the opposite charge injections to maximize the recombination inside the emissive layer. Accumulation of charge carriers and their recombination through non-radiative Auger processes is now the largest source of losses in state-of-the-art LEDs. In 2014, Peng's group pushed even further the comprehension saying that the current injected is not much the main figure of merit than equalizing the hole and electron current reaching the emissive layer. Thus, they incorporated an insulating PMMA layer to decrease the electron flow and balanced the charge injection[140].

NPLs-LED fabrication.

The fabrication process of a LED involves several steps including the patterning of the ITO electrodes using UV lithography, the spin coating of the HTL polymers layers, of the NPLs active layer, and the ZnO ETL layer, the thermal deposition of the silver electrode and finally, the encapsulation of the device.

Transparent electrode patterning: The ITO electrodes are obtained by etching a thin layer of ITO (30 Ω/sq, 80 nm) grown on a glass substrate. The substrates are then cut into 15 mm × 15 mm pieces and cleaned by sonication in acetone for 5 min to remove all the organics stuck on the surface. Then, they are rinsed with acetone and isopropanol before being dried completely with N_2 flow. The substrates are further cleaned with O_2 plasma for 5 min to remove organic residuals on the surface. After cleaning, a promoter (TI-Prime) and photoresist (AZ 5214E) are spin-coated and baked on the surface of ITO substrates. In the next stage, a mask aligner is used to expose the substrates to UV light through a lithography mask (1 mm width). This step enables the photoresist polymerization where the future electrodes will be located. The photoresist is then developed using AZ 726 developer. The substrates are then etched in a 25% HCl (in water) bath for 10 min at 40 °C before they are dipped immediately in deionized water. Finally, the lift-off is conducted in an acetone bath. Before being used, the patterned ITO substrates are cleaned with acetone and isopropanol and put under plasma for 10 min. A sum-up of the ITO etching is shown in **Figure 26a**.

Layers deposition: There are several methods available for the deposition of successive layers. All the materials used (ETL polymers, HTL NPs, NPLs) can be deposited using spin-coating. This process is much easier than CVD deposition or other complex film deposition like interfacial deposition[141] and consumes less material.

Metallic cathode deposition: The metallic cathode is deposited by the thermal evaporation of silver, through a mask with the pixels. The obtained pixels are usually measuring 1x1 mm^2 and correspond to the overlap between the Ag electrode and the ITO pattern (see **Figure 26b**).

Encapsulation process: Despite their higher robustness toward oxidation phenomena, the NPLs need additional protection against oxidation phenomena. So, the pixels are encapsulated under a piece of glass using epoxy glue. This process is conducted under inert atmosphere, to avoid any humidity any oxygen.

In total, around 10 successive steps of fabrication are required in addition to the material synthesis to reach the final structure that is presented in **Figure 26b**.

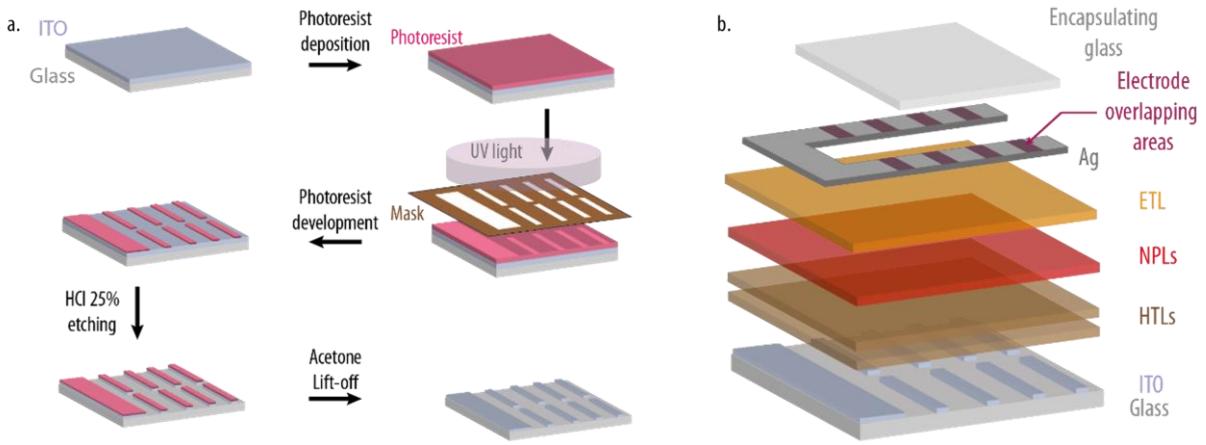

Figure 26: *LED crafting. a. Sketch of the optical lithography route for substrate preparation by ITO etching. b. Sum up on the LED stack.*

Figure-of-merits of LEDs.

To measure the efficiency of a LED, one of the common figures of merit (FOM) is the external quantum efficiency (EQE) that corresponds to the ratio of a photon that effectively escapes from the LED according to the current injected. This efficiency can be divided into several contributions: the quantum efficiency of the material itself (η_{PL}), the charge injection efficiency that depends on the ETL and HTL used to bring charges toward the material (η_{charge}), and the light extraction efficiency that depends on the geometry of the device ($\eta_{geometry}$). The final external quantum efficiency (η_{EQE}) can be determined by:

$$\eta_{EQE} = \eta_{PL} \times \eta_{charge} \times \eta_{geometry}$$

This last contribution is critical in classical planar geometry. Even when the PL and charge injection are ideal (i.e. $\eta_{charge} = \eta_{PL} = 1$), the isotropic light emission of an array of NCs induces a maximum of light extraction of $\eta_{geometry} = 0.2$ due to index mismatch that trap the emitted photon inside the structure, limiting to 20 % the maximum EQE reachable for this LED geometry. Other relevant FOM also exists in LED such as:

- the maximum luminance (in $cd.m^{-2}$) that corresponds to the maximum intensity perceived by the human eyes for a given wavelength.
- the radiance (in $W.Sr^{-1}.m^{-2}$) that corresponds to the extracted photons per solid angle per area. This FOM is mostly used for IR LEDs,
- the turn-on-voltage (in V) that corresponds to the bias threshold that needs to be applied to observe emitted light,
- the half-lifetime (in h) that corresponds to the amount of time before the initial luminance drop by a factor of 2. Usually, the initial luminance is set at 100 $cd.m^{-2}$ which nearly corresponds to the luminance required for smartphone incorporation.

State-of-the-art QD-LEDs:

All those improvements have led to state-of-the-art QD-LED. The current best performances for red, green, and blue QD-LEDs are summed up in **Table 3**.

Table 3: *Sum up the performance of the best red, green, and blue LEDs. In this case, the EQE is overpassing the geometrical limitation thanks to more complex film engineering.*

	Structure	λ_{max} *(nm)*	η_{EQE} *(%)*	*Max. luminance* *(cd.m^{-2})*	*Half lifetime* *(h)*	*Ref*
Red	ZnCdSe/ZnSe/ZnS QDs	597	30%	334 000	1 800 000	142
Green	CdSe/CdZnSe/ZnS QDs	537	28.7%	200 000	2 570 000	143
Blue	CdZnSe/ZnS QDs	479	21.9%	25 000	24 000	143

Two aspects are however limiting the increase in the efficiency of the QD-LED. First, as mentioned, the geometrical parameters limit the EQE to 20 %. Second, at high current density, the efficiency decreases. This behavior is termed the roll-off efficiency and might rise from Auger radiative recombination at high current flow[144] or from an electric-field-induced decrease of the NCs PL.[145].

QD-LEDs are also still suffering from inhomogeneous broadening. As we mentioned earlier, the extension of the color gamut remains one of the major challenges for industrials. With their nearly ideal narrow emission features (see emission spectrum of CdSe 4 ML NPLs **Figure 25c**), NPLs are positioned as the most promising materials to answer this specification.

NPLs-based LEDs.

Compared to NCs, NPLs are not only the narrowest emitters, but they also own other advantages:

- Their large absorption cross-sections are optimal for downconversion in QD-LCDs.
- Their large anisotropic shape can induce polarized emission that would enhance the efficiency of NPLs-LCD displays. This polarization depends on the aspect ratio of the NPLs. In addition, directional emission can also be achieved using NPLs. This is particularly interesting in the optic of LEDs incorporation as it could enable breaking through the 25% maximum EQE associated with the inherent geometry of the LED structure. It has been shown that the efficiency could reach up to 40%[146].
- Their large volume that reduce the non-radiative Auger recombination.

Nevertheless, to benefit from this last point, NPLs need to be self-assembled[147,148] which requires further processing investigations. Other methods will be further explored in the fourth chapter.

Similar to QD-based LEDs, the best efficiencies are obtained when core-shell heterostructures are considered. Several structures have been investigated including core, core-crown, core-shell, and core-crown-shell… some of them are recorded in **Table 4**. It is worth mentioning that the efficiency of core-only NPLs is still low in comparison to core-shell structures. The growth of a crown of CdSe-CdS seems to improve the efficiency, primarily due to an increase in the absorption and due to partial passivation of the lateral trap states[44,149]. However, their current performance remains still modest in comparison to their spherical counterpart. Especially, the device lifetime remains low in comparison to QDs. A few examples of investigated structures associated with their FOM are summed up in **Table 4**. They are now recording EQE up to 19%[150], maximum luminescence up to 46 000 cd.m^{-2} [151], and half lifetime up to 3000h[85].

Table 4: *Sum up the performance of a few NPLs-LEDs. The half lifetime is not always measured due to its general low value.*

Structure	λ_{max} *(nm)*	η_{EQE} *(%)*	*Max. luminance* *(cd.m^{-2})*	*Half lifetime* *(h)*	*Ref*
CdSe-CdS	560	5	33 000		152
CdSe-$CdSe_{0.8}Te_{0.2}$	599	3.57	34 520		153
CdSe-CdS@CdZnS	689	6.8	1300		154
CdSe-$Cd_{0.25}Zn_{0.75}S$	644	19.2	23 490	0.13	150
CdSe@CdS@CdZnS	650	9.9	46 000	560	151
CdSe@$Cd_{0.05}Zn_{0.95}S$	620	5.15	35 100	3160	85

Overall, the performance of NPL-based LED remains lower than in QD-based LED but their anisotropic shapes is promising to breakthrough the geometrical parameters limitations.

5. Conclusion

Since the first demonstration by Ithurria *et al.*, the colloidal synthesis of NPLs has been deeply investigated enabling the creation of a large panel of 2D colloidal materials. According to the growth conditions, a control of the thickness at the atomic layer scale is possible. The resulting particles present no roughness on their surface inducing narrow optical features, especially when comparing to the spherical QDs. This justifies the particular interest that raised those NPLs. Using similar or different strategies, NPLs with various compositions have been synthesized keeping a control of the thickness at the atomic layer scale.

Those particles are also perfect starting building blocks for the design of more complex heterostructures. Their anisotropic shapes enable the formation of two types of heterostructures: the core-shell and the core-crown. The last one has found no counterpart either in the 3D geometry or in MBE. Especially, core-crowns heterostructures enable to widely tune the charge carriers wavefunction localization inside the NPLs. Therefore, a large modulation of the optical properties is possible. In the following chapter, we will take advantages of this geometry to design a complex heterostructure toward the obtention of a bicolor emitting NPLs.

Cd-based NPLs remains the most studied among other materials. However, the wavelength range of application for those particles is limited by the bulk band gap of CdSe. To overcome this limitation, materials owning smaller band gap can be considered. The synthesis of HgTe NPLs through a CE had already been established by Izquierdo *et al.* A deeper investigation will be conducted in the third chapter to generalize the process to other Hg-based NPLs.

Finally, those particles are promising candidates for the design of optoelectronic device. Especially, the incorporation of NPLs as active material in LED have been presented. In the following chapter will be presented the design of a bicolor LED based on heterostructured NPLs and demonstrate the first NPLs-based LED in the NIR starting from HgTe NPLs.

Chapter 2: 2D nanoplatelets for bicolor downconversion.

In this second chapter, I will introduce the design and the synthesis of a heterostructure of NPLs that exhibits bicolor emission. Throughout this project, I designed and synthesized the heterostructure and constructed and characterized a LED stack based on this material. In collaboration with C. Gréboval, I conducted photoemission measurements at the TEMPO beamline of the SOLEIL synchrotron under the supervision of M.G. Silly. The High-Angle Annular Dark-Field Scanning Transmission Electron Spectroscopy (HAADF-STEM) pictures were taken by G. Patriarche at C2N (Université Paris-Saclay). The single-particle measurements and part of the PL measurements were conducted by V. Guilloux and T. Barisien at INSP (Sorbonne Université). The TA measurements and the remaining PL measurements were carried out by B. Diroll at CNM (Argonne National Lab, Chicago). I had the opportunity to go and conduct experiments on this setup, and specifically, the last set of presented data was obtained by myself. Finally, J.I. Climente's team in U. Jaume I in Valence (Spain) conducted the k.p modeling simulations.

In the first short introduction section, I will present **the state-of-the-art regarding bicolor emitting NCs**. The desired specifications will also be outlined, and the advantages of using NPLs for such an application will be revealed.

Following this, in the second part, the **design of 2D bicolor NPLs** will be investigated. Through the analysis of the optical properties of the first two attempts, general rules and trends will be unveiled. Considering these findings, a third optimized heterostructure will be established and synthesized.

The third and fourth parts will focus on the **rationalization of the bicolor emission** and the **examination of the optical properties** of these particles. In particular, the **power dependency** study will reveal the color tunability of the photoluminescence.

In the fifth part, the heterostructure will be integrated into an LED device to demonstrate **bicolor electroluminescence**. The results obtained will be compared with state-of-the-art bicolor emitting LEDs.

Finally, the last two parts will be dedicated to discussing the **perspectives** that can be considered regarding such heterostructures.

Publications associated with this project:

- Dabard, C. *et al.* Double-crowned 2D semiconductor nanoplatelets with bicolor power-tunable emission. *Nat. Commun.* 13, 5094 (**2022**).
- Dabard, C. *et al.* Expanding the color palette of bicolor-emitting nanocrystals, *submitted*.

Content

1. Nanoparticles as bicolor emitters.

a. Challenges to address.

The current red and green emissions in Quantum-Dot Liquid Crystals Displays (QD-LCD) use a blend of two downconverters (a red and a green one). These particles are embedded inside a transparent polymeric matrix that has the dual role of protecting the NCs from oxidation and extracting the heat generated during the down-conversion process. To achieve optimal performance, the polymer needs to be electrochemically inert to enhance long-term stability[155]. Since each downconverter is different, a suitable matrix must be found, taking into consideration the compatibility of the two emitters. In this context, the development of bicolor emitters would enable bypassing these formulation steps.

The design of such a material is not trivial due to Kasha's rule. Initially established for small organic molecules, this rule can also be extended to most emissive systems. It states that when an electron-hole pair is created during the absorption of a photon, the two formed charge carriers relax from highly excited states to the most stable vibronic states through internal conversions. This process occurs rapidly before any recombination takes place. Once the lowest excited state is reached, the exciton can recombine radiatively, emitting a photon. Consequently, only emission from the fundamental excited state should be observed. Overcoming this rule is necessary to achieve a bicolor down-converter.

b. Different strategies for bicolor emission in NPs.

Few reports have already been published on bicolor emitting NCs, including spherical[156–158] or plate-like[77,93] geometries. To overcome Kasha's rule and obtain bicolor emission, different approaches have been considered:

- *Dissociation of the two emissions using a material spacer:* In this approach, the internal conversions of inter-excited states are limited by the presence of a barrier, isolating the two excited states responsible for the dual emission. For example, Brovelli et al. synthesized a dot-in-bulk particle where the red emission is obtained through the emission of a CdSe core, and the green emission is produced by the bulk CdS grown around it. The spacing is achieved by using a ZnS thin shell grown on the CdSe core (see **Figure 27a**)[156,157]. Similar results have been obtained on 2D particles by Moreels' team when they synthesized CdSe-CdS-CdTe core-crown-crown NPLs, with CdS playing the role of a spacer[77].

- *Use of dopant for sub-band gap emission in NPLs:* Dufour et al. obtained bicolor emitting particles starting from CdSe 4 ML NPLs and doping them with Ag^+ cations (see **Figure 27d**)[114]. Similar results have been later achieved using also Ag^{+} [115] cations or Cu^{2+} [116,159] or Yb^{3+} [160]. While the green emission is obtained from the band edge emission of the initial NPLs, the red emission is achieved through the energetic states present within the band gap of the NPLs, associated with the dopants. The variation in dopant concentration inside the particle modulates the density of states within the band gap, enabling saturation of the sub-band gap emission or suppression of the band edge emission.

- *Wavefunction engineering in core-crown NPLs:* Dufour et al. also developed core-crown NPLs with bicolor emission by engineering the localization of charge carriers' wavefunctions within the heterostructure[93]. They achieved this by tuning the relative band alignment of a CdSe-$CdSe_xTe_{1-x}$ heterostructure through changes in the composition of the alloyed crown (see **Figure 27e**). For certain compositions, the energetic offset between the core and the crown CB is lower than the exciton binding energy (typically 250 meV[161]) resulting in a non-zero occupancy probability of the electron in both materials. This leads to a combination of band edge recombination in the alloyed crown and type II interfacial recombination between the core and the crown[93,94].

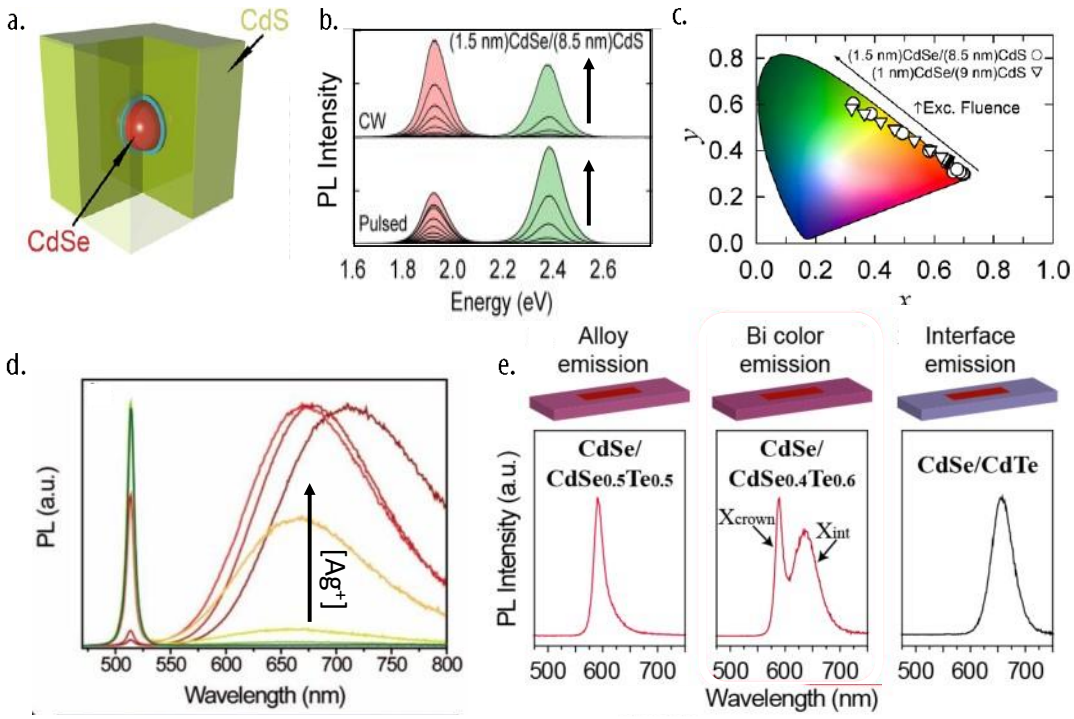

Figure 27: *Bi-emitting nanocrystals. a. Dot-in-bulk structure used for bicolor emission by Brovelli et al. (ref). b. Power dependency of this bicolor photoluminescence. The black arrows show the trend followed by an increase in the incoming excitation power. c. Localization in the CIE diagram of the bicolor emissions according to the incoming excitation power. (a., b., and c. have been adapted from ref [156,157]) d. Photoluminescence spectra of CdSe 4 ML NPLs dopped with Ag^+ according to the concentration in dopant. The black arrow shows the evolution according to the concentration of Ag^+ dopant (d. has been adapted from ref [114]). e. Evolution of the photoluminescence spectrum according to the composition in CdSe-$CdSe_xTe_{1-x}$ 4 ML core-crown NPLs (e. has been adapted from ref [93]).*

c. 2D core-crown particle of II-VI semiconductor.

All of these particles exhibit bicolor emission. However, most of them suffer from major drawbacks. Among them, the unbalanced ratio between the two emission peaks (with one of the two pevailing) and the poor color definition are the primarily limitations. For example, Dufour et al. failed to maximize the color gamut due to a green emission that was too orangish, even overlapping with the red emission. In QD-based bicolor emitters, the green emission is associated with a large full width at half maximum (FWHM) (see **Figure 27b**). Considering the sensitivity of the human eye to the green color, the narrowness of the corresponding emission feature is crucial for extending the color gamut (see **Figure 27c**). Based on all the different experiments and attempts conducted previously, we have established specifications for the targeted structure:

i. The particle should emit green light with a narrow emission spectrum to fully expand the color gamut.
ii. The particle should achieve bicolor emission with two emissions that do not overlap spectrally.
iii. The intensity ratio between the two emissions should be close to unity to generate white light.

Regarding the first point, II-VI semiconductor NPLs-based bicolor emitters are emerging as the most promising materials for extending the color gamut due to their narrow optical features. Specifically, a green emission can be obtained starting from CdSe 4 or 5 ML NPLs, respectively, at 512 and 550 nm[116]. In NPLs, the creation of complex heterostructures allows for wide modulation of the optical features by delocalizing the charge carrier wavefunctions within the structure. Therefore, we decided to investigate the use of such heterostructures to create a bicolor emitting NPL that meets the established specifications. Considering Kasha's rule, obtaining a green emission appears to be the most challenging aspect. Thus, its achievement should guide the direction of the investigation. We first identified the material that exhibits a pure green emission. Among the available options and considering the localization of their emission within the CIE color gamut, the best candidate is the CdSe 4 ML NPLs (see top left red square in **Figure 28a**). Its emission around 512 nm and its small FWHM (7 nm; 25 meV) would enable a significant extension of the color gamut (see **Figure 28c**). Additionally, considering their small lateral size (see TEM picture in **Figure 2b**) and the maturity of their synthesis, these NPLs are remarkable starting building blocks and efficient green emitters.

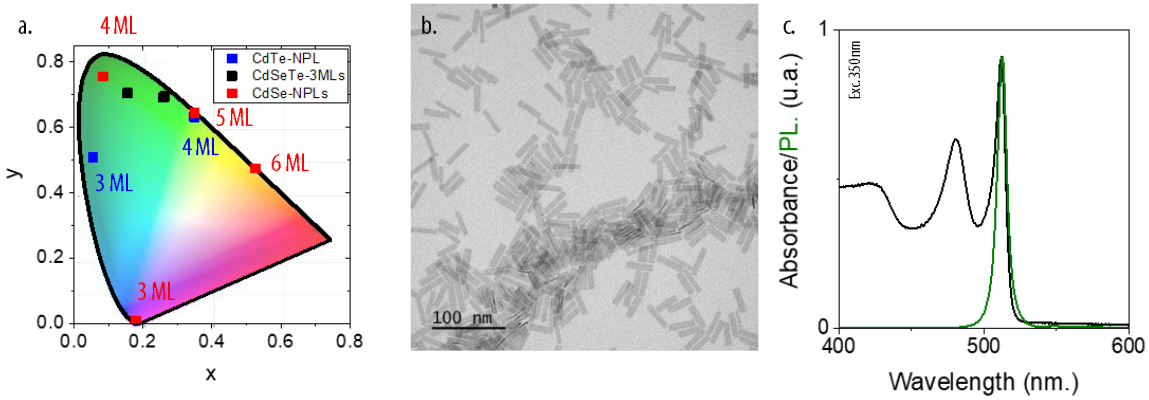

Figure 28: *Choice of the green emission. a. Color gamut presenting the CIE coordinates of different Cd-based NPLs emitters (in blue, CdTe 3 and 4 ML NPLs, in black, alloyed $CdSe_xTe_{1-x}$, 3 ML NPLs and in red CdSe 3-6 ML NPLs). b. TEM picture of core CdSe 4 ML NPLs. c. Absorption (black) and emission (green) spectra of CdSe 4 ML NPLs. The excitation is set at 350 nm.*

To form a heterostructure, a second semiconductor is grown on top of the initial material. In the case of NPLs, this growth can occur in two different directions. Growing a shell on top of the core

material leads to a red-shift in its optical properties and broadening of its emission features due to the change in quantum confinement. On the other hand, lateral growth to form a core-crown heterostructure does not alter the environment in the direction of quantum confinement. Therefore, to preserve the matching green emission of the CdSe 4 ML NPLs, we have decided to prioritize the growth of this second type of heterostructures.

2. Design of a NPL heterostructure for bicolor emission.

Considering CdSe 4 ML NPLs as the initial building blocks, our next objective is to introduce a second emission in the red without altering the green emission. Since the lateral extension of the NPLs keeps the thickness constant, we need to identify a material that exhibits a red emission when its thickness corresponds to 4 ML. Through exploration of various approaches in material synthesis and quantum engineering, this section will present an optimized structure for achieving bicolor emission.

a. Spatial dissociation using a potential barrier.

When a core-crown heterostructure is grown, the charge carriers localize within the particle based on the band alignment of the two materials. The electron (and hole) will be localized in the lowest CB (and highest VB) of the respective materials. This localization can lead to the absence of charge carriers within one of the materials or the formation of a type II interface. In either case, this distribution of charge carriers does not favor bicolor emission. To enable the simultaneous localization of charge carriers within both materials, a spacer can be added between them to disrupt the natural distribution dictated by the band alignment.

In 2020, Moreels' team in Ghent developed similar core-barrier-crown nanoplatelets consisting of CdSe-CdS-CdTe[77]. In this heterostructure, the CdS crown acts as a spacer to separate the CdSe and CdTe regions. The type I band alignment with CdSe allows for observation of band edge recombination in the core. Despite the small size of their CdS crown, they still observed interfacial recombination between CdSe and CdTe through tunneling events. This led us to the idea of increasing the size of the CdS barrier to further enhance the separation of the two materials.

Dual emission from two different materials.

Different approaches can be followed to achieve two distinct color emissions, I will here review some first attempts before describing the final selected structure. Firstly, the band edge recombination of materials with different band gap energies can be utilized. The introduction of a barrier, which is a material with a wide band gap, can separate these two emissions. It is important to ensure that the barrier is large enough to limit the interaction between the two materials, especially in the case where a type II interface might form. Considering the selection of CdSe 4 ML NPLs as the green emitter, we need to find a second material with a narrower band gap to induce a redder emission, while keeping in mind that the thickness of the crown is determined by the cores. The available materials for consideration are pure CdS, CdTe, and alloyed compositions. CdS has a band gap that is too large (for 4 ML, the first excitonic peak is located at 407 nm) and would be better suited as the barrier material. On the other hand, CdTe is not red enough (for 4 ML, the emission maximum is located at 555 nm) and would limit the expansion of the color gamut (see blue square in **Figure 28a**). However, we have previously observed that alloyed materials can have a narrower band gap than individual materials due to the bowing effect. For instance, $CdSe_{0.4}Te_{0.6}$ 4 ML NPLs are expected to exhibit a band gap energy of 2.13 eV (583 nm i.e. yellow)[93,94] which is closer to our expectations. Furthermore, the growth of a

$CdSe_xTe_{1-x}$ crown around a CdSe 4 ML core has already been investigated by both Kelestemur *et al.*[94] and Dufour *et al.*[93].

To maintain a high photoluminescence quantum yield (PLQY) and improve its colloidal stability (with the aim of later achieving processability into high-quality, pinhole-free films), it is important to minimize the lateral extension of the initial cores. Therefore, I first synthesized CdSe 4 ML core NPLs with small lateral dimensions (26x7 nm², see **Figure 28b**). The synthesis process for these cores is the same as described in the introduction chapter. Subsequently, a CdS crown is grown on the cores by slowly adding a TOP:S solution, diluted in ODE, at 215°C to a mixture containing the cores, a cadmium precursor ($Cd(ac)_2$), and oleic acid. This growth process is accompanied by an increase in the absorption features at 407 nm (see the light green absorption spectrum in **Figure 29a**) which corresponds to the CdS 4 ML NPLs. The final heterostructure attains a lateral extension of 79x15 nm². After washing the intermediate core-crown structure, the external crown is further grown by slowly injecting a mixture of TOP:E (E: Se, Te) with the corresponding Se/Te ratios. In terms of absorption, the features of the external crown gradually appear and increase while shifting toward the red region (see the evolution of the absorption spectra around 580 nm in **Figure 29a**). This progression aligns with the growth of the external crown, which is also accompanied by a reduction in lateral quantum confinement.

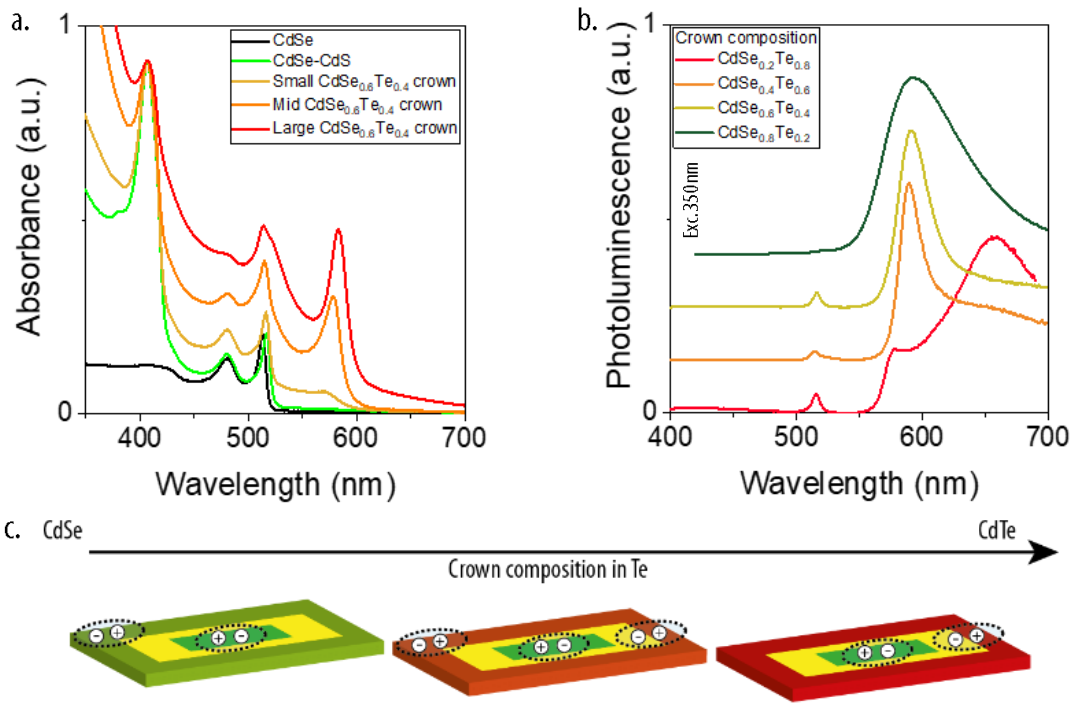

Figure 29: *Bicolor coming from the band edges of two different materials. a. Followed up on the absorption spectra during the synthesis of a CdSe-CdS-$CdSe_{0.4}Te_{0.6}$ heterostructure including absorption spectra of three different sizes of $CdSe_{0.4}Te_{0.6}$ external crown. b. Emission spectra for different composition of the external alloyed crown. The excitation has been conducted at 350 nm. c. Sketch of the heterostructure with the position of the exciton inside the particle according to the composition of the external crown.*

The growth of a CdS/$CdSe_xTe_{1-x}$ interface remains challenging, especially when a high content of Te is used. Delikanli et al. and Dede et al. have demonstrated that the formation of such a heterostructure can result in non-trivial interfaces and a high risk of side nucleation due to the significant lattice mismatch between CdS and CdTe (respectively equal to 5.8 and 6.4 Å)[162,163]. Additionally, they revealed a type II band alignment between CdS and $CdSe_xTe_{1-x}$ for high Te

contents[162]. Since the emission characteristics of the final particle depend on the delocalization of charge carriers after exciton formation, the more complex the band alignment, the more intricate the emission features become (see **Figure 29b-c**). However, when a crown with an intermediate content of Te was used, a spectrally dissociated bicolor emission was observed (see **Figure 29b**). Unfortunately, the red emission was not sufficiently red-shifted to meet the specifications.

Considering the core-crown based heterostructure targeted, we have here demonstrated the limitations of using band edge emissions to obtain a red emission. Therefore, an alternative strategy needs to be adopted to achieve a redder emission. Furthermore, to simplify the luminescence signature, we decide to focus on a specific type of interface around the CdS barrier: CdSe/CdS.

Type II interfacial recombination for red emission.

Due to their large Stokes shifted emission, interfacial recombinations with type II band alignments also appear as good candidates for red emission. In particular, as we have discussed in the introduction chapter, a CdSe-CdTe 4 ML core-crown NPLs structure exhibits sub-band gap recombination at 650 nm, which aligns well with the color requirement. When a CdSe/CdTe type II interface is formed, the exciton becomes directly delocalized at the interface, suppressing the band edge recombination within CdSe. Once again, to spatially separate the CdSe core from the type II interface located in the external part of the NPLs, a large CdS barrier can be grown to separate the two recombinations.

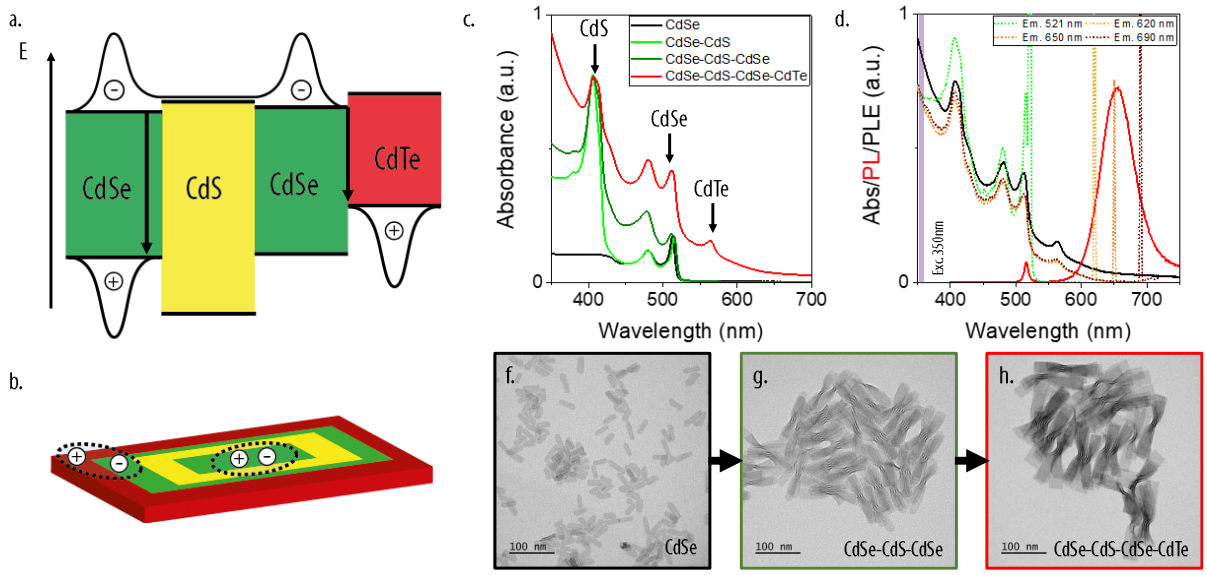

Figure 30: *Bicolor emission from CdSe-CdS-CdSe-CdTe core-multi-crown heterostructure. a. Band alignment of the corresponding heterostructure. The black arrows represent the expected recombination. b. Sketch of the heterostructure with the potential localization of the excitons. c. Absorption spectra at different stages of the heterostructure synthesis. The absorption spectra have been normalized to the CdS first excitonic peak for more clarity. d. Absorption (black) and emission (red) and PLE for various wavelengths (dashed lines) spectra of the final heterostructure. The excitation has been conducted at 350 nm. f-h TEM pictures of CdSe core (f) CdSe-CdS-CdSe core-crown-crown (g) and CdSe-CdS-CdSe-CdTe core-multi-crown (h).*

A core-multi-crown structure of CdSe-CdS-CdSe-CdTe has been investigated (see **Figure 30a-b**). The same initial CdSe-CdS core-crown structure was used for the growth of the type II interface (CdSe core: 26x7 nm²; CdSe-CdS: 79x15 nm²). To prevent the formation of a CdS/CdTe interface, the CdSe crown is first grown, leading to an increase in absorption at a wavelength below 512 nm (see dark green absorption spectrum in **Figure 30c**). The absorption of the external CdSe crown is less defined

here due to additional lateral quantum confinement. The growth of the CdTe external crown is then conducted, resulting in additional absorption features at longer wavelengths. Initially, these features are associated with CdTe crown absorption (up to 555 nm). However, above 555 nm, an increase in the baseline is still observed, which may be attributed to diffusion increase due to particle agglomeration (see TEM picture in **Figure 30f-g**).

Consistent with the structure developed by Khan et al., an exciton can be localized either in the metastable states associated with the core material or at the CdSe/CdTe type II interface (see **Figure 30b**). Therefore, there is a non-zero probability of recombination in the CdSe core, resulting in a bicolor photoluminescence at 512 nm for the band edge emission in CdSe and at 650 nm for the observed type II interface recombination (see **Figure 30d**).

However, this particle suffers from a major drawback, which is the low green-to-red ratio (i.e., the ratio between the two integrated peaks). This ratio is expected to be strongly dependent on the absorption cross-section relative to each emission and thus to their respective area. Based on PLE measurements (see **Figure 30d**), we have determined the following: the green absorption cross-section includes the CdSe core and a part of the CdS crown, while for the red emission, it involves a part of the CdS crown and the external CdSe and CdTe crowns. Here, the geometrical parameters are clearly not favorable for band edge recombination inside the CdSe core. Additionally, interfacial recombination is usually very efficient, leading to an enhancement of the red PL.

To enhance the green emission, one could consider increasing the size of the core. However, the presence of the interface in the outer part of the particle prevents an increase in the ratio, as a larger core would also result in a larger CdSe/CdTe interface. Decreasing the size of the CdS crown would lead to exciton leakage from the core to the type II interface through tunneling across the CdS crown. Finally, decreasing the size of the CdSe crown would result in additional lateral quantum confinement, completely shifting the band alignment at the type II interface. While these options could potentially increase the green-to-red ratio, the absorption cross-section area of the external crown will always be greater than that of the core. Therefore, another strategy is required to balance the two emissions.

This second attempt helped us identify two distinct emissions that would meet the specifications for color gamut extension. However, the particle's geometry needs to be drastically redesigned to improve the green-to-red ratio.

b. Bicolor emission through volume management.

Optimizing the geometric parameters.

The emission of a material is usually proportional to its volume. An increase in volume also favors a lower non-radiative Auger recombination rate due to its inverse volume dependency[164]. Considering the previous attempts, several specifications have been revealed for the design of more efficient bicolor NPLs:

- Association of CdSe 4 ML band edge emission for the green and CdSe/CdTe type II interfacial recombination for the red emission to maximize the color gamut.
- A large volume of CdSe to favor the green emission as $I_{green} \propto V_{CdSe}$.
- A large volume of CdSe to reduce the Auger non-radiative recombination, which is proportional to the inverse of the volume $I_{Auger} \propto \frac{1}{V}$

- A small perimeter for the type II interface to limit the type II recombination as $I_{red} \propto Perimeter_{CdSe/CdTe}$.
- For further use, a simpler structure with no more than two interfaces, preferably identical.

Considering all of these specifications, an inverted structure that localizes the type II interface at the center of the particle should be considered. However, the synthesis of small CdTe 4 ML NPLs is still challenging. Consequently, we decided to form the type II interface starting from small CdSe 4 ML NPLs by adding a crown of CdTe. To limit the extension of the type II interface, the dimensions of this crown should be as small as possible. At this point, the initial green emission should be completely quenched, and only the broad characteristic emission of the type II interface should appear. To restore the green emission from CdSe, we need to increase the volume of CdSe. The only option left is to add a CdSe crown around the CdSe-CdTe core. As the lateral size of this CdSe crown increases, the recombination ratio inside the CdSe is expected to increase due to the larger volume of CdSe (**Figure 31a-b**).

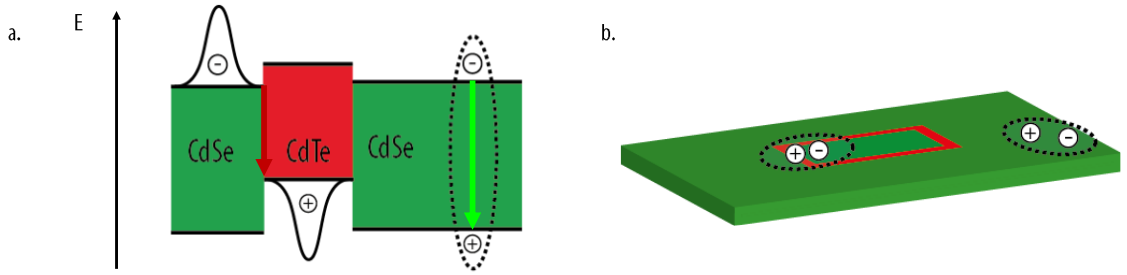

Figure 31: *Inverted heterostructure for bicolor emission. a. Band alignment of the inverted heterostructure. The arrows corresponds to the expected recombinations. The dashed circle represents a metastable excitons that would be localized in the outer CdSe crown. b. Sketch of the inverted heterostructure in which the excitons at the origin of the dual emission are localized (dashed circles).*

Synthesis of the inverted heterostructure

To synthesize this particle, we started with CdSe 4 ML NPLs (36x7.5 nm², as shown by TEM picture **Figure 32c**) as the initial building block. They exhibit a first absorption peak at 511 nm and a second at 480 nm (**Figure 32a**). In the flask, the core NPLs are redispersed in ODE with $Cd(ac)_2$ and OA, and the mixture is degassed at 80°C for 30 minutes. This step is crucial for the growth of the heterostructure, aiming to form the $Cd(ac/OA)_2$ complex, which will serve as the active cadmium species for lateral growth. The ratio between these two species is critical: an excessive amount of $Cd(ac)_2$ (or insufficient OA) could lead to side nucleation during the growth process. Conversely, an excessive amount of OA would prevent the migration of precursors toward the lateral facets, inhibiting heterostructure growth[91].

After the degassing step, the temperature is increased to 215°C. TOP:Te diluted in ODE is slowly injected into the mixture to induce the growth of the CdTe crown. In absorption, CdTe features appear above 550 nm but remain broad due to lateral confinement (see green absorption spectrum in **Figure 32b**). To minimize type II recombination signal, the CdTe crown needs to be as small as possible. However, due to lattice constraints, such a small CdTe crown would be damaged if the particle had to be washed. Therefore, the growth of the second crown is carried out in the same flask. To minimize the amount of remaining TOP:Te inside the mixture when the Se precursor injection begins, a 20-minute annealing step is added between the two steps to ensure maximum fixation of Te on the NPLs.

The growth of the second crown is conducted at a higher temperature (225°C) by injecting a solution of TOP:Se diluted in ODE. This reaction is sensitive to the injection rate and growth temperature: excessively high temperature (or slow injection) tends to induce recrystallization of precursors on top of the wide facets, while excessively low temperature (or fast injection) favors side nucleation of thinner NPLs.

During this second step, small aliquots of the same volume have been collected. An increase in the excitonic absorption features of CdSe is observed, consistent with an increase in the lateral crown extension (as highlights the dark arrow in **Figure 32f**). At the end of the injection, the amount of CdTe is very low (less than 1% Te compared to Se); however, later photoemission analysis will confirm the presence of Te in the particles. Consequently, the absorption features perfectly corresponds to CdSe 4 ML NPLs, with a slight contribution from diffusion due to the large final lateral extension of the heterostructure. However, the emission properties of the particles are drastically different from pure CdSe 4 ML NPLs..

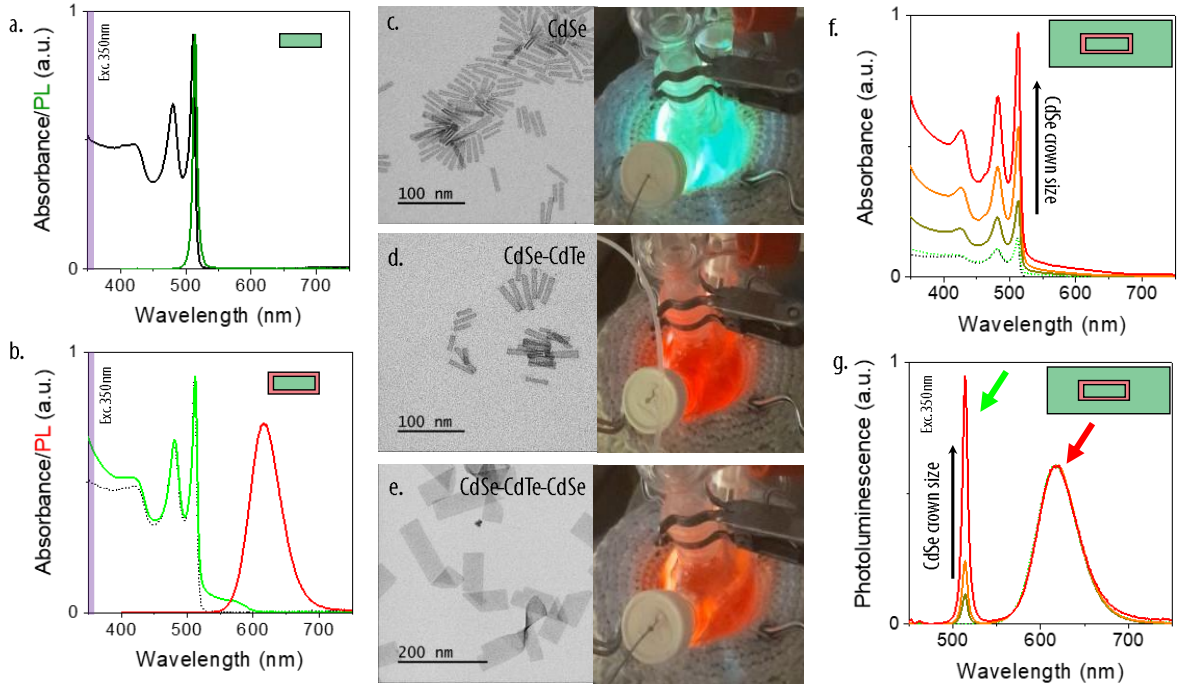

Figure 32: *Synthesis of CdSe-CdTe-CdSe core-crown-crown heterostructure. a. Absorption (black) and emission (green) spectra of the CdSe 4ML core NPLs. b. Absorption (green) and emission (red) spectra of the CdSe-CdTe 4ML intermediate NPLs. c-e. TEM picture and flask luminescence when excited by a 407 nm laser associated to the CdSe 4ML core NPLs (c), the CdSe-CdTe 4ML intermediate NPLs (d) and the CdSe-CdTe-CdSe 4ML NPLs (e). f-g. Absorption (f) and emission (g) spectra of according to the injection time. The black arrows underlines the trend when the size of the lateral CdSe crown size increases. Emission spectra have been normalized to the red maximum in emission and all the excitation spectra have been conducted at 350 nm.*

Before the initial injection, green photoluminescence from CdSe 4 ML NPLs associated with the core emission is observed in the flask (as shown in picture **Figure 32c**). As expected, the addition of the Te precursor induces the formation of the type II interface and fully quenches the green photoluminescence. Instead, a reddish photoluminescence is observed in the flask (as shown in picture **Figure 32d**). This emission is broad (54 nm – 170 meV) with a maximum around 610 nm, consistent with the creation of the type II interface (see **Figure 32b**). When the CdSe external crown is added, the green feature gradually returns and increases with the amount of CdSe added (as highlights the green

arrow in **Figure 32g**). This green-to-red ratio enhancement is consistent with an increase in the lateral extension of the CdSe crown.

At the end of the synthesis, and after the washing steps, the green emission remains narrow, and the interfacial recombination is red-shifted up to 618 nm (see emission spectrum in **Figure 33a**). The final NPLs exhibit large lateral extensions (as shown in TEM picture **Figure 32e**). Over time, these particles tend to settle at the bottom of the flask. However, after sonication, they maintain colloidal stability on a timescale compatible with film deposition, which is critical for further processability. When combined with an InGaN LED (i.e. emission at 460 nm) on the CIE diagram, a larger extension of the color gamut is achieved compared to technologies based on quantum dots (as exhibits the comparison between the gray and orangish triangle in **Figure 33b**). Specifically, the band edge emission from the CdSe enables a significant improvement in the green region, as expected for this work.

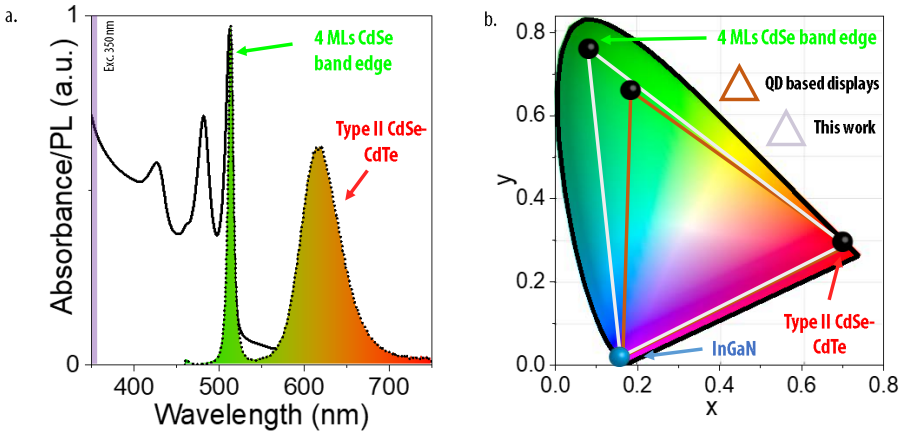

Figure 33 : *Improvement of the color gamut. a. Sum up on the absorption (solid) and photoluminescence (dot) spectra for the synthesized heterostructure. The excitation spectrum has been conducted at 350 nm. b. CIE diagram comparing the red and green emitters from currently used QD-LCD displays and the dual emission observed in the inverted heterostructure. The respective color gamuts are localized in the orange and in the white triangles.*

Characterization of the bicolor emitting heterostructure.

The final NPLs obtained have large lateral extensions (40 x 180 nm²) with a high aspect ratio of 4.5 (as shown by TEM picture in **Figure 32e**). The low amount of TOP:Te added does not enable us to conclude on the presence of CdTe inside the heterostructure using absorption alone. TEM imaging could be a suitable technique to observe variations in size during the growth of the CdTe crown. However, the small lateral extension of the CdTe crown falls in the resolution's limit of the measurements.

An additional technique is required to confirm the presence of Te inside the particle. For example, EDX spectroscopy can be used to conduct elemental analysis of the particle. In the case of the studied heterostructure, tellurium represents less than 1% of the constituent atoms, which is about the resolution of the used detector. Complementary XPS analyses have also been conducted on this heterostructure. The measurements were carried out at the synchrotron SOLEIL on the TEMPO beamline under the supervision of M.G. Silly. An overview of the core levels of the elements constituting the material is presented in **Figure 34b**. In this overview, conducted using a photon energy of 700 eV, several core-level states can be identified: Cd 3d and Cd 4d at 405.4 and 10.9 eV, Se 3p and Se 3d at 160.4 and 53.9 eV, both elements coming from the NPLs; S 2s and S 2p at 228.4 and 164 eV; C 1s at 284.9 eV, both elements coming from the ligand exchange carried out before the

measurements from carboxylates to EDT; Au 4f at 83.9 eV, which comes from the substrate; O 1s at 532.4 eV, which comes from potential air exposure of the NPLs film, and finally Te 3d at 572.9 eV, which confirms the presence of Te inside the NPLs.

XPS and EDX are appropriate techniques to determine the presence of elements inside a structure. However, without coupling them with microscopy, a complete elemental mapping at the NPLs scale is not possible. To determine the localization of the CdTe crown inside the final heterostructure, High Angular Annular Dark Field coupled with Scanning Transmission Electron Microscopy (HAADF-STEM) was conducted by Gilles Patriarche at C2N in Université Paris-Saclay. In the observed NPLs, clear contributions of Se and Cd are observed (**Figure 34c-d**).

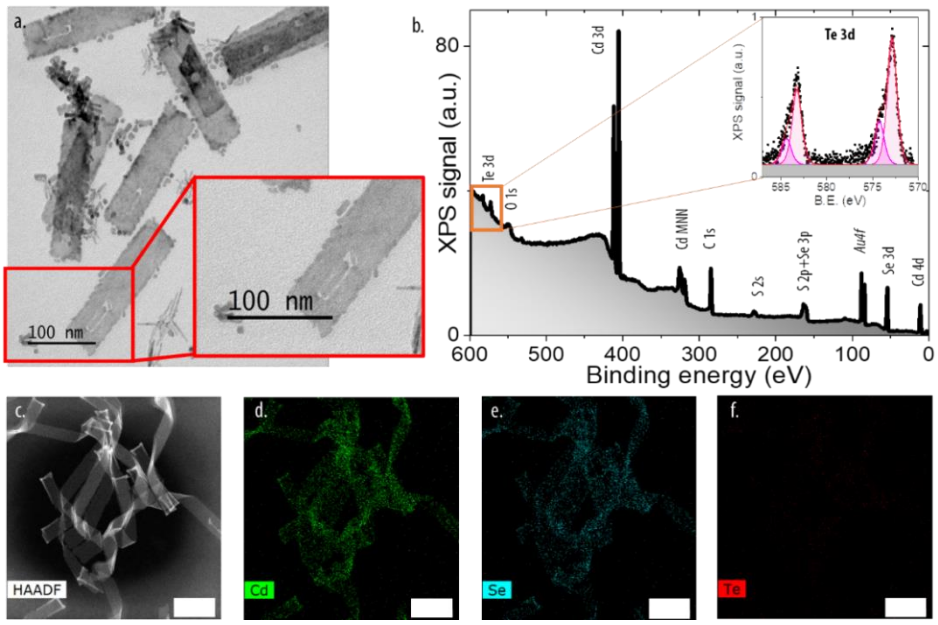

Figure 34: *Structure and composition of the heterostructure. a. TEM pictures of the heterostructure annealed in oleylamine. The red square is a zoom on one of the NPLs where the CdTe crown has been selectively dissolved. b. XPS overview of the heterostructure. The insert is a zoom on the Te 3d core-levels. c. HAADF-STEM pictures of the heterostructure. d-f. EDX mapping of the heterostructure corresponding to Cd (d), Se (e) and Te (f). The mappings have been conducted on the same NPLs than c.*

Finally, to address unveil the core localization, I found a destructive strategy to selectively dissolve the CdTe by annealing the heterostructure in presence of oleylamine. The TEM pictures of the resulting NPLs clearly show the dissolution of a crown inside the NPLs, which corresponds to the CdTe crown (as shown by TEM picture in **Figure 34a**). This core is not located in the center of the particle but rather next to one of the short edges. This is consistent with the previous observations made on CdSe-CdS or CdSe-CdTe core-crown NPLs[78,91].

c. Modulation of the red emission.

On the first sample synthesized, the red contribution appears at 618 nm, which is far from the usual value obtained for type II interface recombination between CdSe and CdTe (656 nm[78,93]). This discrepancy is due to the lateral quantum confinement induced by the small size of the CdTe crown (a few nanometers at maximum with a Bohr radius of 6.5 nm). To investigate this effect, different amounts of CdTe were synthesized (ranging from 0.13 to 1 µmol in tellurium with respect to 3 µmol of core CdSe). In absorption, the intermediate CdSe-CdTe core-crown NPLs exhibit increasing CdTe absorption features, consistent with the increasing quantity of Te injected (see absorption spectra in

Figure 35a). At this point, a difference in emission is already observed based on the quantity of CdTe, with a modulation of the emission from 607 to 640 nm. This observation is in line with the study conducted by Kelestemur et al. on the influence of crown size on the type II recombination in CdSe-CdTe core-crown NPLs[32]. As the external crown of CdSe grows (see emission spectra in **Figure 35b**), the lateral confinement decreases, and the emission is further red-shifted between 618 and 650 nm (isolating ligands adsorbed on the lateral facets are exchanged with CdSe material that has a smaller dielectric constant). However, lateral confinement is still observed an CdTe since emission remains bluer than the one of a CdSe-CdTe core-crown 4 ML NPLs with a large crown of CdTe, where the lateral quantum confinement can be neglected d (as highlights the dark horizontal line in **Figure 35c**).

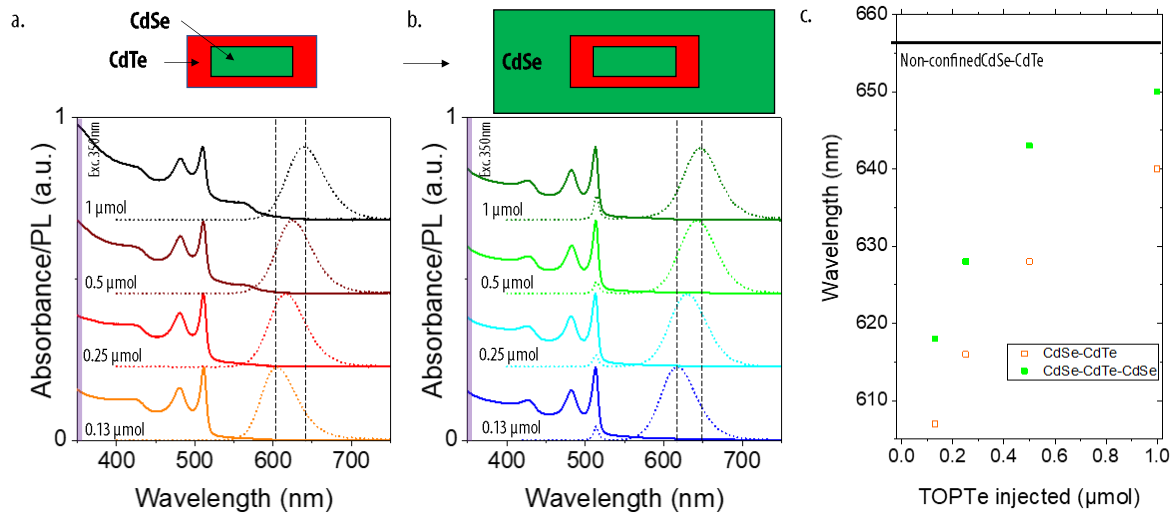

Figure 35: *Influence of the size of the CdTe crown. a. Absorption (solid lines) and photoluminescence (dot lines) spectra of the core-crown CdSe-CdTe NPLs according to the quantity of TOP:Te added. The vertical dash lines correspond to the maximum emission of the smallest and largest quantity of TOP:Te added. b. Corresponding absorption (solid lines) and photoluminescence (dash lines) spectra of the core-crown-crown CdSe-CdTe-CdSe NPLs according to the quantity of TOP:Te added. The vertical dash lines correspond to the maximum emission of the smallest and largest quantity of TOP:Te added. c. Evolution of the maximum emission for core-crown (red hollowed squares) and core-crown-crown (green squares) according to the quantity of TOP:Te added. The horizontal bold line corresponds to a CdSe-CdTe presenting a large crown of CdTe without any lateral quantum confinement.*

Meanwhile, the absorption and green emission remain unchanged at the end of the synthesis, corresponding to CdSe 4 ML NPLs excitonic features. To modulate the green emission, one needs to change the band edge emission of the external crown of CdSe. This can be achieved by using an alloy instead of pure CdSe. However, using $CdSe_xTe_{1-x}$ would result in a red-shifted emission with broad features, which is not desirable in this case. Instead, the use of $CdSe_xS_{1-x}$ can be useful to blue-shift the green emission[71,165]. I will come back to it later to disentangle the degenerated contributions form the core and external crown.

We have presented the design and synthesis of a particle that exhibits a bicolor emission. To achieve this, we optimized the geometrical parameters of a core-crown-crown heterostructure while maintaining simplicity. In this particle, the green emission is expected to originate from the band edge emission of CdSe, while the red emission arises from the type II interface recombination. We will now investigate the optical properties of this particle to better understand the origin of this bicolor emission.

3. Origin of the bicolor emission.

According to Kasha's rule, emission should only occur from the lowest energetic state due to the fast relaxation of the exciton before any other radiative recombinations. As a result, NPLs should not exhibit bicolor emission. Specifically, in this case, the lowest excited energetic state corresponds to the localization of the charge carriers at the interface between CdSe and CdTe, indicating that no green emission should be observed. In the following section, we will investigate the origin of this green emission and the photophysic underlying this bicolor emission.

a. A single bicolor NPL.

According to the photoluminescence measurements conducted on the heterostructure, we effectively observe bicolor emitting features. However, the observed green emission could also be attributed to the side nucleation of CdSe 4 ML NPLs. To confirm that the bicolor emission indeed originates from the heterostructure, we performed PLE measurements (see the summarize in **Figure 36a**). The working concentration was sufficiently low to neglect reabsorption-emission phenomena. When the emission was observed at 615, 645, or 675 nm, the PLE signal perfectly corresponded to the absorption spectrum. This indicates that regardless of where the exciton is created in the NPLs, it can recombine at the interface, which is a direct consequence of Kasha's rule. In terms of the green emission at 518 nm, excitons created inside the CdTe crown should not be involved. On the PLE spectrum, the curve perfectly matched the two CdSe excitons, while the absorption at 350 nm decreased, indicating the absence of CdTe contribution.

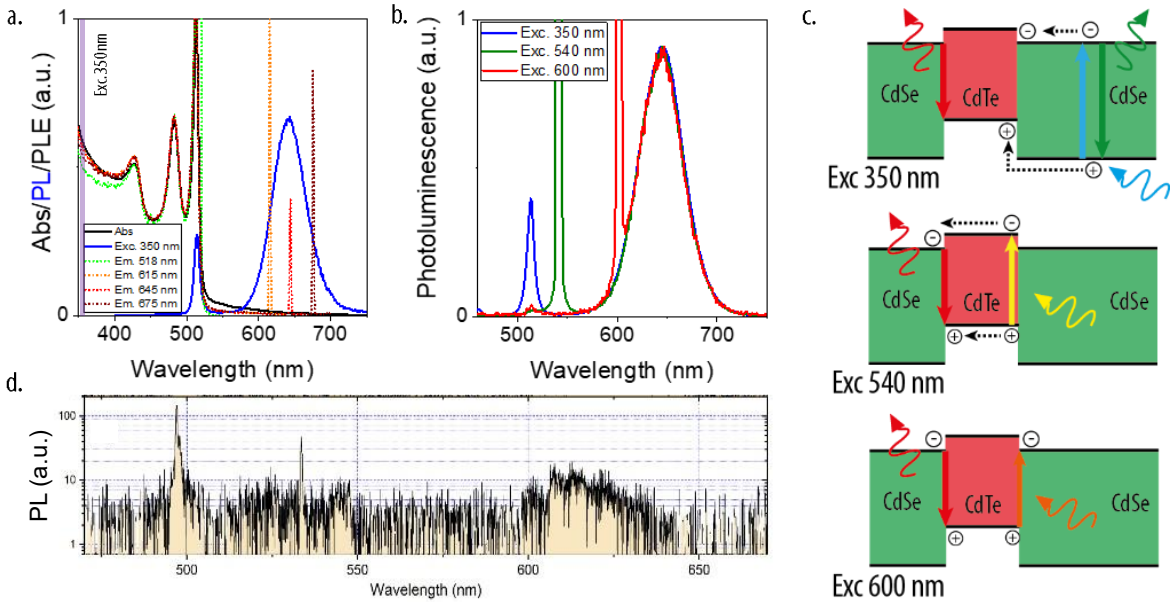

Figure 36: *Bi-emission at the single NPLs scale. a. Absorption (black), emission (blue) and PLE (dot lines) spectra of the heterostructure in diluted solution. The PLE spectra are taken at 518, 615, 645 and 675 nm. b. Emission spectra of the same heterostructure at various excitation wavelength (350, 540 and 600 nm). For clarity, the spectra have been normalized at the maximum red emission peak. c. Sketch of the charge carrier's localization and recombination after various energies excitations. d. Single particle measurement on heterostructure presenting a large CdSe crown.*

The PLE signals focused on the red emission did not return to zero at a higher wavelength than the CdTe 4 ML NPLs absorption band edge (555 nm), revealing traces of sub-band gap absorption. To confirm this observation, PL spectra at various excitation energies are recorded (see PL spectra in **Figure 36b**). When a high-energy photon is absorbed, it could radiatively relax either in the green or in

the red. By selectively exciting the CdTe crown at 540 nm, the red emission persisted while the green emission disappeared (see the sketch of possible deexcitation pathways according to the excitation energy in **Figure 36c**). This is consistent with a localization of the hole inside the CdTe crown without the possibility of delocalizing into the CdSe. However, when an even lower photon energy is used, for example, 600 nm (below the CdTe band gap), the red emission is still observed (see the red PL spectrum in **Figure 36b**). This can be explained by the absorption of a photon right at the interface, leading to an in-situ formation of the exciton at the charge transfer (CT) state. This partly explains the tail observed at higher wavelengths in the absorption. These PLE measurements are consistent with a bicolor emission originating from a single population of NPLs. However, it is also possible that the emission could be obtained by two distinct NPLs from the same population.

To rule out this hypothesis, PL measurements on highly diluted solutions were conducted by Thierry Barisien's team at INSP. To achieve this, the solution was diluted by a factor of 10^3, resulting in NPLs concentrations as low as 10^{-9} mol.L^{-1}. A droplet of the solution was trapped between two coverslips for the measurements. Excitation was provided by a focused pulsed laser (390 nm, spot diameter of 1 µm, 2 ps pulse operated at 82 MHz), and the resulting signal was collected using a cooled CCD camera. To freeze the system and limit overheating processes, the coverslips were placed on a gold finger and cooled down to 7 K. The laser's small waist and thin layer of NPLs allowed for focusing on a very small volume of the solution, enabling PL measurements at the single particle scale. The observation of blinking behavior during the experiment, without being a definite proof, indicates that the single particle regime is most likely reached. Several experiments were conducted, and a representative PL spectrum obtained during these experiments is shown in **Figure 34d**. Both the green and red features were observed, revealing a bicolor emission originating from a single NPL.

b. Dynamic of the two radiative recombination.

We have demonstrated that bicolor emission is achievable at the single particle scale, defying Kasha's rule. To comprehend the origin of this phenomenon, the dynamics of the charge carriers after their formation inside the heterostructure were investigated.

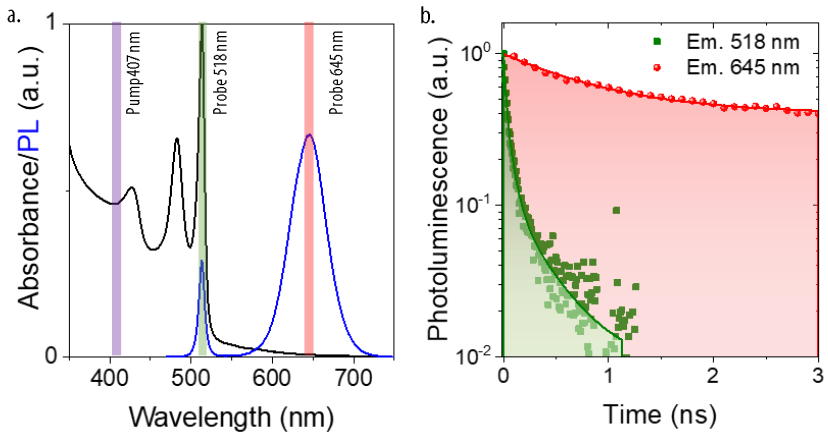

Figure 37: *Dynamic of the two emissions. a. Absorption (black) and emission (blue) spectra of the investigated bicolor heterostructure. The excitation wavelength and the probe position for the green and the red features are underlined by the vertical line. b. PL intensity according to the time right after the excitation pulse for the two emission (at 518 nm for the green emission and at 645 nm for the red emission).*

Time-Resolved Photoluminescence (TR PL) measurements were initially performed on the two emissions by exciting the heterostructure with a blue diode (407 nm) (see the summarize in **Figure 37a**

and the measured dynamics in **Figure 37b**). By capturing photons over time, the radiative relaxation dynamics can be probed. In this heterostructure, the green emission occurs rapidly (sub ns), which aligns with band edge recombination inside CdSe NPLs[29]. In contrast, the relaxation dynamics of the red emission are significantly longer (up to 100 ns). This behavior is characteristic of type II interfaces in NPLs, where the limited overlap of the electron and hole wavefunctions across the interface diminishes the relaxation probability and prolongs the exciton's lifetime[166].

TR PL allows for the investigation of states involved in radiative relaxations but not in other non-radiative processes such as trap-de-trap and exciton diffusion. Additionally, in the current configuration, this technique is limited by the time resolution of the photodetector. Specifically, carrier cooling, which is a rapid process of a few picoseconds, cannot be probed using this conventional detector. Transient Absorption (TA), employed in a synchronized pump-probe configuration, enables the resolution of events down to approximately 50 femtoseconds. In this setup, a pulsed laser source pumps the particles into excited states. The populated excited states are analyzed through difference in absorption using a synchronized white probe source. By utilizing a delay line, the evolution of absorption is monitored over time, resulting in the generation of a 3D map that depicts the difference in absorption before and after the pump pulse, ΔA (color map), as a function of wavelength (x-axis) and time (y-axis). An example of this map can be seen in **Figure 38a**.

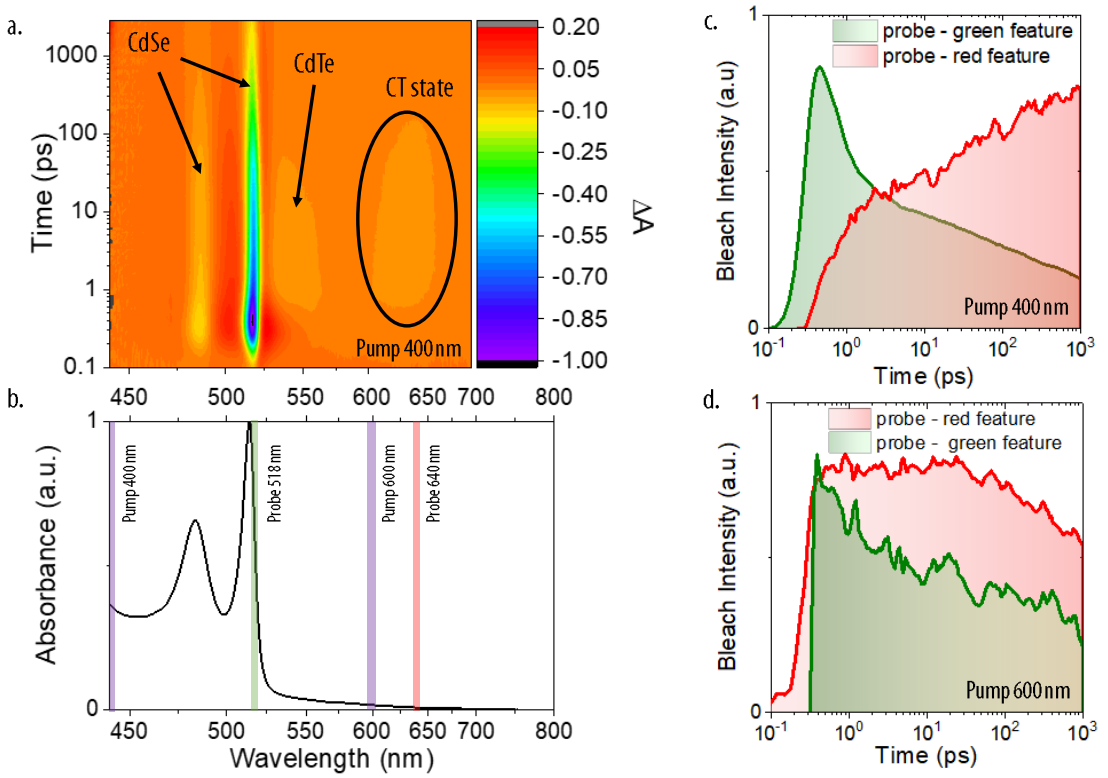

Figure 38: *Transient absorption analysis of the heterostructure. a. TA map of the heterostructure using a 400 nm pump. The ΔA have been normalized for clarity. b. Absorption spectra where are pinpointed the pumping wavelength used (purple) and the localization of the TA slices presented in c. and d. c-d. Vertical slices of a TA map corresponding to a pumping at 400 nm (c) and at 600 nm (d). The signals have been normalized for clarity.*

First, the pump is set at 400 nm to ensure the excitation of all parts of the heterostructure, see **Figure 38b**. The TA map is shown in **Figure 38a**. When excitons are formed in CdSe, the excited states become occupied, resulting in a decrease in the number of available empty states. As a result, a bleach

(i.e., a decrease in absorption) of the corresponding transition is observed. In the presented TA map, this corresponds to the blueish vertical lines (first excitonic transition at 518 nm) and the yellowish vertical lines (second excitonic transition at 485 nm). A vertical slice of the TA map at 518 nm is presented in **Figure 38c** (green line). The initial rise corresponds to the filling of the excited state due to exciton formation. After this rise, a decrease in the bleach is observed, which corresponds to the relaxation of the charge carriers to a second state. It is worth noting that a similar behavior is observed at the CdTe absorption band edge (555 nm). The bleach initially increases due to the filling of the CdTe excited states, and the delocalization of the electron leads to a decrease in the bleach of the CdTe features (pale orange area around 555 nm in **Figure 38a**).

This second state can be either the fundamental state resulting from a non-radiative recombination of the exciton, or the CT state localized at the CdSe/CdTe interface. In fact, as mentioned earlier, excitons can be directly created at the interface, resulting in a non-zero absorption signal at 600 nm. Therefore, in TA, we can possibly observe a bleach of this CT state, which is effectively the case here as highlights the black circle in **Figure 38a**). A slice centered at 640 nm is shown in **Figure 38c** (red line). The evolution of the bleach presents a double slope, with the first rise shifted compared to the one observed in the CdSe features (green line). The tendencies of the two slopes correspond to the decreasing bleach tendencies observed for the green feature. This observation is consistent with the delocalization of the exciton at the interface when initially created inside CdSe. A delay in the rise of the bleach is also observed between the green and red lines. This is a direct consequence of the small absorption cross-section of the CdSe/CdTe interface: a major part of the bleach measured arises from migration of exciton created in the CdSe toward the interface.

The same experiment is then conducted using a 600 nm wavelength pump (see dynamics in **Figure 38d**). The evolution of the CT state absorption exhibits a sharp and unique bleach rise. This corresponds to the direct formation of excitons at the interface following optical pumping. At this energy, excitons can only be formed at the interface, and no further increase in the bleach of the CT state is expected. This is consistent with the observed dynamics. In parallel, the bleach of the CdSe first excitonic transition follows the same trend as the CT state feature, indicating electron localization inside the CdSe, though at higher energy.

Those results are consistent with a type II interfacial recombination for the red emission and a band edge recombination for the green emission. Additionally, a charge transfer from the entire structure to the CdSe/CdTe interface is observed.

c. Investigation on the green emission origin.

Coming back on the TA measurement conducted with a 400 nm pump, the bleach evolution exhibits an unusual shape (see **Figure 38c**). The two slopes observed during the bleach increase (red line) or decrease (green line) reveal the presence of two regimes. First, a fast transfer occurs within a few picoseconds, consistent with an ultrafast migration of the charge carriers toward the interface. Then, a second regime is established, slower than the first one. This observation reveals the presence of a bottleneck effect that limits the filling of the CT state. Its origin can be manifold including Coulomb blockade[167], interface strains[77,168], Auger reheating[169], shallow hole traps in the external crown[170], phonon bottleneck effect[171], and more. In this particular case, the large lateral extension of the NPLs slows down the migration of the exciton created in the outer part of the NPLs. Therefore, radiative relaxation can compete with the diffusion of the exciton toward the type II interface, enabling the observation of green emission.

This slowdown of migration is exacerbated in the synthesized heterostructure due to the anisotropic shape of the particle. As mentioned in the previous section, the CdSe core is not centered in the particle but rather localized in a corner of the final heterostructure. The migration length of an exciton created on the opposite side of the structure is drastically enhanced, favoring green emission. The large aspect ratio of the particle induces a similar effect, as CdSe areas are localized far from the CdSe/CdTe interface. This explanation justifies the choice of a rectangular core instead of a square one.

In conclusion, the overall dynamics measured inside the heterostructure are consistent with our expectations. By controlling the diffusion rate of the excitons toward the type II interface, band edge recombination can be observed inside the external crown of CdSe, enabling the bicolor emission. This effect is particularly enhanced by the strong anisotropic shape of the heterostructure. The NPLs have yet been investigated under low incident power excitation to avoid a multi-excitonic regime. However, as shown by Galland et al. in their dot-in-bulk particles, in heterostructures, a multi-exciton regime can unveil unexpected but properties[167].

4. Multi-excitonic regime in the core-crown-crown heterostructure.

The measurements presented previously have been conducted using low incident power. In this regime, the NPLs usually contain fewer than one exciton per particle. When the incident power is increased, more electron-hole pairs can be created, and multi-exciton regimes can be achieved. It is highly interesting to investigate this regime as nonlinear processes may arise.

a. Tuning the green-to-red ratio.

During the introduction part on the synthesis of the heterostructure, we mentioned that the green-to-red ratio could be adjusted based on the lateral extension of the CdSe external crown. Finding a way to tune this ratio post-synthetically would allow for the adjustment of the emission color of a single particle directly within a device.

Temperature dependency.

As we have seen in the previous section, the absorption cross-section of the CT state is very limited, and the excitons localized in it mostly result from the absorption of the surrounding CdSe. PL measurements with respect to temperature have therefore been conducted by Barisien et al (see the PL spectra in **Figure 39b**). Firstly, as the temperature decreases, both the green and red emissions exhibit a blue-shift. The contraction of the lattice induced by the temperature drop is not strong enough to account for the observed shift. Instead, this blue-shift originates from electron-phonon coupling[16,172], which causes a decrease in the band gap energy with temperature, as established empirically by Varshni *et al.*[173] in 1967.

The most significant change is the inversely proportional evolution of the green-to-red ratio with temperature. While the maximum PL intensities are nearly equal at room temperature, predominantly green emission is observed at 4K. This observation is consistent with the thermally activated kinetic model of exciton displacement in NPLs. At low temperatures, less energy is available for lattice vibrations, reducing the diffusion length of the exciton. Its relaxation lifetime then starts to compete with its diffusion time, thereby enhancing green emission. Consequently, more excitons will recombine within the material where they were created, particularly in the CdSe, which explains the increase in green emission. Thus, a color dependence based on temperature has been revealed.

Power dependency.

In similar particles with complex heterostructures and multiple emissions, the color ratio often depends on the incoming excitation power[157]. To investigate this property in bicolor emitting NPLs, we conducted an initial experiment using a laser diode (405 nm). When the diode was directed towards the bottom of a test tube containing a diluted solution of the bicolor emitting NPLs, the curvature of the glass focused the laser beam like a lens. As we moved closer to the focal point, the color changed from red to green (as shown in picture **Figure 39a**). This effect was particularly pronounced at low concentrations. At the focal plane, the photon flux per unit area reached its maximum value. Therefore, the results support a power-dependent relationship for the green-to-red ratio: a higher incoming excitation flux favors CdSe emission, while a decrease in excitation flux enhances interfacial recombination.

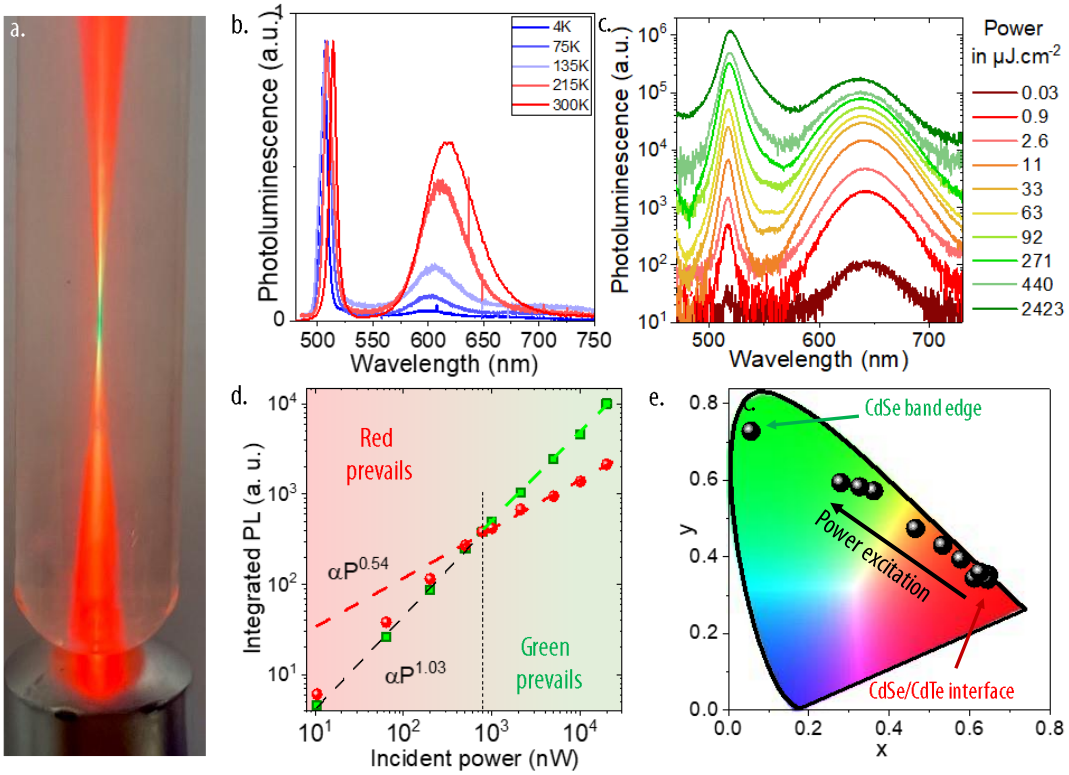

Figure 39: *Power dependency of the green-to-red ratio. a. Picture of a heterostructure solution diluted inside a test tube. The excitation is provided by a 405 nm laser pointer and a filter is used to cut the excitation wavelengths. B. Evolution of the emission spectra according to the temperature. c. Evolution of the PL spectrum according to the incident power excitation. d. Integrated green and red features according to the incident excitation power. The dashed lines correspond to the linear fit of the two emissions before the saturation (black), to the linear fit of the red and green emissions after the saturation (resp. red and green). The prevailing features are underlines by the red and green font color. e. Localization of the emission spectra presented in c. inside the CIE color gamut. The green and red arrows are pinpointing the position of the two emissions taken separately. In all those experiments, the excitation have been conducted at 400 nm.*

More systematic measurements are then conducted by Barisien's team at INSP with various excitation powers (see PL spectra in **Figure 39c**). Initially, the emissions from all features (green CdSe and interfacial red recombination) increased with increasing power excitation. The trend observed in the test tube was subsequently confirmed, showing an increase in the green-to-red ratio in response to the incoming flux. In each spectrum, the green and red emissions were integrated to assess the contribution of each component relative to the excitation flux (as shown in **Figure 39d**). Two tendencies can be observed here. Firstly, for incident powers up to 100 nW, both the green and red

features exhibited a linear dependency on the excitation power. At higher excitation powers, the green emission continued to exhibit a linear dependency, while a different regime was observed for the red emission, following a $P^{0.54}$ power dependency. Consequently, the color evolution with incident power is primarily influenced by a saturation of the red emission rather than an increase in the green emission. By adjusting the incident power, a continuum of colors could be achieved, ranging from the red CdSe/CdTe interface to the green CdSe band edge emission (as highlight the dark dots in the chromaticity diagram shown in **Figure 39e**). This tendency is observed in all studied heterostructures. Changing the geometrical parameters of the heterostructure allowed for altering the threshold of red saturation. For example, a larger CdSe crown resulted in a lower saturation threshold.

b. Spatial origin of the green emission and tricolor emission.

The origin of this power dependency is then investigated. First, a deeper understanding of the nature of the emission is required. While the red emission is associated with the charge transfer state, the green emission could arise from either the core or the external crown of CdSe. To determine the spatial origin of this emission, I considered introducing a third emission in the outer part of the particle to distinguish the degenerated contributions from the core and the external crown. However, introducing such an emission proved to be challenging. The lateral quantum confinement in the small CdTe crown made the use of $CdSe_xTe_{1-x}$ as a new band edge emission unwise due to its overlap with the type-II interface recombination. Nevertheless, we could still blue-shift the CdSe band edge emission by utilizing a CdS_xSe_{1-x} alloy.

A compromise was then necessary regarding the alloy composition: an alloy that is too selenium-rich would exhibit a band edge emission overlapping with that of CdSe, while an alloy that is too sulfur-rich would decrease the recombination probability within the alloy due to the type-I band alignment between CdSe and CdS_xSe_{1-x}. Therefore, we decided to focus on a $CdS_{0.3}Se_{0.7}$ crown composition. To maintain the same interfaces with CdTe and to minimize the lattice mismatch between the CdTe crown and the external CdS_xSe_{1-x} crown, an additional layer of CdSe is inserted between these two crowns (see the NPL sketch and band alignment in **Figure 40a**). This layer needs to be thick enough to prevent type-II recombination across the CdSe crown between CdTe and CdS_xSe_{1-x}, as observed by Khan et al. in the CdSe-CdS-CdTe heterostructure[77].

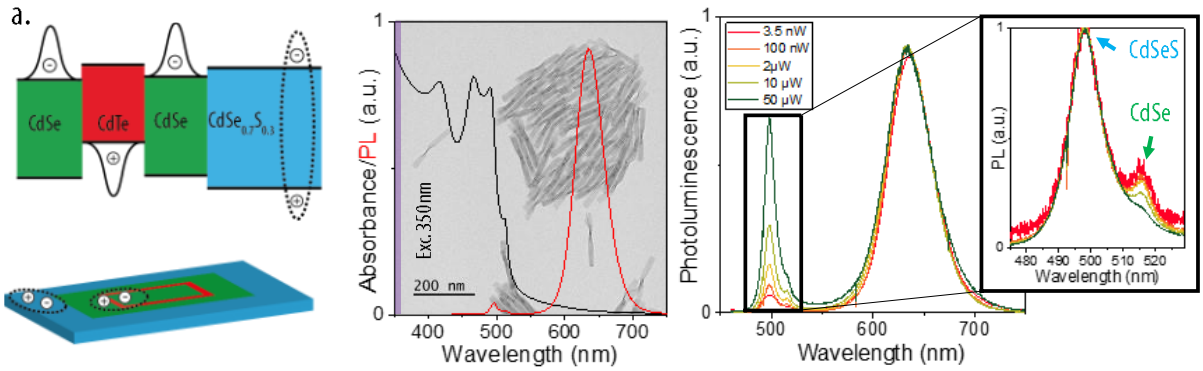

Figure 40: *Tricolor emitting NPLs. a. Sketch and band alignment of the CdSe-CdTe-CdSe-$CdSe_xS_{1-x}$ heterostructure. b. Absorption (black) and PL (red) spectra of the CdSe-CdTe-CdSe-$CdSe_xS_{1-x}$ heterostructure. In the back font is introduced a corresponding TEM picture. The excitation has been conducted at 350 nm c. PL spectra according to the incoming excitation fluence. The panel corresponds to a zoom on the 500 nm region. For clarity, the PL spectra have been normalized to the red emission. The excitation has been conducted at 400 nm.*

In absorption, the presence of CdSe in the core and the first crown is consistent with a shoulder at 510 nm. Due to the alloying effect, the first excitonic peak of the $CdSe_xS_{1-x}$ is shifted to 491 nm (see absorption spectrum in **Figure 40b**). This new structure is exhibiting three emitting features: a red emission at 635 nm, still associated with the type II interface, a green emission at 515 nm, attributed to the CdSe band edge emission, and a bluer emission at 495 nm, corresponding to the CdS_xSe_{1-x} band edge recombination (as highlights the zoom on the PL spectrum in **Figure 40c**). This transition energy aligns with the injected Se/S ratio ($CdS_{0,3}Se_{0,7}$) considering the continuous band gap evolution in alloyed semiconductors[71,165].

In this new structure, the green emission is expected to originate either from the center of the particle or from the small crown added between the CdTe and CdS_xSe_{1-x} crowns. Conversely, the blue emission is expected to arise solely from the external crown. When an increasing incident power is applied, the blue emission is enhanced, similar to the green feature in the CdSe-CdTe-CdSe heterostructure. On the other hand, the green emission also saturates, resulting in a dominant blue feature at high photon flux (see the zoom on the PL spectra in **Figure 40c**). Therefore, we can conclude that the increase in the green feature within the CdSe-CdTe-CdSe heterostructure stems from an enhanced radiative rate recombination in the external crown rather than in the initial CdSe core. Moreover, considering the difference in emission between the CdSe and CdS_xSe_{1-x} crown, it can be inferred that the band edge emission primarily arises from the outer part of the external crown, located far from the interface. These results provide an explanation for the increased green emission observed in heterostructures with larger lateral extensions. Furthermore, they are consistent with the previously proposed mechanism of delayed exciton migration.

c. Investigation of the green-to-red ratio power dependency.

A potential explanation for the saturation of the red emission is a Coulomb blockade effect caused by the presence of holes within the CdTe crown. This hypothesis suggests that the presence of holes at the interface could repel incoming charges, leading to an increased density of holes within the CdSe states. The phenomenon of Coulomb blockade has been previously observed in a dot-in-bulk system by Galland et al., where the injection of a hole into the CdSe core increased the number of shell-states due to Coulomb repulsion, limiting the injection of a second hole[167].

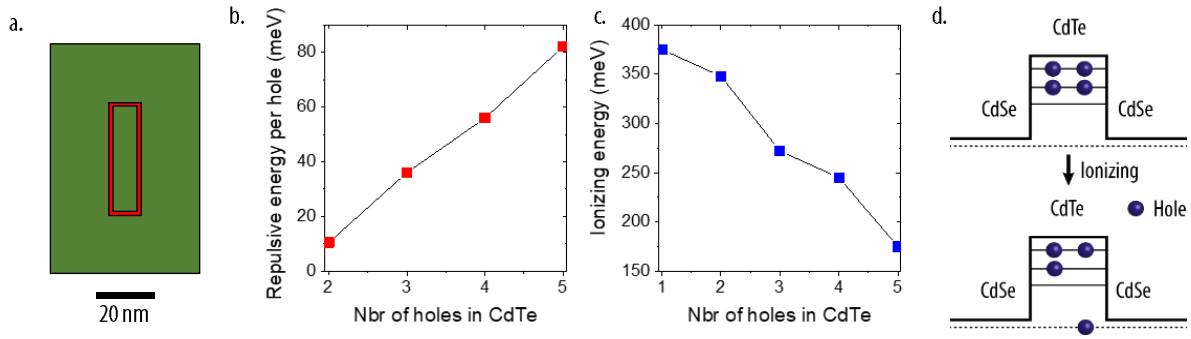

Figure 41: *Coulomb blockade investigation. a. Sketch of the modelized NPLs. b-c. Evolution of the inter-hole repulsion energy (b) and ionizing energy (c) according to the number of holes injected inside the CdTe crown. d. Sketch of the ionizing process.*

To investigate this hypothesis further, Climente's group in Spain conducted calculations using k.p modeling to analyze the energetic landscape of the CdSe/CdTe/CdSe heterostructure. The considered NPLs consist of a 10x30 nm² CdSe core, a homogeneous 1.5 nm CdTe crown (resulting in a final area of 13x33 nm²), and a final CdSe/CdTe/CdSe heterostructure of 42x65 nm² (see the sketch of

the particle in **Figure 41a**). Using this geometry, they calculated the energy required to inject multiple holes into the CdTe crown. If Coulomb blockade were present, the repulsion between holes would need to be high enough to overcome the band offset between CdSe and CdTe (690 meV). The results, depicted in **Figure 41b** show that the inter-hole repulsion remains low compared to the band offset values, even when considering up to five holes injected into the CdTe crown. The ionizing energy, which represents the energy required to promote a hole from CdTe to the CdSe continuum (see the schematic in **Figure 41d**) was also calculated, taking into account pair associations between holes (see **Figure 41c**). For up to five holes, the ionizing energy remains larger than the thermal energy at room temperature (25 meV). Therefore, it can be concluded that Coulomb repulsions do not account for the observed power dependency of the green-to-red ratio.

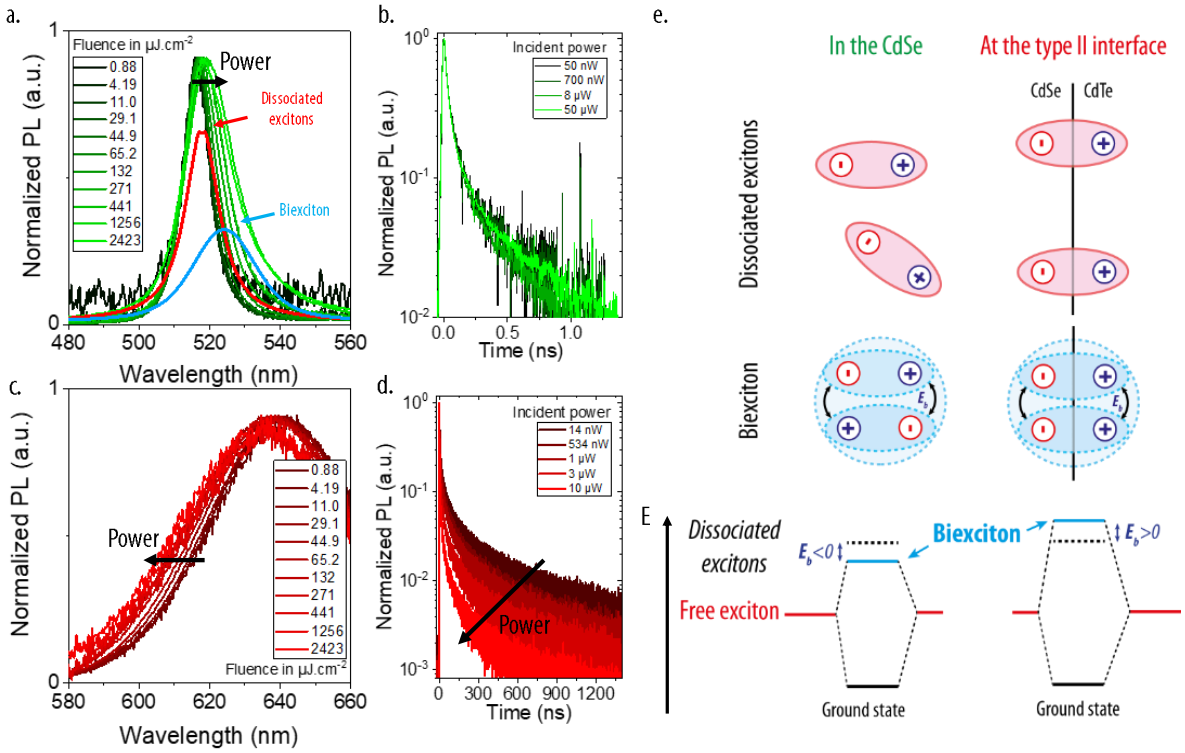

Figure 42: *Biexcitonic regime in CdSe-CdTe-CdSe heterostructure. a. Evolution of the green photoluminescence according to the incoming incident power. The red and blue curves correspond respectively to the contribution of the single and biexciton emission in the photoluminescence spectra taken at the highest incoming power. b. Photoluminescence decays according to the incoming fluence for the green emission. c. Evolution of the red photoluminescence according to the incoming incident power. d. Photoluminescence decays according to the incoming fluence for the red emission. e. Sketch on the interaction possible between two excitons in the CdSe or at the CdSe-CdTe interface. The graph at the bottom shows the respective evolution of the system energy. E_b corresponds to the binding energy of the biexciton.*

To gain a deeper understanding of the saturation mechanism, TRPL measurements of the green and red emissions were conducted as a function of the incident power (see dynamics in **Figure 42b and d**). The relaxation time of the green emission remains constant with respect to the incident power. In contrast, for the red emission, a faster decay in relaxation is observed, indicating the emergence of new non-radiative decay pathways at higher incident power. This behavior is associated with the appearance of Auger recombination. Although this process is typically reduced in type II interfaces due to the distinct dissociation of charge carriers, the CdSe/CdTe interface still exhibits a limited volume compared to the CdSe external crown. As the excitation power increases, the density of excitons within the small volume of the interface becomes favorable to non-radiative Auger

recombination. This assumption aligns with the observed decrease in the saturation threshold as the lateral extension of CdSe increases since a higher absorption cross-section of the NPLs leads to an increased number of charge carriers created and delocalized at the interface.

As mentioned earlier, the power dependency observed in the dot-in-bulk particles developed by Klimov's team was attributed to Coulomb blockade processes. However, in our study, we demonstrate that the color balance is achieved, instead, by adjusting the dynamics of non-radiative Auger recombination. The limited volume of the CdTe crown results in a high concentration of excitons, leading to significant Auger recombination. Conversely, the large volume of the external CdSe crown allows for the dilution of excitons, thereby reducing their non-radiative recombination through this process. This particular property has also generated considerable interest in the design of lasers based on NPLs[174].

d. Toward even higher excitation power.

Investigating the biexciton regime.

In addition to a change in the green-to-red ratio, the increase in power induces broadening and a slight red-shift in the green emission (see PL spectra in **Figure 42a**). This observation is linked to a multi-excitonic regime where excitons can interact with each other, forming biexcitons through Coulomb interactions. The two contributions in the emission can be fitted using Voigt functions (see the blue and red lines in **Figure 42a**, which correspond respectively to single exciton recombination and biexciton recombination). Biexcitons are characterized by their interaction energy between charges (see the bottom panel in **Figure 42e**). The difference in energy between the two transitions is here found to be equal to 27 meV which is consistent with biexciton binding energy found in CdSe 4ML NPLs[175].

Contrary to the green one, this red emission is exhibiting a blue-shift when the fluence increases (see **Figure 42c**). This observation is consistent with previous works conducted on type II NPLs[176] or in type II QDs[177] presenting a CdSe/CdTe interface. At such an interface, the hole is located inside the CdTe, and the electron inside the CdSe. As a consequence, the exciton is oriented at the interface and cannot form the square organization observed in homostructures, see the schematic in **Figure 42e**. Instead, it induces Coulomb repulsions between identical charges, particularly between holes due to the reduced volume of CdTe. However, the picture is nevertheless more complex and also involves the energetic levels available for the excitons[178].

Amplified spontaneous emission from a heterostructure film.

Quantum wells, due to their high density of states at the band edge and their large volume, are promising candidates for laser applications. In this context, the first NPLs-based laser was developed by Guzelturk et al. in 2014 using CdSe-CdS core-crown NPLs[98]. The large volume of the NPLs enables a drastic reduction in Auger recombination, which remains a bottleneck when considering optical gain from QDs. Furthermore, the narrow optical features are also interesting for incorporating the material inside a laser cavity[174].

In such nanometric systems, multi-excitonic regimes are usually necessary to achieve gain within a film. To investigate the potential of these particles as an active medium for lasing, TA signal (ΔA, red) was added to the absorption spectrum (A, black) of the film (summarized in **Figure 43b**). The resulting curve (A+ΔA, blue) exhibits two regimes. For wavelengths below 515 nm, positive values are obtained. Panel c. shows a zoomed-in region above 515 nm. Here, the value of A+ΔA is negative,

indicating the possibility for this material to function as a gain medium. A negative value of A+ΔA is associated with the generation of stimulated emission when the probe pulse interacts with the particles. It is worth noting that both emissions exhibit negative features, suggesting the possibility of dual-mode lasing within a single particle. To confirm this, amplified spontaneous emission (ASE) measurements are conducted.

First, to build up the ASE signal, a high density of NCs is required. Therefore, a close-packed film of NPLs is deposited on a glass substrate by drop casting. To trigger stimulated emission, the beam of a 400 nm laser is shaped using lenses to obtain a focused 4 mm strip on the film (see sketch of the setup in **Figure 43a**). The photons emitted along the strip will trigger the stimulated emission of their excited neighbors, increasing the ASE signal along the light line. A CCD camera coupled with a lens is positioned perpendicular to the glass substrate to collect the light guided in the NC film. Finally, an optical density wheel is added to the beam pathway to modulate the incident power and thus the excitation power density.

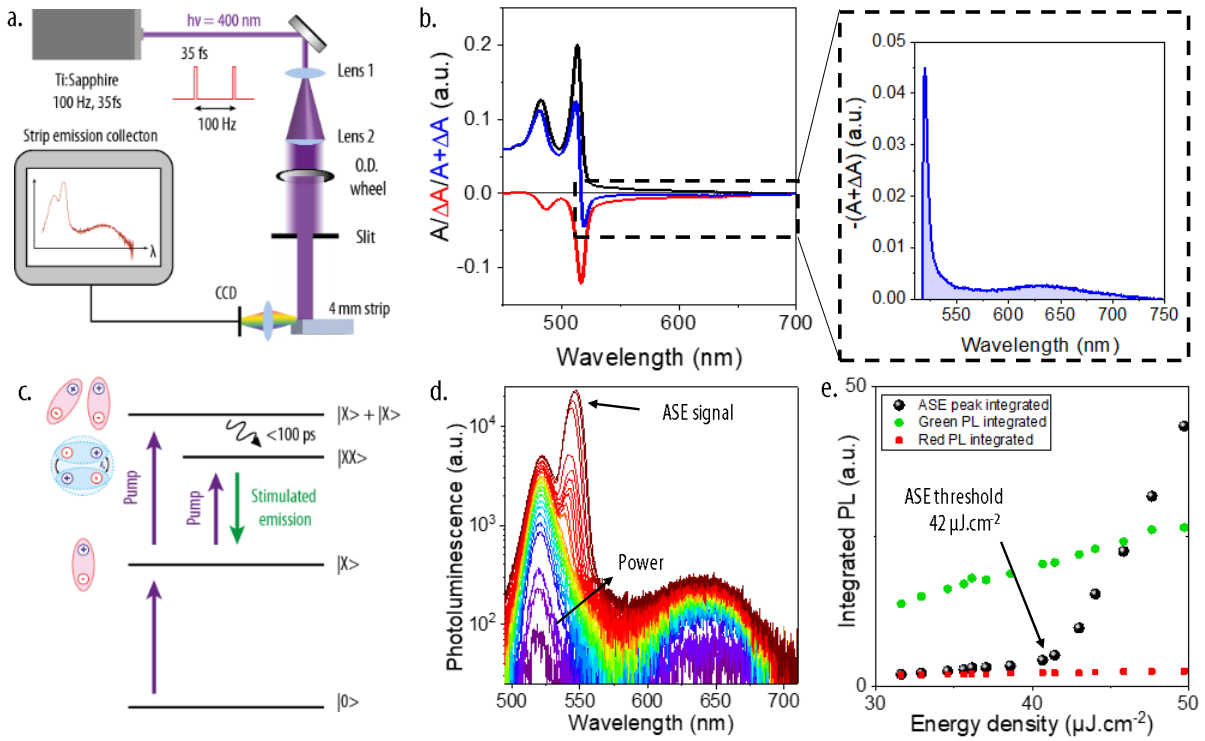

Figure 43: *Amplified spontaneous measurements. a. Sketch of the ASE measurement set-up. The source is a 100 Hz pulsed laser at 400 nm with a 35 fs pulse. b. Graph regrouping the absorption (A, black), the transient absorption after 3 ps (ΔA, red), and the sum of the two (A + ΔA, blue). The panel on the right corresponds to a zoom on the region above 515 nm (taken in absolute value). c. Sketch of the ASE mechanism. The states involved in the ASE are: a ground state |0>, a single exciton state |X>, a dissociated excitons state |X> + |X> and a biexciton state |XX>. d. PL of the strip according to the incident power. e. Evolution of the integrated intensity of the interfacial recombination (red squares), the single exciton recombination in CdSe (green dots), and of the ASE feature (black dots).*

At low pump intensity, the emission spectrum is predominately governed by spontaneous emission (see low power excitation PL spectra in **Figure 43d**). As the fluence increases, an ASE signal appears at 542 nm, red-shifted compared to the band edge emission. This red-shift corresponds to the biexciton emission that was observed when investigating the power dependency of the PL. This biexciton-induced lasing is similar to pioneering works carried out on NCs lasing[175,179,180]. Consequently, the observed optical gain is based on the three-level model shown in **Figure 17c**, involving a ground

state |0>, a single exciton state |X>, a dissociated exciton state |X> + |X>, and a biexciton state |XX>. In this case, the transition involved in the optical gain corresponds to the |XX> -> |X> transition. When the pumping is sufficiently high, the formation of biexcitons from the |X>+|X> state is faster (typically <100 ps[181]) than relaxation through spontaneous emission, leading to population inversion and the observation of gain. In the case of the red emission, despite the observation of gain (see zoom in **Figure 43c**), no ASE signal is observed. This could have been foreseen as interfacial recombination are usually a phonon-assisted process that is not conducive to stimulated emission and significantly reduces the gain value[182].

Returning to the green feature, the relative intensity of each peak (single and biexciton emissions) can be fitted and compared according to the power fluence (see dotted curves in **Figure 43e**). Both the green and red features exhibit a linear dependency characteristic of non-active modes. In comparison, the ASE feature shows two regimes with a slope break occurring at 42 $\mu J.cm^{-2}$. This value corresponds to the excitation required to trigger population inversion and observe ASE. This threshold remains higher than that of typical 2D systems (core-crown-shell CdSe-CdS@CdZnS, which presents a record threshold of 0.8 $\mu J.cm^{-2}$ [183]). This modest efficiency is attributed to CT state, which tends to depopulate the |XX> state, limiting the population inversion necessary to observe ASE. Additionally, the existence of CT states enables re-absorption of the emitted photon, thereby decreasing stimulated emission along the strip.

Finally, these particles enable the observation of gain in both the green and red region. ASE signal has nevertheless been only observed in the green region with features consistent with previous work conducted on CdSe NPLs. Considering the advantageous reduction of the Auger relaxation process, these particles may emerge as promising candidates for the development of low threshold lasers especially toward the obtention of bimodal lasers.

5. Bicolor electroluminescence with bias tunability.

Since last year, QD-LEDs have reached the mass market through their incorporation into TV screens[184]. This state-of-the-art technology uses a blend of three NC emitters (blue, green, and red) that are electrically pumped to produce all the colors represented in the associated color gamut. Compared to the optical pumping required in LCDs, the switch to electrical supply enables significant power savings, which is now critical for smartphone applications. Once again, the particles are embedded inside a matrix to efficiently extract the heat generated by sub-unity efficiency and to isolate the system from air and moisture. Due to the different surface chemistries, careful attention is required during the incorporation process to avoid degradation of the NCs' optical properties. In this regard, the use of a single dual emitter can also reduce the amount of work needed, as the number of different emitters will decrease.

Several studies have focused on the development of dual electroluminescent NCs in this context. Some works have revealed dual electroluminescence from QDs NPs[185] including the dot-in-bulk NPs mentioned in the previous section[156]. More recently, works on 2D NPLs have also unveiled dual electroluminescence from doped CdSe NPLs including Ag[186] and Cu[187] as dopants. In this context, I incorporated the bicolor emitting core-crown-crown NPLs inside a LED.

a. Designing the LED stack.

Band alignment of the heterostructure.

To achieve electroluminescence, the first step is to efficiently inject charges into the active material. Therefore, the choice of the constituent layers in the LED stack should consider the band alignment of the particles. Thus, in the initial step, we established the electronic structure of the active material. To accomplish this, we conducted XPS measurements at Synchrotron SOLEIL to determine the positions of both the Fermi level and the VB, relative to the vacuum. Firstly, the measurement of the secondary electrons' cut-off energy revealed a work function of 4.3 eV for the sample (see the blue fit in **Figure 44a**). Then, by measuring the energy of the least bound electrons, we obtained a VB value of 1.2 eV (see the red fit in **Figure 44b**). To complete the picture, the band gap of the material was considered equal to that of the CdSe 4 ML NPLs (2.4 eV, see red absorption spectrum in **Figure 44d**). The reconstructed band diagram of the NPLs is presented in **Figure 44c**). This band diagram reveals a quasi-intrinsic behavior with a Fermi level close to the mid-gap, within the measurement resolution. In comparison, CdSe 4 ML NPLs exhibit a more "p" type behavior with a VB - E_F value of 0.7 eV. The slight change can be attributed to the presence of the CdTe crown, which is an "n" type material.

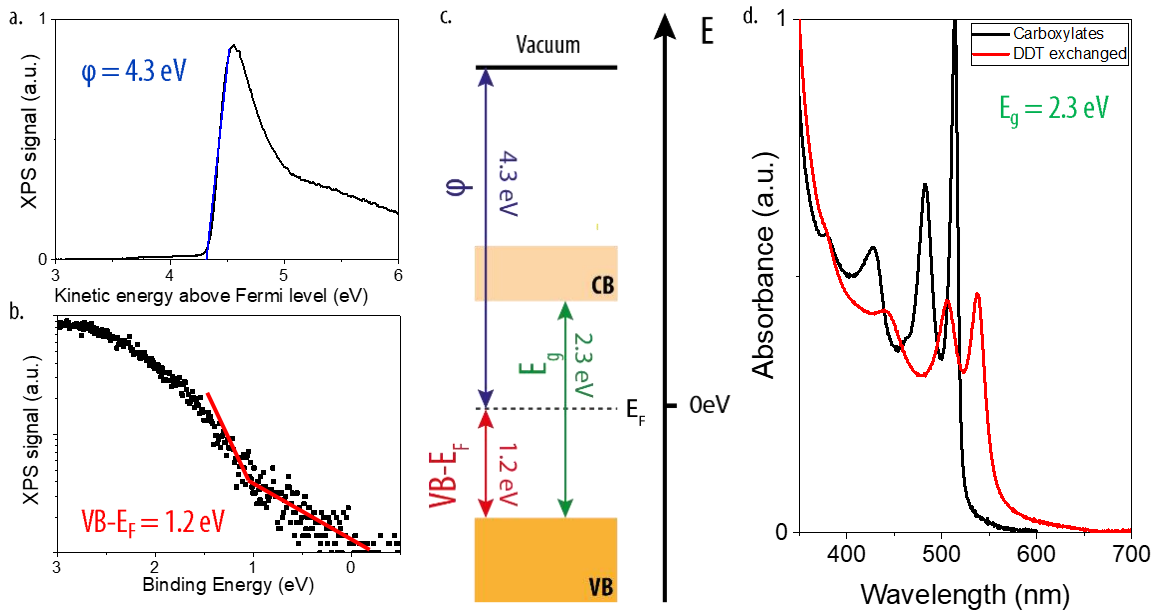

Figure 44: *Band alignment of the bi-emitting heterostructure. a. Secondary electron measurement unveiling a work function of 4.3 eV. b. Measurements of the less bound electrons in the NPLs unveiling a 1.2 eV relative position of the VB in comparison to the Fermi level. c. Complete band diagram of the heterostructure. d. Absorption spectra of the heterostructure before and after ligand exchange to DDT. The extracted band gap is at 2.3 eV.*

We decided to use an LED stack that had previously been used by Dai et al. in 2014 when studying CdSe@CdS core-shell NPLs[140]. In this stack, an indium tin oxide (ITO) transparent electrode is used as the anode (WF = -4.8 eV vs vacuum), poly(ethylene dioxythiophene): polystyrene sulfonate (PEDOT:PSS, WF = -5 eV vs vacuum), poly(N,N'-bis(4-butylphenyl)-N,N'-bis(phenyl)benzidine) (polyTPD, HOMO = -5.2 eV, LUMO = -2.3 eV vs vacuum), and poly(9-vinylcarbazole) (PVK, HOMO = -5.7 eV, LUMO = -2.2 eV vs vacuum) are used as hole-injecting layers (HTL), ZnO NPs (VB = -7.5 eV, CO = -3.8 eV vs vacuum) are used as the electron-injecting layer (ETL), and finally, silver is used as the metallic cathode (WF = -4.2 eV vs vacuum)[140]. The band diagram of the complete stack is presented in **Figure**

45a-b. To obtain an accurate measurement of the thickness of each layer, profilometry measurements were conducted between each layer deposition and are reported in **Figure 45b**.

A PMMA layer to protect the NPL's luminescence.

During the deposition of the ZnO layer directly on the NPLs film, the PL signal drops. This might be induced by the additional ligands (ethanolamine) used to colloidally stabilize the ZnO particles, which can strip off native ligands from the NPL surface. This results in an increase in the number of defects present on the surface, decreasing the PL efficiency. As mentioned in the introduction chapter, a decrease in PL is generally accompanied by a decrease in device efficiency. To avoid such issues, we considered adding a thin protective layer between the ZnO and NPL films. PMMA layers have previously demonstrated compatibility with NPLs and have been used by Dai et al. in LED stacks[140]. In their work, they took advantage of the insulating behavior of PMMA (HOMO = -9.2 eV, LUMO = -0.7 eV vs vacuum) to balance charge injection and, particularly, to limit the overflow of electrons inside the active material layer. Here, the main goal of the PMMA layer remains to protect the NPL film, but a compromise should be found to limit the thickness of this PMMA layer: the thicker the layer, the lower the charge flow through the LED stack. A balance between PL protection and the insulating character of the PMMA layer needs to be achieved. We concluded that a solution of PMMA dissolved in acetone (5 $mg.mL^{-1}$) and deposited by spin coating on top of the NPL film would yield the best performance.

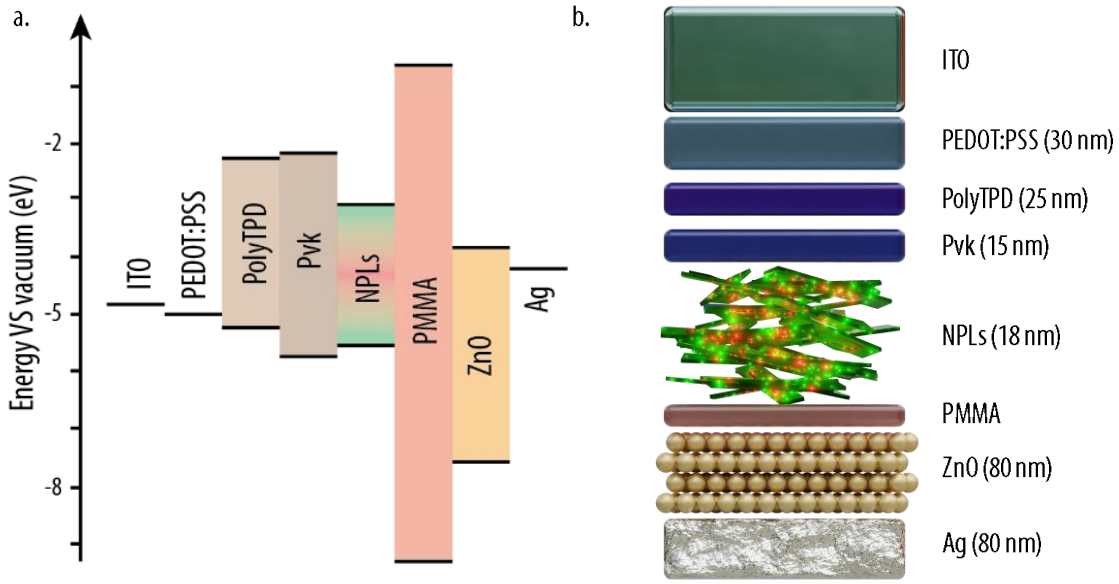

Figure 45: *LED stack toward electroluminescence. a. Band alignment of the different layers that composed the LED stack. The relative localization of the NPLs bands is established according to XPS measurements. b. Sketch of the different layers composing the stack with their associated thickness (except for PMMA which layer was too thin). c.Photoluminescence under a 400 nm diode excitation of a NPLs film after deposition of various layers. d. and e. Current density (d.) and luminance (e.) according to the applied bias through an LED stack as presented in b. with various thickness of PMMA.*

b. LED under bias.

Having optimized the LED stack, we implemented it with the bicolor NPLs. We first tested a heterostructure with a high green-to-red ratio (see **Figure 46a** for the absorption and emission features). When a bias is applied between the two electrodes, green emission is observed (see **Figure 46b** and the front view picture in **Figure 46c**). In comparison to the green-to-red ratio observed in photoluminescence, the electroluminescence signal tends to favor the green signal.

To obtain a better green-to-red ratio, the initial balanced should be more in favor of the red which is obtained using smaller laterally extended NPLs (see PL spectrum in **Figure 46d**). The resulting electroluminescence exhibits the two expected emissions: a narrow green emission at 523 nm and a broad red emission at 647 nm. Once again, the ratio is more in favor of the green emission when switched to electrical pumping. At low bias, the red emission shows broad features that narrow as the applied bias increases (see red EL spectrum in **Figure 46e**). This observation might be attributed to a sub-band gap injection of the charge carriers at low bias. Additionally, the green-to-red ratio can be tuned according to the applied bias (see EL spectra **Figure 46e**): the higher the bias, the greener the emission. As the system is brought further out of equilibrium, charge injection becomes easier above the band edge of CdSe, which enhances band edge recombination, explaining both the narrowing of the emission and the increase in the green-to-red ratio at higher bias. This result is consistent with previous works conducted by Liu *et al.* on bicolor emitting NPLs[186]. It leads to a visible change in the color of the pixel as the bias increases (see pictures on **Figure 46f**). However, this power modulation of color remains limited: as the applied bias increases, the current flowing through the LED drastically increases, which diminishes the electroluminescence, most likely due to heating processes inside the NPL film.

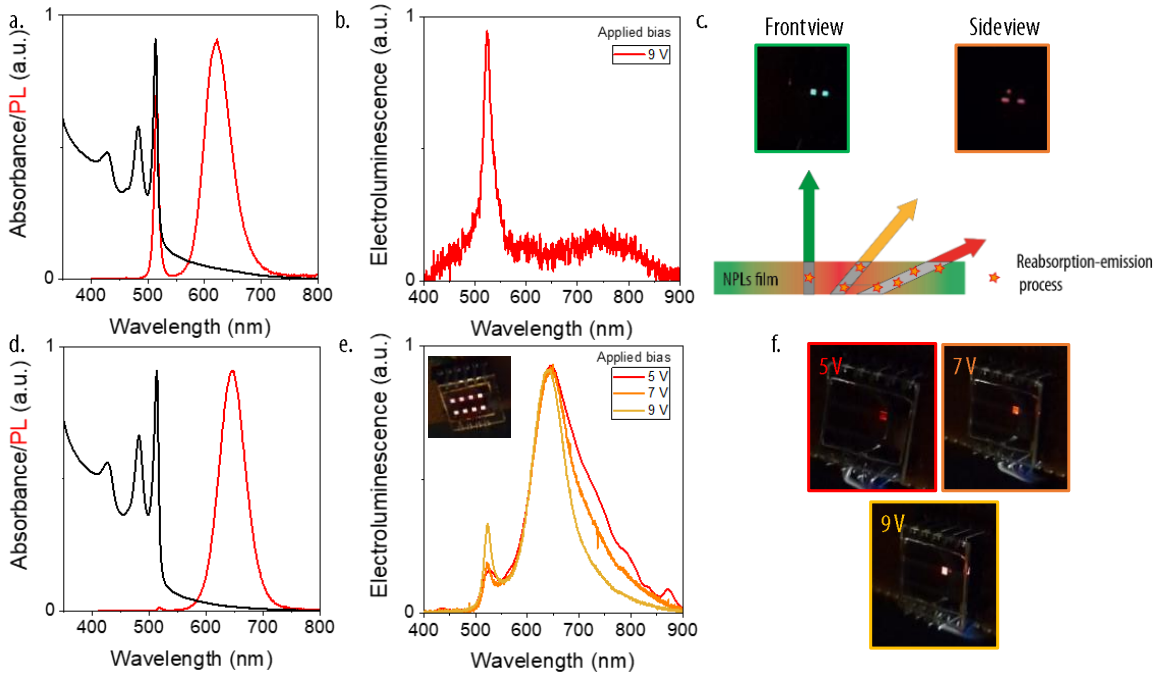

Figure 46: *Electroluminescence of core-crown-crown NPLs. a. (resp. d.) Absorption (black) and photoluminescence (red) spectra of a heterostructure presenting a high (resp. low) green-to-red ratio. b. Electroluminescence obtained for the stack present in* ***Figure 18*** *using the heterostructure presented in a. under 9V. c. Picture of the pixels in front and in side views. The sketch represent the effect of the reabsorption-emission process occuring in a NPLs film. e. Electroluminescence obtained for the stack present in* ***Figure 18*** *using the heterostructure presented in d. under various biases. The inset picture corresponds to 8 pixels working simultaneously. f. Pictures of a pixel under increasing bias application.*

Coming back to the LED made using a large heterostructure (with a high green-to-red ratio) when the observer is in front of the pixel, the electroluminescence seems green. On the contrary, when looking on the side, the electroluminescence is rather taking an orangish color (see the two pictures in **Figure 46c**). Directional emission would be of particular interest, especially regarding the 20 % efficiency limit induced by the non-directional emission of light inside an LED stack. However, the process involved here is more likely attributed to the reabsorption-emission that occurs within a close-

packed film when the diffusion of light increases. The initial energetic green emission will gradually be down-converted by the neighboring NPLs, leading to this angular dependency of the emitted color (see the schematic in **Figure 46c**). This mechanism also explains the slight red-shifted observed between PL and EL (from 518 to 523 nm).

Finally, to compare the performance of the obtained LED with previous works, the current, voltage, and luminance have been collected to extract the classical LED figure-of-merits. A summary of other type II-based NPLs LEDs is presented in **Table 5**.

Table 5: *Figure-of-merit sums up different type II NPLs-based LEDs.*

Structure	*Turn-on voltage (V)*	*EQE (%)*	*Max. Luminance (cd.m^{-2})*	*Ref*
CdSe-CdSe$_{0.8}$Te$_{0.2}$	1.9	3.6	34,500	153
CdSe-CdTe-CdSe	3	7.8	10,800	188
CdSe-CdSe$_{0.7}$Te$_{0.3}$-CdSe-CdS	1.7	9.3	36,600	162
This work	1.65	0.01	100	189

First, the maximum value recorded for the EQE of our LED reaches 0.03%, which remains far from the 19.2% maximum EQE obtained in core-shell-based LEDs[75]. Even among type II-based NPLs, values up to 9.3% can be obtained[188]. As mentioned in the previous chapter, the EQE can be seen as a combination of three contributions: (i) light extraction, limited to a maximum of 20% EQE, (ii) injection efficiency (equal to 1 when all injected charges form electron-hole pairs inside the emissive layer), and (iii) the PLQY of the particles themselves. The main issue here remains the drop in the PL QY of the NPLs when deposited onto a film. Nevertheless, other contributions might also decrease this value, for example, the possibility of unbalanced charge distribution induced by the PMMA layer and the twisting of the NPLs hindering non-homogeneous films[163]...

Overall, despite modest luminance compared to state-of-the-art NPL-based LEDs (up to two orders of magnitude for the best type II NPL-based LED[162]), the presented stack remains very efficient for this type of NPLs, with a sub-band gap turn-on threshold of 1.65 V, which is the smallest among type II NPL-based LEDs (see **Table 5**). This observation also confirms the XPS measurements carried out on the heterostructure. This work is also the first bicolor electroluminescent LED based on a heterostructure of NPLs. In addition, the structure figure-of-merit properties remain modest but comparable to the bicolor emitting NPL-based LEDs developed by Liu et al[186,187], see **Table 6**. The bicolor emission obtained in their work is based on the doping of CdSe NPLs with metallic cations. Thus, our heterostructure strategy comes as a complementary technique to achieve bicolor electroluminescence from a single particle. To improve the results, growing a shell on top of those NPLs would preserve the PL of the particles, decreasing their sensitivity to changes in their surface chemistry when deposited on a film. In particular, the shell would limit the drop in PL induced by the ZnO deposition, which would also reduce the need for a PMMA layer.

Table 6: *Figures-of-merit of bicolor LEDs based on NPLs.*

Structure	*Turn-on voltage (V)*	*EQE (%)*	*Max. Luminance (cd.m^{-2})*	*Ref*
Ag doped CdSe	2.2	0.06	1,300	186
Flexible Ag doped CdSe	2.3	0.09	500	186
Cu doped CdSe	2.4	0.15	1,200	187
This work	1.65	0.01	100	189

6. Blue-shifting the green and red emissions.

a. Type II CdSe/CdTe interface in 3 ML NPLs

Contrary to the core-crown structure, the growth of a shell on top of NPLs induces a red-shift in their optical properties. Therefore, when considering core-shell structures for obtaining bright green and red bicolor emission, one should anticipate the red-shift of the core emission. One way to counter this is by initially blue-shifting the emission features of the material before growing the shell. In the case of NPLs, the easiest method to achieve this is by making the NPLs thinner to increase quantum confinement. For CdSe, reducing the thickness from 4 ML to 3 ML results in a shift of the band edge emission from 510 nm to 460 nm. Between CdSe 3 and 4 ML NPLs, the band gap energy is shifted by 270 meV. Consequently, the band alignment may also be shifted in a type II CdSe/CdTe 3 ML NPLs interface. However, this specific type of interface has not been reported yet. Therefore, I began by synthesizing a CdSe-CdTe core-crown structure with a large CdTe lateral extension. In absorption, the growth of the CdTe crown leads to the emergence of a first peak at 500 nm, corresponding to the first excitonic peak of the CdTe 3 ML NPLs. The second CdTe excitonic peak overlaps with the absorption features of the CdSe 3 ML NPLs, explaining the broadening of the absorption around 450 nm (see dotted lines in **Figure 47a**).

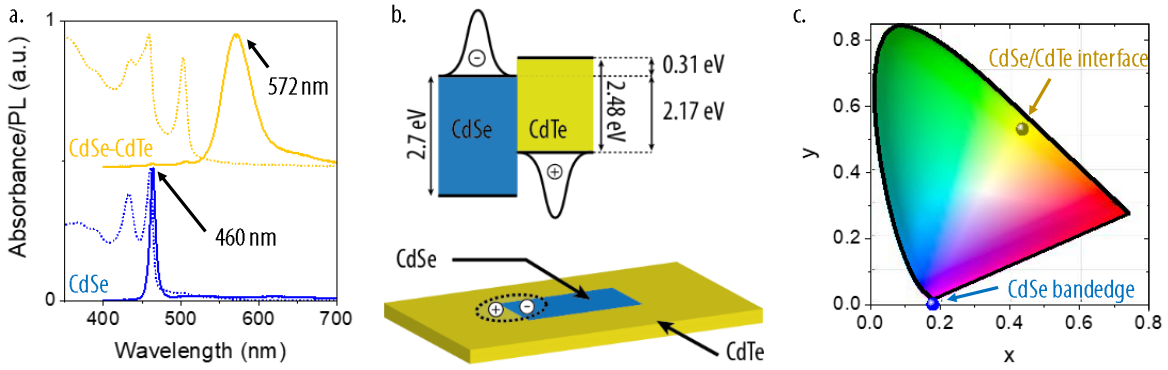

Figure 47: *Band alignment in CdSe-CdTe 3 ML core-crown heterostructure. Absorption (dot lines) and photoluminescence (solid lines) spectra of CdSe core NPLs (blue) and CdSe-CdTe core-crown NPLs (yellow). For clarity, the spectra have been normalized and artificially shifted. b. Band alignment and sketch of the type II interface between CdSe and CdTe. c. Chromaticity diagram where the two different emissions are localized. The black line corresponds to the expected color modulation with the blue-to-yellow ratio.*

In terms of PL, the initial band edge emission of the CdSe 3 ML NPLs is replaced by a broad yellow feature, which corresponds to interfacial recombination (see solid lines in **Figure 47a**). This confirms the assumption made regarding the band alignment between CdSe and CdTe. The maximum emission of this type II interface is observed at 572 nm (2.17 eV). By considering the band gaps of CdSe (2.7 eV) and CdTe (2.48 eV), the relative band alignment of this heterostructure has been determined. The band offset between the CBs of CdTe and CdSe is found to be 310 meV, which is higher than what was observed in their 4 ML counterparts. Based on this, we can assume that the electrons will be primarily localized within the CdSe CB, while the holes will be localized in the CdTe VB (see **Figure 47b**).

b. Blue and yellow bicolor emission.

Synthesis of the core-multi-crown heterostructure.

A CdSe-CdTe-CdSe core-crown-crown heterostructure is synthesized using CdSe 3 ML NPLs (a summary is shown in **Figure 48**). To limit the lateral extension of the particle, the smallest possible

cores are synthesized. The synthesis process for these small CdSe 3 ML core NPLs is adapted from literature[190], resulting in the formation of small disks with diameters up to 10 nm (as shown in TEM picture in **Figure 48f**). The synthesis involved mixing cadmium decanoate, cadmium acetate, and bis(stearoyl)selenide in ODE. After degassing the mixture at room temperature for 1 hour and switching to an inert atmosphere, the temperature was set to 160°C and the growth was carried out for 6 hours. The resulting NPLs were washed three times with toluene and a minimal amount of isopropanol. This particular synthesis process utilized the bis(stearoyl)selenide precursor, which exhibits higher reactivity, enabling nucleation and growth of NPLs even at low temperature[191].

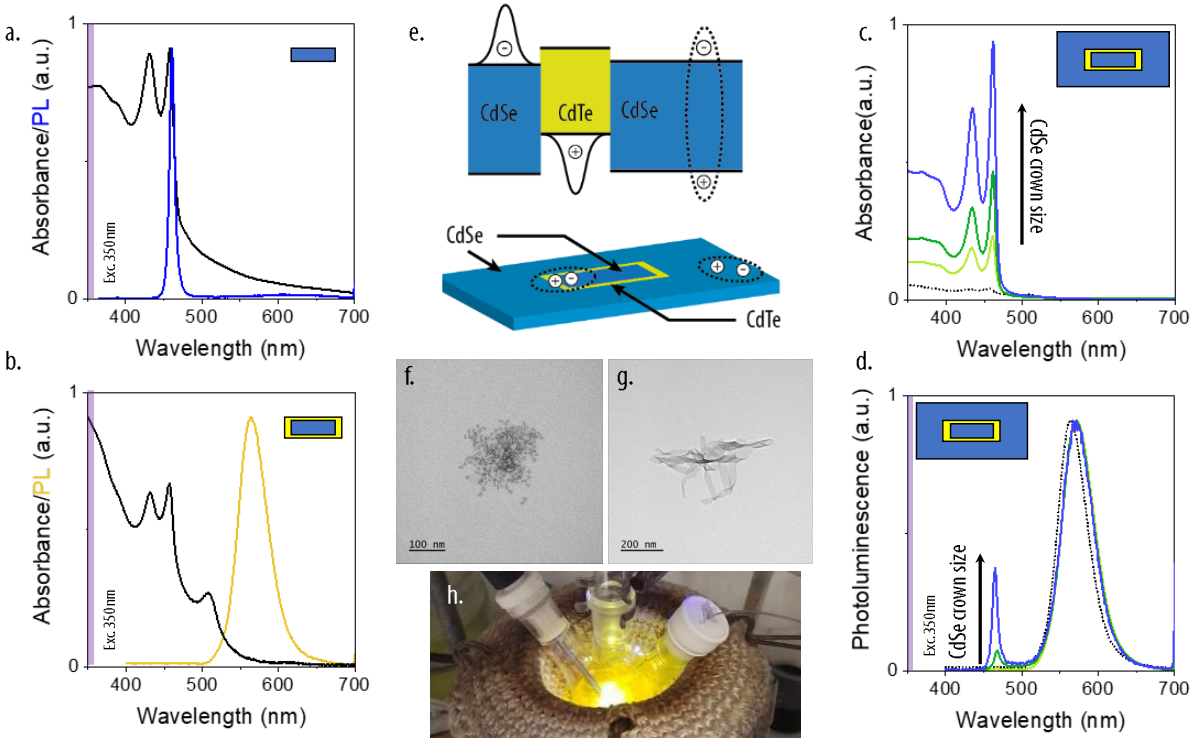

Figure 48: *Synthesis of the CdSe-CdTe-CdSe 3 ML NPLs heterostructure. a. Absorption (black) and photoluminescence (blue) spectra of the CdSe cores b. Absorption (black) and photoluminescence (yellow) spectra of the CdSe-CdTe core-crown. c. (resp. d.) Evolution of the absorption (resp. photoluminescence) spectra according to the lateral extension of the CdSe external crown e. Band alignment and sketch of the final heterostructure. f-g. TEM picture respectively of the CdSe core and of the final heterostructure. h. Picture of the mixture photoluminescence during the external crown growth.*

In terms of the absorption spectrum, the characteristic excitonic features of NPLs are observed, with a first exciton peak at 458 nm and a second exciton peak at 431 nm. These excitonic peaks are slightly blue-shifted and less defined compared to the standard value of CdSe 3 ML NPLs, due to lateral quantum confinement. The washed NPLs are then redissolved in ODE in the presence of $Cd(ac)_2$ and oleic acid to facilitate the lateral growth of CdSe and CdTe. The process involves the injection of TOP:Te at 195°C to ensure maximum tellurium incorporation into the NPLs, followed by a 15-minutes delay before the second injection of TOP:Se at 205°C. As a result of the TOP:Te injection, the first excitonic peak of CdTe appeared around 500 nm (see the absorption spectra in **Figure 48b**). During the second injection, the overall absorbance increases, with the absorption spectrum mainly dominated by the CdSe features at the end of the addition (as highlights the dark arrow in **Figure 48c**). Consistent with the formation of a type II interface between CdSe and CdTe, a slight increase in sub-band gap absorption was observed, indicating the presence of charge transfer states.

In terms of emission, the behavior is similar to that observed for thick 4 ML NPLs. Initially, before the addition of TOP:Te, the mixture exhibits a narrow blue photoluminescence, which is indicative of band edge recombination in CdSe. However, as the growth of the type II interface progresses, the emission undergoes a significant red-shift to 570 nm, resulting in a bright yellow photoluminescence (see PL spectrum in **Figure 48b** and picture in **Figure 48h**). The introduction of the external CdSe crown causes a slight red-shift in the yellow interface recombination due to a reduction in lateral confinement (see PL spectra in **Figure 48d**). Once again, the QY appears to be optimal when CdTe is sandwiched between the CdSe layers, but it rapidly decreases as the lateral extension of CdSe increases. This decrease is accompanied by a resurgence of the band edge emission from CdSe. TRPL measurements are then conducted on these particles and revealed a short lifetime for the blue band edge recombination (approximately 1 ns) and a longer decay for the yellow interfacial emission (tens of nanoseconds) (see dynamics in **Figure 49b**). The latter value is higher than that observed in 4 ML bicolor emitting NPLs.

Power dependency of the blue-to-yellow ratio.

The same experiment using the bottom of a test tube as a lens is conducted, revealing a power dependency similar to the one previously observed. The photoluminescence of diluted solutions displayed changes based on the focalization of the laser pointer, resulting in increased blue emission in the focal plane of the laser (see the test-tube picture in **Figure 49a**). Once again, we decided to perform more quantitative measurements to understand the power dependency of the blue-to-yellow ratio. At low fluence, the yellow emission appears to dominate over the blue emission. However, as the pump fluence increased, a n inversion occurs in this trend (see PL spectra in **Figure 49c**). To investigate this effect further, we fitted the intensity of both the yellow and blue emission and plotted their respective intensities according to the incident power (see dotted lines in **Figure 49e**). Similar to the 4 ML heterostructure, a linear dependency was observed for the blue emission, with the intensity being proportional to $P^{0.9}$. The intensity of the yellow emission initially exhibited a linear dependency before saturating and following a $P^{0.4}$ dependency. Therefore, we can hypothesize a similar mechanism with saturation of the yellow emission caused by an accelerated Auger relaxation rate due to the small volume of the CdSe/CdTe interface.

As the incoming power increased, a broadening of the blue emission was observed. This broadening resembled the shoulder noted in the 4 ML heterostructures and was attributed to emission from biexcitons. By fitting the emission using two Voigt functions, we determined a binding energy of 38 meV for the biexciton, which was larger than that observed for less confined NPLs previously studied (see blue and red curves in **Figure 49d**). This trend aligns with the findings of Li et al. on CdSe 3, 4, and 5 ML NPLs, where they observed an enhanced biexciton binding energy with increased confinement[192]. Additionally, a blue-shift of the yellow emission was also observed, consistent with the presence of biexcitons localized at a type II interface[176].

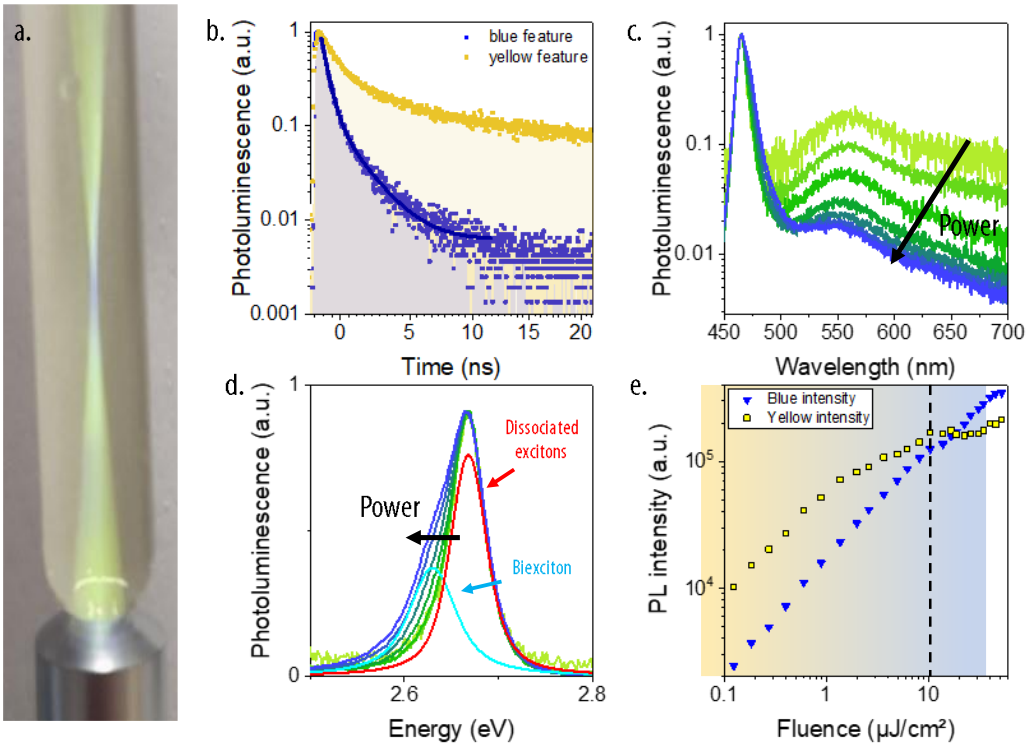

Figure 49: *Power dependency of the blue-to-yellow ratio. a. Time-resolved photoluminescence at 460 nm (blue) and 560 nm (yellow). For clarity, the two curves have been normalized to the maximum intensity after the pulse excitation. b. Picture of the test-tube experiment. c. Photoluminescence spectra according to the incoming excitation power. For clarity, the spectra have been normalized to the maximum in the blue emission. d. Zoom on the blue emission peak according to incoming power dependency. The red and cyan lines correspond respectively to the single exciton and bi-excitonic emissions.*

Modulation of the yellow emission.

Finally, we also examined the impact of the lateral extension of each crown. As demonstrated during the growth of the external crown, the blue-to-yellow emission can be adjusted by altering the lateral extension of the CdSe external crown or by varying the incident power. Similar to the 4 ML heterostructure, the maximum wavelength of the yellow emission can be controlled by modifying the lateral extension of the CdTe crown. A large CdTe crown, where lateral quantum confinement is negligible, allows for the generation of yellow emission with a peak wavelength at 572 nm. By reducing the size of the CdTe crown, this emission can be blue-shifted (as highlights the dark arrow in **Figure 50a**). Consequently, by adjusting either the lateral extension of the CdSe or the CdTe, a wide range of colors can be achieved using a similar heterostructure (see the red and blue lines in **Figure 50b**).

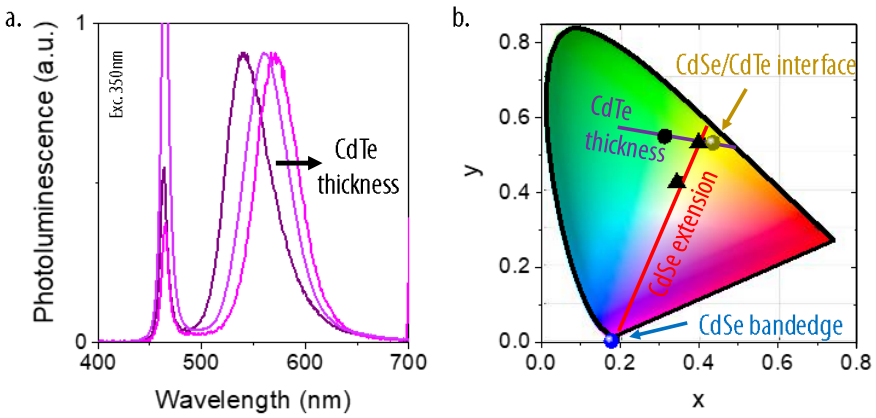

Figure 50: *Influence of the geometrical parameters. a. Evolution of the photoluminescence spectra according to the size of the CdTe crown. For clarity, the spectra have been normalized to the yellow emission. b. Photoluminescence localization inside the CIE color diagram. The series of the NPLs with increasing CdTe (resp. CdSe) lateral extension are following the purple (resp. red) dot line. The blue emission is localized by a blue half circle.*

7. Conclusion and perspectives

We present here the synthesis of a CdSe-CdTe-CdSe core-crown-crown heterostructure of NPLs that exhibits bicolor emission both in the green and red. The green emission corresponds to the band edge recombination inside the external CdSe crown, while the red emission is generated by the sub-band gap emission at the CdSe/CdTe interface. Compared to current displays, these two emissions offer an expanded color gamut, particularly in the green region, thanks to the narrow band edge emission in CdSe. This bicolor emitting phenomenon has been demonstrated at the single-particle level and attributed to the diffusion time towards the interface competing with the band edge relaxation time of excitons.

A power dependency of the green-to-red ratio has also been observed. Upon investigation, this behavior has been attributed to the saturation of the red emission caused by accelerated Auger recombination processes occurring at the interface. A similar, albeit less pronounced, power dependency has also been observed in electroluminescence.

In comparison to studies on doped NPLs, this research presents a new dimension in achieving bicolor emitting particles using NPLs. However, to enhance competitiveness, both the quantum yield efficiency and stability need significant improvement. One possibility is to grow a shell on top of such particles. Growing a shell on large NPLs containing CdTe remains a challenge. To address the red-shift induced by shell growth, an initial blue-shift of the optical properties is necessary. In this study, we have demonstrated the ability to blue-shift both emissions by reducing the thickness of the NPLs and increasing quantum confinement. Notably, the resulting particle shows potential for achieving white light emission from a single particle. This work paves the way for further advancements involving the formation of more complex core-multi-crown@shell heterostructures with tunable emission properties, high quantum efficiency, and improved electroluminescent properties.

Finally, this study has focused on obtaining a narrow energetic emission (either green or blue) at the expense of the second emission. A future objective could be to leverage the narrow band edge emission of the NPLs to achieve two distinct narrow emissions.

Chapter 3: Synthesis and characterization of $HgSe_xTe_{1-x}$ nanoplatelets.

In the previous chapter, I tried and succeeded in synthesizing a promising particle to improve color quality and reduce electrical consumption in future displays. These results were obtained in the visible range. Regarding their narrow emission, NPLs are also appealing materials in the near infra-red (NIR) range. In this domain, obtaining narrow photoluminescence remains challenging. In this third chapter, I will try to address this issue through the work I have done on the synthesis of $HgSe_xTe_{1-x}$ 3ML NPLs. During this project, I synthesized the initial NPLs and optimized the conditions for obtaining Hg-based NPLs. I also built and characterized the FET transistors. I conducted photoemission measurements on the TEMPO beamline of the synchrotron SOLEIL under the supervision of M.G. Silly, in collaboration with C. Gréboval. The k.p modeling simulations have been conducted by J.I. Climente's team in U. Jaume I in Valence, Spain.

Direct synthesis of Hg-based NPLs is currently not possible. Instead, a cation exchange (CE) process is required to convert Cd-based NPLs into their Hg-based counterparts. This procedure, has been developed by Izquierdo *et al.* in 2016[38] and implemented on CdTe NPLs. This process yielded satisfying optical properties but only for HgTe 3 ML NPLs, which limits their range of applications.

In this context, the first section of this chapter will present the **state-of-the-art concerning the NIR-emitting NCs**. An overview on the initial synthesis of Hg-based 3 ML NPLs will be provided to understand the challenges addressed during the optimization process.

Following this introduction, the second and third parts will be dedicated **to material synthesis**. Starting with the synthesis of the initial $CdSe_xTe_{1-x}$ 3 ML NPLs, we will swiftly move to the optimization I conducted to obtained **$HgSe_xTe_{1-x}$ 3 ML NPLs**. Specifically, three parameters (solvent, temperature, and ligands) will be investigated. Finally, we will report the first PL results obtained from $HgSe_xTe_{1-x}$ 3 ML NPLs.

Lastly, the final part will focus on the **electronic structure of the newly synthesized NPLs**. The evolution of the band alignment with respect to the chalcogen ratio in $HgSe_xTe_{1-x}$ 3 ML NPLs will be **established using XPS measurements**. This will be further confirmed through a new and uncommon time-resolved X-ray photoemission spectroscopy technique conducted at the TEMPO beamline in synchrotron SOLEIL.

Publication associated to this project:

- **C. Dabard** *et al*., Optimized Cation Exchange for Mercury Chalcogenide 2D Nanoplatelets and Its Application for Alloys. *Chem. Mater.*, *33*, 9252 (2021)

Content

1. Infrared NCs.

NPLs present the narrowest optical features among NCs. By changing their thickness, one can modulate the quantum confinement and thus their optical properties. However, when aiming for longer wavelengths, it is not possible to go below the band gap energy of the bulk material. For Cd-based materials, the band gaps are 2.42 eV (512 nm) for CdS, 1.79 eV (693 nm) for CdSe, and 1.49 eV (832 nm) for CdTe. To explore longer wavelengths range more extensively, one should consider a material possessing a narrower band gap.

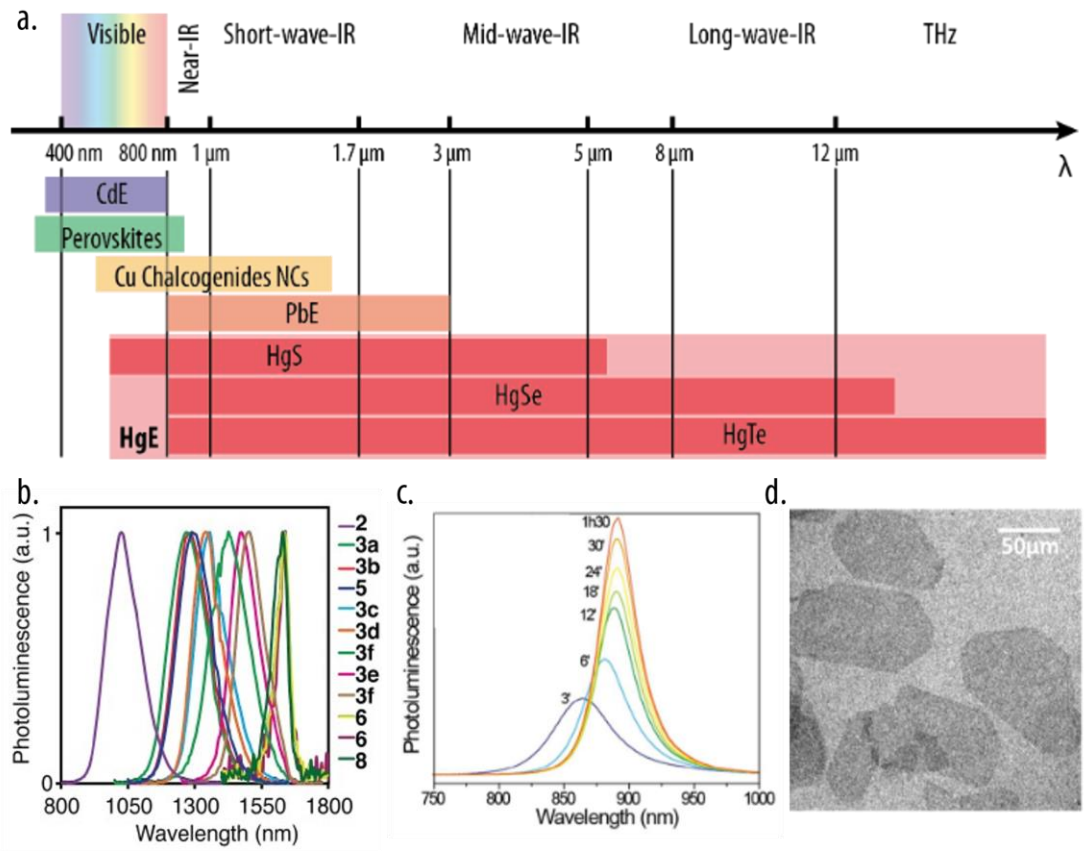

Figure 51: *State-of-the-art NCs emitting in the NIR. a. Energetic scale representing different materials and their regions of applications. b. Emission features of PbS NCs in the SWIR region using different S precursors, reproduced from ref [196], c. Emission evolution of HgTe NPLs during their formation by CE, d. Associated TEM picture, c and d are reproduced from ref [38].*

To push into the NIR region, materials such as copper chalcogenides[193–195] or lead sulfides[9,102,196] NCs have been investigated (see **Figure 51a**). The former exhibit interesting

biocompatibility and wavelength modulation through their various sizes and compositions. Lead sulfides also offer the ability to obtain different shapes including 2D particles[9,102]. However, in both cases, the emission remains broad (over 100 nm), which is a critical drawback in the 900 nm region (see **Figure 51b**). Mercury chalcogenides, particularly HgSe and HgTe, are also promising candidates due to the absence of a band gap in their bulk form. In such materials, the band gap modulation occurs solely through quantum confinement induced by their large Bohr radius. Consequently, a wide modulation of their optical properties is possible across the entire optical spectrum[17]. Significant efforts have been dedicated to controlling the size of Hg-based quantum dots to reach longer wavelengths for both HgTe[197–199] and HgSe[200] , thus covering a large range from SWIR to THz (see **Figure 51a**). However, obtaining efficient materials (characterized by a narrow emission with high QY) in the NIR remains challenging due to the small size of the associated QDs. Therefore, chemists have turned their attention to the synthesis of thin Hg-based NPLs, considering their potential applications in optoelectronic devices like LEDs or lasers. Since the synthesis of mercury chalcogenide particles requires low temperatures, direct pathways have not yet been established for this type of material. Nevertheless, it is still possible to obtain HgE NPLs (E = Se, Te) using a full CE route starting from Cd-based NPLs.

As mentioned in the introduction chapter, several parameters need to be considered to properly conduct a CE. One of these parameters relates to the crystallography of the initial and final materials. In order to minimize the strains induced during this process, it is desirable for the two materials to crystallize in the same structure and to have similar lattice parameters. In the case of CdTe and HgTe, this requirement is indeed met, as both crystallized in the ZB structure and have comparable lattice parameters (a_{CdTe} = 6.48 Å; a_{HgTe} = 6.46 Å). Based on this favorable match, an initial CE process was implemented on CdTe QDs, resulting in the formation of $Hg_xCd_{1-x}Te$ alloys with emission properties spanning on the 600-1000 nm range[201]. Subsequently, in 2016, Izquierdo *et al.* successfully achieved the synthesis of 3ML HgTe NPLs through a complete CE starting from CdTe NPLs[38]. The newly synthesized NPLs exhibited a narrow emission centered around 900 nm (see **Figure 51c-d**).

Nevertheless, this method remained specific to obtaining HgTe 3ML NPLs, strongly limiting the modulation of wavelengths in this spectral range. In particular, the CE on HgSe NPLs did not yield satisfactory optical properties. The CE process is also limited in terms of thickness. In 2020, Izquierdo *et al.* demonstrated its limitation to two cation planes on thick CdSe NPLs[80]. The same behavior is observed in CdTe NPLs, where no complete CE has been reported on NPLs with more than 3 ML. Overall, the achievement of thicker Hg-based NPLs remains challenging in these materials, which hinders the ability to tune the band gap through quantum confinement.

Another way to achieve spectral tunability is through alloying. In this context, I have developed an optimized CE procedure to expand this process to HgSe and $HgSe_xTe_{1-x}$ 3ML NPLs. In this chapter, I will present the advancements made in this CE method to obtain photoluminescent $HgSe_xTe_{1-x}$ 3 ML NPLs that exhibit spectral tunability in the NIR range.

8. Synthesis of initial $CdSe_xTe_{1-x}$ 3 ML NPLs.

The first step to obtain Hg-based NPLs is to synthesize the initial Cd-based NPLs. Due to the different reactivity of Te and Se precursors, the protocols to obtain CdTe, CdSe and $CdSe_xTe_{1-x}$ 3 ML NPLs are slightly different from each other.

a. Synthesis of CdTe 3 ML NPLs.

The first CdTe NPLs were synthesized by Ithurria *et al.* in 2011[29]. At that time, the synthesis had not been optimized, resulting in a mixture of various thickness. Two years later, Pedetti *et al.* optimized the synthesis and successfully obtained monodisperse CdTe 3ML NPLs[41].

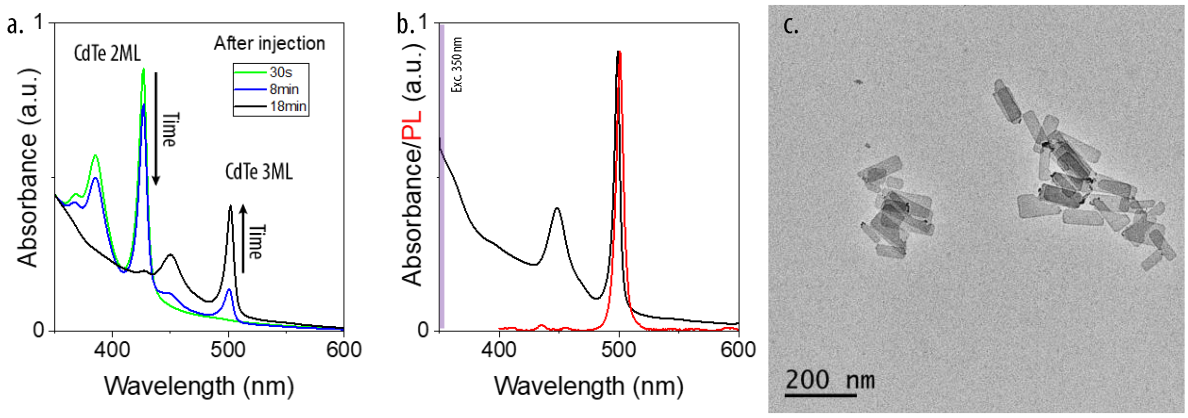

Figure 52: *Synthesis of CdTe 3ML NPLs. a. Absorption evolution showing first the formation of 2ML CdTe then their dissolution in favor of the growth of 3ML CdTe. b. Absorption (black) and emission (red) spectra of the final 3ML CdTe. The excitation has been conducted at 350 nm. c. TEM picture of the obtained NPLs.*

In this synthesis, cadmium propionate ($Cd(prop)_2$), used as the Cd source, and OA are mixed in ODE and degassed for 1 h at 90 °C. After switching to an inert atmosphere, the temperature is raised up to 210 °C. Once it stabilizes, a mixture of TOP:Te (1 M) in ODE is swiftly added to the solution. This injection triggers the formation of nuclei that will laterally extend due to the presence of a mix of carboxylates with a long (OA) and a short (propionic acid) aliphatic chain. As mentioned in the introduction chapter, the synthesis involves first the nucleation of small seeds with various thicknesses. The thinner nuclei, in this case the 2 ML CdTe, extend first (see the green curve in **Figure 52a**). These NPLs exhibit a first excitonic peak at 428 nm and a second one at 385 nm. According to the kinetic model developed by Norris group[60–62], the 2 ML NPLs slowly dissolve, providing the monomers required for the lateral extension of the 3 ML NPLs through interparticle Ostwald ripening. If the reaction is conducted for too long, the subsequent population (the 4 ML NPLs) gradually replaces the 3 ML NPLs, resulting in a mixture of populations. Finally, we obtain 3 ML CdTe NPLs with a first excitonic peak at 500 nm and the second one at 450 nm. They also exhibit a PL peak at 501 nm with a FWHM of 7 nm (40 meV), which is the smallest among NCs (see **Figure 52b**).

Figure 52c shows a TEM picture of the NPLs. Depending on the injection process and injection temperature, the NPLs can exhibit different lateral extensions, ranging from tens of nm^2 up to hundreds of nm^2. This trend is consistent with the Lamer theory: a swift injection leads to the nucleation of more seeds, resulting in smaller final NPLs. The large lateral dimensions also explain the modest QY of 1% observed for these NPLs as an increase in the lateral extension will also increase the probability for a NPLs to embedded deep traps states.

b. Synthesis of CdSe 3 ML NPLs.

In addition to the synthesis of 3 ML CdTe and 4 ML CdSe NPLs, Ithurria *et al.* simultaneously developed the synthesis of 3 ML CdSe NPLs[29]. Syntheses of 3 ML CdSe NPLs are now well-established, and various protocols exist to synthesize those particles with a wide range of lateral dimensions, ranging from small[63] to large dimensions[56]. In order to minimize the effects of lateral quantum

confinement that occur when the lateral dimensions are small, I employed a protocol that yields 3 ML CdSe NPLs with large lateral extensions (see TEM picture in **Figure 53b**).

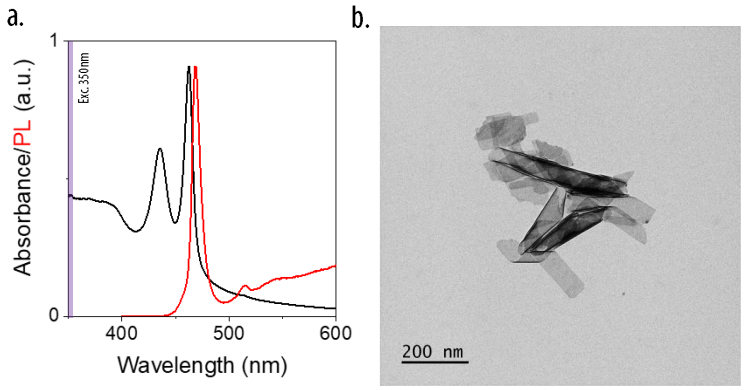

Figure 53: *CdSe 3ML NPLs. a. Absorption (black) and emission (red) of the synthesized 3ML NPLs. The excitation has been conducted at 350 nm. b. Associated TEM picture.*

The NPLs are obtain by the slow injection, at 190 °C, of a mixture containing OA and TOP:Se into a reacting medium containing $Cd(ac)_2$ as a Cd precursor. The anisotropic growth is here again triggered by the duality between short (acetic acid) and long (OA) carbon chains ligands. As the slow injection is carried out over a long time, the occurrence of side nucleation for new seeds of 3 ML NPLs is unlikely, resulting in NPLs with uniform lateral extensions. At the end of the synthesis, the NPLs exhibit a first excitonic peak at 462 nm and a second at 430 nm. Due to their larger size, they display an absorption spectrum that is not flat above the band gap. This is attributed to the diffusion process that takes place when the lateral dimensions reach the same order of magnitude as the incident wavelength. The QY remains modest (3 %) due to the NPLs' significant lateral extensions.

In the TEM picture, we can see that these large NPLs form tube-like structures (see **Figure 53b**). This phenomenon occurs as a result of the tensile strains induced by the ligands on the material's surface. Due to their thin thickness, those NPLs are flexible and tend to fold upon themselves, thereby reducing the overall surface energy[202].

c. Synthesis of alloyed NPLs.

The synthesis of $CdSe_xTe_{1-x}$ 3 ML NPLs was developed by Tenne *et al*. in 2016 and is similar to the one developed for the synthesis of CdSe 4 ML NPLs[69]. $Cd(myr)_2$ is initially used as Cd precursor in ODE. After degassing and switching to argon, the temperature is set at 230 °C. Once stabilized, a mixture of $Cd(ac)_2$ and $Cd(prop)_2$ is introduced. A solution of TOP:E (E: Se, Te) with a specific Se/Te ratio is slowly injected. Tenne *et al.* have determined both the ratio between the two short-chain carboxylates and the injection speed to ensure similar reactivity for both TOP:Se and TOP:Te throughout the synthesis.

Three different compositions have been specifically synthesized here: $CdSe_{0.25}Te_{0.75}$, $CdSe_{0.50}Te_{0.50}$ and $CdSe_{0.75}Te_{0.25}$. The lateral dimensions of the final NPLs may vary between samples but remain close to those obtained for 3 ML CdSe NPLs (see **Figure 54f-g**). The final compositions of the NPLs have been verified by EDX and correspond to the incorporated Se/Te ratio. XRD experiments (see **Figure 54b**) have also been conducted, revealing the presence of (111), (200) and (311) peaks, which are characteristic of the ZB structure in all the synthesized alloys. Following the Vegard's law, it also demonstrates a correlation between the positions of the diffraction peaks and the Se/Te ratio of

the alloys, thus validating their compositions (see the evolution in between the colored vertical lines in **Figure 54b**).

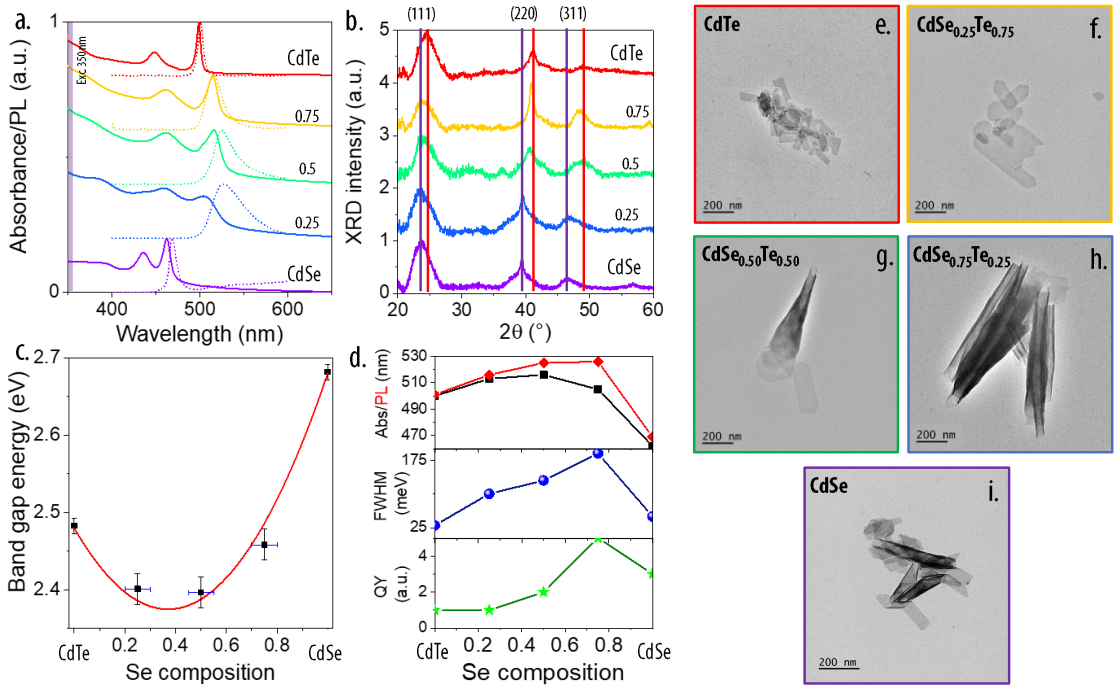

Figure 54: *Sum up of the optical features of 3 ML $CdSe_xTe_{1-x}$ NPLs with 0≤x≤1. a. Absorption (plain) and emission (dots) spectra for 3 ML $CdSe_xTe_{1-x}$ NPLs. For clarity, the absorption and emission spectra have been shift by pairs of same composition. The excitation have been conducted at 350 nm. b. XRD diffractograms of 3 ML $CdSe_xTe_{1-x}$ NPLs. The diffraction peaks are labeled on top of the window, the red (resp. purple) dashed line corresponds to the position of the corresponding diffraction peak for CdTe (resp. CdSe). For clarity, the curves have been shifted. c. Band gap energy according to the comsposition is Se (x) in $CdSe_xTe_{1-x}$ 3ML NPLs. The red fitting curve unveils the bowing effect in these alloys. d. Maximum in absorption (in red) and emission (in bleack), full width at half maximum (in blue) and quantum yield (in green) of the 3ML $CdSe_xTe_{1-x}$ NPLs according to their composition in Se (x). e-i. TEM pictures of respectively CdTe, $CdSe_{0.25}Te_{0.75}$, $CdSe_{0.5}Te_{0.5}$, $CdSe_{0.75}Te_{0.25}$ and CdSe 3ML NPLs.*

As mentioned in the introduction chapter, the optical properties of these alloyed NPLs are particularly intriguing. While the absorption spectra of the CdTe and CdSe NPLs exhibit sharp excitonic features, their counterpart in alloyed NPLs are less distinct and become broader as the ratio Se/Te increases. The position of this absorption is also not shifting continuously: for Se/Te ratios below 0.8, the band gap of the particle is lower than that of the two pure materials. This effect is consistent with the observed band gap bowing in bulk $CdSe_xTe_{1-x}$ alloys[70,203]. The bowing factor (b) characterizing this band gap bowing is calculated using the following expression:

$$E_{CdSe_xTe_{1-x}}(x) = xE_{CdSe} + (1-x)E_{CdTe} - bx(1-x)$$

where x represents the fractional composition of Se, b denotes the bowing parameter, and E_{CdSe}, $E_{CdSexTe1-x}$ and E_{CdTe} correspond to the band gap energy of CdSe, $CdSe_xTe_{1-x}$ and CdTe, respectively. This expression yields a bowing factor of 0.78 eV which is close to the one observed in the bulk form (0.74 eV) (see fit **Figure 54c**)[203].

The emission follows a similar trend as the bowing effect in NPLs having the smallest Se/Te ratio. However, when the fraction of Se exceeds 0.5, it starts to deviate, and only a continuous red-

shift is observed, accompanied by a broadening[69]. This effect arises from the appearance of Te-associated hole traps above the VB as we transition from an alloyed to a dopped regime in the low Te composition. This observation is consistent with the broadening of the absorption features as the Te content decreases and is similar to other bulk alloyed systems[203].

To summarize, we have successfully synthesized 3ML NPLs of $CdSe_xTe_{1-x}$ with various compositions expending ranging from pure CdSe to pure CdTe. In the next section, we will investigate the CE with mercury to extend the process to alloyed NPLs.

9. Cation exchange on Cd-based NPLs.

After synthesizing the initial Cd-based NPLs, a CE procedure can be implemented to obtain their Hg-based counterparts. These materials are softer compared to the Cd-based ones, which can pose challenges. The removal of cations during the CE process can destabilize the anion lattice, making the material more fragile and susceptible to surface reorganization processes in order to attain a more stable form. QDs, with their lower surface-to-volume ratio, minimize surface strains and are typically formed during surface reorganization processes[111,118]. To address this issue, Izquierdo *et al.* employed a bulky precursor of mercury, specifically mercury acetate ($Hg(ac)_2$) dissolved in OLAm, to slow down the reaction. Additionally, the use of an amine facilitates the efficient extraction of the Cd^{2+} due to the relative hardness of both the organic compound and the cation according to Pearson's theory.

a. Absorption to monitor the cation exchange.

During the CE a significant color change is observed. The initially yellow solution rapidly turns dark brown upon completion of the exchange. Therefore, absorption spectroscopy is employed to monitor the CE process (see **Figure 55d**). Initially, CdTe 3ML NPLs exhibit two excitonic features respectively at 500 nm and 450 nm in their absorption spectrum. This absorption structure initially disappears before gradually recovering, but red-shifted, showing new excitonic features presenting a first excitonic peak at 880 nm and a second at 730 nm. Those features correspond to HgTe 3ML NPLs.

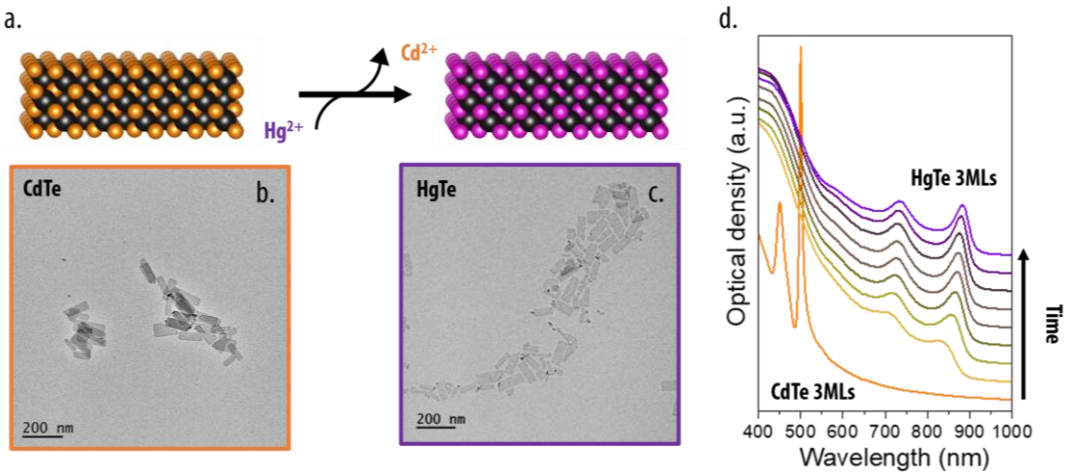

Figure 55: *How to follow the cation exchange. a. Skecth of the cation exchange with TEM pictures before (in orange) and after (in purple) the CE. b. Evolution of the absorption features according to the time during the CE.*

During the CE, the photoluminescence in the NIR initially increases and undergoes a red-shift due to the expansion of the exchanged areas within the NPLs. The resulting HgTe NPLs exhibit a band edge emission at 900 nm with a small FWHM of 80 nm. However, this emission is not stable over time

or after the washing process. Gradually, a second contribution at lower wavelengths emerges and surpasses the initial emission while also red-shifting over time. Caram's team at UCLA has studied this phenomenon and attributed it to the formation of small dots on the particle's surface caused by a surface reorganization. This aspect will be further addressed in the following chapter[57,204].

b. Limit of the cation exchange.

In previous work, a CE has also been conducted on CdSe 3ML NPLs[38] with a similar protocol to the one established by Izquierdo *et al*. for obtaining 3 ML HgTe NPLs. The results of this exchange are similar to those conducted on CdTe NPLs except for the slower reaction rate observed in the case of CdSe NPLs. The main reason for this could be the slower diffusion of Hg^{2+} cations inside the NPLs. Due to its smaller lattice parameter (6.05 nm for CdSe, 6.48 nm for CdTe), the diffusion through the Se anion lattice is slower compared to the equivalent Te network. Additionally, no PL has been observed for these particles.

When a similar procedure is carried out on $CdSe_xTe_{1-x}$, the NPLs are destroyed during the process, resulting in particles with stair-like edges (see **Figure 56a**). During the final washing process, a dark-colored supernatant is also observed. Due to their large size, the NPLs easily fall during centrifugation. The dark supernatant is likely due to the presence of small dots of HgTe or fragments of destroyed NPLs that remain colloidally stable. These dots may originate from surface reorganization or recrystallization of monomers coming from the dissolution of the particles during the CE process. For instance, **Figure 56a** shows a TEM picture of exchanged $HgSe_{0.5}Te_{0.5}$ 3 ML NPLs with black spots that could correspond to such side nucleation. This poses a significant challenge for the final optical properties of Hg-based NPLs. Owning a larger Bohr radius, these materials are more susceptible to the presence of defects, particularly voids within the structure.

Using 8 bands k.p modelling, the team led by J. I. Climente at Universidad Jaume I in Spain has shown the influence of small holes in NPLs. To do so, they established the band diagram of HgTe NPLs based on the particle's thickness using a one-dimensional quantum well Hamiltonian. By identifying the bands involved in the different transitions, they successfully simulated the absorption diagram of HgTe NPLs. The result is very similar to the one experimentally obtained[39]. Only a small redshift is observed, but it can be attributed to a non-trivial surface chemistry that would induce small shifts.

Having successfully determine the band diagram of HgTe 3 ML NPLs, they simulated the influence of several holes inside small NPLs of HgTe (see **Figure 56b**). To do so, they modeled a NPLs with dimensions of 50x20x1 nm^3, which is consistent with the smallest HgTe synthesized, and introduced defects through depletion terraces of 5x5x0.5 nm^3. Due to the thinner thickness of the HgTe, the quantum confinement is significantly increased inside the terraces. As a result, the exciton will preferentially be localized in the defect-free region. With an increasing number of defects, the lateral extension of these defect-free decreases, causing a new lateral quantum confinement that results in a blue shift the NPLs' optical properties. The lateral extension of these areas is also sensitive to the localization of the defects inside the particle: the closer the defects are from the edges, the larger the available areas will remain, limiting the additional quantum confinement. This is effectively what they observed during their experiments: a small number of off-centered defects has a minor effect on the band edge position while an increase in the number of centered defects induces a larger blue-shift of the band edge, up to tens of meV.

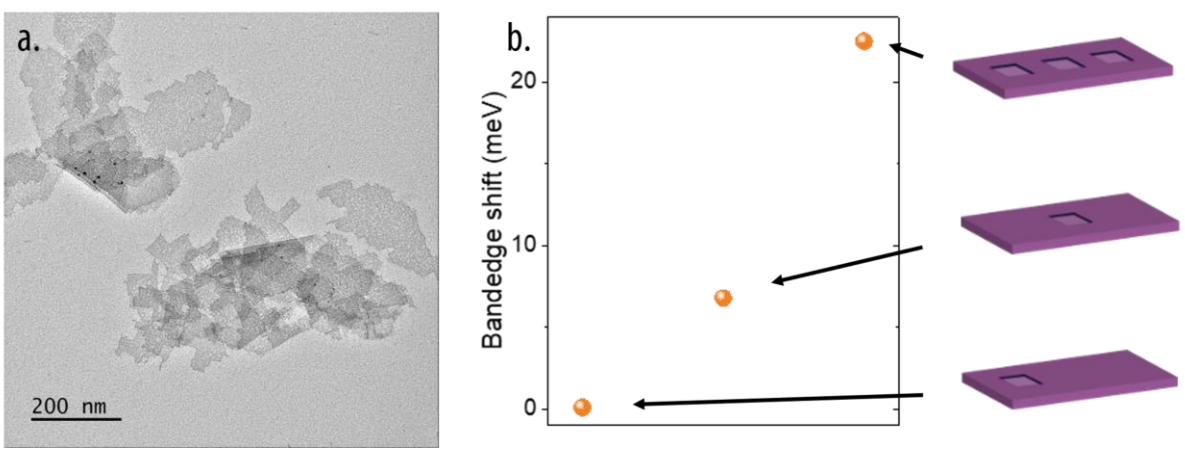

Figure 56: *Limit of the initial procedure. a. TEM picture of $CdSe_{0.5}Te_{0.5}$ 3ML NPLs after performing CE. b. Simulated bandedge shift according to the position on number of defect in the NPLs (the skecth of the NPLs simulated are shown next to the plot). The simualtion has been carried out by J.I.Climente's team in Spain using k.p model.*

This result, along with the observed degradation, calls for an optimization of the CE process to obtain defect-free NPLs of $HgSe_xTe_{1-x}$ and HgSe with well-defined optical features.

c. Cation exchange optimization.

As describes in the introduction, the CE can be divided into several steps:

- 1. Migration toward the surface and desolvation of the incoming cations.
- 2. Diffusion of the host and incoming cations, respectively, out and into the anion lattice.
- 3. Solvation of the outgoing cations.

Following the same idea as Izquierdo *et al.*, I decided to slow down the reaction even further. The diffusion of the cations inside the anion lattice is determined by the studied structure and cannot be easily modulated. On the other hand, the migration of the incoming cations toward the surface can be facilitated or prevented depending on the ligands present on the surface and solvating the cations. For example, Izquierdo *et al.* used a bulky precursor of mercury to slow down the migration of incoming cations. Other parameters can be changed to achieve similar effects. Three of them will be investigated and optimized in the following sections.

Optimization of the solvent.

A first parameter that can be changed is the solvent. The initial procedure was carried out in hexane or toluene, which are non-polar and non-coordinating solvents. However, other solvents can be considered. For example, the tetrachloroethylene (TCE) is commonly used in the NIR due to its complete transparency at those wavelengths. The exchange was then conducted under the same conditions in toluene, hexane, and TCE on 3 ML $CdSe_{0.5}Te_{0.5}$ NPLs (**Figure 57**). In all three solvents, the features of CdTe completely disappear at the end of the reaction, and the EDX measurements show no remaining cadmium after the particles washing. The TEM pictures show similar results in all cases with some degradations visible on the particle edges (see **Figure 57c-e**). In terms of absorption, the excitonic features of the final NPLs are more defined when exchanged in TCE (**Figure 57a-b**). Additionally, for NPLs exchanged in hexane and toluene, an increase in the baseline above 900 nm is visible. This is likely caused by the formation of small dots through surface reorganization. Regarding the band gap of these particles, the size of the formed dots is small and might not be seen on TEM

pictures. Nevertheless, the presence of a dark supernatant during the washing process seems consistent with this hypothesis.

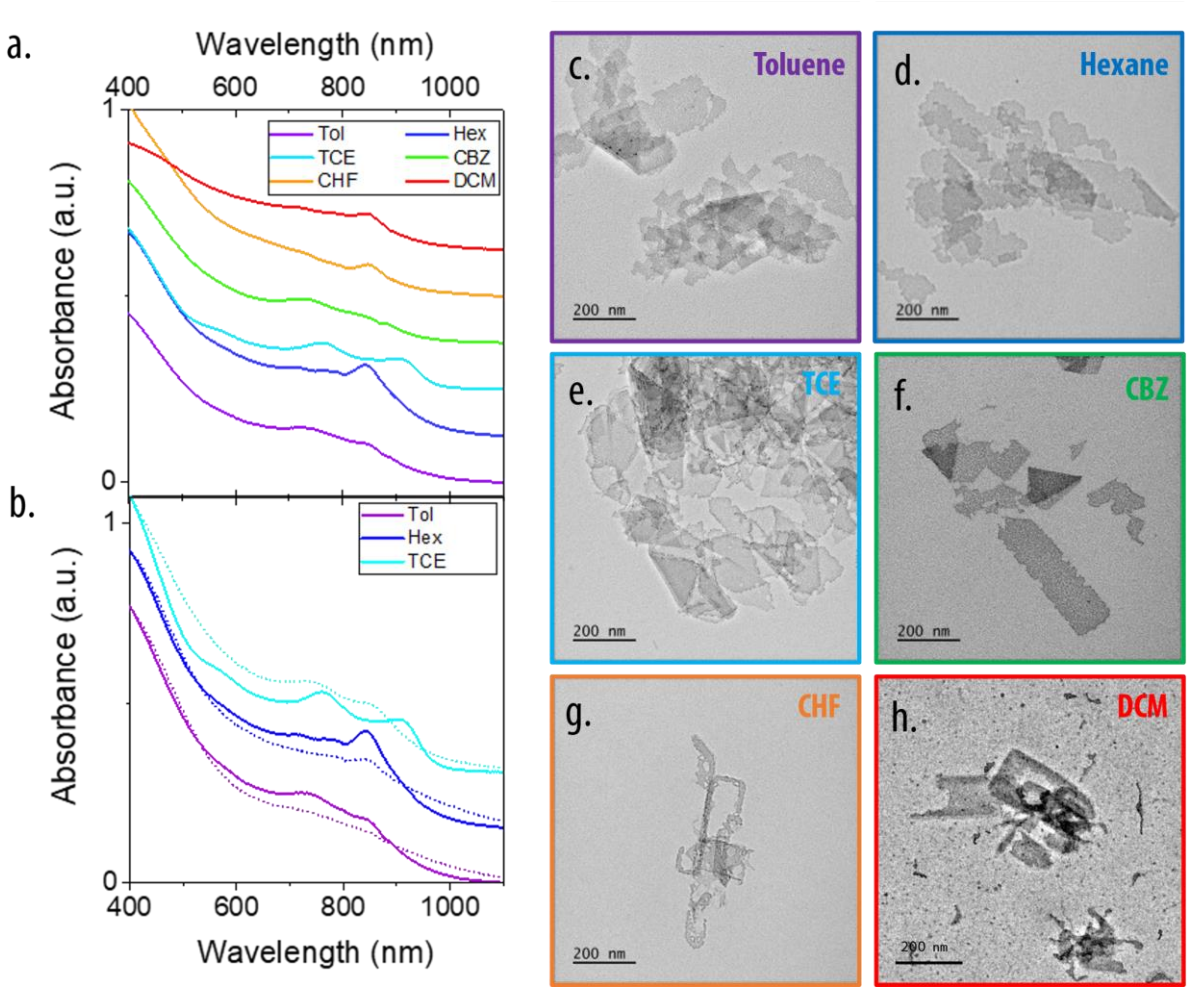

Figure 57: *Solvent optimization. a. Absorption spectra of the NPLs using different solvents after the cation exchange but before the washing process. b. Absorption spectra of the $HgSe_{0.5}Te_{0.5}$ before (plain) and after (dots) washing process. The NPLs are redispersed in hexane. c-f. TEM pictures of the exchanged NPLs in different solvents.*

Another interesting feature concerns band edge energy. In fact, it is red-shifted in TCE compared to the two other non-coordinating solvents (see **Figure 57a**). This might result from additional interactions between the chloride electronic doublets and the cations located on the surface (interactions that do not exist in non-coordinating solvents). However, this must be nuanced as a partial dissolution of the NPLs in the case of hexane and toluene can lead to poorly defined and blue-shifted optical features. To confirm the influence of the Cl bonding on the NPLs' surface, we also conducted the CE in other chlorinated solvents available in the laboratory: chlorobenzene (CBZ), chloroform (CHF) and dichloromethane (DCM)(see **Figure 57a**). While CBZ presents results similar to TCE except for the red-shift of the optical features, the last two solvents completely destroy the particles during the exchange. This result is consistent with the observations made by Lim *et al*. on the photodegradation of CdSe NPLs in presence of chlorinated alkyl solvents (DCM or CHF)[205]. It is worth noting that the availability of Cl doublets on the CBZ is weaker than in TCE. Therefore, we can assume that the observed red-shift originates from an interaction between the available Cl doublets present in TCE and the surface of the NPLs.

When the NPLs are stored in TCE, they tend to degrade. Thus, after washing, the particles are redispersed in hexane. The absorption features of the NPLs exchanged in TCE blue-shift towards the position of the NPLs exchanged in a non-coordinating solvent. The role of the chlorinated solvent seems here again effectively link to the observed spectral red-shift during the cation exchange process. This might be attributed to the larger delocalization of the wavefunction due to the coordination of the chloride atom to the surface. However, this assertion remains uncertain, and further DFT calculations could reveal the organization of the ligand and solvent molecules on the surface.

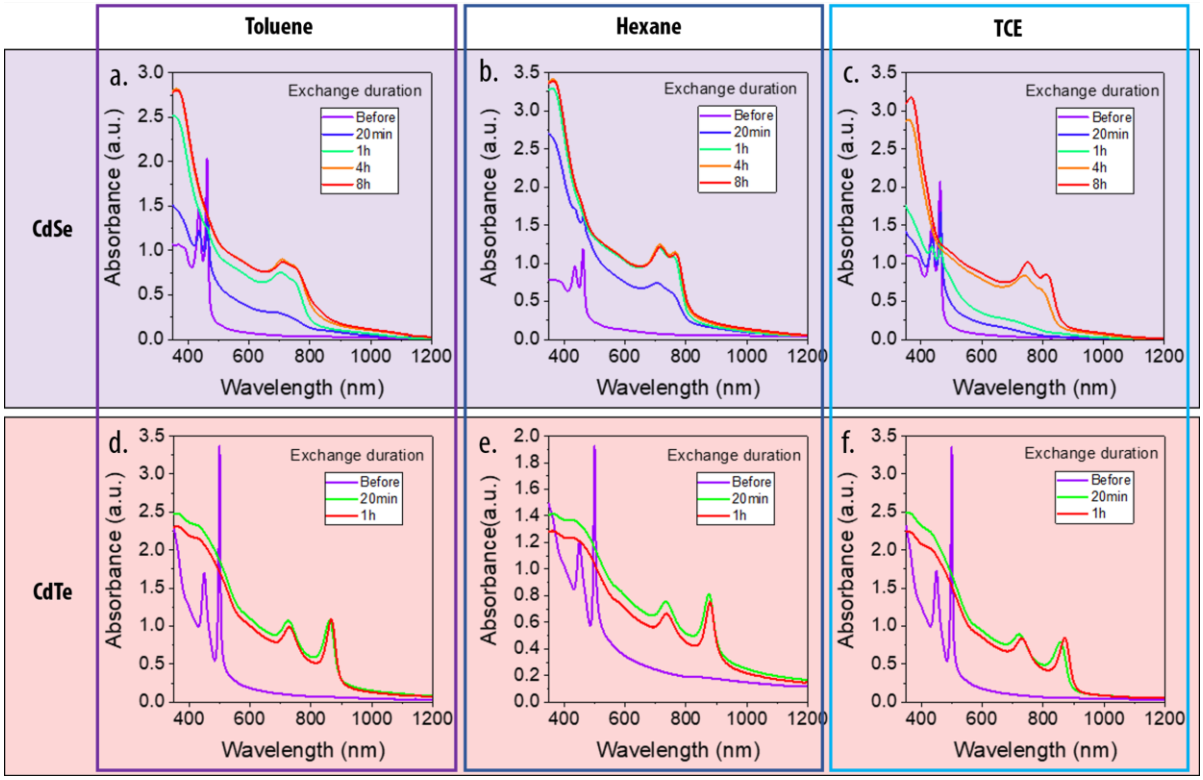

Figure 58: *Focus on TCE, toluene and hexane. a-c. Evolution in time of the absorption during cation exchange conducted on CdSe 3ML NPLs using respectively toluene, hexane and TCE as solvent. d-f. Evolution in time of the absorption during cation exchange conducted on CdTe 3ML NPLs using respectively toluene, hexane and TCE as solvent.*

To gain deeper understanding of the influence of TCE on the CE of alloyed NPLs, we conducted the process using the same three solvents: hexane, toluene, and TCE, for 3 ML NPLs of pure CdTe and pure CdSe (see **Figure 58**). For the pure CdSe, it is evident that the TCE slows down the rate of the reaction, resulting in well-defined excitonic features at the end of the process (see **Figure 58c**). The reaction is significantly faster when toluene or hexane is used. Additionally, a shoulder at longer wavelengths is observed when the reaction is conducted in toluene, which can be attributed to the degradation of the NPLs into small dots (see **Figure 58a-b**). As for CdTe, the exchange appears similar for toluene and TCE (see **Figure 58d, f**), while in hexane, the increased baseline at longer wavelengths indicates particle aggregation or partial degradation (see **Figure 58e**).

Overall, considering both the edge aspects and the shape of absorption features, we can conclude that TCE appears to be a better candidate than the non-polar solvents. Therefore, we have decided to use TCE for the subsequent optimizations.

Optimization of the temperature.

Each step of the CE is associated with an activation barrier. Therefore, decreasing the total system energy would reduce the probability of surpassing the successive activation energies, thus limiting the reaction kinetically and preserving the NPLs from shape degradation. To achieve this, the reaction can be conducted at lower temperatures to decrease the thermal energy introduced into the system, simultaneously reducing thermally activated surface reorganization processes. Initially performed at room temperature, I decided to decrease the CE temperature down to 5°C and -20°C. Since the mercury precursor solution tends to freeze at temperatures below 15°C due to the presence of OLAm, we first cooled down the NPLs solution in the solvent before introducing the mercury precursor. The volumes added are small enough to consider the NPLs solution as a thermostat. The results are presented in **Figure 59**.

During the CE conducted at lower temperatures, a color change is still observed, but it occurs over a longer period of time. This process can be monitored using absorption spectroscopy: after two days of exchange, the features of the initial NPLs exchanged at room temperature and at 5°C are no longer visible. Among the two, the features of the $HgSe_{0.5}Te_{0.5}$ obtained at 5°C are the most well-defined. Thus, the slowdown of the process seems effectively limits the degradation of the NPLs, preserving their optical features.

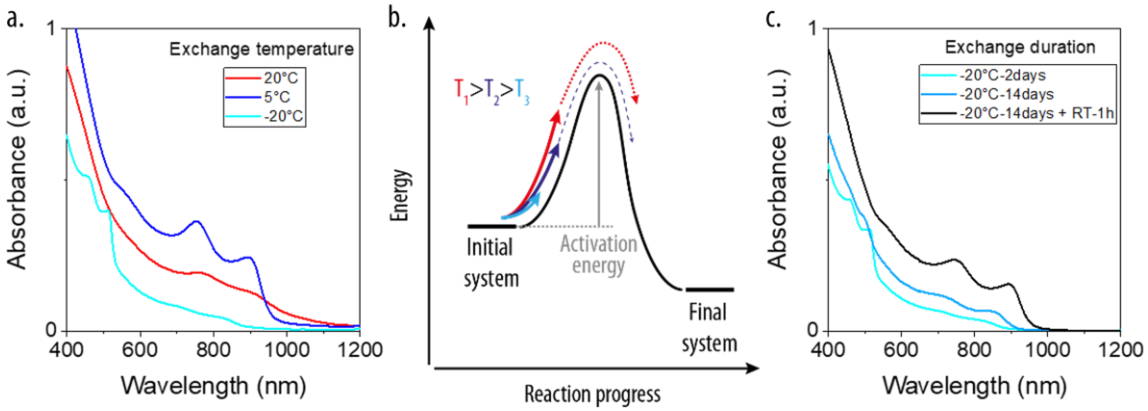

Figure 59: *Influence of the temperature on the cation exchange. a. Absorption spectra of the cation exchange solution after two days carried out in TCE at 20°C (red), 5°C (dark blue), and -20°C (light blue). b. Energetic diagram sketch of the influence of the temperature on the probability to overpass the activation barrier. c. Absorption spectra of the cation exchange conducted at -20°C for 14 days and at RT for 1h. This last graph unveils the kinetic blockade that can be performed on such a reaction.*

In the case of the reaction conducted at an even lower temperature (-20°C), the features of the initial 3 ML $CdSe_{0.5}Te_{0.5}$ NPLs are still visible after two days, despite the emergence of doublet features at longer wavelengths, which indicates the coexistence of areas that remained unaffected. Furthermore, after 14 days, the exchange is still incomplete. Thus, under these conditions, the kinetic of the reaction is almost frozen. However, when the medium is heated back to room temperature, the exchange is completed within an hour. This last observation serves as a proof that kinetic blockade is possible.

In conclusion, we have demonstrated that a trade-off between particle shape reorganization and reaction time of is necessary. This can be achieved by adjusting the reaction temperature. In this case, we have determined that 5 °C is the optimal temperature for the CE.

Optimization of the ligands involved during the process.

In parallel with the kinetic study, we decided to investigate the use of bulkier ligands during the CE. This has a dual effect: partially capping the NPLs with these bulky ligands and complexing the incoming cations, which leads to a slower diffusion of the precursors toward the surface.

To achieve this, we added both oleic acid (OA) and metal oleate ($Cd(OA)_2$) during the CE (see **Figure 60**). The TEM images at the end of the reaction under these conditions are striking: the final edges of the NPLs are almost undamaged during the exchange, and this preservation continues even after the washing step (see **Figure 60c-d**). To assess the role of OA and metal oleate during the CE, we also conducted a washing step on the reference sample with a similar amount of OA added before the centrifugation (see **Figure 60b**). In this case, we observe well-dispersed NPLs in the TEM image, but the edges were still poorly defined. This result emphasizes the importance of the washing step in achieving the desired aspect of the NPLs. In fact, despite the easy precipitation of the large particles limiting the addition of non-solvent, the washing process induces ligand striping off the NPLs and agglomeration of the particles. These two factors combined can make it difficult to redisperse the particles after the exchange, as the NPLs washed without proper care tend to pack (see **Figure 60a**).

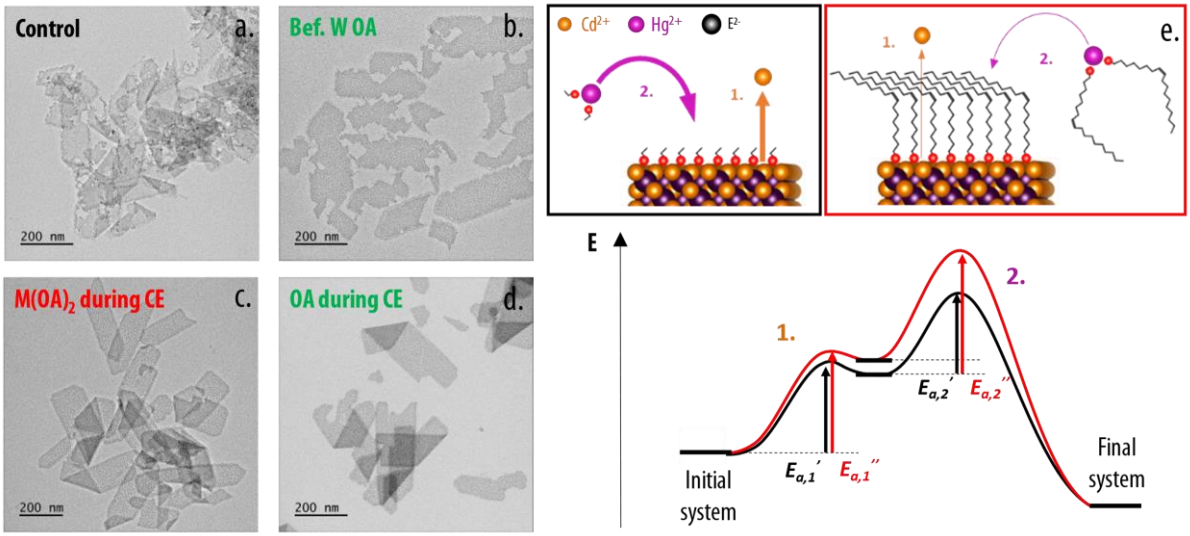

Figure 60: *Influence of the addition of bulky ligands during the cation exchange. a-d. TEM pictures of $HgSe_{0.5}Te_{0.5}$ after exchange using different conditions at RT in TCE: a. reference sample exchanged in TCE, b. same as a. but with addition of OA before the washing process, c. same as a. but adding few drops of $Cd(OA)_2$ (0.1 M in OA) before the exchange, d. same as a. but adding OA before the cation exchange. e. Sketch of the cation exchanged procedure seen as successive activations barriers. The small panel describes situations where small/bulky ligands are introduced before the cation exchange.*

To unpack them, one can sonicate the solution. However, the energy brought by sonication might break or trigger surface reorganizations on Hg-based NPLs that have already been weakened by the loss of ligands. After the exchange, the surface of the NPLs is mostly constituted by a mixture of native ligands and acetate that have been introduced through the mercury precursor. Those ligands are short and do not favor good redispersion of the particles. The addition of oleic acid increases the steric hindrance between the particles, limiting their aggregation and facilitating their redispersion. Working in excess of ligands might also decrease the number of ligands stripped off during centrifugation.

This experiment enables us to conclude that the addition of bulky ligands before centrifugation improves the colloidal stability of the NPLs after the CE. Nevertheless, better results are obtained when

they are introduced right from the beginning of the exchange. In this latter case, the ligands present on the surface already contain bulky ones which also favors of a good redispersion of the particle.

In comparison to temperature optimization, we do not decrease the total energy of the system to slow down the reaction, instead, we increase the activation barriers. In fact, as mentioned in the introduction, we can divide the CE into several steps. First, there is a migration of the host cation out of the NPLs through the ligand layer and second, there is the migration of the incoming cation toward the surface through the ligand shell (see small panels **Figure 60e**). By increasing the steric hindrance on the surface, we also increase the activation energy required for these two steps (see **Figure 60e**). Consequently, the overall process is slowed down.

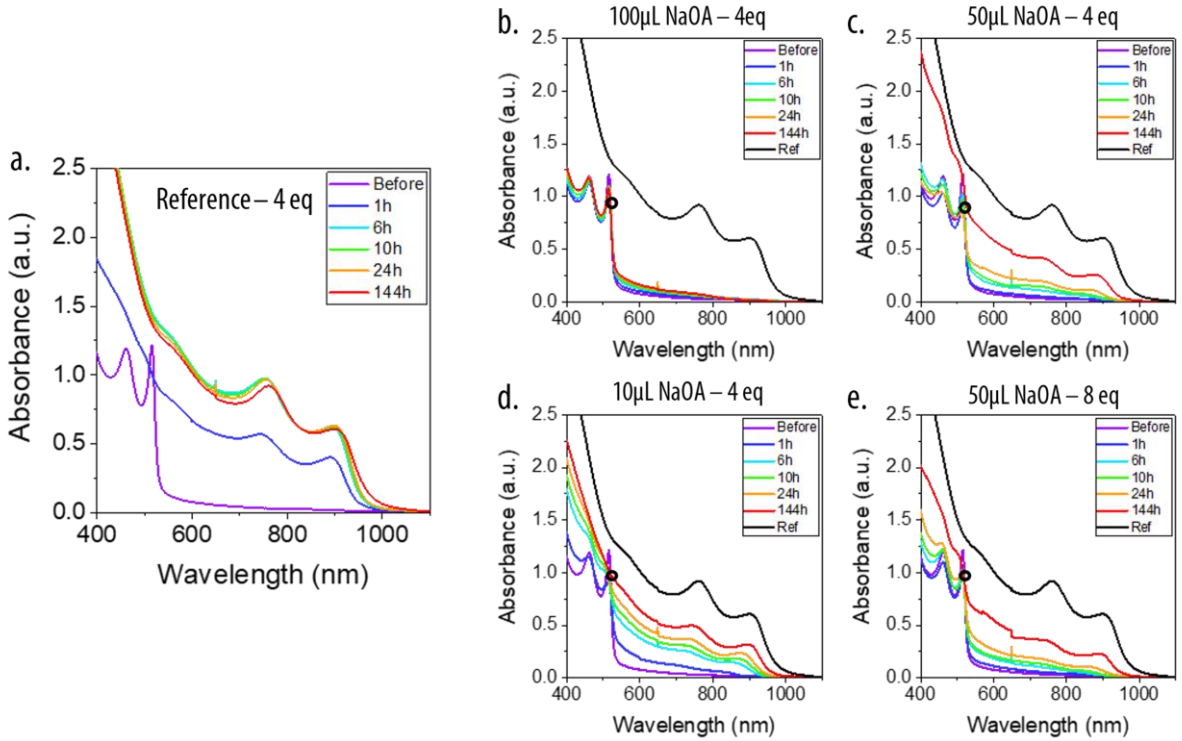

Figure 61: *Optimization of the bulky ligands used for the cation exchange. a. Initial cation exchange procedure followed by absorption. b-e. Optimized cation exchange procedure followed by absorption with different amount of NaOA and Hg(0Ac) solutions. For all the plots, the used conditions are written on top of the graph, 1 eq being calculated according to the quantity of Cd contained in the initial NPLs.*

The use of OA and, even more oleates, induces a benefit on the CE. Therefore, we decided to investigated the optimal number of ligands to add before the CE. The investigation was carried out using NaOA instead of $Cd(OA)_2$, as an addition of cadmium cations might not favor of a complete extraction of the host cations from the NPLs. Specifically, we tested three different amounts of NaOA for the same concentration of NPLs: 100 µL of NPLs (1 µmol) in 3 mL TCE with various amounts of NaOA (0.1 M in OA). The mixtures were cooled down to 5 °C before the addition of several equivalents of $Hg(ac)_2$ (0.1 M in OLAm) (see **Figure 61**).

We observed that the higher the quantity of NaOA injected, the slower the reaction, which is consistent with increasing steric hindrance. Furthermore, a complete CE is observed for an addition of 10 µL of NaOA (see **Figure 61c**), while when more bulky ligands are added, the exchange seems incomplete as features around 500 nm are still visible. Similar to the exchange carried out at -20°C, the reaction appears frozen when too much NaOA is added (see **Figure 61b**). It is also worth mentioning

that an increase in the precursor amount does not significatively increase the pace of the reaction (see **Figure 61c and e**).

The overlay of the absorption curves according to the exchange time reveals a specific point in the CE conducted with oleate (see black circles at 510 nm in **Figure 61b-e**). This point is observed when the final particle exhibits the best overall aspect with no degradation noticed on the edges. This specific point is similar the isosbestic point observed in spectrochemistry and could indicate a conversion from $CdSe_{0.5}Te_{0.5}$ to $HgSe_{0.5}Te_{0.5}$ without material losses due to degradation or to the formation of a side products. Overall, when such a point is not observed during the CE, the NPLs usually have poorly defined edges or exhibit aggregation, as is the case in the control experiment shown in **Figure 61a**.

After optimizing the CE conducted in this section on $CdSe_{0,5}Te_{0,5}$, we implemented it for other alloys compositions with the aim of obtaining $HgSe_xTe_{1-x}$ 3ML NPLs with different compositions.

d. Cation exchange implemented on $CdSe_xTe_{1-x}$ 3 ML NPLs.

The optimized parameters were used to performed CE on a series of 3 ML $CdSe_xTe_{1-x}$ NPLs to obtain their Hg-based equivalents. **Figure 62** shows the results obtained for CE performed on the same amounts of 3 ML CdSe, $CdSe_{0,75}Te_{0,25}$, $CdSe_{0,5}Te_{0,5}$ and $CdSe_{0,25}Te_{0,75}$ NPLs using 10 µL of NaOA. The CE performed on a similar amount of NPLs using the protocol initially developed by Izquierdo *et al.* is presented in black. The absorption spectra evolution of the Ce using optimized conditions (TCE as a solvent, 5°C exchange, 10 µL of NaOA) for all the composition are presented in color.

Once again, we observe a similar isosbestic point in all the CEs performed using the optimized quantities, revealing well-conducted exchanges. This point is not observed during the same process carried out using the initial procedure (see black curves in **Figure 62**). Instead, for selenium-rich alloys (**Figure 62c-d**), the absorption decreases significantly during the process, indicating particle dissolution. In the case of tellurium-rich alloys (**Figure 62a-b**), the increase in absorption at high energies is most likely due to particle aggregation, resulting in a more diffusive solution.

Coming back on the optimized procedure, consistently with previous observations, an increase in the selenium content in alloys corresponds to a slowdown of the CE. This unfortunately leads an incomplete CE for selenium-rich NPLs. To counterbalance this slow process, we increased the ratio of NPLs-to-NaOA (by a factor 4). Additionally, to ensure complete exchange, the solution is brought back to room temperature for an additional one hour before the washing process. This final step aims at extracting the last remaining Cd atoms inside the NPLs. As most of the cations have already been exchanged, this last annealing step is expected to preserve the NPLs' shape while accelerating the extraction of the remaining Cd. Finally, to avoid the introduction of additional elements into the exchange solution, mercury oleate ($Hg(OA)_2$, 0.08 M in OA) was used instead of NaOA (0.1 M in OA). The use of $Hg(OA)_2$ appears to have a lesser influence on the CE, resulting in a slight acceleration, especially in the case of selenium-rich alloys. Nevertheless, several days are still required to obtain well-defined HgSe NPLs.

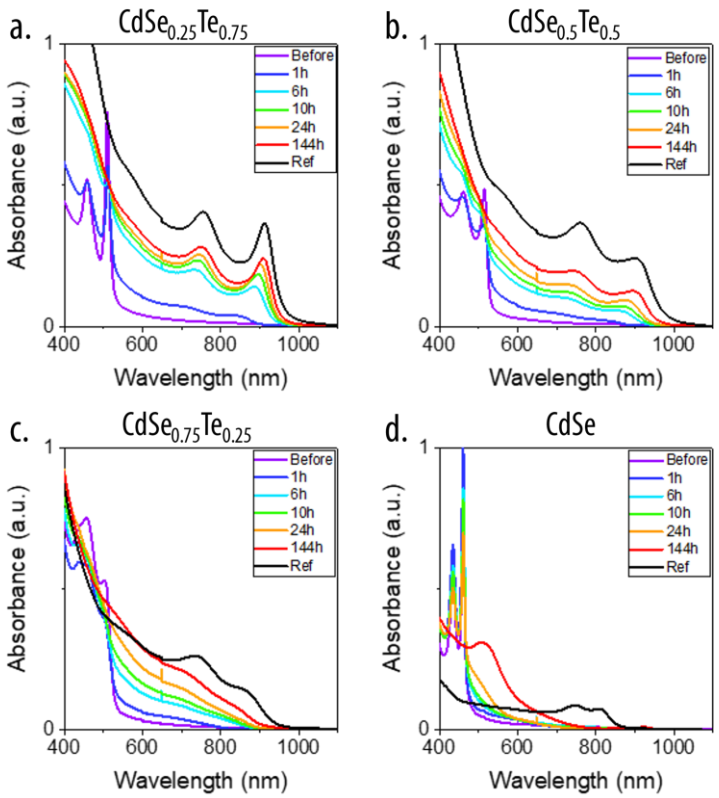

Figure 62: *Cation exchange speed on $CdSe_xTe_{1-x}$ with different alloys compositions. a-d. Absorption spectra of the solution according to the time during the CE of respectively $CdSe_{0,25}Te_{0,75}$ (a), $CdSe_{0,5}Te_{0,5}$ (b), $CdSe_{0,75}Te_{0,25}$ (c), and CdSe (d) 3ML NPLs using exact same conditions. A black reference curve is added on all the graph to compare the optimized CE with the initial one on a similar amount of NPLs.*

This final optimized CE was performed on the $CdSe_xTe_{1-x}$ 3ML NPLs with various alloy compositions corresponding those presented in **Figure 54**. To ensure the proper extraction of the Cd from the NPLs, EDX measurements were performed, revealing a complete CE (within the resolution of the measurement). XRD diffraction was also conducted to confirm the structure of the final NPLs, as shown in **Figure 63**. The obtained diffractograms exhibit the characteristic peaks of the ZB crystal structure, namely (111), (220) and (311).

Those peaks are broad due to the small size of the particles and continuously shift with the alloy compositions. This observation can be interpretated by the Vegard's law, which demonstrates a linear dependency of the lattice parameter in an alloyed structure based on the alloy composition:

$$a_{HgSe_xTe_{1-x}} = x.a_{HgSe} + (1-x)a_{HgTe}$$

where x corresponds to the alloy composition and a_{Hgse}, a_{HgTe}, and $a_{HgSexTe1-x}$ respectively correspond to the lattice parameter of HgSe, HgTe and $HgSe_xTe_{1-x}$. Consistent with this equation, the positions of the (111), (220), and (311) peak linearly shift according to the composition, with only small deviations that can be induced by the uncertainty in the peak position measurement (see **Figure 63b**).

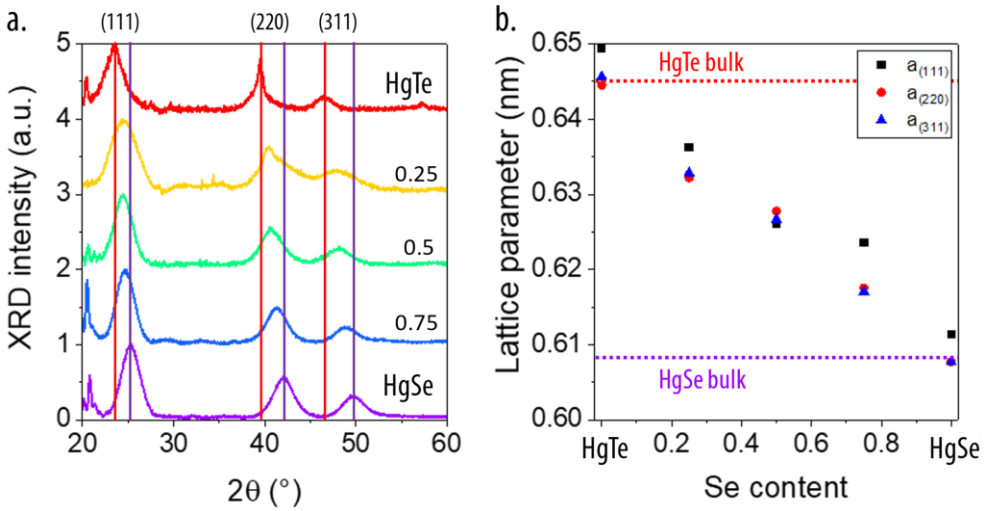

Figure 63: *Vegard's law for $HgSe_xTe_{1-x}$ 3ML NPLs. a. XRD diffractograms of the $HgSe_xTe_{1-x}$ NPLs. The diffractograms intensity have been shifted for clarity. The dashed lines have been added to point the position of the (111), (220), and (311) peak for HgTe (red) and HgSe(purple). b. Lattice parameter calculated from the position of the (111) (black squares), the (220) (red circles) and the (311) (blue triangles) diffraction peaks, according to the Se content. The colored lines correspond to the bulk lattice parameter of bulk HgTe (red) and bulk HgSe (purple).*

The TEM pictures and optical features of the obtained NPLs are summarized in the **Figure 64**. Through TEM, we first observed the attainment of well-defined edges at the end of the CE for all the compositions (see **Figure 64d-h**). For larger NPLs, some cracks may appear inside the NPLs on the TEM grids. However, it is difficult to determine whether those cracks are created in solution or if they result from particle deposition and their observation under the electron beam.

Another striking observation relates to the rolling of NPLs. Similar to the CdSe NPLs presented in the introduction, $CdSe_xTe_{1-x}$ 3 ML NPLs with larger lateral extensions can roll on themselves, creating helices. After the CE, the NPLs unroll and lay flat on the TEM grid. This phenomenon can be explained by the softness of the Hg-based materials compared to Cd-based ones. The new material is more capable of absorbing the constrains imposed by the ligands. Therefore, the NPLs do not need to minimize their surface energy by creating helices, which explains their unfolding on a substrate (see **Figure 64d-h**).

The obtained Hg-based NPLs lie flat on the TEM grids for all the compositions, while their equivalent Cd-based ones roll on themselves. This behavior has already been observed for HgTe NPLs and has been attributed to the higher softness of the Hg-based material, which absorbs the surface constrains brought by the ligands[202].

Regarding the optical properties, the observed features are very similar to those of the Cd-based NPLs. Firstly, the band gap does not shift linearly with the composition, as shown in **Figure 64b-c**. However, this bowing effect is smaller than the one observed in Cd-based alloys. In fact, the band edge of the NPLs owning a composition $x > 0.3$ is nearly the same, with only a few meV of divergence. This smaller effect is accompanied by a smaller bowing factor of 0.36 eV. Consistent with the Cd-based NPLs, the optical properties also become broader as the ratio of Se increases (see **Figure 64c**). Once again, this observation may be attributed to the formation of shallow trap states above the VB, which are related with the presence of Te in low proportions[69]. As the ratio of Te increases, the material becomes closer to a homogeneous alloy, creating a continuum instead of trap-like states, explaining the narrower optical properties observed.

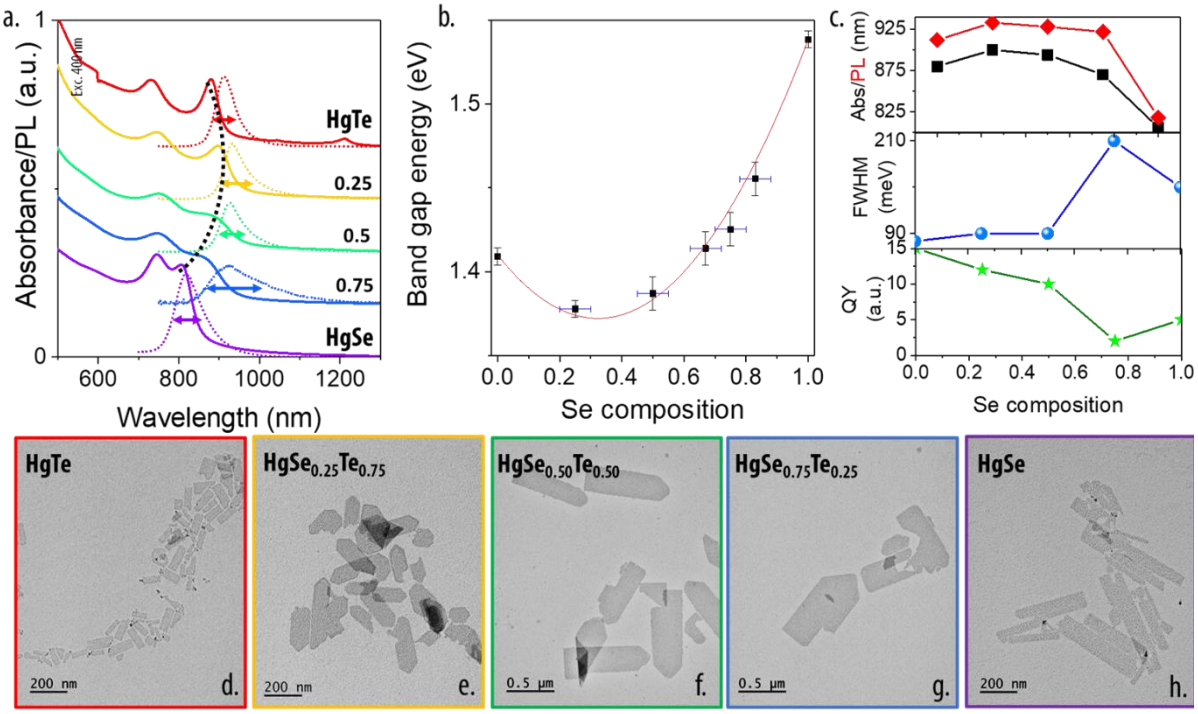

Figure 64: *Sum up of the optical features of $HgSe_xTe_{1-x}$ 3ML NPLs with 0≤x≤1 obtained through optimized CE. a. Absorption (plain) and emission (dots) spectra for $HgSe_xTe_{1-x}$ 3ML NPLs. For clarity, the absorption and emission spectra have been shifted by pairs of the same composition. The excitation have been conducted at 400 nm. b. Band gap energy according to the composition is Se (x) in $CdSe_xTe_{1-x}$ 3ML NPLs. The red fitting curve unveils the bowing effect in these alloys. c. Maximum in absorption (in red) and emission (in black), full width at half maximum (in blue), and quantum yield (in green) of the $CdSe_xTe_{1-x}$ 3ML NPLs according to their composition in Se (x). d-h. TEM pictures of respectively CdTe, $HgSe_{0.25}Te_{0.75}$, $HgSe_{0.5}Te_{0.5}$, $HgSe_{0.75}Te_{0.25}$, and HgSe 3ML NPLs.*

Finally, another striking feature is observed: for the first time, PL has been observed for HgSe and $HgSe_xTe_{1-x}$ NPLs (see **Figure 64a**). The shape of the emission resembles the one observed in the case of Cd-based NPLs, with a relatively thin emission for HgTe (around 90 meV) that gradually increases with the selenium ratio (up to 210 meV for x=0.75). It is worth mentioning that the FWHM is slightly higher than the one observed by Izquierdo *et al*. as the surface chemistry is more complex[38], resulting in a broadening of the optical features (see **Figure 64c**). The QY of those synthesized particles is quite significant with higher value obtained for higher tellurium ratio in the alloy (up to 15 % in the case of HgTe). It is worth mentioning that this value is higher than the one obtained in the case of Cd-based NPLs. This may arise from the lower effect of the trap states, which are less stabilizing in the case of Hg-based NPLs compared to Cd-based NPLs.

These newly synthesized Hg-based NPLs exhibit spectral tunability of their band edge emission between 800 nm and 925 nm. Despite their broad emission for low Te compositions, the obtaining of emission for $HgSe_xTe_{1-x}$ NPLs is promising for further incorporation of those materials into devices. However, to optimize their use in optoelectronics, their band alignment needs to be unveiled to facilitate charge transfers in the device.

10. Band alignment evolution in $HgSe_xTe_{1-x}$ 3 ML NPLs.

Regarding their narrow emission features, Hg-based NPLs would be great candidates for electroluminescence in the NIR region. However, to optimize an LED stack including HTL, ETL and

electrodes, the band alignment must be unveiled to limit the losses and the Schottky barriers encountered by the charge carriers in the structure. One important property that can be investigated is the dynamic of the charge carriers, especially the identification of the majority carriers inside the semiconductor. One method to determine their nature involves integrating them as active material inside a field-effect-transistor (FET).

a. Measuring majority charge carriers using field-effect-transistor.

In an FET, the current going through an array of NCs is monitored based on the nature of the charges injected into this array through a gate effect. This enables the unveiling of the majority carriers' nature inside a NCs array and the relative location of the Fermi level within the band gap.

The transport properties of the alloyed $HgSe_xTe_{1-x}$ 3 ML NPLs have thus been investigated. The particles are first deposited through drop casting in a hexane/octane mixture (9:1 in volume). In a semiconductor array, conduction is mostly driven by hopping transport. This phenomenon is based on the tunneling effect between two neighboring NCs. To enhance the coupling between the neighbors, a reduction in ligand size is required. In fact, the native ligands present on the surface are a mix of carboxylates and amines, many of which have long aliphatic chains like oleic acid and oleylamine. We decided to conduct a post-deposition ligand exchange using ethanedithiol (EDT), which has the double advantage of presenting two anchoring groups and a small carbon chain.

The deposition of NPLs films is particularly sensitive as the large size of the particles induces a complex packing in films. Thus, a thick film ensures the full coverage of the surface. It is worth mentioning that the volume reduction induced by the ligand exchange might create cracks in the film that could limit hopping transport through the film. To avoid such issues, several layers are successively drop-casted and EDT-exchanged to optimize coverage and the percolating path through the NC array. For thick NC films, the choice of the dielectric is crucial. Here, the use of an electrolytic matrix of polyethylene glycol containing lithium perchlorate ($LiClO_4$) helps overcome this issue. The final device is topped by a copper grid to induce the gate effect inside the NCs array.

Previous work conducted by Livache *et al.* investigated the majority carriers' nature inside an array of HgTe NPLs. They observed a p-type behavior for particles capped with EDT. They also unveiled a modulation of the majority carriers according to the surface chemistry: switching the EDT surface ligand to sulfides (S^{2-}) radically changes the doping toward a n-type behavior[130]. In parallel, Izquierdo *et al.* have also shown that HgSe NPLs exhibit a strong n-type behavior, nearly degenerate with the conduction band, with a S^{2-} surface chemistry[80].

In this context, we measured the transfer curves for different compositions of alloys including pure HgTe and HgSe. The HgTe films exhibit an increasing conductivity for a negative gate bias V_{GS} unveiling a p-type behavior consistent with the work by Livache *et al.* (see **Figure 65b**). On the contrary, films of HgSe capped with EDT exhibit an increase in conductance for positive biases V_{GS} which is associated with a n-type behavior this time (see **Figure 65a**).

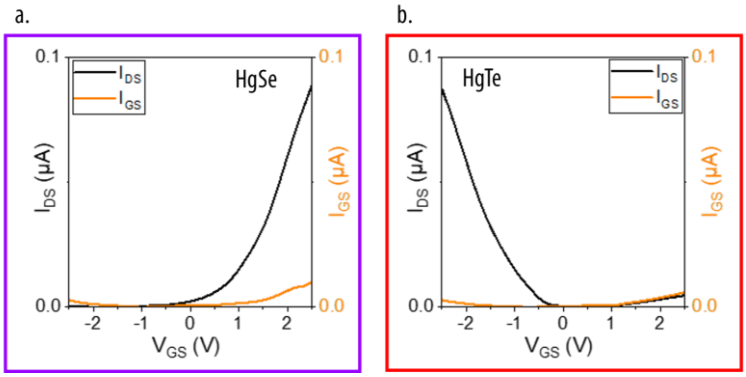

Figure 65: *FET measurements. a-b. Intensity received at the drain (in black) and at the gate (in orange) according to the gate bias for HgSe (a) and. HgTe (b) 3ML NPLs.*

As the Fermi level is expected to evolve continuously within the gap according to the alloy composition, we anticipate to see a crossover from a p-type to a n-type semiconductor for an intermediate composition. However, due to intrinsic nature of the material, the FETs based on intermediate compositions exhibit weaker conductance, resulting in significant leakages through the gate and preventing definitive conclusions. An additional measurement is therefore required to fully depict the evolution of band alignment according to the composition.

b. Photoemission to unveil band alignment.

As mentioned in the introduction chapter, a classical method used to unveil the band alignment of a material is X-ray photoelectron spectroscopy (XPS). This analytical technique, based on the photoelectric effect, allows for the determination of the relative position of the Fermi level and the VB with vacuum as a reference. I had the opportunity to conduct these experiments at the TEMPO beamline of the SOLEIL synchrotron.

Band alignment vs vacuum using static photoemission.

During XPS measurements, the extraction of electrons through the photoelectric effect can induce charge accumulation on the NCs film. To avoid such inconvenience, the NPLs are redispersed in a hexane/octane mixture (9:1 in volume) and drop-cast onto a substrate to obtain a thin homogeneous film. Gold is chosen as substrate to efficiently bring electrons and balance the photo-holes created. Similarly to the film preparation for FET, long ligands remain on the surface of the NPLs, limiting the conduction within the film. Thus, an EDT ligand exchange is conducted to replace the bulky ligands with shorter ones and increase the carrier's mobility in the film. This ligand exchange also induces a shrinkage of the film volume. To fill the cracks created, several layers are successively deposited and EDT-exchanged to cover a maximum area of the gold substrate. The samples are finally placed in ultra-high vacuum for analysis.

First, an overview of the core-levels using a photon energy of 600 eV is conducted to investigate the elemental composition of the samples. In the overview shown in **Figure 66a** (and conducted on 3 ML $HgSe_{0.5}Te_{0.5}$ NPLs), several groups of peaks can be observed. The Hg 4f, Se 3d and Te 4d core-level peaks are visible at 100, 55 and 40 eV, respectively. The presence of those groups confirms the NPLs composition. On the other hand, peaks located around 405 eV correspond to Cd 3d core-levels, which are not expected and most likely result from a poor washing process. In addition, S 2p and S 2s features are observed around 160 and 225 eV, respectively. The sulfur observed does not come from the inorganic core of the particle itself but rather from the ligand exchange performed to

make the film conductive. The two groups around 284 and 532 eV correspond to the C 1s and O 1s core-level peaks which most likely come from the ligands on the surface or from other chemical pollution.

When focusing on the Hg 4f core-level of the mercury, two contributions are observed (see **Figure 66b**). The smaller one at higher energies can be attributed to the surface Hg atoms that are bond to the S coming from the thiols. The higher electronegativity of the sulfur justifies the higher binding energy of the associated Hg 4f electrons. Obtaining a clear picture for the Se 3d and Te 4d states is harder due to the complex organization possible around these atoms inside an alloy.

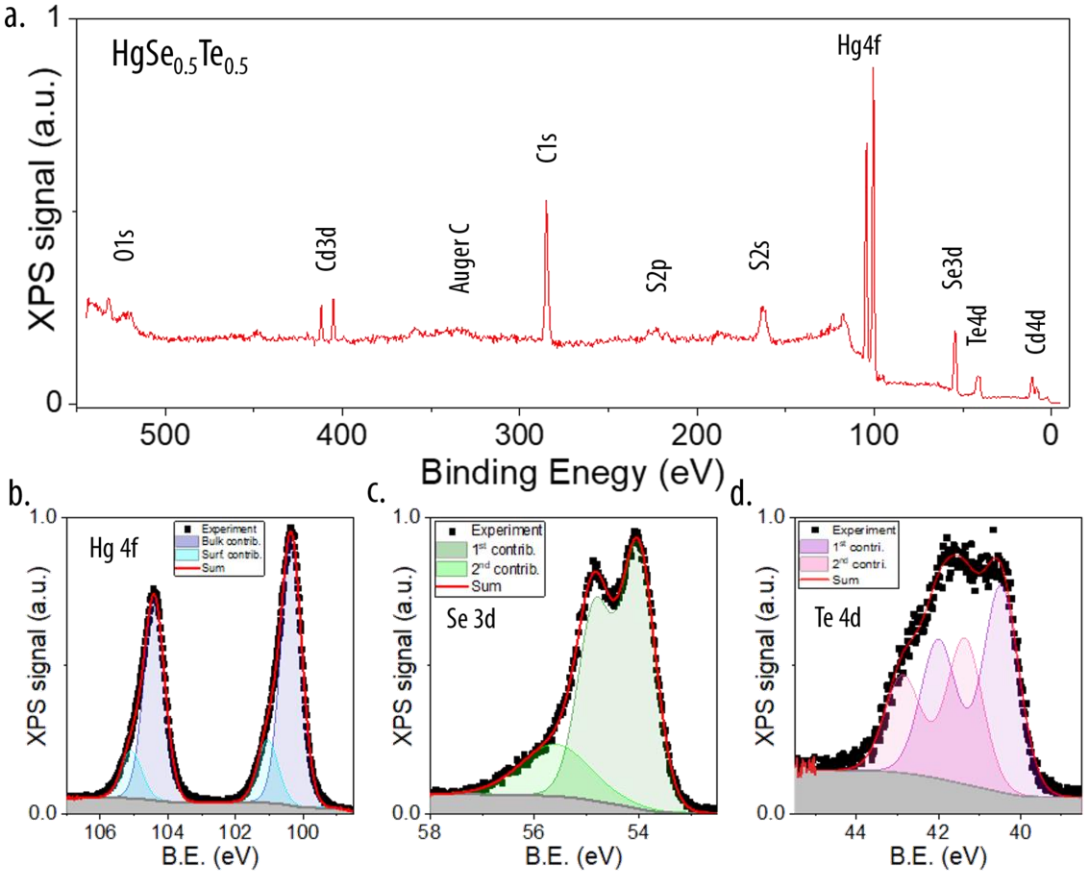

Figure 66: *Overview of the core levels present in 3 ML $HgSe_{0.5}Te_{0.5}$ NPLs. a. Overview conducted at a photon energy of 600 eV. b-d. Zoom on the core-level states of Hg 4f (b), Se 3d (c) and Te 4d (d). The black squares correspond to the experimental data. The colored curves correspond to the different contributions observed within the same core-level. The red curve corresponds to the sum of all the fitted contributions.*

Overall, except for the presence of Se inside the sample, these results are consistent with the ones observed for HgTe 3 ML NPLs presented in the introduction chapter. To gain more insights into the band alignment in these alloys, we need to measure the band gap energy of the material, determine its work function, and measure its valence band.

The band gap energy and the band alignment diagram strongly depend on the surface chemistry of the material[206]. Therefore, in order to accurately measure the band gap energy, we replicate the surface chemistry of the prepared samples by replacing the native ligands on the surface of the NPLs with dodecanethiol (DDT). This is achieved by adding an excess of DDT ligands and stirring the mixture overnight. The band gap is then obtained by absorption spectroscopy (see **Figure 67d**).

After the ligand exchange, the optical features are all broader and shifted to the red. For example, the band edge of HgTe is shifted from 1.35 eV to 1.17 eV when capped by thiols. This behavior is also observed on Cd-based NPLs and can be explain either by a larger delocalization of the wavelength inside the ligand shell or by an increased thickness induced by the in-plane constrains imposed by the ligands[202,206]. When comparing to other alloy compositions, the characteristic bowing effect is still observed, although it is less visible. Measuring the band gap (E_g) is challenging here due to the low resolution of the excitonic peak. Thus, we decided to use a second derivative process to measure this energy. The values obtained are summarized in the table in **Figure 68a**.

Next, the localization of the VB and Fermi level (E_F) are determined by measuring either the binding energy (BE) of the least bound electrons or the kinetic energy (KE) of the secondary electrons. In the case of the BE measurement, obtaining a precise value can be challenging, especially on poorly processed film where the Fermi level of the gold substrate is visible. To increase the precision, the value is measured on a logarithmical scale. The example of 3 ML $HgSe_{0.5}Te_{0.5}$ NPLs is shown in **Figure 67a-b**. A VB of 0.8 eV is found, and a work function (φ) of 4.2 eV is measured. Considering the previously measured band gap energy, the complete band alignment of the material can be established (see **Figure 67c**). In this case, the Fermi level is found to be closer to the CB revealing a p-type behavior for 3 ML $HgSe_{0.5}Te_{0.5}$ NPLs.

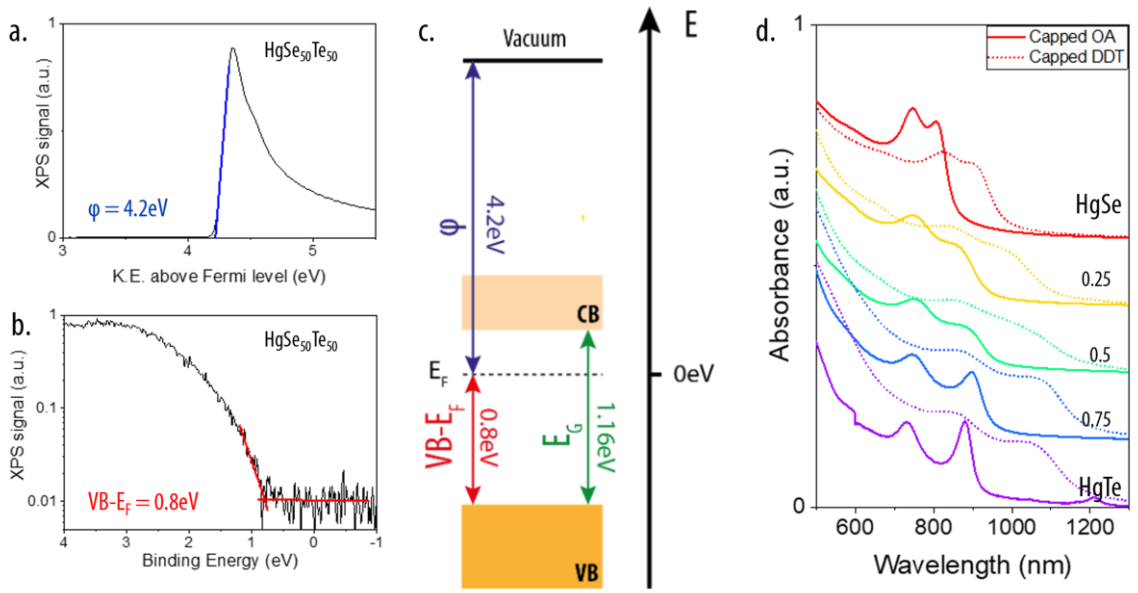

Figure 67: *Establishment of band diagram using XPS in $HgSe_xTe_{1-x}$ 3 ML NPLs. a. Secondary electron measurement for work-function determination in the case of $HgSe_{0.5}Te_{0.5}$ 3 ML NPLs. In blue, the fitting curve used to determine the work-function. B. Lowest bound electron measurement for VB-E_F determination in the case of $HgSe_{0.5}Te_{0.5}$ 3 ML NPLs. In red, the fitting curves used to determine the VB-E_F value. c. Sketch of the establishment of the band diagram using VB-E_F, the work-function, and the band gap in the case of $HgSe_{0.5}Te_{0.5}$ 3 ML NPLs. d. Absorption spectra of $HgSe_xTe_{1-x}$ 3 ML NPLs as a function of the alloy composition and the surface chemistry (in plain NPLs capped with native ligands and in dot, with DDT).*

In **Figure 68a**, the relative positions of VB-E_F, ϕ, and E_g for the five different Se/Te compositions studied are summarized, and the associated band diagrams are plotted (see **Figure 68b**). One notable observation is the evolution of the VB and CB relative positions. The increase in band gap with the selenium composition is primarily associated with a modulation of the VB, while the CB remains relatively flat below x_{Se} = 0.5. This was expected as the VB is predominantly composed of the full p

orbitals of the chalcogens. Therefore, as the chalcogen changes, the VB is likely to shift due to the changing overlap of the orbitals.

Furthermore, two different regimes are observed within this range: for high tellurium compositions, the Fermi level is closer to the VB, while for high selenium contents, it is the opposite. The crossover from a p-type behavior (for tellurium-rich alloys) to a n-type behavior (for selenium-rich alloys) appears to occur around x≈0.25. This finding is consistent with the assumption made based on the FET measurements, which indicated a switch between a p-type behavior for HgTe to a n-type for HgSe.

a.

(eV)	HgSe	$HgSe_{0.75}Te_{0.25}$	$HgSe_{0.5}Te_{0.5}$	$HgSe_{0.25}Te_{0.75}$	HgTe
VB-E_F	1	0.9	0.79	0.51	0.35
φ	3.6	3.99	4.22	4.1	4.02
E_g (DDT capped)	1.4	1.25	1.16	1.15	1.17

b.

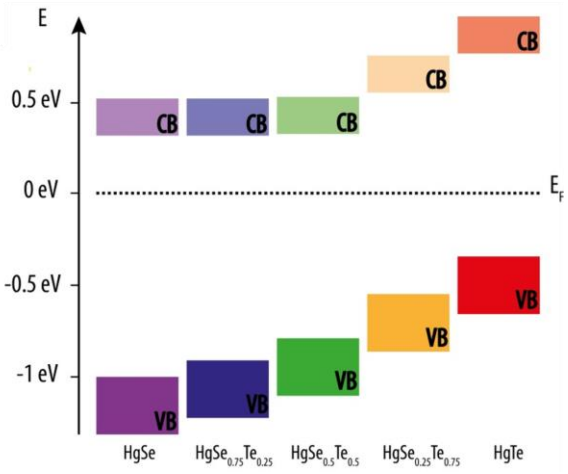

Figure 68: *Band alignment establishment. a. Table summing up the energetical value extracted from valence band and work-function measurements, and optical measurements for all the alloy compositions. b. Plotted band diagram with Fermi level set at 0 eV according to the alloy's composition.*

This observation can be nuanced in comparison to the work conducted by Jagtap *et al*. in 2018. In their study, they unveiled a modulation primarily originating from the CB in a series of HgTe QDs with increasing diameter[207]: larger dots exhibited n-type characteristics, while smaller ones showed p-type behavior. This tuning of the Fermi level position, however, is accompanied by a change in the band gap energy. In our study, given the relatively low modulation of this parameter within the $HgSe_xTe_{1-x}$ NPLs, especially for low content of Se, the relative band alignment can be tuned without altering the optical properties.

To confirm the observed cross-over from static XPS measurements, we decided to validate our results by investigating other properties of the semiconductors. This alternative technique, less commonly used, is based on time-resolved XPS, which allows to examine the carrier dynamics at the semiconductor surface by probing the surface photovoltage (SPV) induced under illumination.

Surface photovoltage as marks of the doping behavior.

In a semiconductor, the behavior of the VB and the CB at the surface is slightly different from the bulk. This behavior is induced by the presence of charged trap states on the surface. To ensure its electroneutrality, a bending of the VB and CB at the vacuum/material interface is observed (see the left panel of **Figure 69a**). The direction of the bending reflects the type of semiconductor involved: a n-type semiconductor will present an upward bending, while a p-type semiconductor will present a downward bending. This behavior spreads over tens of nanometers deep inside the material depending on the material or the doping density. The region where it is observed is called the depletion

layer (or surface charge layer). This scale is larger than the size of nanoplatelets: thus, this bending is happening at the film scale rather than at the NCs scale.

When exposed to light, electron-holes pairs can be created inside the material and either recombine or be separated. In a p-type semiconductor, due to the bending of the bands at the surface, the majority carriers (here holes) move away from it while the minority carriers (here the electrons) get attracted in the depletion layer (see middle panel in **Figure 69a**). Their accumulation creates an additional polarization called surface photovoltage (SPV), which sign is depending on the majority carriers inside the material. SPV slowly increases as the charges accumulate at the surface. This process is self-limited by the migration of minority carriers within the material. Probing the buildup of SPV would unveil the dynamics of minority carriers (see **Figure 69a**).

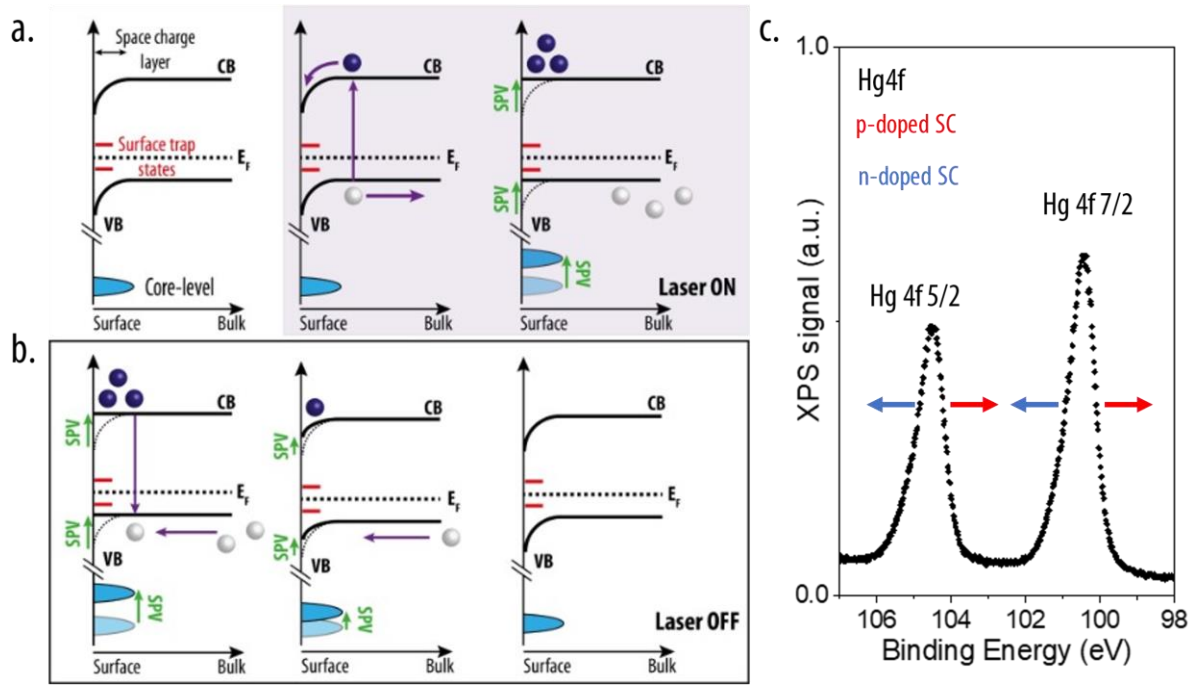

Figure 69: *SPV investigation a. Sketch of the build-in process of SPV in a p-type semiconductor under UV excitation. b. Sketch of the recovery of the band bending in absence of UV excitation c. XPS shows the expected influence of an SPV apparition on Hg4f core-level in both a p- (red) and n-type (blue) semiconductor.*

Under a long enough exposure, the depletion layer can finally be filed by charge carriers up to the point where the bands get flat again (see right panel in **Figure 69a**). At that point, an equilibrium is restored between the newly created electron-hole pairs, the built electric field, and the diffusion of the respective charge carriers toward their respective lower density regions. When the excitation source is removed, no more photogenerated carriers are created, and the majority carriers initially sent to the bulk, flow back to the surface to refill the surface trap states and recombine with the minority carriers, leading to the relaxation of the SPV. This process is limited by the diffusion of the majority charge carriers toward the surface and gets slower and slower as the band bending is recovered. By monitoring this SPV relaxation, the dynamics of the majority carriers can be probed (**Figure 69b**).

As opposite behaviors are expected according to the nature of the majority carriers, the SPV measurement is interesting to: (i) determine the nature of the majority carriers and (ii) determine the diffusion time of both the minority (characteristic time for turn on) and the majority (characteristic

time for turn off) carriers. Time resolved XPS is a good technic to monitor these SPV. In fact, the built SPV induces a rigid shift of all the core-levels of the material. Thus, by focusing on a specific one, the SPV formation and disappearance can be easily monitored (see **Figure 69c**).

We used this technique on the TEMPO beamline at synchrotron SOLEIL. In the used set up, the nanocrystals are excited using a square pulsed laser diode (405 nm, 100 mW, electrically chopped at 10 kHZ with a 40% duty cycle (40 µs On for 60 µs Off)) to form the photocharges. We then decided to probe the Hg4f core-levels by photoemission to monitor the SPV dynamics. The photoelectrons generated by the synchrotron source are collected and analyzed by the hemispherical analyzer equipped with a delay line detector (DLD). The first step requires overlapping both the laser and synchrotron beams on the same spot (they measure 400 µm x 2 mm and 300 µm x 300 µm, respectively). This step is critical to maximize the signal. The alignment is done by acquiring the current mapping of a silicon diode using both the X-ray source and the pulsed laser. The latter is slowly tilted to improve the overlap.

The Hg4f core-levels position evolution is monitored by successive acquisitions every 1 µs (it is worth mentioning that the detector time resolution goes down to 30ns which is far below the acquisition time). Each obtained photoemission spectrum is fitted using two Gaussians and the maximum of the Hg 4f 7/2 peak is plotted as a function of the time (see **Figure 70a**).

The time 0 corresponding to the laser trigger might not be synchronized with the DLD reference. Thanks to the asymmetric duty cycle implemented, the discrimination between On VS Off time is straightforward. Looking at **Figure 70a**, two different regimes can be clearly extracted: the laser ON and the laser OFF, which each corresponds to 40 µs and 60 µs of the temporal window. Consistently with the SPV buildup limited by the diffusion of the minority carriers toward the surface, the shift observed when the laser is turned on is very fast, below the resolution of the measurement (see **Figure 70a**). On the other hand, the relaxation time when the laser is turn off is longer, which is consistent with the lowest mobility of the majority charge carriers (see the red curves in **Figure 70a**).

Having identified the two regimes, we first notice that, according to the alloy composition, a change in the sign of the binding energy shift is observed (see **Figure 70b**). This is consistent with the cross-over observed in static XPS measurements, despite a small deviation as the intermediate composition seems closer to x_{Se}=0.5 rather than the x_{Se}=0.75 value observed in the previous experiments. The binding shift appears to be maximum for the two pure compositions and both have an absolute energy shift of 50 meV. This negative binding energy shift observed for HgTe NPLs here is consistent with the previous work by Livache *et al*.[130].

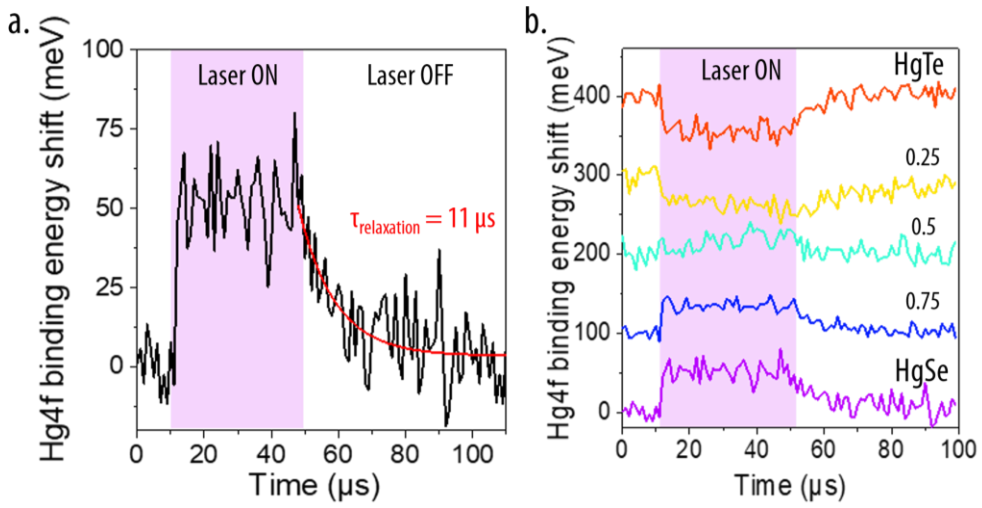

Figure 70: *Unveiling charge carrier dynamics in $HgSe_xTe_{1-x}$ 3ML NPLs. a. TRXPS spectrum of HgSe 3ML NPLs. The Hg4f core-level are shifting toward higher BE when under illumination. The 10 first µs before the rise have been reported at the end of the window to fully visualize the SPV relaxation. The red curve corresponds to the fitting of the SPV relaxation. b. Sum up of the TRXPS as a function of the alloy composition. The curves have been shifted for more clarity.*

The relaxation times are long here (up to several tens of µs). They are much longer than the results reported by Greboval *et al*. for both QDs and NPLs (around 250 ns)[208]. However, it is difficult to get a precise picture of the origin of such deviation due to the limited number of works focusing on this kind of measurements. Nevertheless, a few explanations can be postulated, including deep-trap-states delays as seen in PbS NCs[209–211], delayed recombination due to robustness toward defects as observed in perovskites[212], or different surface chemistry inducing delayed hopping transport.

In conclusion, this measurement method is an additional technique that enables the investigation of charge carrier dynamics inside a film of semiconductor. This method is particularly interesting as it does not require electrodes to collect the charges. It is also a robust method as it limits the impact of the sample aging, which typically results in a broadening of the core-level signal. It is worth mentioning that by synchronizing the laser pulse with a single bunch of electrons, the temporal resolution of this experiment could be improved to the temporal resolution of the electron bunch (tens of picoseconds according to the filling mode of the synchrotron), enabling the probing of even faster processes such as the buildup of the SPV during illumination, for example[213].

11. Conclusion and perspectives.

In this third chapter, we optimized the cation exchange procedure initially used to obtain HgTe 3ML NPLs. To do so, we tried to reduce the speed of the exchange to minimize the surface reorganization that can occur during this process. Thus, we investigated the influence of three different parameters: the solvent, the temperature, and the addition of bulky ligands during the CE. Although TCE has been demonstrated to be the most efficient solvent, conducting the reaction at a lower temperature and in the presence of bulky ligands appears to enhance cation exchange as well.

By implementing this approach to $CdSe_xTe_{1-x}$ 3ML NPLs, we obtained well-defined $HgSe_xTe_{1-x}$ 3ML NPLs with clear optical features and particularly noteworthy is the first recorded emission coming from HgSe NPLs, enabling a wavelength modulation of the emission around 900 nm. This result is interesting as a few emitters have been investigated in this spectral range. Considering the narrow

optical properties of the NPLs, these results hold promise for the development of optoelectronic devices such as LEDs or NIR laser.

For such application, the establishment of the band diagram is crucial to optimize the charge injection and mobility inside the device. We here implemented three different techniques to elucidate the electronic structure of the synthesized NPLs: FET, static XPS, and time-resolved XPS. The obtained results were consistent and exhibited a cross-over between p-type HgTe NPLs to n-type HgSe NPLs. Those findings are interesting regarding the formation of p-n junction based on particles with similar band gap energy.

Despite the favorable emission properties uncovered in this chapter, further efforts are still required before incorporating such material into optoelectronic devices. However, another challenge now needs to be tackled to fulfill this goal. In fact, the emission properties of Hg-based 3ML NPLs have been shown to be not stable in time with especially the apparition of traps like emission that red-shift in the time[57,204]. In the following chapter, I will attempt to overcome this limitation and demonstrate the first Hg-based NPLs LED in the NIR.

Chapter 4: Electroluminescence and directional photoluminescence from 2D HgTe nanoplatelets.

In the previous chapter, we successfully synthesized a new class of material emitting in the NIR range: the 3 ML $HgSe_xTe_{1-x}$ NPLs. This material emerges as a promising candidate for achieving a tunable narrow emission in this spectral range, which has mainly been characterized by broad emissions. However, for further utilization in optoelectronic devices, and especially LEDs, it still faces challenges such as a low stability of optical properties and poor processability. In this final chapter, my focus will be on strengthening and enhancing their photoluminescence over time. Specifically, I will investigate the more mature 3 ML HgTe NPLs, enabling the design of the first LED utilizing Hg-based NPLs as active material. Throughout this project, I synthesized the initial NPLs and developed post-synthetic treatments to stabilize the HgTe PL. Transient absorption measurements were conducted at the Argonne National Laboratory using the setup built by B.T. Diroll. Additionally, I built and characterized the LED devices. The gratings employed for directional emission were developed, fabricated, and characterized by T. Dang and E. Bossavit using the setup built by A. Degiron at Laboratoire MPQ in Paris.

In this context, after providing an introductory section discussing the **state-of-the-art optoelectronic devices incorporating Hg-based material**, I will proceed to a second section focusing on the synthesis of **small HgTe NPLs to improve the processability** of this material. We will also explore **the aging process** of these particles and develop a post-synthetic treatment for **stabilizing the PL** of HgTe based NPLs.

Using this material, I designed the first **LED incorporating Hg-based NPLs** and demonstrated electroluminescence in a third section. Finally, in the two last sections, I will investigate two possibilities to further enhance the quantum efficiency: I will discuss the coupling of HgTe NPLs film with carefully chosen **plasmonic gratings** to achieve **oriented emission** before moving on to the synthesis of a new **HgTe-HgS core-crown heterostructure** to mitigate the degradation of HgTe NPLs.

Publication associated to this project:

- **C. Dabard** *et al*., Electroluminescence and Plasmon-Assisted Directional Photoluminescence from 2D HgTe Nanoplatelets, *submitted*, (2023).

Content

In the visible range, Cd- and Zn-based NPLs remain the most commonly used material for the design of opto-electronics among NPLs. However, due to their wide band gap energy, achieving emission the NIR and SWIR range remains a challenge. On the other hand, as we observed in the previous chapter, narrow bandgap materials such as Hg-based NCs are more suitable for this purpose. This holds true when it comes to designing optoelectronic devices.

1. NIR and SWIR LEDs.

An attractive advantage of working with NIR and SWIR fluorophores relates to their water transparency in this range, justifying the extensive investigation of NIR-SWIR NCs for biological applications such as bioimaging. Moreover, at those wavelengths, Rayleigh scattering is drastically reduced in comparison to the visible range, enabling an enhancement of the imaging depth through fog, tissues or even bones[214,215]. However, the current technologies are limited by their high cost of fabrication. Therefore, their use is generally limited to applications in defense and astronomy. The development of NIR-SWIR colloidal particles, like Hg-based NCs, would position these materials as attractive candidates for expansion into other application domains.

Table 7: *Sum up of the figure-of-merit of various LEDs based on HgTe NCs.*

Particle	*EQE (%)*	*Wavelength (nm)*	*Max radiance ($W.sr^{-1}m^{-2}$)*	*Lifetime (h)*	*Turn on voltage (V)*	*Ref*
HgTe QDs	0.001	1300			10	216
HgTe QDs	0.02	1600	150 $nW.mm^{-2}$		1	217
HgTe QDs	0.25	1400	20	80	0.6	218
HgTe QDs	2.2	1300	3			219
HgTe QDs	0.3	2150	2	10	0.6	220
HgTe QDs	0.7	1250-1600	9	30	0.6	221
HgTe QDs		4000				222

Up to now, Hg-based NIR-SWIR optoelectronic devices have primarily been investigated for their absorption features, including photodetectors[223,224], SWIR-cameras[225], photovoltaics[226] … However, recent studies have unveiled the possibility of using HgE (E : S, Se, Te) NCs as an active layer inside LED stacks[219,220,222] or as an optical gain medium[227,228]. For example, a complete active imaging

device, capable of both light emission and detection, using only HgTe NCs, has recently been developed[219]. A summary of the figure-of-merit of the NIR LEDs currently developed using HgTe NCs is presented in **Table 7**.

A major drawback concerning the electroluminescence (EL) obtained using these materials remains their broad spectral linewidth. This property is intrinsic to the synthesis and purification of the NCs, which leads to inhomogeneous broadening of their optical features. Thanks to their atomically defined syntheses, this is not the case for NPLs. By varying the NPLs' thickness or composition, Zn- and Cd-based NPLs have enabled a high degree of tunability in their optical features and have produced bright LEDs spanning the entire visible range. Considering their lower band gap, Hg-based NPLs LEDs would be of great interest for achieving narrow EL in the NIR-SWIR range, but they have not yet been successful. This is likely due to low stability and degradation of the HgTe NPLs within the device structure. Thus, the production of robust HgTe NPLs films appears crucial before transitioning to EL.

2. HgTe NPLs for device incorporation.

In the previous chapter, we successfully obtained NIR-emitting NPLs consisting of 3 ML $HgSe_xTe_{1-x}$. These particles exhibited the first PL tunability based on NPLs materials in this range. However, we did not discuss about their emission stability over longer timescales, despite the crucial importance of this property for further applications. Additionally, the initial Cd-based NPLs typically had large lateral extensions and so a tendency to aggregate, limiting their processability. To address these issues, this section will focus on investigating a new synthesis method to produce small laterally extended HgTe NPLs facilitating film formation. We will then delve into a detailed examination of the aging effects on the NPLs' PL. Specifically, by monitoring the dynamics of the charge carriers, we aim to understand the underlying mechanism of this process. Finally, we will implement a new strategy to stabilize the HgTe NPLs through a post-synthetic treatment of the NPLs film.

a. Improving the processability.

Considering the vertical geometry of the studied LED, the NPLs used should exhibit the best possible colloidal stability to prevent the formation of inhomogeneous films. As discussed in the previous chapter, Hg-based NPLs are obtained through a CE starting from 3 ML CdTe NPLs. However the initial synthesis of 3 ML CdTe NPLs resulted in the formation of large NPLs[39,41], which is not favorable for achieving suitable colloidal stability. To improve this, one straightforward approach is to reduce the lateral extension of the particle. Additionally, reducing the size of the NPLs should also decrease the probability of including defects, thereby enhancing the PL efficiency. Therefore, we developed a synthesis method that enables the production of small laterally extended NPLs.

In the classical synthesis, $Cd(prop)_2$ and OA are mixed in ODE and degassed in the first step[41]. TOP:Te is then introduced as the tellurium precursor at high temperature under an inert atmosphere to initiate nucleation. At this stage of the reaction, the presence of both long and short carboxylic chains ensures the anisotropic growth of the particle. The use of this precursor reduces the reactivity of the tellurium precursor due to complexation. As a result, the nucleation process is slowed down leading to the formation of a lower number of nuclei and subsequently, the growth of large CdTe NPLs.

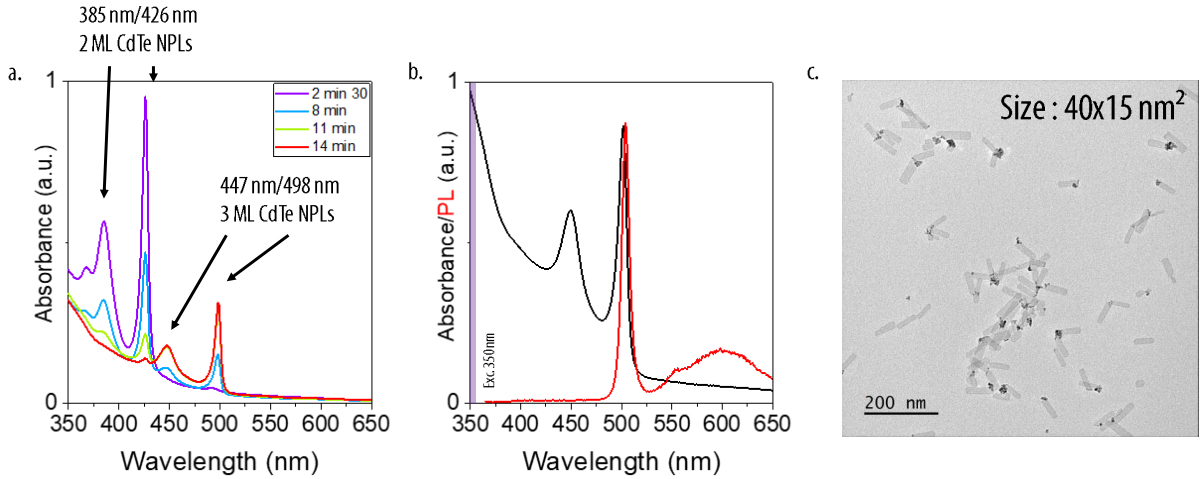

Figure 71: *Small CdTe 3 ML NPLs synthesis. a. Evolution of the absorption spectrum according to the time of annealing during the synthesis. b. Absorption (black) and photoluminescence (red) spectra of the final CdTe NPLs. The excitation has been conducted at 350 nm. c. TEM images of the final particles.*

In order to reduce the size of the final particle, I decided to replicate the synthesis methods used to produce small laterally extended CdSe 4 ML NPLs[29], which I presented in the introduction chapter. In this synthesis, $Cd(myr)_2$ is used instead of $Cd(prop)_2$ and selenium powder is introduced at the very beginning of the reaction. At this point, only long chain carboxylates are present in the solution, leading to the formation of small NCs seeds. $Cd(ac)_2$ is added at a higher temperature to introduce the short carbon chain carboxylate required for their anisotropic growth.

The exact growth mechanism in each case is not precisely known. However, the order of precursor injection determines the final lateral extension. In the classical CdTe 3 ML NPLs synthesis, we can assume that the nuclei are formed during the injection of the TOP:Te. The TOP decomplexation would result in the slow release of tellurium precursors in solution. Therefore, the chalcogen precursors would react primarily on the edges of the existing nuclei rather than creating new ones. In parallel to my work, Anand *et al*. proposed a different strategy based on the use of a more reactive tellurium precursor (tributyl phosphine tellurium, TBP:Te) to enhance the nucleation. They successfully obtain smaller CdTe 3 ML NPLs[229], which agrees with the postulated mechanism. This approach differs from the one used to form the small CdSe 4 ML NPLs. In this reaction, the anisotropic growth is triggered when the number of nuclei has already reached its maximum. Consequently, the final NPLs are expected to have smaller lateral dimensions.

So, considering this second strategy, I introduced cadmium decanoate ($Cd(deca)_2$), OA and ODE into a three-neck flask. After degassing, the temperature is set at 210 °C. At 190 °C, TOP:Te diluted in ODE is swiftly added. At this stage, the color of the solution quickly turns from colorless to orangish. This corresponds to the nucleation of small NCs seeds, similar to the CdSe 4 ML NPLs synthesis. To induce their lateral extension, propionic acid is added when an orange color is reached. The addition of a liquid enables fast homogenization of the solution. The NPLs' growth is monitored by absorption (see **Figure 71a**). Initially, two absorption features are observed at 426 and 385 nm, corresponding to the first and second excitonic peaks of CdTe 2 ML NPLs. After several minutes, these features disappear before recovering, red-shifted at 498 and 447 nm, respectively. The large CdTe 3 ML NPLs typically exhibit a first excitonic peak at 500 nm. The slight blue-shift observed is attributed to additional lateral quantum confinement, which is consistent with the production of smaller NPLs.

During the synthesis, the absorption appears sharper than in the previous 3 ML CdTe synthesis. This can be attributed to the lower diffusion background associated with the formation of smaller NPLs. It can be inferred that this synthetic pathway effectively triggers larger nucleation, resulting in smaller NPLs. At the end of the reaction, the mixture contains a blend of 2D NPLs and of quantum dots. The NPLs are precipitated using a minimal amount of ethanol to remove a maximum amount of the reaction's side products. The final NPLs exhibit a size of 40 x 15 nm² (see **Figure 71c**).

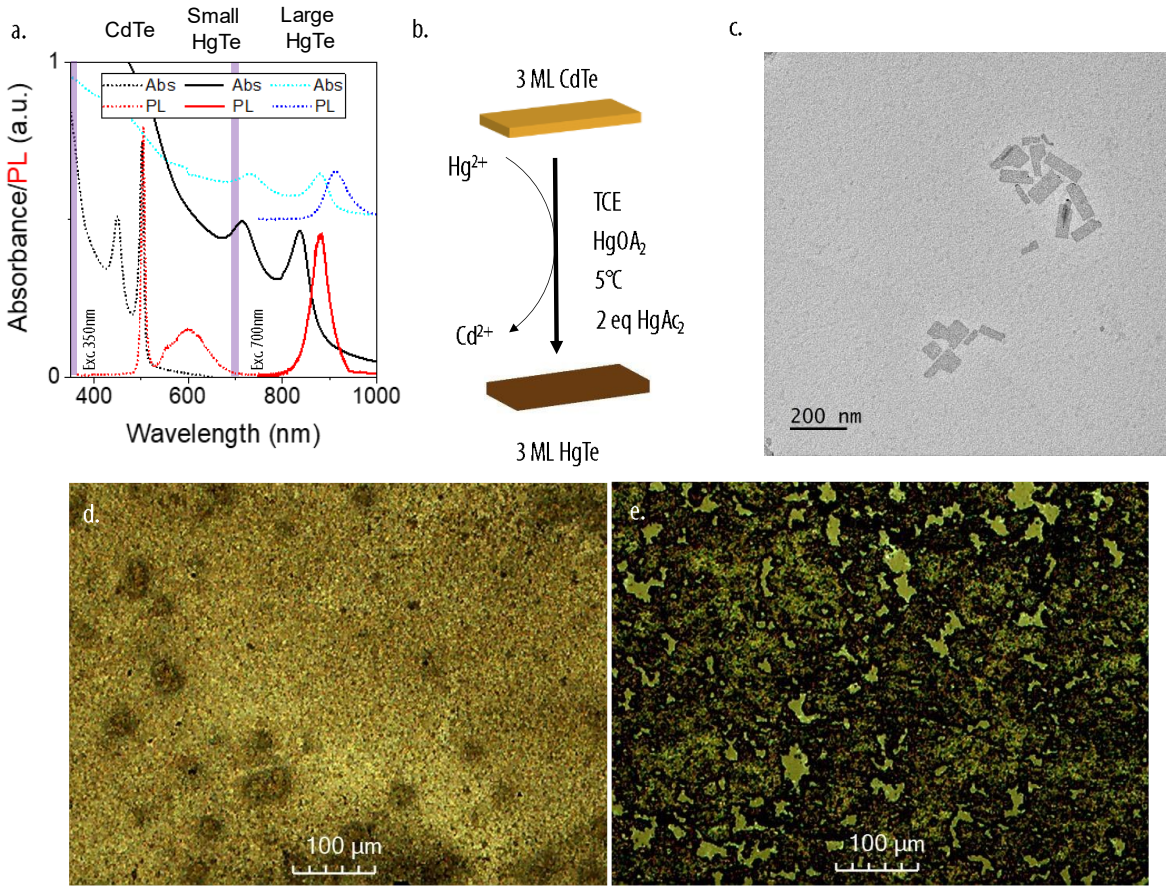

Figure 72: *Small HgTe 3 ML NPLs. a. Absorption (black) and PL (red) spectra before (dashed) and after (plain) cation exchange. The photoluminescence curves have been normalized. On the same graph has been added, shifted, the HgTe 3 ML features for large NPLs ((absorption in light blue and photoluminescence in dark blue). The excitation for the photoluminescence measurements has been set at 350 nm for CdTe 3 ML NPLs and 700 nm for HgTe 3ML NPLs. b. Sum up on the conditions used for the optimized cation exchange. c. TEM pictures of the final HgTe 3 ML NPLs. d-e. Optical microscopic picture of small (d) and large (e) laterally extended HgTe 3 ML NPLs films.*

A CE is then performed on the NPLs using the optimized protocol developed in the previous chapter. The final particles present two excitonic features at 715 and 837 nm (see **Figure 72a-c**). Once again, the small lateral extension induces a lateral quantum confinement, resulting in a blue-shift of the typical features observed for HgTe 3 ML NPLs (usually first and second excitons appear at 880 and 735 nm, indicated as blue-dot curves in **Figure 72a**). This shift is more pronounced compared to the initial CdTe NPLs due to the larger Bohr radius of HgTe (40 nm). When freshly synthesized, these NPLs, exhibit a band edge emission centered at 884 nm (910 nm for large CdTe NPLs).

In terms of colloidal stability, the small NPLs solution is more homogeneous than its larger counterpart, and this remains true over the time. During deposition through spin-coating, the resulting films appear more uniform (see **Figure 72d and e**). In the case of the large laterally extended HgTe

NPLs, aggregates appear on the film, leading to the formation of voids within the film. Therefore, we can conclude that this new synthetic pathway for the formation of CdTe 3 ML NPLs enables the formation of small sized HgTe 3 ML NPLs, facilitating the deposition process of those particles. Now, a second challenge arises: ensuring the PL stability over extended periods.

b. HgTe NPLs aging.

In the previous chapter, we successfully obtained PL from NIR $HgSe_xTe_{1-x}$ 3 ML NPLs. However, we only measured their optical features on a short timescale. Tenney *et al.* have shown that the PL characteristic of HgTe 3 ML NPLs undergo a red-shift over time (see **Figure 73a**)[204]. Specifically, a transition between two emissive regimes has been observed. On a short timescale (up to few hours), a narrow emission corresponding to the recombination at the band edge is observed. After a longer period (hours to days), a broad red-shifted emission is detected. During the transition period, both features are present is measured. This observation led them to conclude that the two emissions have distinct origins. It is worth noting that this behavior is not exclusive to HgTe NPLs as HgSe and $HgSe_xTe_{1-x}$ NPLs are also exhibit similar characteristics[204].

Nature of the emission

To complete the picture, no significant shift is observed in absorption. EDX measurements also reveal a complete exchange of the Cd with Hg. Taken together, these findings led Tenney *et al.* to exclude the possibility of CdTe/HgTe interfaces or $Cd_xHg_{1-x}Te$ alloys formations[230]. Instead, they attributed this PL evolution to the creation of QDs on top of the NPLs[204] (see sketch of **Figure 73a**). The mechanism underlying the appearance of these small dots is still debated but could be attributed either to secondary nucleation of small nuclei adhering to the NPLs' surface or to surface reorganization of the NPLs themself. It is worth mentioning that a similar red-shift has also been observed by Sokolova *et al*. when they doped Hg-based NPLs with Pb cations[231].

This PL aging is accelerated when the NPLs are deposited as a film, which poses challenges for their future use in devices. Therefore, in order to understand and confirm the origin of the PL red-shift, we investigated carrier dynamics through TA spectroscopy using the setup designed by Dr B.T. Diroll at Argonne National Laboratory (Chicago). For this purpose, an 800 nm pulsed laser is split into pump and probe pulses. The pump passes through an optical parametric amplifier to obtain a 700 nm pulsed pump (i.e. a non-resonant excitation). The probe is directed onto a sapphire plate to generate a continuum source in the NIR. The delay between the pump and the probe is controlled using a delay line stage. The final TA mapping is obtained by subtracting the pump-on and pump-off signals. The NPLs are then deposited onto a film and the pump and the probe beams are aligned to overlap on the sample.

The measurements have been conducted on both freshly synthesized NPLs and aged samples. When considering fresh particles, only the bleach of the first excitonic absorption features is observed on the TA map (indicated by the blueish line on **Figure 73b**), and no transfer is detected (see **Figure 73b**). This result is consistent with a recombination at the band edge of the charge carriers inside the particle without further delocalization. In aged NPLs, a bleach is observed within 10 ps at higher wavelengths, i.e. below the band gap (**Figure 73c**). This bleach is slightly delayed compared to the excitonic peak bleach of fresh HgTe NPLs, indicating a transfer from the excitonic state to a second excited state. This transfer is particularly efficient, as shown by the weak bleach signal of the first excitonic transition. This result resembles the transfer towards the CT state observed in CdSe-CdTe-

CdSe NPLs studied in the second chapter. However, the exact nature of this CT state remains unclear as it could be associated with a second material (the QDs suspected by Tenney *et al.*) or to trap states.

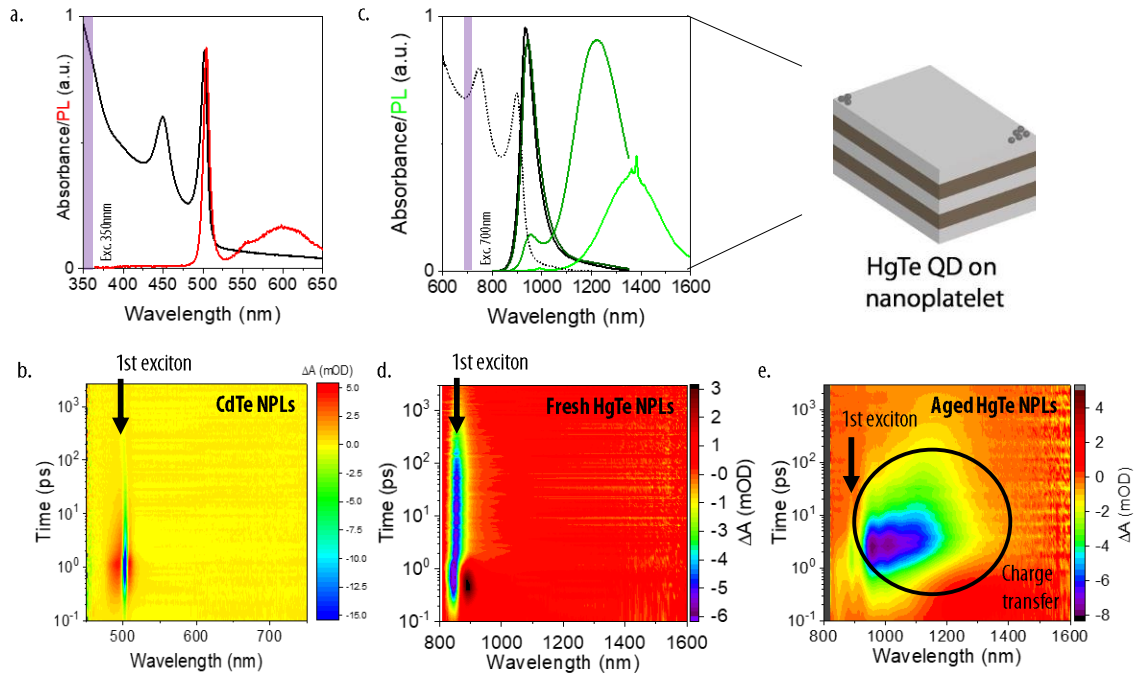

Figure 73: *Aging of HgTe 3 ML NPLs. a. Absorption spectrum (black dot line) and photoluminescence spectra (colored lines, exc. 700 nm) evolution of HgTe 3 ML NPLs according to the time. The sketch on the side is adapted from ref [190] and represents the HgTe 3 ML NPLs after aging and after the formation of small dots on it. b. Transient absorption map of freshly synthesized HgTe 3 ML NPLs (exc. 700 nm) c. Transient absorption map of aged HgTe 3 ML NPLs (exc. 700 nm). d. Absorption (black) and photoluminescence spectra (red, exc. 350 nm) of CdTe 3 ML NPLs. e. Transient absorption map of CdTe 3 ML NPLs (exc. 400 nm).*

To ensure that the CT state is not induced by traps, we compared these TA measurements with those conducted on CdTe 3 ML NPLs (see **Figure 73e**). In these NPLs, a narrow band edge emission at 500 nm is observe alongside a second broad contribution around 600 nm. This second emission is associated with radiative recombination in trap states, revealing their presence in the particle. Thus, a CT between the band edge states and the trap states is anticipated. However, this transfer is not observed (no increases in ΔA is observed is the TA map around 600 nm, **Figure 73e**). This mainly arises from the low oscillator strength of the trap states which results in low absorption. This is consistent with the absence of absorption detected below the band gap, despite the possibility for a photon to be directly created inside the trap states (see dot line in **Figure 73a**). In comparison, a clear transfer is observed in the aged HgTe NPLs. Therefore, we can exclude that the red-shifted emission observed in those particles is coming from a trap state emission, but rather from a non-intrinsic excited state. Taken together, these results support the postulated formation of dot on these NPLs.

Transfer mechanism

This transfer can occur according to different mechanisms: by a direct transfer through intraband cooling (faster than a ps[34]), or by a hopping process in-between neighboring NPLs, or by a mechanism similar to Förster Resonance Energy Transfer (FRET) that occurs at short distances.

- The first possibility can be excluded regarding the measured dynamics that are too slow (few ps) to correspond to a cooling of the electron towards the CT states. For example, in

heterostructure CdSe-CdTe (either NPLs[166] or nanorods[232]), the cooling of the charge carriers occurs at the sub-ps scale. In dot-on-plate heterostructure PbSe-CdSe, the cooling occurs within 600 fs[233]. Therefore, we can conclude that the small dots formed are not merged on the NPLs but are rather attached to them.

- Regarding the second possible mechanism, hopping transport can be characterized by a charge transfer duration of $\tau_{hop} = \frac{eR^2}{6\mu kT}$ where e is the proton charge, R is the hopping distance, μ is the carrier mobility and kT is the thermal energy. The ligands present on the surface of the NPLs are long insulating carbon chains (C_{18}), which induce a spacing of 3 nm between the NPLs and the small QDs leading to a low mobility in the film (10^{-6} $cm^2V^{-1}s^{-1}$ for long carbon chain). Taken together, a characteristic hopping duration of 600 ns is found which is too slow to correspond to the observed transfer.
- On the other hand, resonant energy transfer like FRET can occur between two dipoles separated by a very small distance (typically 1-10 nm)[234]. In this case, the transfer dynamic is dictated by the relaxation time of the donor. Here the relaxation dynamics of the fresh HgTe NPLs occur within a ns (as seen in the first exciton bleach decrease in **Figure 73b**), which is consistent with the observed transfer time (≈ 1 ns, as seen in the charge transfer dynamics in **Figure 73d**). Additionally, the very close distance between these two particles (1-2 nm) suggests a FRET transfer between the NPLs and the small QDs.

We can thus conclude from this study that the red-shift of the PL of HgTe 3 ML NPLs might indeed arise from the creation of small QDs on the surface of the NPLs as postulated Tenney *et al.* Through very efficient FRET, an energy transfer between the two dipoles occurs, completely quenching the emission of the NPLs. Thus, it seems difficult to avoid the shift of the PL induced by the deposition of the NPLs in film form. Nevertheless, we can still take advantages of this second emission. In fact, this emission has been shown to be very efficient and could be used, when stabilized, to obtain highly efficient emitters in the NIR.

c. Stabilizing the PL of HgTe NPLs.

Regarding the aging of the HgTe NPLs, it is necessary to stabilize and increase the PL efficiency before considering their use as active layer in devices. I was inspired by previous works that enhanced the initial PL efficiency of ZB CdSe NPLs[43,82] or of HgTe QDs[219] by capping it with halides. I implemented this procedure to HgTe 3 ML NPLs. However, when the ligand exchange is performed in solution, the particles tend to aggregate, which hampers further processing of the particle. Therefore, I decided to conduct the ligand exchange directly on the deposited film of HgTe NPLs.

Optimization of the halide treatment

The films are first deposited by spin coating. Since the NPLs own small lateral extensions, the resulting films are relatively homogeneous. To induce the ligand exchange, the films are swiftly immersed in an exchange solution containing $HgBr_2$ (5 – 50 mM) dissolved in IPA or MeOH (see **Figure 74a**). To prevent delamination (i.e. the films peeling off due to volume reduction), the solution should not be too concentrated. Next, the films are washed in the solvent used to dissolve the mercury salt. In a second step, the films are immersed in a solution containing butylamine (10 % in volume in MeOH or IPA). This second step owns multiple purposes: firstly, it helps to remove any remaining mercury salts that may have recrystallized on the film during the halide exchange. Secondly, it introduces amine ligands to mimic the surface chemistry that will be obtained in an LED stack as closely as possible.

Additionally, it has been demonstrated that amines can interact with halides present on the NPLs' surface through hydrogen bounds, co-passivating it[43,235].

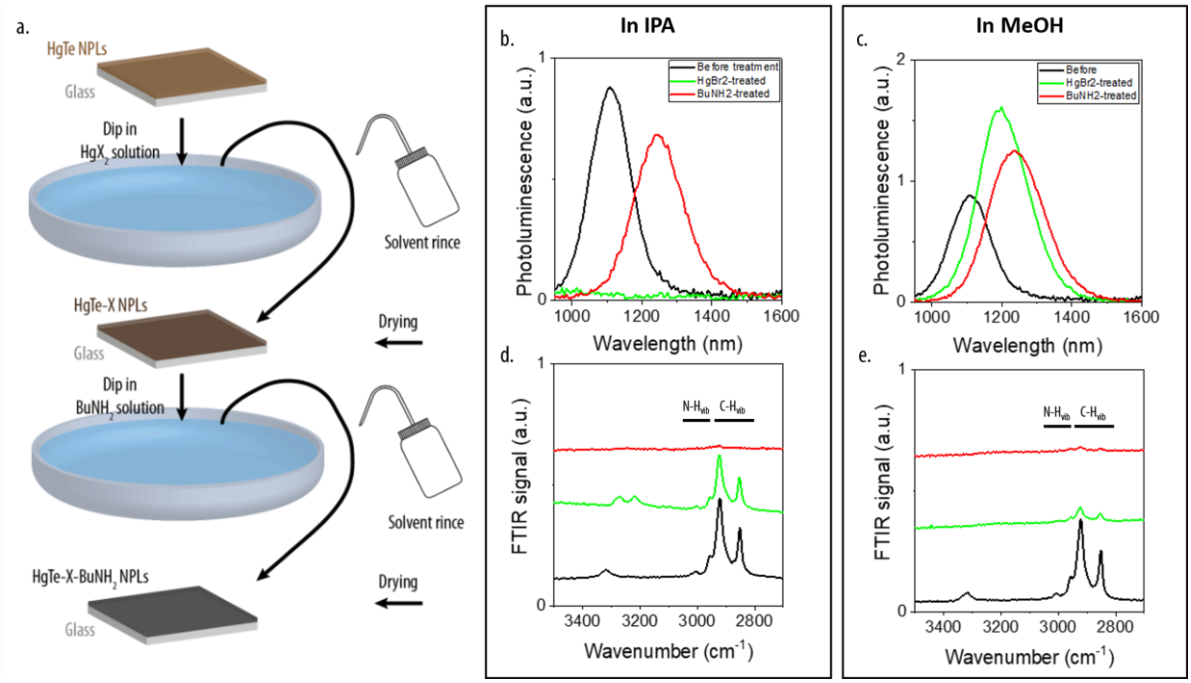

Figure 74: *Ligand exchange from native to halogenide co-stabilized by amine surface chemistry. a. Sketch of the steps realized during the ligand exchange procedure. b-c. Photoluminescence spectra of the films during the different steps when the exchange is conducted resp. in isopropanol and in methanol. All the photoluminescence spectra have been measured using a 405 nm excitation. d-e. FTIR spectra of the film during the different steps when the exchange is conducted resp. in isopropanol and in methanol.*

At this end of the treatment, the PL of the particle is red-shifted compared to the initial PL. This observation is consistent with both a partial delocalization of the wavefunction over the halides and the release of out-of-plane constrains imposed by the native ligands. The latter effect results in a slight increase in the particle's thickness of the particle and a decrease in the quantum confinement. This finding aligns with previous studies conducted on CdSe NPLs[43,82]

This ligand exchange can be monitored through FTIR analysis performed directly on a film (see **Figure 74d-e**). For this purpose, the same deposition followed by exchange is carried out on a silica substrate. The initial film exhibits two strong signals between 2800 and 3000 cm^{-1} corresponding to the C-H vibration. The small feature around 3000 cm^{-1} and the one at 3280 cm^{-1} are the characteristic of an amine. In our case, they correspond to oleylamine originating from the CE procedure and that remained attached to the surface during the washing steps. After the initial treatment using the mercury halide salts, these signals are reduced. This effect is more pronounced when MeOh is used (see **Figure 74e**). Due to its higher polarity, MeOH strips more ligands from the surface compared to IPA. Following immersion in the $BuNH_2$ solution, nearly no C-H vibration is observed, which is consistent with the transition from a C_{18} toward a C_4 carbon chain ligand.

Other halides, including chloride and iodide, have been tested. While the former tends to destroy the HgTe particles, the latter induces a very slow ligand exchange, likely due to the slower diffusion of iodide through the HgTe film. Overall, the exchange using MeOH as the solvent and $HgBr_2$ as the halide source leads to the most enhanced PL, and therefore, we chose to continue with these conditions for subsequent experiments.

Photostability of the treated films

The photoluminescence of the films obtained after ligand exchange was compared to that of untreated films. Particularly, under a constant illumination by a laser diode (405 nm), the PL signal of the untreated NPLs films tends to decrease drastically after few seconds. In comparison, the PL signal of the treated film only exhibit a slow decrease over time. This behavior can be attributed to a desorption of the surface ligands induced by the energy from the UV light. This process results in an unpassivated surface, opening up non-radiative relaxation pathway on the particle's surface.

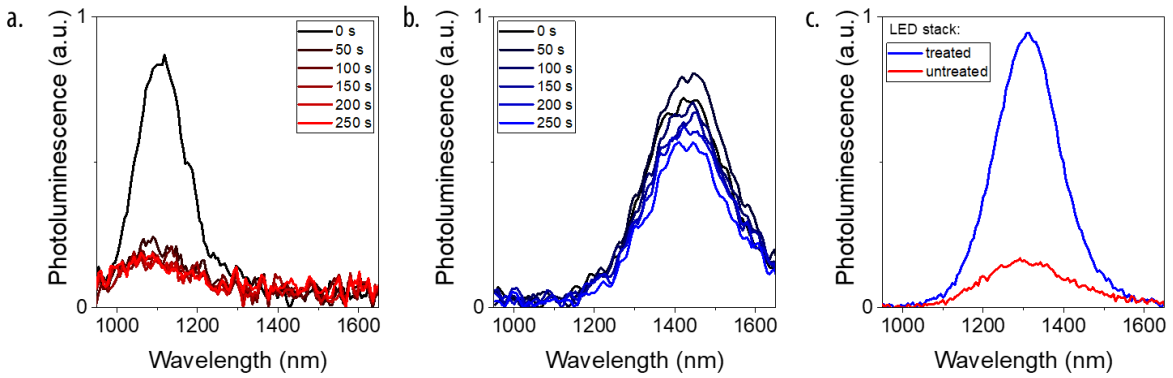

Figure 75: *PL stability of the HgTe 3 ML films. a-b. Evolution of the PL for respectively untreated and treated HgTe 3 ML NPLs films under constant enlightening for 250 s. c. PL spectra of a classical LED stack using a treated (blue) (resp. an untreated (red)) active layer of HgTe 3 ML NPLs. All the photoluminescence spectra have been measured using a 405 nm excitation.*

After investigating the charge transfer occurring within the NPLs film through TA measurement, we have developed a post-deposition treatment based on ligand exchange, from native to halide ligands. This process has been optimized and now allows for the enhancement and strengthening of PL. We will now proceed with the incorporate of these treated films as active layers in devices.

3. Incorporation inside an LED.

In the first two sections of this chapter, we focused on stabilizing and the enhancing the optical properties of HgTe NPLs. By successfully engineering HgTe NPLs films with improved PL robustness, we can now consider their integration into a diode stack for electroluminescence.

a. NIR LED structure.

The diode stack we are considering is similar to the one developed by Dai *et al.*[140] which we previously used to achieve bicolor electroluminescence in the second chapter. In the introductory chapter, we investigated the band alignment of the HgTe 3 ML NPLs (CB = -3.7 eV, W_F = -4 eV, VB = -4.8 eV; see electronic structure **Figure 76a**, obtained by photoemission measurements). In comparison with the core-crown-crown-based LEDs developed in the second chapter, the VB of HgTe NPLs is shifted toward higher energies. Therefore, we decided to use a single layer of PEDOT:PSS for hole injection, instead of the PEDOT: PSS-pTPD-Pvk stack. Consequently, the following LED stack was constructed: a transparent ITO electrode as the anode (W_F = -4.8 eV vs vacuum), PEDOT: PSS as hole injection and electron blocking layer (HOMO = -5 eV, LUMO = -2.2 eV vs vacuum), ZnO NPs as electron injection and hole blocking layer (VB = -7.5 eV, W_F = -3.8 eV vs vacuum) and, finally, silver as the metallic cathode (W_F = -4.2 eV vs vacuum). The band diagram of the complete stack is presented in **Figure 76a-**

b. To determine the precise thickness of each layer, profilometry measurements were conducted in between each layer deposition, and the results are shown in **Figure 76b**.

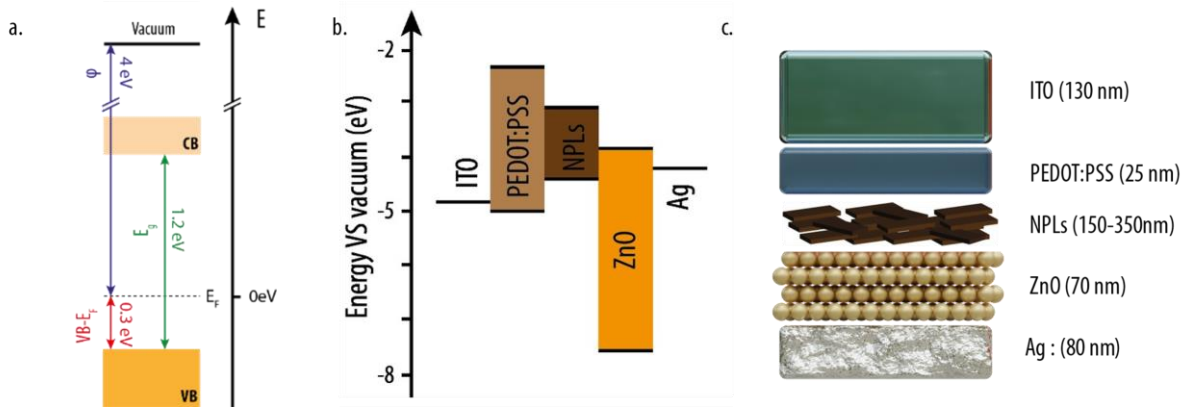

Figure 76: *HgTe 3 ML NPLs LED stack. a. 3 ML HgTe NPLs band alignment established using XPS. b.Band alignment of the LED stack calculated for an untreated HgTe 3 ML NPLs film. b. Sketch of the LED stack associated with the thickness of the different layers.*

For the deposition of the NPLs film, the concentration of the NPLs solution needs to be low enough to create films that are not too thick, thus avoiding delamination during the ligand exchange process. As mentioned earlier, this ligand exchange, which involves replacing the native long carbon chains toward short halides, causes a significant contraction of the film volume. This shrinkage leads to the formation of cracks on the NPLs film. To mitigate the leakage resulting from these cracks, three successive depositions of HgTe NPLs were performed, each followed by a $HgBr_2$ treatment, to fill the voids created during the ligand exchange. As a result, the NPLs film reaches an approximative thickness of 300 nm. However, this value is averaged due to the roughness of the NPLs layer. The high roughness measured is primarily attributed to the partial packing of the NPLs but could also arise from the recrystallisation of mercury salts following the cation exchange.

b. Electroluminescence from HgTe NPLs.

The exact same stack is built without performing the post-deposition treatment of the NPLs. Prior to applying bias, a comparison of the PL is conducted, revealing lower emission in the case of the untreated LED film (see **Figure 75c**). Subsequently, a 5V bias was applied on the two LED stacks (see the black curves in **Figure 77a-b**). No EL was observed in the untreated stack, whereas the second stack exhibits an EL signal centered at 1380 nm. The two stacks are perfectly identical except for the halide treatment. Therefore, we can conclude that the EL detected is coming only from the HgTe NPLs, and that a halide treatment is required to observe EL from those particles. A bias threshold of 0.9 V is measured in this structure (see **Figure 77c**), which is consistent with the EL maximum in emission. Thus, we can conclude that, despite the difference in surface chemistry between the HgTe NPLs band alignment established in the introduction chapter (capped with EDT) and the one used here (capped with bromide:amine), the employed stack seems to suit the band alignment of the halide-capped HgTe NPLs.

Nevertheless, the performance of this device remains limited. Above 5 V, the EL becomes unstable and tends to degrade. Over several cycles, the efficiency also rapidly decreases. This behavior is well-known on HgTe NCs and is typically attributed to from a sintering caused by heat generation[219]. The measured EQE is also very low (10^{-2}%). This is mainly due to the significant decrease in PL efficiency

within the LED stack during the successive depositions. Despite its lower performances compared to the state-of-the-art NIR LEDs, this result remains encouraging as it represents the first EL device incorporating Hg-based NPLs, paving the way for the development of Hg-based NPLs as active layers for EL.

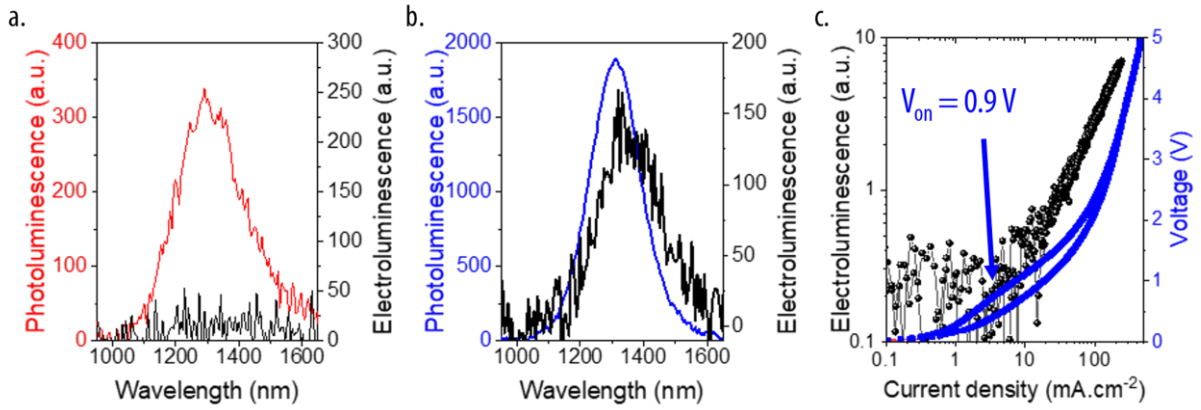

Figure 77: *Electroluminescence comparison between treated and untreated LED. a. Photoluminescence (red, exc. 405 nm, and electroluminescence (black) of the LED stack based on untreated HgTe 3 ML NPLs. b. Photoluminescence (blue, exc. 405 nm)) and electroluminescence (black) of the LED stack based on treated HgTe 3 ML NPLs. c. Evolution of the electroluminescence (black) and imposed bias (blue) according to the current density going through the stack.*

4. PL enhancement through plasmonic gratings.

Beyond the modest performance obtained in the HgTe-NPLs-based LED, researchers are currently facing a new challenge in improving the LED efficiency: surpassing the 20 % limit imposed by the device vertical geometry. This limit has already been reached in the visible range[75]. In this context, the development of films that exhibit oriented emission is emerging as a promising approach to efficiently extract light from an LED stack. Several strategies have been developed, including the management of self-assembled NPLs films[148,236] or the use of metallic nanostructures[237–239]. The former procedure has already been implemented to improve the performance of LEDs based on CdSe@$Cd_{0.25}Zn_{0.75}S$ core-shell NPLs, resulting in a 70 % enhancement in EQE when comparing random and oriented NPLs-based LEDs[147]. However, methods for obtaining oriented films of NPLs are not yet versatile and have mainly been implemented on Cd-based NPLs.

Metallic nanostructures have been utilized to enhance the light-matter interactions in a NCs films[237,240]. Placing an emitter in the vicinity of such resonators allows for modification of its emission intensity, lifetime, directivity and spectral shape[241]. Consequently, there is growing interest in employing these nanostructures as tools for manipulating electromagnetic radiation at the nanoscale. Various structures have been investigated including nano-antennas[239,242], nanobumps[228], linear[237,238], and concentric gratings[239]. In this context, we designed a grating that enables oriented emission in a HgTe NPLs film. For this project, the design and fabrication of the gratings were conducted by Tung Huu Dang and Erwan Bossavit, while I performed the synthesis and deposition of the NPLs film. The measurements were carried out using Dr. Degiron's setup at Laboratoire MPQ (Paris Cité).

a. Design of the resonator.

We first decided to develop a metallic grating made of gold on top of an Si/SiO_2 substrate (see **Figure 78a and b**). Considering the thermal sensitivity of the HgTe 3 ML NPLs, the design of nanostructure needs to avoid heating the NCs film. Therefore, we decided to pattern the grating before

depositing the NPLs film. In this configuration, a surface plasmon can be generated in the transverse magnetic (TM) polarization through Bragg scattering. The oriented emission is expected to occur through the coupling of NPLs with the surface plasmon's dispersion induced by the metallic grating[243,244]. Hence, we can express the following equation for the resonance inside the nanostructure:

$$k_0 \sin(\theta) = \frac{2\pi n_{eff}}{\lambda_{em}} \pm \frac{m2\pi}{\Lambda}$$

where k_0 is the incident wavevector, θ is the incident angle defined with respect to the normal, n_{eff} is the effective refraction index, λ_{em} is the PL wavelength, m is the diffraction order, and Λ is the period of the grating (see **Figure 78c**)[239]. In our case, we aim to achieve directional emission normal to the substrate (θ=0, m=1) to maximize the light extraction. Thus, the equation can be simplified as:

$$\Lambda = \frac{\lambda_{em}}{n_{eff}}$$

We assume a refractive index of 2 (for HgTe without ligands) in the case of HgTe[238], and a PL wavelength of 1.2 µm is considered to match the NPLs PL. Consequently, we determine an optimized grating with a period of 600 nm. Due to plasmon leakage and the presence of ligands, the effective refractive index is usually smaller than expected[238]. To compensate for this, we design a set of five resonators with varying periods between 600 and 1000 nm to account for errors in film thickness or inaccuracies in the tabulated parameters. The final resonator consists of a Si substrate covered by a 400 nm SiO_2 layer, topped with 300 nm wide gold digits periodically spaced (see **Figure 78a-d**).

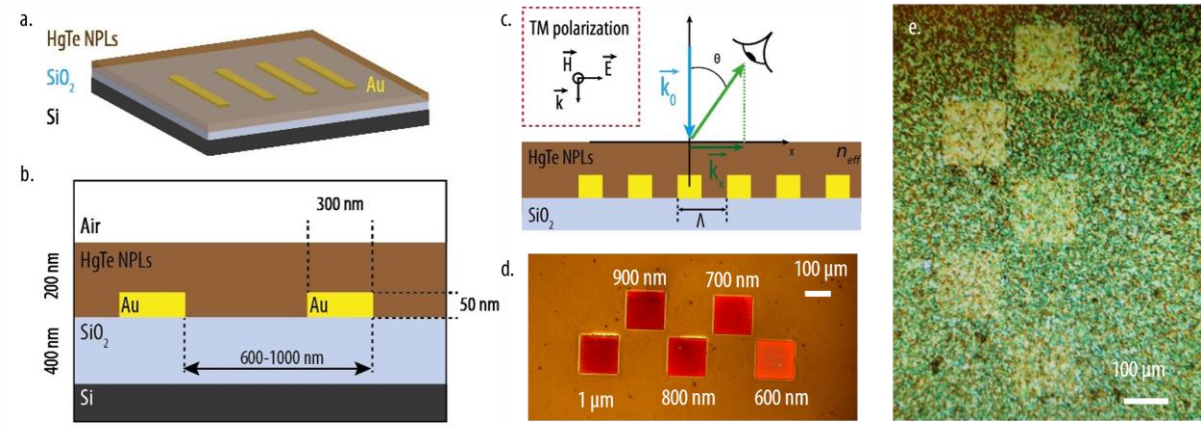

Figure 78: *Design of the resonator. a-b. Sketch of the top (resp. side) view of the grating resonator. c. Sketch of the oriented emission. d-e. Optical microscope picture of the five different gratings patterned before (d) and after (e) the HgTe NPLs deposition and treatment.*

Finally, the film of NPLs is deposited on top of the grating using spin-coating. Considering the photosensitivity of the HgTe NPLs, we decided to stabilize the PL by employing the post synthetic treatment developed in the previous sections. During the $HgBr_2$ treatment process, the film becomes very fragile, especially in the area of the grating. Therefore, we adopt a smoother rinsing step to prevent the peeling off of the NPL film. This careful washing, coupled with the limited colloidal stability of the particles, may account for the appearance of whitish spots on the surface, which likely

correspond to NPLs aggregates or recrystallization of mercury salts (see the white spots on the pictures in **Figure 78e**).

b. Photoluminescence enhancement.

The NC film on top of the grating is then excited at 633 nm (as shown in the colored picture **Figure 79a**). When comparing the different visible areas, the PL obtained on top of the grating is surprisingly enhanced by 60 % compared to the PL measured outside the grating (see **Figure 79a and b**).

The origin of this PL enhancement is multifaceted. First, due to the gold acting as mirror, the distance travelled by the light is doubled. Since the material has a low absorption coefficient[237], the 200 nm thick film does not fully absorb the exciting light. Therefore, by increasing the optical path inside the film, its absorption at 633 nm increases, leading to an enhanced emission (indicated by the blue arrow in **Figure 79c**). Additionally, the PL signal is also enhanced due to the difference in optical index between gold and silica, resulting in an increased amount of PL escaping from the film (as shown by the red arrow in **Figure 79c**). Both two effects are proportional to the gold filling factor.

Second, as mentioned earlier in this chapter, the grating period has been chosen to form a plasmon that would resonate with an emission at 1200 nm. The formation of such plasmon enhances the electric field in the vicinity of the metallic grating. The coupling between the NCs and the formed plasmon will further enhances their emission (as depicted in the sketch of enhanced electric field in **Figure 79c**).

The largest enhancement is observed for an 800 nm grating in the series of gratings studied ranging from 600 – 1000 nm periods. This slight deviation from the predicted plasmon resonant is most likely induced by differences in the effective refractive index, which can vary slightly from the one considered in the calculation, especially considering the presence of ligands in the film.

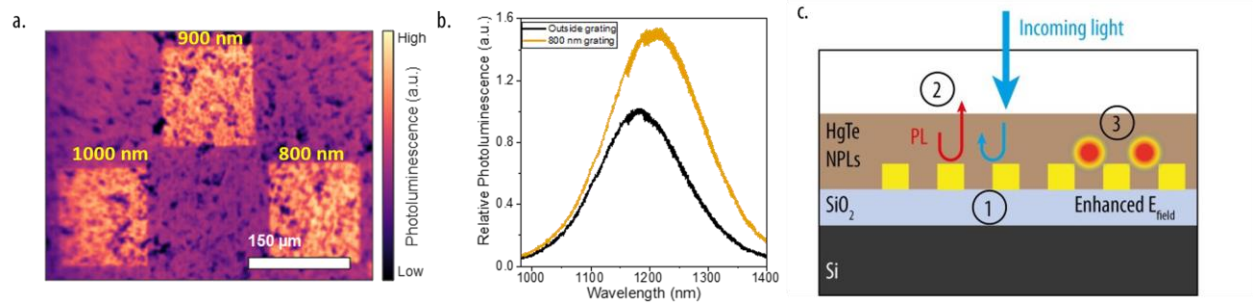

Figure 79: *PL enhancement induced by the metallic grating. a. Colored picture of the PL from NPLs film deposited over three gratings with different periods. b. Relative PL measured outside the gratings (black curve) and on the 800 nm period grating (orange curve), the two curves have been normalized to the PL outside the grating. c. Sketch of the different mechanism responsible for the PL enhancement.*

c. Oriented emission.

Beyond this PL enhancement, these types of gratings are interesting for achieving directional PL in a NC film because plasmon modes exhibit strong dispersion[238,239,243,244]. Therefore, we conducted angle-resolved PL measurements to investigate the dispersion map. We excited the film above the grating normally and measured the incoming PL from the NPLs film based on the incident angle θ defined with respect to the normal. By imaging the back focal plane of the microscope, we obtained access to the angular repartition of the PL. The resulting dispersion map is defined as the PL intensity

plotted against its energy (in eV) and the normalized x component of the incoming wavevector $k_x = \frac{2\pi}{\lambda}\sin(\theta)$.

First, we measured the dispersion map in an area without any imprinted gratings. As expected, the dispersion map showed isotropic emission (as seen in the horizontal continuum in **Figure 80a**). This was expected since the NPLs are randomly organized in the film.

Next, we measured the PL in the imprinted area and acquired the corresponding dispersion map in TM polarization, the one expected to exhibit oriented emission (see **Figure 80b**)[238,243]. The received PL included two contributions. The first contribution, similar to **Figure 80a**, was non-dispersive. This could arise from the NPLs located outside the grating but still excited by the incoming light (the patterned squares are 150 x 150 µm² and the excitation spot measure has a 250 µm diameter). It could also come from NPLs that are not coupled to the grating due to the film's large thickness.

The second contribution appeared as two tilted lines on top of the isotropic signal. These contributions are highlighted by the two solid white lines in **Figure 80b**. They correspond to the coupling of the NPLs with the dispersion of the surface plasmon through the metallic grating. Based on this dispersion map, we can plot the PL spectra according to the measurements. For example, in **Figure 80c**, three slices at 0°, 17° and 37° are plotted, and the corresponding positions of each slice are indicated by vertical-colored dashed lines in **Figure 80b**. Under normal incidence, we observed an enhancement of the PL. Interestingly, the position of this enhancement and thus the emission direction can be adjusted by varying parameters such as the thickness of the NCs film and the grating period[237–239]. This enables control over the direction of enhancement.

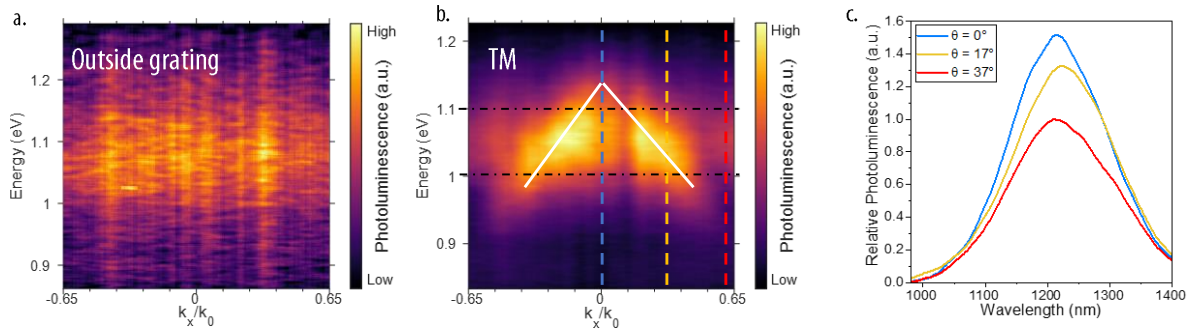

Figure 80: *Oriented emission induced by metallic grating. a. Colored picture of the PL from NPLs film deposited over three gratings with different periods. b. Relative PL measured outside the gratings (black curve) and on the 800 nm period grating (orange curve), the two curves have been normalized to the PL outside the grating. c. Sketch of the surface representing the link between the measurement angle ϑ and the k_x wavevector. d. Dispersive map (PL according to the energy and the incident angle of observation) outside the grating*

Using this metallic nanostructure, we have demonstrated oriented PL whose direction can be tuned according to the grating period. This result is particularly interesting as it can be coupled with to a modulation of the spectral shape[237]. The next step would be to incorporate this type of grating into an LED stack to enhance electroluminescence extraction.

5. Heterostructure to stabilize the photoluminescence.

Despite all the efforts that have been conducted here to stabilize the PL of HgTe NPLs, the deposition of HgTe NPLs on a film still leads to broad emission, losing the advantages of the NPLs narrow emission. Another approach to strengthen and enhance the PL while preserving their optical

properties would be to create core-shell heterostructures utilizing materials such as CdS for the shell. However, the thermal instability of HgTe NPLs complicates this process. Nonetheless, Tenney *et al.* observed that the degradation of the NPLs primarily occurred at the edges of the particles rather than at the center[204]. This finding aligns with previous studies conducted by Lim *et al.* on ZB CdSe NPLs[205]. Therefore, growing a crown around HgTe could potentially stabilize the PL.

To achieve the growth of a crown around the core material, heating is required to activate the reactivity of the precursors and facilitates their migration toward the lateral facets. Thus, I propose creating the crown before conducting of the CE to stabilize the HgTe core.

a. A CdTe-CdS core crown NPLs.

As mentioned in the previous chapters, the formation of a core-crown NPLs structure could also enhance the PL efficiency by carefully engineering the band alignment between the core and the crown. This approach offers the potential for increasing the QY, while preventing degradation at the edges and preserving the integrity of the HgTe core.

Therefore, we considered synthesizing a CdTe-CdS core-crown structure. In the second chapter, we discussed the challenges associated with forming CdTe-CdS 4 ML heterostructures due to the significant lattice mismatch between CdS and CdTe. In this case, lateral extension would occur on CdTe 3 ML NPLs. The thinner thickness is expected to facilitate the adhesion of CdS on the lateral facets by releasing constrains. However, these particles are also more fragile, and some CdTe is expected to dissolve prior to the growth of the external crown, releasing cadmium and tellurium precursors into the solution. This can be beneficial for the synthesis, enabling a smooth composition transition from the CdTe core to the CdS external crown. To limit the final lateral extension of the particle, the cores of CdTe are taken as small as possible (40 x 15 nm², see **Figure 81b**). Subsequently, the growth of the external crown is carried out under conditions similar to classical lateral extension.

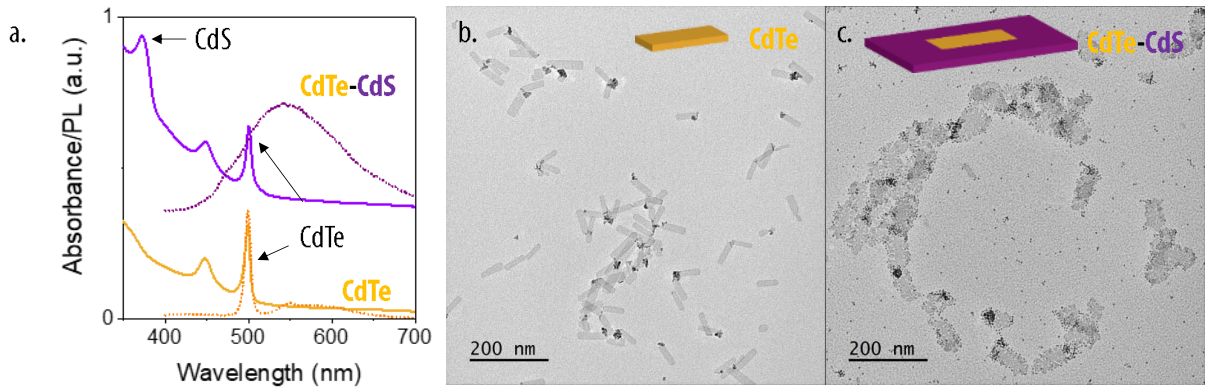

Figure 81: *CdTe-CdS 3 ML core-crown: a. Absorption (plain lines) and photoluminescence (dashed lines, exc. 350 nm) of the CdTe core before the TOP:S injection (orangish) and the CdTe-CdS core-crown (purple). The absorption features of CdS and CdTe are pointed by the arrows. b-c. TEM pictures of respectively the core-only NPLs and the CdTe-CdS heterostructure.*

To prevent the degradation of the core, the CdTe NPLs are first dispersed and degassed in ODE for 2 h at 90°C. In parallel, a growth mixture of oleic acid and cadmium acetate in ODE is also degassed using the same conditions. After this first step, the growth mixture is added to the core flask and heated at 170 °C. The temperature is critical here, as a to high temperature would lead to the complete dissolution of the CdTe core, while a to low temperature would prevent the growth of CdS around the CdTe core. The core-only NPLs are then annealed for 15 min. At this stage, the solution turns dark,

indicating partial redissolution of CdTe within the mixture. The absorption spectrum taken at this stage still exhibits features of CdTe 3 ML NPLs (first excitonic peak at 499 nm) and a bright green emission (at 501 nm) is observed in the balloon (see yellow curves in **Figure 81a**).

To attach a crown of CdS around the NPLs, TOP:S (0.1 M in ODE) is slowly added to the mixture to trigger the growth of the external CdS crown. The presence of a small amount of tellurium within the mixture, due to the annealing step, facilitates the addition of the CdS crown. In fact, the formation of an alloy smoothes the lattice mismatch between CdS and CdTe, which improves the growth[163]. At the end of the reaction, the absorption features exhibit the excitonic features of the CdTe at respectively 450 and 500 nm, and of the CdS at 374 nm. This last value corresponds to CdS 3 ML NPLs[37]. Additionally, TEM pictures of the final particle show an increase in the lateral extension of the particles (see **Figure 81c**), indicating the formation of an external crown of CdS around the core of CdTe.

These particles present a broad, complex emission that may contained broad band edge emission for CdS_xTe_{1-x} alloys and/or type II CdTe/CdS interfacial recombination[162,163] (see purple PL spectrum in **Figure 81a**). However, since the external crown is made of CdS, the core CdTe is expected to be protected during and after the CE. To prove this, I performed this exchange process on these particles and compared it to the same CE on core-only particles.

b. Stabilization of the HgTe band-edge emission.

The optimized protocol was then used to conduct the cation exchange. **Figure 82** summarizes the evolution of the PL during the exchange. In the case of the CdTe core, a similar behavior is observed, with the emergence of the band edge emission of HgTe 3 ML NPLs after a short period of time (see **Figure 82a**). The evolution is slightly different in the case of the CdTe-CdS heterostructure. Similar to the exchange in core-only particles, the band edge emission of HgTe appears shortly after the start of the cation exchange. However, the exchange seems to be slower, and an additional feature is observed at shorter wavelengths. This feature could be attributed to a partial exchange within the CdS external crown, resulting in the formation of HgS regions. This process is expected to be slower than the exchange of the core material due to the smaller lattice of the CdS[39], but the formation of CdS_xTe_{1-x} alloys might facilitate the diffusion of the Hg cation within the lattice. This alloy formation could also be responsible for the broad features observed at shorter wavelengths.

The PL of the exchanged core particles slightly shifts on a short timescale (see **Figure 82a**). Interestingly, this is not the case for the PL of the core-crown particles (see **Figure 82b**). This observation remains consistent on a longer timescale as well (see **Figure 82c**). After three days, the band edge emission of the HgTe core particles disappears, and instead, a broad redshifted emission in the NIR region is observed (see solid orange curves in **Figure 82c**). This behavior aligns with the degradation of the optical properties observed so far. On the other hand, the emission of the core-crown exchanged particles does not shift even after three days, with only a small increase in the background signal observed in the NIR (see solid purple curves in **Figure 82c**). Even after ten days, the emission features of the HgTe band-edge are still present. However, the PL intensity remains significantly decreased (see dashed line in **Figure 82c**). Overall, the growth of a CdS crown appears to preserve the band-edge emission of the HgTe core.

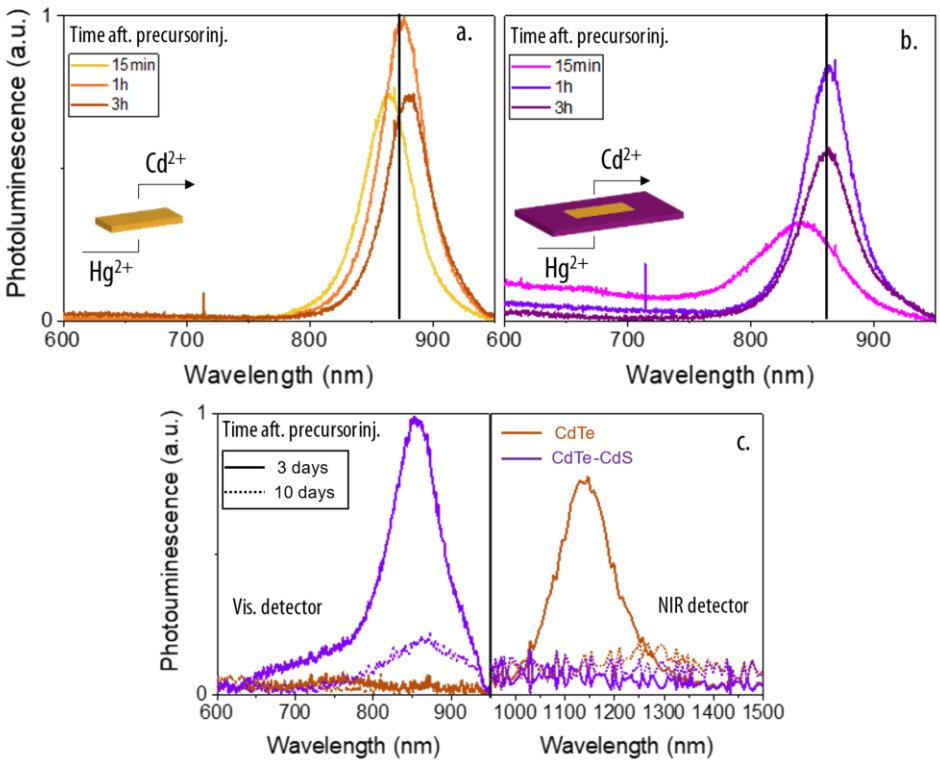

Figure 82: *Cation exchange on CdTe-CdS 3 ML NPLs. a-b. Photoluminescence spectra according to the time during the cation exchange performed on CdTe 3 ML cores (a) and on CdTe-CdS 3 ML NPLs (b). The dashed vertical line underlines the position of the maximum emission peak after 1h. c. Photoluminescence spectra of the two exchanged particles in solution after 3 (plain) and 10 (dashed) days. The left panel measurements have been obtained using a Flame Visible spectrometer while the right one has been measured using a Flame NIR spectrometer. All the measurements have been done with a 405 nm excitation.*

Further investigations are required here to fully understand what is truly stabilizing the band-edge emission of the HgTe. However, based on previous works conducted by Lim *et al.* on edge degradation in CdSe NPLs, by Tenney *et al.* on the formation of dots during CE, and by myself on the CE on alloyed NPLs, a preliminary mechanism can be proposed. The formation of the alloyed $Cd_xHg_{1-x}S$ crown helps limit dissolution and surface reorganization at the edges during and after the CE, thus reducing the formation of dots on top of the HgTe core. This procedure currently has limitations in term of overall yield but can be improved to enable the utilization of these particles in optoelectronic devices. Additionally, the heterostructure is not yet fully optimized but provides a pathway to further improvements in stabilizing the optical features of HgTe NPLs.

6. Conclusion and perspectives.

Throughout this final chapter, we have addressed the challenge of designing a LED based on HgTe NPLs. We optimized the processability of the particle by developing a new synthesis method to obtain smaller laterally extended NPLs. After investigating the aging mechanism within the NPLs using transient absorption spectroscopy, we developed a treatment method to stabilize the emission of the fragile HgTe NPLs. This allowed us to achieve stable photoluminescence from an HgTe film in the near-infrared range and integrate it into an LED. As a result, we have reported, for the first time, electroluminescence from Hg-based NPLs.

However, the quantum efficiency still remains problematic compared to the most efficient emitters in this range. Additionally, the narrow emission benefits of the NPLs are compromised due to the significantly increase in the full-width-at-half-maximum. Consequently, we explored two different

possibilities to enhance electroluminescence. Firstly, by designing a metallic nanostructure, we successfully enhanced the photoluminescence signal and achieved directional emission from the NPLs film. Secondly, we developed a CdTe-CdS heterostructure to mitigate lateral degradation of the NPLs. This latter improvement shows promise in obtaining narrower optical properties in the near-infrared using Hg-based NPLs.

Nevertheless, further optimization is needed for this synthesis, especially regarding the composition of the external crown. The formation of thicker Hg-NPLs could also be beneficial in strengthening the fragile HgTe 3 ML NPLs. One potential approach is to grow a shell on top of the HgTe NPLs. However, this possibility poses challenging due to the low stability of these particles under the conditions typically used for growing core-shell structure (high temperature).

Conclusion and perspectives.

II-VI semiconductor nanoplatelets exhibit unique optical properties. Thanks to their synthesis controlled at the atomic layer scale, no inhomogeneous broadening is observed in those particles, making them appealing materials to produce narrow photo- and electroluminescence. The possibility to tune their band gap energy through quantum confinement and composition modulations enables those materials to cover the entire visible spectral range. These 2D anisotropic materials are also interesting building blocks for the formation of more complex heterostructures. In this manuscript, I took advantage of these peculiar properties of the NPLs to design new materials, from bicolor- emitting particles to Hg-based NPLs for NIR narrow photo- and electroluminescence.

In a first chapter, I introduced the synthesis of a core-crown-crown 3 ML CdSe-CdTe-CdSe particle, aiming to obtain bicolor emission. The use of different materials in the various heterostructure areas enables meticulous localization of the wavefunctions through band alignment engineering. Thus, a broad red emission has been obtained through the sub-band gap recombination of an exciton at the CdSe/CdTe interface, while the band edge recombination in the large external crown provides a green emission. This feature is narrower than current technologies used in displays, which is promising for enhancing their color gamut. By studying the dynamic of the two emissions and the photoluminescence at the single particle scale, we confirmed the origin of the two emissions from a single particle. The green-to-red ratio can be changed by the dimensions of the CdSe external crown, as well as through modulation of the excitation power. This is achieved by tuning the Auger recombination rate in the different areas: the limited volume of the CdSe/CdTe interface limits the number of excitons that can be in this region, whereas it is not the case in the large CdSe external crown. This property is of utmost interest regarding a post-synthetic means to tune the final emitted color. Finally, electroluminescence has been achieved using these particles paving the way for more efficient bicolor electroluminescence.

Only a few works have been dedicated for core-multi-crown heterostructures. However, they offer a versatile playground for designing complex emission patterns. By finely tuning the band alignment in the heterostructure, it is possible to achieve different color combinations in addition to the green-red and blue-yellow particles synthesized in this manuscript. Regarding the lowest energy emission, efforts can be made to reduce its full width at half maximum. For example, developing particles in which both emissions come from band edge recombinations would be of great interest. Going further in the complexity of the heterostructure, tricolor emission could also be achieved, as we have already observed with the CdSe-CdTe-CdSe-CdSSe particles. To achieve this, a solution could arise from the combination of two complementary techniques: band alignment engineering and cation doping.

Finally, due to their large lateral extension, these particles still exhibit low quantum yield efficiencies, especially when deposited on a film. A straightforward idea to improve the performance of these particles would be to grow a shell on top of them. However, shell growth would also reduce the quantum confinement in the thickness, leading to a red-shift of the optical properties. To remain in the visible range, I developed a bicolor emission from bluer particles that have a similar CdSe/CdTe/CdSe heterostructure but with a smaller thickness. The growth of such shell is yet well-

established for small laterally extended NPLs. However, when it comes to large NPLs, only c-ALD and recrystallisation processes enable a homogeneous shell growth. A breakthrough would come with the development of shell growth methods that combine compatibility with such wide objects and the enhancement of optical properties achieved by hot injection in core-shell heterostructure.

In a second chapter, I reported the first synthesis of $HgSe_xTe_{1-x}$ 3 ML NPLs with tunable photoluminescence in the NIR. Those particles cannot be synthesized directly. Instead, $CdSe_xTe_{1-x}$ 3 ML NPLs are synthesized and then undergo cation exchange to obtain their Hg-based counterparts. This pathway has been demonstrated by Izquierdo *et al*., but it only enabled to achieve 3 ML HgTe NPLs. To extended this procedure to alloys, the solvent, temperature, and nature of the involved ligands during the exchange have been investigated to slow down the process. Consequently, photoluminescence from $HgSe_xTe_{1-x}$ 3 ML NPLs has been observed for the first time. In the scope of future incorporation inside optoelectronic devices, the band alignment of these particles has been unveiled through X-ray photoemission spectroscopy and confirmed by the analyzing the surface photovoltage of a film of those NPLs.

This relative band alignment unveils a cross-over from a p-type semiconductor for HgTe to a n-type semiconductor for HgSe NPLs. The evolution of the Fermi level position inside the band gap mainly arises from the valence band. The band gap energy of the Hg-based 3 ML NPLs is not shifting largely, especially at high Te content unlike in the Cd-based alloys. Therefore, the position of the Fermi level inside the band gap can be modulated through the composition of the alloy. Interestingly, this evolution is inverse to the one observed when modulating the diameter of HgTe QDs. It would be interesting to observe the influence of an increase in the NPLs thickness on the position of the Fermi level. It could then serve at an additional parameter to tune the band alignment of the material.

To confirm these measurements, the relative band alignment in $HgSe_xTe_{1-x}$ 3 ML NPLs could be investigated by forming Hg-based NPLs heterostructures, similar to what has been done by Dufour *et al.* on 4 ML $CdSe_xTe_{1-x}$ NPLs[93]. By carefully selecting the initial heterostructure, the possibility of achieving bicolor emission in the NIR range could even be considered. In particular, the disparity in reaction rates between CdS, CdSe and, CdTe towards the cation exchange could be utilized to selectively exchange CdTe to formed hybrid heterostructure containing both Cd- and Hg-based materials. Given the significant band gap difference between these materials, type-I core-crown particles could be generated to enhance the emission quantum yield in the NIR range.

Finally, the transition from Cd-based to Hg-based NPLs has enabled a shift in the optical properties towards the NIR range and has facilitated the induction of quantum confinement conditions that are difficult to achieve in Hg-based QDs. Efforts should now be dedicated to obtaining thicker Hg-based NPLs in order to increase the modulation of the band gap energy within a wider wavelength range. However, this remains challenging due to the limitation of the cation exchange to two cation planes. Research on intermediate cations as catalysts for the exchange or on the surface chemistry could be conducted to improve further the cation exchange of thicker NPLs.

In the final chapter, I investigated the design of a LED based on HgTe NPLs. Despite improvements in the cation exchange procedure, the photoluminescence stability of such particles

remains limited. In particular, a red-shift of the luminescence is observed over time, which has been attributed to the formation of small dots on top of the NPLs. Comparing the photoluminescence dynamics of these particles revealed a transfer from the NPLs to a charge transfer state, likely associated with the small dots previously observed. This transfer occurs through resonant energy transfer mechanism between the NPLs and the dots. Consequently, the formation of these QDs is the reason for the degradation of the optical properties. To limit the occurrence of such features, efforts should be dedicated to strengthening the particles. In this context, I introduced the formation of a $Hg_xCd_{1-x}S$-HgTe to mitigate degradation at the edges of the particles. While this method stabilizes the photoluminescence of the particles, it remains sub-optimal, primarily due to the challenges in forming the CdTe/CdS interface. Therefore, efforts could be focused on the designing a heterostructure that provides better interface definition. In addition to a core-crown heterostructure, a core-shell structure could also be considered to enhance the stability and robustness of HgTe luminescence. However, this option has been weakly investigated due to the fragility of the HgTe NPLs.

In order to use NPLs in devices, they also need to be deposited as films where their optical properties are even less stable. To mitigate further degradation of the luminescence, I conducted a ligand exchange from native carboxylate/amine to bromide. This treatment helped stabilize the photoluminescence. Additionally, the large lateral extension of the initial Cd-based NPLs limits the colloidal stability and processability of these particles. To improve this, I synthesized smaller 3 ML CdTe NPLs to obtain colloidally stable HgTe particles. Collectively, these optimizations enabled the design of the first LED constituted of Hg-based NPLs. The modest efficiency of this LED is mainly attributed to the low quantum efficiency of the particles themselves. Therefore, improving the photoluminescence would result in an enhancement of the electroluminescence efficiency.

Another approach to improve the external quantum efficiency in LEDs is to achieve oriented emission. In this context, we coupled a film of HgTe NPLs with a metallic nanostructure. Through plasmonic coupling, we achieved enhanced photoluminescence and oriented emission. This hold promises for light extraction from LEDs. Similar results could be obtained by depositing NPLs in an oriented manner on a film, but it would require significantly more efforts. Instead, incorporating metallic nanostructures within an LED stack would offer benefits across the entire optical spectrum. For example, coupling of two plasmonic resonances within a film of bicolor-emitting NPLs could enable the achievement of oriented bicolor emissions, allowing for color tuning with angular resolution.

Annexes

Precursor Synthesis

TOP:S precursor 1M: In a glove box, 20 mL of TOP are mixed with 0.64 mg of S powder. The mixture is stirred for a whole night and is then stored in the glovebox.

TOP:Se precursor 1M: In a glove box, 20 mL of TOP are mixed with 1.58 mg of Se powder. The mixture is stirred for a whole night and is then stored in the glovebox.

TOP:Te precursor 1M: In a three neck flask, 2.54 g of Te powder are mixed in 20 mL of TOP. The flask is kept under vacuum at room temperature for 5 min and then the temperature is raised to 100 °C. Furthermore, degassing of the flask is conducted for the next 20 min. The atmosphere is then switched to argon and the temperature is raised to 275 °C. The solution is stirred until a clear orange coloration is obtained. The flask is cooled down to room temperature and the color changes to yellow. This solution is finally transferred in a glovebox.

Bis(stearoyl)selenide precursor: In a 50 mL three-neck flask, 20 mL of dried THF are mixed with 0.192 Se powder and cooled down to -10°C using an ice bath filled with NaCl. 72 mg of $LiAlH_4$ are swiftly added and the system is put under argon flux. A greyish color is observed. After 30 min, add 0.68 mL of stearoyl chloride in 2 min. Repeat the operation at 60, 90, 120, and 150 min. The color goes from yellowish to cream to white. Add 25 mL of diethyl ether and wash 5 times with a saturated solution of NaCl. At this point, the mixture should be brown. Using a heat gun, heat around 50°C until the solution becomes clear. And wait overnight for the crystallization. The solid is then filtered using a Büchner filter. The solid is kept under vacuum for the night and stored in a glovebox for further used.

Cadmium propionate ($Cd(prop)_2$) precursor: In a 50 mL three necks flask, 2.56 g of cadmium oxide and 25mL of propionic acid are mixed. Under argon, the temperature is set at 70°C. After 1h, the mixture is degassed until half the volume remains (to get ride of a part of the water produced and the reactant that did not react). The solution is cooled down and the formed white solid is precipited 4 times using acetone. The solid is finally dried overnight at 70°C under vacuum.

Cadmium decanoate ($Cd(deca)_2$) precursor: In a 100 mL three-neck flask, 2 g of CdO (15.7 mmol) and 6.9 g (40 mmol) of decanoic acid are mixed and heated at 210 °C for 1 h under argon atmosphere. When the entire solid is dissolved and a colorless solution is obtained, the heating is stopped and acetone is added to precipitate cadmium decanoate. The powder is centrifugated and washed at least 3 times with acetone then set under vacuum over the night.

Cadmium myristate ($Cd(myr)_2$) precursor: In a 50 mL three necks flask, 2.56 g of cadmium oxide and 11 g of myristic acid are mixed and degassed at 80 °C for 30 min. The atmosphere is then switched to argon and the temperature is set at 200 °C. The mixture is heated for 40 min until the solution becomes colorless. The solution is then cooled down and 30 mL of methanol are added at 60 °C. The formed cadmium myristate is washed 5 times by centrifugation using methanol. The solid is finally dried overnight at 70°C under vacuum.

Hg oleate ($Hg(OA)_2$) precursor: In a 50 mL three neck flask, 0.5 g of mercury acetate are added with 20 mL of oleic acid. The mixture is heated at 80°C for 30 min and then cooled down to room temperature. At this stage, the mixture is put under vacuum to remove the remaining acetate. The final solution is then kept in a vial and can be used for approximately three weeks.

Nanoplatelets synthesis

Synthesis of CdS NPLs:

CdS 3 ML: In 50 mL three-neck flask, 53 mg of $Cd(ac)_2.2H_2O$, 1 mL of S-ODE solution (0.01 M), 46 mg of myristic acid and 3 mL of ODE are degassed for 10 min at room temperature. The mixture is then heated at 180°C in 8 min and kept at this temperature for 30 min. The end of the reaction is determined by absorption when only the feature of 3 ML CdS NPLs are visible. The particles are washed by selective precipitation using hexane and ethanol. This synthesis is adapted from Li *et al.*[37]

CdS 4 ML: In 50 mL three-neck flask, 53 mg of $Cd(ac)_2.2H_2O$, 1 mL of S-ODE solution (0.01 M), 65 µL of myristic acid and 3 mL of ODE are degassed for 10 min at room temperature. The mixture is then heated at 260°C in 12 min and kept at this temperature for 30 min. The end of the reaction is determined by absorption when only the feature of 4 ML CdS NPLs are visible. The particles are washed by selective precipitation using hexane and ethanol. This synthesis is adapted from Li *et al.*[37]

Synthesis of CdSe NPLs:

CdSe 3ML (large): In a 50 mL three-neck flask, 240 mg of $Cd(ac)_2$ and 15 mL of ODE are mixed and degassed at 60 °C for 30 min. Under argon flow, the temperature is set to 190 °C then a mixture of 600 µL of TOPSe 1M, 200 µL of OA and 5 mL of ODE, is added dropwise at a 4 $mL.h^{-1}$ rate. The mixture is then cooled down to room temperature. The NPLs are centrifugated twice with 15 mL of hexane and 15 mL of ethanol then redispersed in 10 mL of hexane.

CdSe 3ML (small): In a 50 mL three-neck flask, 68 mg of $Cd(deca)_2$, 63 mg of bis(stearoyl)selenide, 107 mg of $Cd(ac)_2.2H_2O$ mg of $Cd(myr)_2$ are added in 15 mL of ODE and the mixture is degassed for 1 h at room temperature. The atmosphere is then switched to argon and the temperature is set at 160°C. The mixture is kept at this T for 6 h. The solution is then cooled down to room temperature and the NPLs are precipitated using toluene and a minimum amount of isopropanol. The washing is repeated two times using a minimum of isopropanol. The NPLs are redispersed in 10 mL of ODE. This synthesis is adapted from Khoshkhoo *et al.*[190]

CdSe 4ML: In a three neck flask, 340 mg of $Cd(myr)_2$, 24 mg of Se powder and 25 mL of ODE are added and degassed for 20 min at room temperature. The atmosphere is then switch to argon and the temperature is set at 235°C. Around 203°C, 110 mg of $Cd(ac)_2.2H_2O$ are swiftly added. The reaction is heated for another 20 min and is then cooled down to room temperature. At 160°C, 1 mL of oleic acid are added to the mixture. The obtained NPLs are then separated from the side product by a selective precipitation using 20 mL of hexane and 30 mL of ethanol. The NPLs are then washed a second time using a smaller amount of ethanol.

Synthesis of CdTe NPLs:

CdTe 3ML (large): 390 mg of cadmium propionate, 80 µL of oleic acid and 10 mL of ODE are degassed for 1h at 90°C. The atmosphere is then switch to argon and the temperature is set at 210°C. When the temperature stabilized, 300 µL of TOP:Te (1M) dispersed in 500 µL of ODE is swiftly added to the mixture. The reaction is then followed by absorption and is cooled down when the features of the 2 ML NPLs disappear.

CdTe 3ML (small): 230 mg of cadmium decanoate, 80 µL of oleic acid and 5 mL of ODE are degassed for 1h at 90°C. The atmosphere is then switch to argon and the temperature is set at 220°C. When the temperature reached 180 °C, 100 µL of TOP:Te (1M) dispersed in 500 µL of ODE is swiftly added to the mixture followed by 70 µL of propionic acid in 500 µL of ODE when the mixture turns orange. The

reaction is then followed by absorption and is cooled down when the features of the 2 ML NPLs disappear.

Synthesis of alloyed $CdSe_xTe_{1-x}$ NPLs:

$CdSe_{1-x}Te_x$ 3 ML: In a 50 mL three-neck flask, 120 mg of $Cd(myr)_2$ and 12 mL of ODE are mixed and degassed at room temperature for 30 min. The atmosphere is switched to argon and the temperature increased to 230°C. A mix of 60 mg of $Cd(ac)_2$ and 160 mg of $Cd(prop)_2$ is added. 1 min later, a mix of 150 µL of different ratios of TOP:Te and TOPSe, 200 µL of OA and 2 mL of ODE is added at a 8 $mL.h^{-1}$ rate. After 30 min, the reaction is quenched by cooling down and adding oleic acid. The NPLs are centrifugated twice with 15 mL of hexane and 15 mL of ethanol then redispersed in 10 mL of hexane. Different ratios of Se:Te have been used to modify the composition of the nanoplatelets and are in good agreement with the measure realized.

Synthesis of HgTe NPLs:

Hg optimized cation exchange procedure: In a glass tube, add 1 mL $CdSe_{1-x}Te_x$ (20 µmol of Cd) redispersed in 6 mL of TCE. The tubes are stored in a fridge until the temperature reaches 5°C. Then, 200 µL of $Hg(OA)_2$ (0.08 M in OA) and 2 eq (for CdTe), 4 eq (for $CdSe_{0.25}Te_{0.75}$), 6 eq (for $CdSe_{0.5}Te_{0.5}$), 8 eq (for $CdSe_{0.75}Te_{0.25}$), 10 eq (for CdSe) of $Hg(Ac)_2$ (0.1 M in OLAm; 1eq = 200 µL) are added. The reaction is over when the absorption features stabilize. The NPLs are then precipitated by adding few drops of ethanol and centrifugated at 12000 rpm for 1 min. The NPLs are finally suspended in 500 µL of toluene (final concentration of around 10 $mg.mL^{-1}$)

Synthesis of heterostructured NPLs:

Core-crown-crown on 3 ML NPLs:

CdTe crown in CdSe/CdTe core crown: In a three-neck flask, 1 mL of 3 ML CdSe NPLs, 92 mg of dried $Cd(OAc)_2$ and 180 µL of OA are added to 3 mL ODE. The mixture is degassed under vacuum ay 70°C for 1 h. The atmosphere is then switched to argon and the temperature is set at 180°C. When the temperature stabilizes, 0.25 mL of TOPTe in ODE (0.005 M starting from a 1 M TOPTe solution) is added at a 2 $mL.h^{-1}$ rate.

CdSe crown in CdSe/CdTe/CdSe core crown: After the growth of the CdTe crown, the mixture is kept at 180°C for 10 min. The temperature is then set at 190°C and 2 mL of TOPSe (0.1 M starting form a 1 M TOPSe solution) is added at a 2 $mL.^{-1}$. At the end of the injection, the mixture is cool down to room temperature. They are precipitated twice using hexane and a minimum of ethanol.

CdS crown in CdTe/CdS core crown: In a 25mL three neck flask, 350 µL of the CdTe core solution (10 µmol Te) and 3mL ODE are degassed for 2h at 90°C. 2mL of a growth solution (450µL OA + 240mg $Cd(Ac)_2$ in 10mL ODE degassed 1h at 90°C) are added and the temperature is set at 170°C. After 15min, 2mL of TOPS (0.025M) are added at $2mL.h^{-1}$. The temperature is then raised at 180°C and the reaction is stopped after 1h. The final NPLs are washed by precipitation using a 1:1 hexane ethanol mixture.

Core-crown-crown on 4 ML NPLs:

CdS crown in CdSe/CdS core crown: In a 25 mL here-neck flask, 500 µL of 4 ML CdSe NPLs, 240 mg $Cd(OAc)_2.2H_2O$, and 440 µL OA are added to 3 mL ODE. The mixture is degassed under vacuum at 60°C for 1h30. The atmosphere is switched to argon and the temperature is set at 210°C. 10 mL of a solution of TOPS in ODE (0.1 M starting from a 1 M TOPS solution) is added at a 12 $mL.h^{-1}$ speed starting from 180°C. When the T reach 210°C, the injection rate is slowed down to 2 $mL.h^{-1}$. At the end of the injection, the NPLs are kept 10 min at 210°C before cooling down to room temperature. The NPLs are

precipitated twice using hexane and a minimum of ethanol. The final NPLs are redispersed in 10 mL hexane.

CdTe crown in CdSe/CdTe core crown: In a 25 mL three-neck flask, 92 mg of dried $Cd(OAc)_2$, 180 µL of oleic acid and 1 mL of CdSe 4ML core NPLs (O.D. : 1 at 512 nm for 50 µL in 3 mL of hexane) redispersed in 5 mL of ODE are degassed for 30 min at room temperature then 30 min at 80°C. The atmosphere is switched to argon and the temperature is set at 205°C. When the temperature is stabilized, 0.25mL (1eq) of a solution of TOP:Te (1 M) in ODE (final concentration 0.01M) is added at a 2 $mL.h^{-1}$ rate. After the injection, the mixture is further heated for 10min.

CdSe crown in CdSe/CdTe/CdSe core crown: After the growth of the CdTe crown, the temperature is set at 215 °C. When the temperature is stabilized, 2 mL of TOP:Se (1 M) in ODE (final concentration 0.1 M) is added at a 1 $mL.h^{-1}$ rate. After the injection, the mixture is cooled down to room temperature and the NPLs are precipitated with hexane and ethanol for 5 min. The final pellets are redispersed in hexane.

Characterization procedures

Structural analysis :

Transmission electron microscopy (TEM): A drop of the NC solution is drop-casted onto a copper grid covered with an amorphous carbon film. The grid is degassed overnight to reduce future contamination. A JEOL 2010F is used for the acquisition of pictures and operated at 200 kV.

High-angular annular dark field STEM (HAADF-STEM): Using similar grids, TEM/STEM observations were made on a Titan Themis 200 microscope (FEI/Thermo Fischer Scientific) equipped with a geometric aberration corrector on the probe. The microscope was also equipped with the "Super-X" systems for EDX analysis with a detection angle of 0.9 steradian. The observations were made at 200 kV with a probe current of about 35 pA and a half-angle of convergence of 17 mrad. HAADF-STEM images were acquired with a camera length of 110 mm (inner/outer collection angles were respectively 69 and 200 mrad). Those measurements have been conducted by G. Patriarche at C_2N.

Elemental analysis using X-ray dispersive spectroscopy (EDX): For EDX analysis, the particles are deposited on a Si substrate. The EDX analysis is performed by a FEI Magellan scanning electron microscope operated at 15 kV and 1.6 nA. The X-ray analysis is made with an Oxford probe.

X-ray diffraction (XRD): X-ray diffraction (XRD) sample is obtained by drop-casting the solution of nanocrystals on a Si wafer. The diffractometer is a Philips X'Pert, based on the emission of the Cu K_α (λ=0.154 nm) line operated at 40 kV and 40 mA current.

Optical Spectroscopy

Absorption/PL measurements: UV-visible spectra are acquired with a Cary 5000 spectrometer. Photoluminescence and excitation spectra are obtained with an Edinburgh instrument spectrometer. During the measurements, the NPLs are dispersed in hexane. For PL excitation measurements, care has been taken to work in diluted solution to limit emission reabsorption phenomena.

µ-photoluminescence: A homogeneous excited volume corresponding to the waist region of the incident beam was addressed with a confocal-like setup (afocal configuration) using the spectrometer slit (Princeton Instruments, Acton SP2750) as a spatial filter. To reach strong rejection and select the waist emission, the latter was coupled to an infinity corrected microscope objective (NA ≈ 0.6, equivalent focal length ≈ 6 mm) used to excite and collect light in reflection configuration. A cooled CCD (Spec10, PI) was used as a detector at the exit of the spectrometer. The excitation was supplied by a laser diode (Alphalas) operating at 407 nm ($\Delta t \approx 70$ ps). The repetition rate was adjusted at ≈ 300 kHz to allow complete inter-pulse relaxation of the long lifetime species responsible for the red emission. A long-pass edge filter (LP03-458RE-25, $\lambda_{cut\text{-}off} \approx 458$ nm) from Semrock company was also placed along the detection path to suppress scattered light from the excitation beam.

Time-resolved photoluminescence: PL time-resolved measurements were performed using the same 'confocal' configuration; with two different methods. Relatively 'long' lifetime decays (associated to the red emission) were characterized through TCSPC using a correlator board from Picoquant (TimeHarp 260), an avalanche photodiode for the detection (MPD company, PDM module accommodating a dark count rate of ≈ 25 counts/s) and an Alphalas laser diode to excite the material ($\lambda \approx 407$ nm, $\Delta t \approx 70$ ps). The setup IRF is then measured to be ≈ 220 ps. Fast decays (green emission) were measured with a streak-camera (C5680 model from Hamamatsu incorporating an M5675 synchroscan unit) coupled to our Acton SP2750 spectrometer. In this configuration, the excitation

(pulses of ≈ 2 ps duration) is the second harmonic of a Titanium-sapphire laser operating at 82 MHz and a temporal resolution of ≈15 ps is typically obtained depending on the dispersion of the PL through the spectrometer. Different filters combinations are used throughout time-resolved experiments: colored filters - from Corning and Thorlabs – in order to extract the spectrum part of interest as well as an additional highly selective Semrock filter (to reject photons from the laser). Due to the high emission yield of the system, a great attention was drawn during TCSPC to keep the ratio of the count rate to the excitation frequency below 2%, in order to avoid pile-up effects deleterious to the counting statistics.

Transient absorption: Transient absorption measurements were performed by splitting the 800 nm fundamental of a 2 kHz 35 fs Ti:Sapphire laser (SpectraPhysics) into two branches. One branch, the pump, was frequency-doubled to 400 nm, chopped to 1 kHz, and focused on the sample. The other branch, the probe, was focused into a 2 mm sapphire disk to generate a white light supercontinuum and then focused onto the sample. The beams were overlapped spatially on the sample and the pump-probe delay was controlled by a delay stage. Spectra of the white light supercontinuum were collected under pump-on and pump-off conditions to generate ΔA data using Helios software (Ultrafast systems).

Amplified spontaneous emission: Amplified spontaneous emission (ASE) measurements were performed using a frequency-doubled Ti:Sapphire pump excitation (400 nm, ≈35 fs, 100 Hz) focused as a 4 mm stripe on a thin-film sample of nanoplatelets. The pump power was controlled with continuous optical density wheels. Emitted light was collected normal to the pump excitation direction, focused into a fiber, and directed to a spectrometer and CCD. Films for measurements were prepared by drop-casting 9:1 hexane: octane solutions of nanoplatelets onto clean glass slides, to form smooth, reflective films. A similar configuration (using a circular lens with front-face collection) was employed to perform power-dependent photoluminescence experiments on dilute samples in cuvettes.

Single particle measurements: Here, PL is collected with a 0.6 NA, infinity corrected objective (producing a <1 µm diameter spot) and analyzed using a 2750 Acton Spectrometer from Princeton Instruments, keeping the confocal configuration described for the Time-resolved photoluminescence. The NPLs were dispersed on ≈ 120 microns thick coverslips that were 'stuck' to the cold finger of a He-flow micro-photoluminescence cryostat (Oxford Instruments) with silver particles-based varnish to ensure a good thermal contact. The excitation was tuned at 390 nm (SHG of a Ti-Sapphire laser delivering ps duration pulses). A dichroic filter (from Semrock company) was placed along the optical path (FF01-430/LP-25) to suppress scattering from the excitation beam.

Photoemission Spectroscopy

All XPS measurements have been conducted under the supervision of M. Silly.

Sample preparation for photoemission*:* Silicon wafers are rinsed with acetone, sonicated in acetone for 5 minutes. They are rinsed again with acetone and isopropanol and dried with N_2 gun. A 5 nm layer of Cr and an 80 nm layer of Au are deposited using thermal evaporation. A diluted solution of NPLs in a mix of hexane octane (9:1) is drop-casted on the prepared substrate. After drying, the film is dipped in a solution of EDT (1% in acetonitrile) for 1 min. The procedure is repeated 3 times. The final film is stored under inert atmosphere before its introduction into the preparation chamber, where it is degassed for at least two hours and then transferred to the analysis chamber.

Photoemission data acquisition: XPS experiments are carried out on the TEMPO beamline from SOLEIL synchrotron. The photon sources were HU80 and HU44 Apple II undulators set to deliver linearly polarized light. The photon energy is selected using a high-resolution plane grating monochromator.

The spot size is 100x80 µm². The signal is acquired onto an MBS A-1 photoelectron analyzer equipped with a delay line detector developed by Elettra.

Energy calibration: Valence and secondary electron cut-off measurements are conducted at 150 eV which corresponds to a surface sensitive condition, while core levels are typically acquired using a 700 eV photon energy. The photon energy is precisely measured by comparing the first and second order kinetic energy of a given core level using the formula: $h\nu_{exp} = KE_{2^{nd}} - KE_{1^{st}}$. The work function of the analyzer (WF_A) is determined by measuring the kinetic energy of electrons at the Fermi level from a gold reference sample. The binding energy of the Fermi level is set to 0 eV. $WF_A = h\nu_{exp} - KE_{Fermi}$

Valence band measurement ($VB\text{-}E_F$): We determine the value of V_B-E_F by looking at high KE electrons. We measure the highest kinetic energy available (KE_{VB}) and extract V_B-E_F with the formula: $VB - E_F = h\nu_{exp} - KE_{VB} - WF_A$.

Core level: All spectra are calibrated in energy by shifting them so that the Fermi level of metallic samples presents null binding energy. A Shirley background is subtracted in all core level spectra. The core level is then fitted using a Voigt curve.

Work function measurement: In order to measure the work function, which is the difference in energy between vacuum level and Fermi level, we look for the cut-off of secondary electrons ($KE_{Cut\ off}$). We start by polarizing the sample using an 18 V (Pol_{Bias}) voltage supply (TDK lambda) and we look for the energy edge of the lowest kinetic energy photoelectrons. The work function is deduced with the formula: $\phi_{Sample} = KE_{Cut\ off} - Pol_{Bias}$.

Time resolved X-ray photoemission measurements (TrXPS): The sample is excited by a 405 nm pulsed laser diode (10 kHz, duty cycle of 40 %). The output equivalent CW power used for the experiment is 100 mW and the beam spot is typically 300 µm × 300 µm (synchrotron beam) and 400 µm × 2 mm (laser beam). The laser beam is spatially aligned to overlap with the synchrotron beam on the sample holder using a Si diode. The pump probe TrXPS is conducted in a stroboscopic configuration where the temporal resolution is given by the time response of the photoemission analyzer. The latter is estimated to be 30 ns, limited by the spread of the electrons between the hemispheres. Then, the photoemission spectrum of a given core level is acquired every 10 ns. Each spectrum of the series is fitted by two Gaussians to extract the kinetic energy of each peak. This procedure enables to follow energy shifts as small as 5 meV.

LED fabrication and characterization

Synthesis of ZnO nanoparticles: The procedure is taken from ref [245]. In flask A, 3 mmol of zinc acetate are dissolved in 30 mL of DMSO by vigorous stirring. At the same time, 5.5 mmol of TMAOH are dissolved with 10 mL of ethanol in flask B. Then the contents of the two flasks are mixed and stirred for 24 hours under ambient conditions. The reaction mixture turns whitish during the first few seconds and becomes clear soon after. ZnO particles are precipitated by ethyl acetate and redisperse in ethanol. 160 µL of 2-ethanolamine are added to stabilize the nanoparticles before they are precipitated and redispersed with ethyl acetate and ethanol respectively again. Finally, the ZnO nanoparticles in ethanol are filtered using a 0.22 µm PTFE filter.

ITO substrate patterning: ITO substrates (30 Ω/sq) are cut into 15 mm × 15 mm pieces and cleaned by sonication in acetone for 5 min. After sonication, the substrates are rinsed with acetone and isopropanol before being dried completely with N_2 flow. The substrates are further cleaned with O_2 plasma for 5 min to remove organic residuals on the surface. After cleaning, TI-Prime and AZ 5214E photoresist are sequentially spin-coated on the surface of ITO substrates at the rate of 4000 rpm for 30 s and baked at 110 °C for 120 s and 90 s, respectively. In the next stage, a mask aligner is used to expose the substrates to UV light for 20 s through a lithography mask (1 mm width). A photoresist is then developed using AZ 726 developer for 20 s before rinsing with deionized water and drying with N_2 flux. After another 5-minute plasma cleaning, the substrates are etched in a 25% HCl (in water) bath for 10 min at 40 °C before they are dipped immediately in deionized water. Finally, the lift-off is conducted in an acetone bath. Before being used, the patterned ITO substrates are cleaned with acetone and isopropanol first and put under plasma for 10 min.

LED fabrication: PEDOT:PSS solution (filtered through 0.45 µm filter) is spin-coated on a patterned ITO glass electrode at 4000 rpm for 60 s and annealed at 140 °C for 10 min in air. Inside a nitrogen-filled glovebox, Poly-TPD (8 mg.mL^{-1} in chlorobenzene), PVK (1.5 mg.mL^{-1} in m-xylene), NPLs (in a mix of hexane/octane (9:1)), PMMA (5mg.mL^{-1} in acetone) and ZnO nanoparticles are successively spin-coated at 2000 rpm for 45 s on the PEDOT: PSS-coated substrate. After the deposition of Poly-TPD, the sample is annealed at 110 °C for 20 min, and for PVK the annealing is at 170 °C for 30 min. Finally, 80 nm of Ag is deposited on top of the ZnO using a shadow mask by thermal evaporation. The thickness of NPL and ZnO layers are 18 nm and 80 nm respectively, as obtained by profilometry. The devices are encapsulated inside the glove box with a piece of glass by epoxy-glue. The size of the pixel is 1 mm^2 which is the overlap of ITO and Ag electrodes.

LED characterization: Considering the Lambertian emission of LED device, the flux leaving the device directly can be described as $F_{ext} = \int_0^{\pi/2} 2\pi L_0 \, cos\theta sin\theta d\theta = \pi L_0$, with L_0 the flux per solid angle of light leaving the device in the forward direction. Since the solid angle from the photodetector to the light source is $\Omega = \frac{S_1}{l^2}$ with S_1 the area of the detector and l the distance between the light source and detector, then $L_0 = \frac{P_{det}}{\Omega} = \frac{P_{det} l^2}{s_1}$ and $F_{ext} = \frac{\pi P_{det} l^2}{s_1}$. The number of photons emitted per second to the forward direction can then be calculated by $N_P = \frac{F_{ext}}{h\nu} = \frac{\pi P_{det} l^2 \lambda}{s_1 hc}$, with λ the wavelength of electroluminescence, h the Plank's constant and c the speed of light. The number of electrons injected per second can be obtained by $N_P = \frac{I}{e}$, with I the current flow of the device. Thus, the EQE can be calculated as $EQE = \frac{N_p}{N_e} = \frac{\pi P_{det} l^2 \lambda e}{s_1 hcI}$. The irradiance of the device is $R = \frac{F_{ext}}{s_2} = \frac{\pi P_{det} l^2}{s_1 s_2}$, with S_2 the area of the pixel. The luminance L of the device is $L = \frac{683.V(\lambda).F_{ext}}{\pi.S_2}$, with $V(\lambda)$ the function of photonic eye sensitivity. For the characterization, we collected current-voltage-radiance characteristics with a Keithley K2400B sourcemeter unit and a PM100A powermeter coupled with a S120C Si detector from Thorlabs (for visible measurements) and with a the S122C Ge detector from Thorlabs (for NIR

measurments). Knowing that the working diameter of the detector area is 9.5 mm and assuming the distance between detector and device to be 6.5 mm, the geometry-related value is $\frac{l^2}{s_1} \approx 0.6$.

List of publications

2023 :

1. *Coupling Ferroelectric to colloidal Nanocrystals as a Generic Strategy to Engineer the Carrier Density Landscape*, M. Cavallo, E. Bossavit, S. Matzen, T. Maroutian, R. Alchaar, T. H. Dang, A. Khalili, **C. Dabard**, H. Zhang, Y. Prado, C. Abadie, J. Utterback, J. F. Dayen, M. Silly, P. Dudin, J. Avila, E. Lhuillier, D. Pierucci, *Adv. Funct. Mater.*, 2300846
2. *Bias Reconfigurable Photoresponse of an Infrared Nanocrystal Film Integrated into a Coupled Fabry-Perot Resonator*, T. H. Dang, C. Abadie, A. Chu, M. Cavallo, A. Khalili, **C. Dabard**, E. Bossavit, H. Zhang, Y. Prado, D. Pierucci, J. Utterback, Y. Todorov, C. Sirtori, J. Jaeck, G. Vincent, A. Vasanelli, B. Fix, E. Lhuillier, *ACS Photonics* 2023, 10, 1601
3. *Mid-wave infrared sensitized InGaAs using intraband transition in doped colloidal II–VI nanocrystals*, A. Khalili, M. Cavallo, T. H. Dang, **C. Dabard**, H. Zhang, E. Bossavit, C. Abadie, Y. Prado, X. Xu, S. Ithurria, G. Vincent, C. Coinon, L. Desplanque, E. Lhuillier, *J. Chem. Phys.* 158, 094702
4. *2D II–VI Semiconductor Nanoplatelets: From Material Synthesis to Optoelectronic Integration*, B.T Diroll, B. Guzelturk, H. Po, **C. Dabard**, N. Fu, L. Makke, E. Lhuillier, S. Ithurria, *Chem. Rev.* 2023, 123, 3543
5. *Visible and Infrared Nanocrystal-based Light Modulator with CMOS Compatible Bias Operation*, H. Zhang, V. Guilloux, E. Bossavit, N. Fu, **C. Dabard**, M. Cavallo, T. H. Dang, A. Khalili, C. Abadie, R. Alchaar, C. Gréboval, X. Xu, J.K Utterback, D. Pierucci, S. Ithurria, J.I Climente, T. Barisien, E. Lhuillier, *ACS Photonics* 2023, 10, 430
6. *Mapping the Energy Landscape from a Nanocrystal-Based Field Effect Transistor under Operation using Nanobeam Photoemission Spectroscopy*, M. Cavallo, E. Bossavit, H. Zhang, **C. Dabard**, T. H. Dang, A. Khalili, C. Abadie, R. Alchaar, D. Mastrippolito, Y. Prado, L. Becerra, M. Rosticher, M.G Silly, J.K Utterback, S. Ithurria, J. Avila, D. Pierucci, E. Lhuillier, *Nano Lett.* 2023, 23, 1363
7. *On the Suitable choice of Metal for HgTe Nanocrystal-based Photodiode: to Amalgam or not to Amalgam*, R. Alchaar, **C. Dabard**, D. Mastrippolito, E. Bossavit, T. H. Dang, M. Cavallo, A. Khalili, H. Zhang, L. Domenach, N. Ledos, Y. Prado, D. Troadec, J. Dai, M. Tallarida, F. Bisti, F. Cadiz, G. Patriarche, J. Avila, E. Lhuillier, D. Pierucci, *J. Phys. Chem. C*

2022 :

8. *2D Nanoplatelets with Bicolor Power Tunable Emission,* **C. Dabard**, V. Guilloux, C. Gréboval, H. Po, L. Makke, N. Fu, X. Xu, M.G Silly, G. Patriarche, E. Lhuillier, T. Barisien, J.I Climente, B.T Diroll, S. Ithurria, *Nat Commun* **13**, 5094
9. *Guided-Mode Resonator Coupled with Nanocrystal Intraband Absorption*, A. Khalili, M. Weis, S. G. Mizrahi, A. Chu, T. H. Dang, C. Abadie, C. Gréboval, **C. Dabard**, Y. Prado, X. Xu, E. Péronne, C. Livache, S. Ithurria, G. Patriarche, J. Ramade, G. Vincent, D. Boschetto, E. Lhuillier, *ACS Photonics*, 3, 985
10. *Electroluminescence from nanocrystals above 2 µm lectroluminescence from nanocrystals above 2 µm*, J. Qu, M. Weis, E. Izquierdo, S. G. Mizrahi, A. Chu, **C. Dabard**, C. Gréboval, E. Bossavit, Y. Prado, E. Péronn, S. Ithurria, G. Patriarche, M. Silly, G. Vincent, D. Boschetto, E. Lhuillier *Nature Photonics,* 16, 38 (**2022**)
11. *Colloidal II–VI—Epitaxial III–V heterostructure: A strategy to expand InGaAs spectral response*, A. Khalili, C. Abadie, T. Dang, A. Chu, E. Izquierdo, **C. Dabard**, C. Gréboval, M. Cavallo, H. Zhang, S. Pierini, Y. Prado, X. Xu, S. Ithurria, G. Vincent, C. Coinon, L. Desplanque, E. Lhuillier, Appl. Phys. Lett. 120, 051101 (**2022**)
12. *Optimized Infrared LED and Its Use in an All-HgTe Nanocrystal-Based Active Imaging Setup*, E. Bossavit, J. Qu, C. Abadie, **C. Dabard**, T. Dang, E. Izquierdo, A. Khalili, C. Gréboval, A. Chu, S. Pierini, M. Cavallo, Y. Prado, V. Parahyba, X. Xu, A. Decamps-Mandine, M. Silly, S. Ithurria, E. Lhuillier *Adv. Opt. Mat.*, 10, 2101755 (**2022**)
13. *Chiral Helices Formation by Self-Assembled Molecules on Semiconductor Flexible Substrates* H. Po, **C. Dabard**, B. Roman, E. Reyssat, J. Bico, B. Baptiste, E. Lhuillier, S. Ithurria *ACS Nano,* 16, 2901 (2022)

14. *Helmoltz Resonator Applied to Nanocrystal-Based Infrared Sensing*, C. Abadie, L. Paggi, A. Fabas, A. Khalili, T. Dang, **C. Dabard**, M. Cavallo, R. Alchaar, H. Zhang, Y. Prado, N. Bardou, C. Dupuis, X. Xu, S. Ithurria, D. Pierucci, J. Utterback, B. Fix, G. Vincent, P. Bouchon, E. Lhuillier *Nano Lett.* 2022, 22, 8779
15. *Material Perspective on HgTe Nanocrystal-Based Short-Wave Infrared Focal Plane Arrays*, C. H. Zhang, R. Alchaar, Y. Prado, , A. Khalili, C. Gréboval, M. Cavallo, E. Bossavit, **C. Dabard**, T. Dang, C. Abadie, C. Methivier, D. Darson, V. Parahyba, P. Potet, J. Ramade, M. Silly, J. Utterback, D. Pierucci, S. Ithurria, E. Lhuillier, *Chem. Mater.*, 34, 10964

2021 :

16. *Optimized Cation Exchange for Mercury Chalcogenide 2D Nanoplatelets and Its Application for Alloys,* **C. Dabard**, J. Planelles, H. Po, E. Izquierdo, L. Makke, C. Gréboval, N. Moghaddam, A. Khalili, T. Dang, A. Chu, S. Pierini, C. Abadie, M. Cavallo, E. Bossavit, X. Xu, P. Hollander, M. Silly, E. Lhuillier, J. I. Climente, S. Ithurria, *Chem. Mater.* 2021, 33, 9252
17. *Surface Modification of CdE (E: S, Se, and Te) Nanoplatelets to Reach Thicker Nanoplatelets and Homostructures with Confinement-Induced Intraparticle Type I Energy Level Alignment*, N. Moghaddam, **C. Dabard**, M. Dufour, H. Po, X. Xu, T. Pons, E. Lhuillier and S. Ithurria, *J. Am. Chem. Soc.* 2021, 143, 1863
18. *Seeded Growth of HgTe Nanocrystals for Shape Control and Their Use in Narrow Infrared Electroluminescence*, Y. Prado, J. Qu, C. Gréboval, **C. Dabard,** P. Rastogi, A. Chu, A. Khalili, X. Xu, C. Delerue, S. Ithurria, and E. Lhuillier, *Chem. Mater.* 2021, 33, 2054
19. *Correlating Structure and Detection Properties in HgTe Nanocrystal Films,* S. Chee, C. Gréboval, D. Vale Magalhaes, J. Ramade, A. Chu, J. Qu, P. Rastogi, A. Khalili, T. Dang, **C. Dabard**, Y. Prado, G. Patriarche, J. Chaste, M. Rosticher, S. Bals, C. Delerue, and E. Lhuillier, *Nano Lett.* 2021, 21, 4145
20. *Complex Optical Index of HgTe Nanocrystal Infrared Thin Films and Its Use for Short Wave Infrared Photodiode Design,* P. Rastogi, A. Chu, T. Dang, Y. Prado, C. Gréboval, J. Qu, **C. Dabard**, A. Khalili, E. Dandeu, B. Fix, X. Xu, S. Ithurria, G. Vincent, B. Gallas, E. Lhuillier, 2021, 9, 10 202, 2002066
21. *2D Monolayer of the 1T' Phase of Alloyed WSSe from Colloidal Synthesis,* A. Shahmanesh, D. Romanin, **C. Dabard**, S. Chee, C. Gréboval, C. Methivier, M. G. Silly, J. Chaste, M. Bugnet, D. Pierucci, A. Ouerghi, M. Calandra, E. Lhuillier, B. Mahler, *J. Phys. Chem. C* 125, 11058
22. Split-Gate Photodiode Based on Graphene/HgTe Heterostructures with a Few Nanosecond Photoresponse C. Gréboval, **C. Dabard**, N. Konstantinov, M. Cavallo, S. Chee, A. Chu, T. Dang, A. Khalili, E. Izquierdo, Y. Prado, H. Majjad, X. Xu, J.-F. Dayen, E. Lhuillier, *ACS Appl. Electron. Mater.* 3, 4681

2020 :

23. *Gate tunable vertical geometry phototransistor based on infrared HgTe nanocrystals,* C. Gréboval, U. Nguétchuissi Noumbé, A. Chu, Y. Prado, A. Khalili, **C. Dabard**, *T.* Dang, S. Colis, J. Chaste, A. Ouerghi, J.F. Dayen, E. Lhuillier , Appl. Phys. Lett. 117, 251104
24. *Time-Resolved Photoemission to Unveil Electronic Coupling between Absorbing and Transport Layers in a Quantum Dot-Based Solar Cell,* C. Gréboval, P. Rastogi, J. Qu, A. Chu, J. Ramade, A. Khalili, **C. Dabard**, T. Dang, H. Cruguel, A. Ouerghi, N. Witkowski, M. G. Silly, E. Lhuillier, *J. Phys. Chem. C*, 124, 23400
25. *Electroluminescence from HgTe Nanocrystals and Its Use for Active Imaging,* J. Qu, P. Rastogi, C. Gréboval, D. Lagarde, A. Chu, **C. Dabard**, A. Khalili, H. Cruguel, C. Robert, X. Xu, S. Ithurria, M. G. Silly, S. Ferré, X. Marie, and E. Lhuillier *Nano Lett.*, 20, 6185

Bibliography

(1) Destriau, G. Recherches sur les scintillations des sulfures de zinc aux rayons α. *J. Chim. Phys.* **1936**, *33*, 587–625.

(2) Lossev, O. V. CII. Luminous Carborundum Detector and Detection Effect and Oscillations with Crystals. *Lond. Edinb. Dublin Philos. Mag. J. Sci.* **1928**, *6*, 1024–1044.

(3) Holonyak, N., Jr.; Bevacqua, S. F. Coherent visible light emission from Ga($As_{1-x}P_x$) junctions. *Appl. Phys. Lett.* **2004**, *1*, 82–83.

(4) Murray, C. B.; Norris, D. J.; Bawendi, M. G. Synthesis and Characterization of Nearly Monodisperse CdE (E = Sulfur, Selenium, Tellurium) Semiconductor Nanocrystallites. *J. Am. Chem. Soc.* **1993**, *115*, 8706–8715.

(5) Ithurria, S.; Dubertret, B. Quasi 2D Colloidal CdSe Platelets with Thicknesses Controlled at the Atomic Level. *J. Am. Chem. Soc.* **2008**, *130*, 16504–16505.

(6) Bouet, C.; Tessier, M. D.; Ithurria, S.; Mahler, B.; Nadal, B.; Dubertret, B. Flat Colloidal Semiconductor Nanoplatelets. *Chem. Mater.* **2013**, *25*, 1262–1271.

(7) Nasilowski, M.; Mahler, B.; Lhuillier, E.; Ithurria, S.; Dubertret, B. Two-Dimensional Colloidal Nanocrystals. *Chem. Rev.* **2016**, *116*, 10934–10982.

(8) Sharma, M.; Delikanli, S.; Demir, H. V. Two-Dimensional CdSe-Based Nanoplatelets: Their Heterostructures, Doping, Photophysical Properties, and Applications. *Proc. IEEE* **2020**, *108*, 655–675.

(9) Schliehe, C.; Juarez, B. H.; Pelletier, M.; Jander, S.; Greshnykh, D.; Nagel, M.; Meyer, A.; Foerster, S.; Kornowski, A.; Klinke, C.; Weller, H. Ultrathin PbS Sheets by Two-Dimensional Oriented Attachment. *Science* **2010**, *329*, 550–553.

(10) Sun, Y.; Terrones, M.; Schaak, R. E. Colloidal Nanostructures of Transition-Metal Dichalcogenides. *Acc. Chem. Res.* **2021**, *54*, 1517–1527.

(11) Rossetti, R.; Nakahara, S.; Brus, L. E. Quantum Size Effects in the Redox Potentials, Resonance Raman Spectra, and Electronic Spectra of CdS Crystallites in Aqueous Solution. *J. Chem. Phys.* **1983**, *79*, 1086–1088.

(12) Ekimov, A. I.; Onushchenko, A. A. Quantum Size Effect in Three-Dimensional Microscopic Semiconductor Crystals. *ZhETF Pisma Redaktsiiu* **1981**, *34*, 363.

(13) Efros, A.; Efros, A. Interband Absorption of Light in a Semiconductor Sphere. *SPIE Milest. Ser.* **2005**.

(14) Ekimov, A. I.; Efros, Al. L.; Onushchenko, A. A. Quantum Size Effect in Semiconductor Microcrystals. *Solid State Commun.* **1985**, *56*, 921–924.

(15) Brus, L. Electronic Wave Functions in Semiconductor Clusters: Experiment and Theory. *J. Phys. Chem.* **1986**, *90*, 2555–2560.

(16) Moghaddam, N.; Gréboval, C.; Qu, J.; Chu, A.; Rastogi, P.; Livache, C.; Khalili, A.; Xu, X. Z.; Baptiste, B.; Klotz, S.; Fishman, G.; Capitani, F.; Ithurria, S.; Sauvage, S.; Lhuillier, E. The Strong Confinement Regime in HgTe Two-Dimensional Nanoplatelets. *J. Phys. Chem. C* **2020**, *124*, 23460–23468.

(17) Gréboval, C.; Chu, A.; Goubet, N.; Livache, C.; Ithurria, S.; Lhuillier, E. Mercury Chalcogenide Quantum Dots: Material Perspective for Device Integration. *Chem. Rev.* **2021**, *121*, 3627–3700.

(18) Cubic Cadmium Selenide (c-CdSe). In *Handbook on Physical Properties of Semiconductors: Volume 3: II–VI Compound Semiconductors*; Adachi, S., Ed.; Springer US: Boston, MA, 2004; pp 311–328.

(19) Petrov, D. V.; Santos, B. S.; Pereira, G. A. L.; de Mello Donegá, C. Size and Band-Gap Dependences of the First Hyperpolarizability of CdxZn1-XS Nanocrystals. *J. Phys. Chem. B* **2002**, *106*, 5325–5334.

(20) Kyhm, K.; Kim, J. H.; Kim, S. M.; Yang, H. Gain Dynamics and Excitonic Transition in CdSe Colloidal Quantum Dots. *Opt. Mater.* **2007**, *30*, 158–160.

(21) Martinez, B.; Livache, C.; Notemgnou Mouafo, L. D.; Goubet, N.; Keuleyan, S.; Cruguel, H.; Ithurria, S.; Aubin, H.; Ouerghi, A.; Doudin, B.; Lacaze, E.; Dubertret, B.; Silly, M. G.; Lobo, R. P. S. M.; Dayen, J.-F.; Lhuillier, E. HgSe Self-Doped Nanocrystals as a Platform to Investigate the Effects of Vanishing Confinement. *ACS Appl. Mater. Interfaces* **2017**, *9*, 36173–36180.

(22) Rinnerbauer, V.; Hingerl, K.; Kovalenko, M.; Heiss, W. Effect of Quantum Confinement on Higher Transitions in HgTe Nanocrystals. *Appl. Phys. Lett.* **2006**, *89*, 193114.

(23) Dietl, T.; Szymańska, W. Electron Scattering in HgSe. *J. Phys. Chem. Solids* **1978**, *39*, 1041–1057.

(24) Yang, Y. A.; Wu, H.; Williams, K. R.; Cao, Y. C. Synthesis of CdSe and CdTe Nanocrystals without Precursor Injection. *Angew. Chem.* **2005**, *117*, 6870–6873.

(25) Pradhan, N.; Xu, H.; Peng, X. Colloidal CdSe Quantum Wires by Oriented Attachment. *Nano Lett.* **2006**, *6*, 720–724.

(26) Manna, L.; Scher, E. C.; Alivisatos, A. P. Synthesis of Soluble and Processable Rod-, Arrow-, Teardrop-, and Tetrapod-Shaped CdSe Nanocrystals. *J. Am. Chem. Soc.* **2000**, *122*, 12700–12706.

(27) Joo, J.; Son, J. S.; Kwon, S. G.; Yu, J. H.; Hyeon, T. Low-Temperature Solution-Phase Synthesis of Quantum Well Structured CdSe Nanoribbons. *J. Am. Chem. Soc.* **2006**, *128*, 5632–5633.

(28) Ouyang, J.; Zaman, Md. B.; Yan, F. J.; Johnston, D.; Li, G.; Wu, X.; Leek, D.; Ratcliffe, C. I.; Ripmeester, J. A.; Yu, K. Multiple Families of Magic-Sized CdSe Nanocrystals with Strong Bandgap Photoluminescence via Noninjection One-Pot Syntheses. *J. Phys. Chem. C* **2008**, *112*, 13805–13811.

(29) Ithurria, S.; Tessier, M. D.; Mahler, B.; Lobo, R. P. S. M.; Dubertret, B.; Efros, A. L. Colloidal Nanoplatelets with Two-Dimensional Electronic Structure. *Nat. Mater.* **2011**, *10*, 936–941.
(30) Klimov, V. I.; Mikhailovsky, A. A.; McBranch, D. W.; Leatherdale, C. A.; Bawendi, M. G. Quantization of Multiparticle Auger Rates in Semiconductor Quantum Dots. *Science* **2000**, *287*, 1011–1013.
(31) Pietryga, J. M.; Park, Y.-S.; Lim, J.; Fidler, A. F.; Bae, W. K.; Brovelli, S.; Klimov, V. I. Spectroscopic and Device Aspects of Nanocrystal Quantum Dots. *Chem. Rev.* **2016**, *116*, 10513–10622.
(32) Kelestemur, Y.; Olutas, M.; Delikanli, S.; Guzelturk, B.; Akgul, M. Z.; Demir, H. V. Type-II Colloidal Quantum Wells: CdSe/CdTe Core/Crown Heteronanoplatelets. *J. Phys. Chem. C* **2015**, *119*, 2177–2185.
(33) Romeo, A.; Artegiani, E.; Menossi, D. Low Substrate Temperature CdTe Solar Cells: A Review. *Sol. Energy* **2018**, *175*, 9–15.
(34) Sippel, P.; Albrecht, W.; van der Bok, J. C.; Van Dijk-Moes, R. J. A.; Hannappel, T.; Eichberger, R.; Vanmaekelbergh, D. Femtosecond Cooling of Hot Electrons in CdSe Quantum-Well Platelets. *Nano Lett.* **2015**, *15*, 2409–2416.
(35) Moghaddam, N.; Dabard, C.; Dufour, M.; Po, H.; Xu, X.; Pons, T.; Lhuillier, E.; Ithurria, S. Surface Modification of CdE (E: S, Se, and Te) Nanoplatelets to Reach Thicker Nanoplatelets and Homostructures with Confinement-Induced Intraparticle Type I Energy Level Alignment. *J. Am. Chem. Soc.* **2021**, *143*, 1863–1872.
(36) Cunningham, P. D.; Coropceanu, I.; Mulloy, K.; Cho, W.; Talapin, D. V. Quantized Reaction Pathways for Solution Synthesis of Colloidal ZnSe Nanostructures: A Connection between Clusters, Nanowires, and Two-Dimensional Nanoplatelets. *ACS Nano* **2020**, *14*, 3847–3857.
(37) Li, Z.; Qin, H.; Guzun, D.; Benamara, M.; Salamo, G.; Peng, X. Uniform Thickness and Colloidal-Stable CdS Quantum Disks with Tunable Thickness: Synthesis and Properties. *Nano Res.* **2012**, *5*, 337–351.
(38) Izquierdo, E.; Robin, A.; Keuleyan, S.; Lequeux, N.; Lhuillier, E.; Ithurria, S. Strongly Confined HgTe 2D Nanoplatelets as Narrow Near-Infrared Emitters. *J. Am. Chem. Soc.* **2016**, *138*, 10496–10501.
(39) Dabard, C.; Planelles, J.; Po, H.; Izquierdo, E.; Makke, L.; Gréboval, C.; Moghaddam, N.; Khalili, A.; Dang, T. H.; Chu, A.; Pierini, S.; Abadie, C.; Cavallo, M.; Bossavit, E.; Xu, X. Z.; Hollander, P.; Silly, M.; Lhuillier, E.; Climente, J. I.; Ithurria, S. Optimized Cation Exchange for Mercury Chalcogenide 2D Nanoplatelets and Its Application for Alloys. *Chem. Mater.* **2021**, *33*, 9252–9261.
(40) Tessier, M. D.; Javaux, C.; Maksimovic, I.; Loriette, V.; Dubertret, B. Spectroscopy of Single CdSe Nanoplatelets. *ACS Nano* **2012**, *6*, 6751–6758.
(41) Pedetti, S.; Nadal, B.; Lhuillier, E.; Mahler, B.; Bouet, C.; Abécassis, B.; Xu, X.; Dubertret, B. Optimized Synthesis of CdTe Nanoplatelets and Photoresponse of CdTe Nanoplatelets Films. *Chem. Mater.* **2013**, *25*, 2455–2462.
(42) Erdem, O.; Gungor, K.; Guzelturk, B.; Tanriover, I.; Sak, M.; Olutas, M.; Dede, D.; Kelestemur, Y.; Demir, H. V. Orientation-Controlled Nonradiative Energy Transfer to Colloidal Nanoplatelets: Engineering Dipole Orientation Factor. *Nano Lett.* **2019**, *19*, 4297–4305.
(43) Dufour, M.; Qu, J.; Greboval, C.; Méthivier, C.; Lhuillier, E.; Ithurria, S. Halide Ligands To Release Strain in Cadmium Chalcogenide Nanoplatelets and Achieve High Brightness. *ACS Nano* **2019**, *13*, 5326–5334.
(44) Leemans, J.; Singh, S.; Li, C.; Ten Brinck, S.; Bals, S.; Infante, I.; Moreels, I.; Hens, Z. Near-Edge Ligand Stripping and Robust Radiative Exciton Recombination in CdSe/CdS Core/Crown Nanoplatelets. *J. Phys. Chem. Lett.* **2020**, *11*, 3339–3344.
(45) Nawrot, K. C.; Sharma, M.; Cichy, B.; Sharma, A.; Delikanli, S.; Samoć, M.; Demir, H. V.; Nyk, M. Spectrally Resolved Nonlinear Optical Properties of Doped Versus Undoped Quasi-2D Semiconductor Nanocrystals: Copper and Silver Doping Provokes Strong Nonlinearity in Colloidal CdSe Nanoplatelets. *ACS Photonics* **2022**, *9*, 256–267.
(46) Hinterding, S. O. M.; Salzmann, B. B. V.; Vonk, S. J. W.; Vanmaekelbergh, D.; Weckhuysen, B. M.; Hutter, E. M.; Rabouw, F. T. Single Trap States in Single CdSe Nanoplatelets. *ACS Nano* **2021**, *15*, 7216–7225.
(47) Scott, R.; Achtstein, A. W.; Prudnikau, A. V.; Antanovich, A.; Siebbeles, L. D. A.; Artemyev, M.; Woggon, U. Time-Resolved Stark Spectroscopy in CdSe Nanoplatelets: Exciton Binding Energy, Polarizability, and Field-Dependent Radiative Rates. *Nano Lett.* **2016**, *16*, 6576–6583.
(48) Wang, G.; Chernikov, A.; Glazov, M. M.; Heinz, T. F.; Marie, X.; Amand, T.; Urbaszek, B. Colloquium: Excitons in Atomically Thin Transition Metal Dichalcogenides. *Rev. Mod. Phys.* **2018**, *90*, 021001.
(49) Pradhan, N.; Efrima, S. Single-Precursor, One-Pot Versatile Synthesis under near Ambient Conditions of Tunable, Single and Dual Band Fluorescing Metal Sulfide Nanoparticles. *J. Am. Chem. Soc.* **2003**, *125*, 2050–2051.
(50) Qu, L.; Peng, Z. A.; Peng, X. Alternative Routes toward High Quality CdSe Nanocrystals. *Nano Lett.* **2001**, *1*, 333–337.
(51) Peng, Z. A.; Peng, X. Formation of High-Quality CdTe, CdSe, and CdS Nanocrystals Using CdO as Precursor. *J. Am. Chem. Soc.* **2001**, *123*, 183–184.
(52) Yu, W. W.; Wang, Y. A.; Peng, X. Formation and Stability of Size-, Shape-, and Structure-Controlled CdTe Nanocrystals: Ligand Effects on Monomers and Nanocrystals. *Chem. Mater.* **2003**, *15*, 4300–4308.
(53) Talapin, D. V.; Haubold, S.; Rogach, A. L.; Kornowski, A.; Haase, M.; Weller, H. A Novel Organometallic Synthesis of Highly Luminescent CdTe Nanocrystals. *J. Phys. Chem. B* **2001**, *105*, 2260–2263.
(54) Cao, Y. C.; Wang, J. One-Pot Synthesis of High-Quality Zinc-Blende CdS Nanocrystals. *J. Am. Chem. Soc.* **2004**, *126*, 14336–14337.
(55) Ithurria, S.; Bousquet, G.; Dubertret, B. Continuous Transition from 3D to 1D Confinement Observed during the Formation of CdSe Nanoplatelets. *J. Am. Chem. Soc.* **2011**, *133*, 3070–3077.
(56) Bouet, C.; Mahler, B.; Nadal, B.; Abecassis, B.; Tessier, M. D.; Ithurria, S.; Xu, X.; Dubertret, B. Two-Dimensional Growth of CdSe Nanocrystals, from Nanoplatelets to Nanosheets. *Chem. Mater.* **2013**, *25*, 639–645.

(57) Tenney, S. M.; Tan, L. A.; Sonnleitner, M. L.; Sica, A. V.; Shin, A. J.; Ronquillo, R.; Ahmed, T.; Atallah, T. L.; Caram, J. R. Mesoscale Quantum-Confined Semiconductor Nanoplatelets through Seeded Growth. *Chem. Mater.* **2022**, *34*, 6048–6056.

(58) Chen, Y.; Chen, D.; Li, Z.; Peng, X. Symmetry-Breaking for Formation of Rectangular CdSe Two-Dimensional Nanocrystals in Zinc-Blende Structure. *J. Am. Chem. Soc.* **2017**, *139*, 10009–10019.

(59) Lyashchova, A.; Dmytruk, A.; Dmitruk, I.; Klimusheva, G.; Mirnaya, T.; Asaula, V. Optical Absorption, Induced Bleaching, and Photoluminescence of CdSe Nanoplatelets Grown in Cadmium Octanoate Matrix. *Nanoscale Res. Lett.* **2014**, *9*, 88.

(60) Riedinger, A.; Ott, F. D.; Mule, A.; Mazzotti, S.; Knüsel, P. N.; Kress, S. J. P.; Prins, F.; Erwin, S. C.; Norris, D. J. An Intrinsic Growth Instability in Isotropic Materials Leads to Quasi-Two-Dimensional Nanoplatelets. *Nat. Mater.* **2017**, *16*, 743–748.

(61) Ott, F. D.; Riedinger, A.; Ochsenbein, D. R.; Knüsel, P. N.; Erwin, S. C.; Mazzotti, M.; Norris, D. J. Ripening of Semiconductor Nanoplatelets. *Nano Lett.* **2017**, *17*, 6870–6877.

(62) Knüsel, P. N.; Riedinger, A.; Rossinelli, A. A.; Ott, F. D.; Mule, A. S.; Norris, D. J. Experimental Evidence for Two-Dimensional Ostwald Ripening in Semiconductor Nanoplatelets. *Chem. Mater.* **2020**, *32*, 3312–3319.

(63) Di Giacomo, A.; Rodà, C.; Khan, A. H.; Moreels, I. Colloidal Synthesis of Laterally Confined Blue-Emitting 3.5 Monolayer CdSe Nanoplatelets. *Chem. Mater.* **2020**, *32*, 9260–9267.

(64) Bertrand, G. H. V.; Polovitsyn, A.; Christodoulou, S.; Khan, A. H.; Moreels, I. Shape Control of Zincblende CdSe Nanoplatelets. *Chem. Commun.* **2016**, *52*, 11975–11978.

(65) Meerbach, C.; Wu, C.; Erwin, S. C.; Dang, Z.; Prudnikau, A.; Lesnyak, V. Halide-Assisted Synthesis of Cadmium Chalcogenide Nanoplatelets. *Chem. Mater.* **2020**, *32*, 566–574.

(66) Cho, W.; Kim, S.; Coropceanu, I.; Srivastava, V.; Diroll, B. T.; Hazarika, A.; Fedin, I.; Galli, G.; Schaller, R. D.; Talapin, D. V. Direct Synthesis of Six-Monolayer (1.9 Nm) Thick Zinc-Blende CdSe Nanoplatelets Emitting at 585 Nm. *Chem. Mater.* **2018**, *30*, 6957–6960.

(67) Christodoulou, S.; Climente, J. I.; Planelles, J.; Brescia, R.; Prato, M.; Martín-García, B.; Khan, A. H.; Moreels, I. Chloride-Induced Thickness Control in CdSe Nanoplatelets. *Nano Lett.* **2018**, *18*, 6248–6254.

(68) Fan, F.; Kanjanaboos, P.; Saravanapavanantham, M.; Beauregard, E.; Ingram, G.; Yassitepe, E.; Adachi, M. M.; Voznyy, O.; Johnston, A. K.; Walters, G.; Kim, G.-H.; Lu, Z.-H.; Sargent, E. H. Colloidal CdSe1–XSx Nanoplatelets with Narrow and Continuously-Tunable Electroluminescence. *Nano Lett.* **2015**, *15*, 4611–4615.

(69) Tenne, R.; Pedetti, S.; Kazes, M.; Ithurria, S.; Houben, L.; Nadal, B.; Oron, D.; Dubertret, B. From Dilute Isovalent Substitution to Alloying in CdSeTe Nanoplatelets. *Phys. Chem. Chem. Phys.* **2016**, *18*, 15295–15303.

(70) Wei, S.-H.; Zhang, S. B.; Zunger, A. First-Principles Calculation of Band Offsets, Optical Bowings, and Defects in CdS, CdSe, CdTe, and Their Alloys. *J. Appl. Phys.* **2000**, *87*, 1304–1311.

(71) Kelestemur, Y.; Dede, D.; Gungor, K.; Usanmaz, C. F.; Erdem, O.; Demir, H. V. Alloyed Heterostructures of CdSexS1–x Nanoplatelets with Highly Tunable Optical Gain Performance. *Chem. Mater.* **2017**, *29*, 4857–4865.

(72) Ithurria, S.; Talapin, D. V. Colloidal Atomic Layer Deposition (c-ALD) Using Self-Limiting Reactions at Nanocrystal Surface Coupled to Phase Transfer between Polar and Nonpolar Media. *J. Am. Chem. Soc.* **2012**, *134*, 18585–18590.

(73) Lhuillier, E.; Pedetti, S.; Ithurria, S.; Heuclin, H.; Nadal, B.; Robin, A.; Patriarche, G.; Lequeux, N.; Dubertret, B. Electrolyte-Gated Field Effect Transistor to Probe the Surface Defects and Morphology in Films of Thick CdSe Colloidal Nanoplatelets. *ACS Nano* **2014**, *8*, 3813–3820.

(74) Mahler, B.; Nadal, B.; Bouet, C.; Patriarche, G.; Dubertret, B. Core/Shell Colloidal Semiconductor Nanoplatelets. *J. Am. Chem. Soc.* **2012**, *134*, 18591–18598.

(75) Altintas, Y.; Quliyeva, U.; Gungor, K.; Erdem, O.; Kelestemur, Y.; Mutlugun, E.; Kovalenko, M. V.; Demir, H. V. Highly Stable, Near-Unity Efficiency Atomically Flat Semiconductor Nanocrystals of CdSe/ZnS Hetero-Nanoplatelets Enabled by ZnS-Shell Hot-Injection Growth. *Small* **2019**, *15*, 1804854.

(76) Rossinelli, A. A.; Riedinger, A.; Marqués-Gallego, P.; Knüsel, P. N.; Antolinez, F. V.; Norris, D. J. High-Temperature Growth of Thick-Shell CdSe/CdS Core/Shell Nanoplatelets. *Chem. Commun.* **2017**, *53*, 9938–9941.

(77) Khan, A. H.; Bertrand, G. H. V.; Teitelboim, A.; Sekhar M., C.; Polovitsyn, A.; Brescia, R.; Planelles, J.; Climente, J. I.; Oron, D.; Moreels, I. CdSe/CdS/CdTe Core/Barrier/Crown Nanoplatelets: Synthesis, Optoelectronic Properties, and Multiphoton Fluorescence Upconversion. *ACS Nano* **2020**, *14*, 4206–4215.

(78) Pedetti, S.; Ithurria, S.; Heuclin, H.; Patriarche, G.; Dubertret, B. Type-II CdSe/CdTe Core/Crown Semiconductor Nanoplatelets. *J. Am. Chem. Soc.* **2014**, *136*, 16430–16438.

(79) Antanovich, A. V.; Prudnikau, A. V.; Melnikau, D.; Rakovich, Y. P.; Chuvilin, A.; Woggon, U.; Achtstein, A. W.; Artemyev, M. V. Colloidal Synthesis and Optical Properties of Type-II CdSe–CdTe and Inverted CdTe–CdSe Core–Wing Heteronanoplatelets. *Nanoscale* **2015**, *7*, 8084–8092.

(80) Izquierdo, E.; Dufour, M.; Chu, A.; Livache, C.; Martinez, B.; Amelot, D.; Patriarche, G.; Lequeux, N.; Lhuillier, E.; Ithurria, S. Coupled HgSe Colloidal Quantum Wells through a Tunable Barrier: A Strategy To Uncouple Optical and Transport Band Gap. *Chem. Mater.* **2018**, *30*, 4065–4072.

(81) Kim, S.; Fisher, B.; Eisler, H.-J.; Bawendi, M. Type-II Quantum Dots: CdTe/CdSe(Core/Shell) and CdSe/ZnTe(Core/Shell) Heterostructures. *J. Am. Chem. Soc.* **2003**, *125*, 11466–11467.

(82) Zhang, Z.; Thung, Y. T.; Wang, L.; Chen, X.; Ding, L.; Fan, W.; Sun, H. Surface Depletion Effects in Bromide-Ligated Colloidal Cadmium Selenide Nanoplatelets: Toward Efficient Emission at High Temperature. *J. Phys. Chem. Lett.* **2021**, *12*, 9086–9093.

(83) Hines, M. A.; Guyot-Sionnest, P. Synthesis and Characterization of Strongly Luminescing ZnS-Capped CdSe Nanocrystals. *J. Phys. Chem.* **1996**, *100*, 468–471.
(84) Feng, F.; NGuyen, L. T.; Nasilowski, M.; Nadal, B.; Dubertret, B.; Maître, A.; Coolen, L. Probing the Fluorescence Dipoles of Single Cubic CdSe/CdS Nanoplatelets with Vertical or Horizontal Orientations. *ACS Photonics* **2018**, *5*, 1994–1999.
(85) Qu, J.; Rastogi, P.; Gréboval, C.; Livache, C.; Dufour, M.; Chu, A.; Chee, S.-S.; Ramade, J.; Xu, X. Z.; Ithurria, S.; Lhuillier, E. Nanoplatelet-Based Light-Emitting Diode and Its Use in All-Nanocrystal LiFi-like Communication. *ACS Appl. Mater. Interfaces* **2020**, *12*, 22058–22065.
(86) Yang, Z.; Pelton, M.; Fedin, I.; Talapin, D. V.; Waks, E. A Room Temperature Continuous-Wave Nanolaser Using Colloidal Quantum Wells. *Nat. Commun.* **2017**, *8*, 143.
(87) Altintas, Y.; Gungor, K.; Gao, Y.; Sak, M.; Quliyeva, U.; Bappi, G.; Mutlugun, E.; Sargent, E. H.; Demir, H. V. Giant Alloyed Hot Injection Shells Enable Ultralow Optical Gain Threshold in Colloidal Quantum Wells. *ACS Nano* **2019**, *13*, 10662–10670.
(88) Duan, R.; Zhang, Z.; Xiao, L.; Zhao, X.; Thung, Y. T.; Ding, L.; Liu, Z.; Yang, J.; Ta, V. D.; Sun, H. Ultralow-Threshold and High-Quality Whispering-Gallery-Mode Lasing from Colloidal Core/Hybrid-Shell Quantum Wells. *Adv. Mater.* **2022**, *34*, 2108884.
(89) Yu, J.; Sharma, M.; Li, M.; Delikanli, S.; Sharma, A.; Taimoor, M.; Altintas, Y.; McBride, J. R.; Kusserow, T.; Sum, T.-C.; Demir, H. V.; Dang, C. Low-Threshold Lasing from Copper-Doped CdSe Colloidal Quantum Wells. *Laser Photonics Rev.* **2021**, *15*, 2100034.
(90) Prudnikau, A.; Chuvilin, A.; Artemyev, M. CdSe–CdS Nanoheteroplatelets with Efficient Photoexcitation of Central CdSe Region through Epitaxially Grown CdS Wings. *J. Am. Chem. Soc.* **2013**, *135*, 14476–14479.
(91) Tessier, M. D.; Spinicelli, P.; Dupont, D.; Patriarche, G.; Ithurria, S.; Dubertret, B. Efficient Exciton Concentrators Built from Colloidal Core/Crown CdSe/CdS Semiconductor Nanoplatelets. *Nano Lett.* **2014**, *14*, 207–213.
(92) Delikanli, S.; Guzelturk, B.; Hernández-Martínez, P. L.; Erdem, T.; Kelestemur, Y.; Olutas, M.; Akgul, M. Z.; Demir, H. V. Continuously Tunable Emission in Inverted Type-I CdS/CdSe Core/Crown Semiconductor Nanoplatelets. *Adv. Funct. Mater.* **2015**, *25*, 4282–4289.
(93) Dufour, M.; Steinmetz, V.; Izquierdo, E.; Pons, T.; Lequeux, N.; Lhuillier, E.; Legrand, L.; Chamarro, M.; Barisien, T.; Ithurria, S. Engineering Bicolor Emission in 2D Core/Crown CdSe/CdSe1–XTex Nanoplatelet Heterostructures Using Band-Offset Tuning. *J. Phys. Chem. C* **2017**, *121*, 24816–24823.
(94) Kelestemur, Y.; Guzelturk, B.; Erdem, O.; Olutas, M.; Erdem, T.; Usanmaz, C. F.; Gungor, K.; Demir, H. V. CdSe/CdSe1–XTex Core/Crown Heteronanoplatelets: Tuning the Excitonic Properties without Changing the Thickness. *J. Phys. Chem. C* **2017**, *121*, 4650–4658.
(95) Schlosser, A.; Graf, R. T.; Bigall, N. C. CdS Crown Growth on CdSe Nanoplatelets: Core Shape Matters. *Nanoscale Adv.* **2020**, *2*, 4604–4614.
(96) Wen, Z.; Liu, P.; Ma, J.; Jia, S.; Xiao, X.; Ding, S.; Tang, H.; Yang, H.; Zhang, C.; Qu, X.; Xu, B.; Wang, K.; Teo, K. L.; Sun, X. W. High-Performance Ultrapure Green CdSe/CdS Core/Crown Nanoplatelet Light-Emitting Diodes by Suppressing Nonradiative Energy Transfer. *Adv. Electron. Mater.* **2021**, *7*, 2000965.
(97) Wen, Z.; Zhang, C.; Zhou, Z.; Xu, B.; Wang, K.; Teo, K. L.; Sun, X. W. Ultrapure Green Light-Emitting Diodes Based on CdSe/CdS Core/Crown Nanoplatelets. *IEEE J. Quantum Electron.* **2020**, *56*, 1–6.
(98) Guzelturk, B.; Kelestemur, Y.; Olutas, M.; Delikanli, S.; Demir, H. V. Amplified Spontaneous Emission and Lasing in Colloidal Nanoplatelets. *ACS Nano* **2014**, *8*, 6599–6605.
(99) Pandya, R.; Chen, R. Y. S.; Cheminal, A.; Dufour, M.; Richter, J. M.; Thomas, T. H.; Ahmed, S.; Sadhanala, A.; Booker, E. P.; Divitini, G.; Deschler, F.; Greenham, N. C.; Ithurria, S.; Rao, A. Exciton–Phonon Interactions Govern Charge-Transfer-State Dynamics in CdSe/CdTe Two-Dimensional Colloidal Heterostructures. *J. Am. Chem. Soc.* **2018**, *140*, 14097–14111.
(100) Chin, P. T. K.; de Mello Donegá, C.; van Bavel, S. S.; Meskers, S. C. J.; Sommerdijk, N. A. J. M.; Janssen, R. A. J. Highly Luminescent CdTe/CdSe Colloidal Heteronanocrystals with Temperature-Dependent Emission Color. *J. Am. Chem. Soc.* **2007**, *129*, 14880–14886.
(101) Zhang, W.; Chen, G.; Wang, J.; Ye, B.-C.; Zhong, X. Design and Synthesis of Highly Luminescent Near-Infrared-Emitting Water-Soluble CdTe/CdSe/ZnS Core/Shell/Shell Quantum Dots. *Inorg. Chem.* **2009**, *48*, 9723–9731.
(102) Khan, A. H.; Brescia, R.; Polovitsyn, A.; Angeloni, I.; Martín-García, B.; Moreels, I. Near-Infrared Emitting Colloidal PbS Nanoplatelets: Lateral Size Control and Optical Spectroscopy. *Chem. Mater.* **2017**, *29*, 2883–2889.
(103) Pang, Y.; Zhang, M.; Chen, D.; Chen, W.; Wang, F.; Anwar, S. J.; Saunders, M.; Rowles, M. R.; Liu, L.; Liu, S.; Sitt, A.; Li, C.; Jia, G. Why Do Colloidal Wurtzite Semiconductor Nanoplatelets Have an Atomically Uniform Thickness of Eight Monolayers? *J. Phys. Chem. Lett.* **2019**, *10*, 3465–3471.
(104) Alchaar, R.; Dabard, C.; Mastrippolito, D.; Bossavit, E.; Dang, T. H.; Cavallo, M.; Khalili, A.; Zhang, H.; Domenach, L.; Ledos, N.; Prado, Y.; Troadec, D.; Dai, J.; Tallarida, M.; Bisti, F.; Cadiz, F.; Patriarche, G.; Avila, J.; Lhuillier, E.; Pierucci, D. On the Suitable Choice of Metal for HgTe Nanocrystal-Based Photodiode: To Amalgam or Not to Amalgam. *J. Phys. Chem. C* **2023**, *127*, 12218–12225.
(105) Kachurin, G. A.; Tyschenko, I. E.; Fedina, L. I. High-Temperature Ion Implantation in Silicon. *Nucl. Instrum. Methods Phys. Res. Sect. B Beam Interact. Mater. At.* **1992**, *68*, 323–330.
(106) Schooss, D.; Mews, A.; Eychmüller, A.; Weller, H. Quantum-Dot Quantum Well CdS/HgS/CdS: Theory and Experiment. *Phys. Rev. B* **1994**, *49*, 17072–17078.

(107) Akkerman, Q. A.; Rainò, G.; Kovalenko, M. V.; Manna, L. Genesis, Challenges and Opportunities for Colloidal Lead Halide Perovskite Nanocrystals. *Nat. Mater.* **2018**, *17*, 394–405.
(108) De Trizio, L.; Manna, L. Forging Colloidal Nanostructures via Cation Exchange Reactions. *Chem. Rev.* **2016**, *116*, 10852–10887.
(109) Jain, P. K.; Amirav, L.; Aloni, S.; Alivisatos, A. P. Nanoheterostructure Cation Exchange: Anionic Framework Conservation. *J. Am. Chem. Soc.* **2010**, *132*, 9997–9999.
(110) Rivest, J. B.; Jain, P. K. Cation Exchange on the Nanoscale: An Emerging Technique for New Material Synthesis, Device Fabrication, and Chemical Sensing. *Chem. Soc. Rev.* **2012**, *42*, 89–96.
(111) Son, D. H.; Hughes, S. M.; Yin, Y.; Paul Alivisatos, A. Cation Exchange Reactions in Ionic Nanocrystals. *Science* **2004**, *306*, 1009–1012.
(112) Jeong, S.; Han, J. H.; Jang, J.; Seo, J.; Kim, J.-G.; Cheon, J. Transformative Two-Dimensional Layered Nanocrystals. *J. Am. Chem. Soc.* **2011**, *133*, 14500–14503.
(113) Groeneveld, E.; Witteman, L.; Lefferts, M.; Ke, X.; Bals, S.; Van Tendeloo, G.; de Mello Donega, C. Tailoring ZnSe–CdSe Colloidal Quantum Dots via Cation Exchange: From Core/Shell to Alloy Nanocrystals. *ACS Nano* **2013**, *7*, 7913–7930.
(114) Dufour, M.; Izquierdo, E.; Livache, C.; Martinez, B.; Silly, M. G.; Pons, T.; Lhuillier, E.; Delerue, C.; Ithurria, S. Doping as a Strategy to Tune Color of 2D Colloidal Nanoplatelets. *ACS Appl. Mater. Interfaces* **2019**, *11*, 10128–10134.
(115) Khan, A. H.; Pinchetti, V.; Tanghe, I.; Dang, Z.; Martín-García, B.; Hens, Z.; Van Thourhout, D.; Geiregat, P.; Brovelli, S.; Moreels, I. Tunable and Efficient Red to Near-Infrared Photoluminescence by Synergistic Exploitation of Core and Surface Silver Doping of CdSe Nanoplatelets. *Chem. Mater.* **2019**, *31*, 1450–1459.
(116) Sharma, A.; Sharma, M.; Gungor, K.; Olutas, M.; Dede, D.; Demir, H. V. Near-Infrared-Emitting Five-Monolayer Thick Copper-Doped CdSe Nanoplatelets. *Adv. Opt. Mater.* **2019**, *7*, 1900831.
(117) Mitrofanov, A.; Prudnikau, A.; Di Stasio, F.; Weiß, N.; Hübner, R.; Dominic, A. M.; Borchert, K. B. L.; Lesnyak, V.; Eychmüller, A. Near-Infrared-Emitting CdxHg1–XSe-Based Core/Shell Nanoplatelets. *Chem. Mater.* **2021**, *33*, 7693–7702.
(118) Bouet, C.; Laufer, D.; Mahler, B.; Nadal, B.; Heuclin, H.; Pedetti, S.; Patriarche, G.; Dubertret, B. Synthesis of Zinc and Lead Chalcogenide Core and Core/Shell Nanoplatelets Using Sequential Cation Exchange Reactions. *Chem. Mater.* **2014**, *26*, 3002–3008.
(119) De Trizio, L.; Gaspari, R.; Bertoni, G.; Kriegel, I.; Moretti, L.; Scotognella, F.; Maserati, L.; Zhang, Y.; Messina, G. C.; Prato, M.; Marras, S.; Cavalli, A.; Manna, L. Cu3-XP Nanocrystals as a Material Platform for Near-Infrared Plasmonics and Cation Exchange Reactions. *Chem. Mater.* **2015**, *27*, 1120–1128.
(120) Koh, S.; Kim, W. D.; Bae, W. K.; Lee, Y. K.; Lee, D. C. Controlling Ion-Exchange Balance and Morphology in Cation Exchange from Cu3–XP Nanoplatelets into InP Crystals. *Chem. Mater.* **2019**, *31*, 1990–2001.
(121) Wang, Y.; Zhukovskyi, M.; Tongying, P.; Tian, Y.; Kuno, M. Synthesis of Ultrathin and Thickness-Controlled Cu2–XSe Nanosheets via Cation Exchange. *J. Phys. Chem. Lett.* **2014**, *5*, 3608–3613.
(122) Berends, A. C.; van der Stam, W.; Akkerman, Q. A.; Meeldijk, J. D.; van der Lit, J.; de Mello Donega, C. Anisotropic 2D Cu2–XSe Nanocrystals from Dodecaneselenol and Their Conversion to CdSe and CuInSe2 Nanoparticles. *Chem. Mater.* **2018**, *30*, 3836–3846.
(123) Galle, T.; Samadi Khoshkhoo, M.; Martin-Garcia, B.; Meerbach, C.; Sayevich, V.; Koitzsch, A.; Lesnyak, V.; Eychmüller, A. Colloidal PbSe Nanoplatelets of Varied Thickness with Tunable Optical Properties. *Chem. Mater.* **2019**, *31*, 3803–3811.
(124) Klepzig, L. F.; Biesterfeld, L.; Romain, M.; Niebur, A.; Schlosser, A.; Hübner, J.; Lauth, J. Colloidal 2D PbSe Nanoplatelets with Efficient Emission Reaching the Telecom O-, E- and S-Band. *Nanoscale Adv.* **2022**, *4*, 590–599.
(125) Salzmann, B. B. V.; Wit, J. de; Li, C.; Arenas-Esteban, D.; Bals, S.; Meijerink, A.; Vanmaekelbergh, D. Two-Dimensional CdSe-PbSe Heterostructures and PbSe Nanoplatelets: Formation, Atomic Structure, and Optical Properties. *J. Phys. Chem. C* **2022**, *126*, 1513–1522.
(126) Lehmann, A.; Böhm, M.; Miehling, D.; Pfaffinger, M.; Stelter, S.; Uhlig, F.; Ali, A.; Belias, A.; Dzhygadlo, R.; Gerhardt, A.; Krebs, M.; Lehmann, D.; Peters, K.; Schepers, G.; Schwarz, C.; Schwiening, J.; Traxler, M.; Schmitt, L.; Düren, M.; Etzelmüller, E.; Föhl, K.; Hayrapetyan, A.; Kreutzfeld, K.; Rieke, J.; Schmidt, M.; Wasem, T.; Sfienti, C. Recent Progress with Microchannel-Plate PMTs. *Nucl. Instrum. Methods Phys. Res. Sect. Accel. Spectrometers Detect. Assoc. Equip.* **2020**, *952*, 161821.
(127) Liu, Y.; Gibbs, M.; Puthussery, J.; Gaik, S.; Ihly, R.; Hillhouse, H. W.; Law, M. Dependence of Carrier Mobility on Nanocrystal Size and Ligand Length in PbSe Nanocrystal Solids. *Nano Lett.* **2010**, *10*, 1960–1969.
(128) Nag, A.; Kovalenko, M. V.; Lee, J.-S.; Liu, W.; Spokoyny, B.; Talapin, D. V. Metal-Free Inorganic Ligands for Colloidal Nanocrystals: S2–, HS–, Se2–, HSe–, Te2–, HTe–, TeS32–, OH–, and NH2– as Surface Ligands. *J. Am. Chem. Soc.* **2011**, *133*, 10612–10620.
(129) Jacoboni, C.; Canali, C.; Ottaviani, G.; Alberigi Quaranta, A. A Review of Some Charge Transport Properties of Silicon. *Solid-State Electron.* **1977**, *20*, 77–89.
(130) Livache, C.; Izquierdo, E.; Martinez, B.; Dufour, M.; Pierucci, D.; Keuleyan, S.; Cruguel, H.; Becerra, L.; Fave, J. L.; Aubin, H.; Ouerghi, A.; Lacaze, E.; Silly, M. G.; Dubertret, B.; Ithurria, S.; Lhuillier, E. Charge Dynamics and Optolectronic Properties in HgTe Colloidal Quantum Wells. *Nano Lett.* **2017**, *17*, 4067–4074.
(131) Kovalenko, M. V.; Scheele, M.; Talapin, D. V. Colloidal Nanocrystals with Molecular Metal Chalcogenide Surface Ligands. *Science* **2009**, *324*, 1417–1420.

(132) Lhuillier, E.; Ithurria, S.; Descamps-Mandine, A.; Douillard, T.; Castaing, R.; Xu, X. Z.; Taberna, P.-L.; Simon, P.; Aubin, H.; Dubertret, B. Investigating the N- and p-Type Electrolytic Charging of Colloidal Nanoplatelets. *J. Phys. Chem. C* **2015**, *119*, 21795–21799.

(133) Polack, F.; Silly, M.; Chauvet, C.; Lagarde, B.; Bergeard, N.; Izquierdo, M.; Chubar, O.; Krizmancic, D.; Ribbens, M.; Duval, J. -P.; Basset, C.; Kubsky, S.; Sirotti, F. TEMPO: A New Insertion Device Beamline at SOLEIL for Time Resolved Photoelectron Spectroscopy Experiments on Solids and Interfaces. *AIP Conf. Proc.* **2010**, *1234*, 185–188.

(134) Guyot-Sionnest, P. Charging Colloidal Quantum Dots by Electrochemistry. *Microchim. Acta* **2008**, *160*, 309–314.

(135) Peric, N.; Lambert, Y.; Singh, S.; Khan, A. H.; Franchina Vergel, N. A.; Deresmes, D.; Berthe, M.; Hens, Z.; Moreels, I.; Delerue, C.; Grandidier, B.; Biadala, L. Van Hove Singularities and Trap States in Two-Dimensional CdSe Nanoplatelets. *Nano Lett.* **2021**, *21*, 1702–1708.

(136) Sugimoto, A.; Ochi, H.; Fujimura, S.; Yoshida, A.; Miyadera, T.; Tsuchida, M. Flexible OLED Displays Using Plastic Substrates. *IEEE J. Sel. Top. Quantum Electron.* **2004**, *10*, 107–114.

(137) Shu, Y.; Lin, X.; Qin, H.; Hu, Z.; Jin, Y.; Peng, X. Quantum Dots for Display Applications. *Angew. Chem. Int. Ed.* **2020**, *59*, 22312–22323.

(138) Hoshi, T.; Kumagai, K.; Inoue, K.; Enomoto, S.; Nobe, Y.; Kobayashi, M. Electronic Absorption and Emission Spectra of Alq3 in Solution with Special Attention to a Delayed Fluorescence. *J. Lumin.* **2008**, *128*, 1353–1358.

(139) Colvin, V. L.; Schlamp, M. C.; Alivisatos, A. P. Light-Emitting Diodes Made from Cadmium Selenide Nanocrystals and a Semiconducting Polymer. *Nature* **1994**, *370*, 354–357.

(140) Dai, X.; Zhang, Z.; Jin, Y.; Niu, Y.; Cao, H.; Liang, X.; Chen, L.; Wang, J.; Peng, X. Solution-Processed, High-Performance Light-Emitting Diodes Based on Quantum Dots. *Nature* **2014**, *515*, 96–99.

(141) Thung, Y. T.; Duan, R.; Durmusoglu, E. G.; He, Y.; Xiao, L.; Lee, C. X. X.; Lew, W. S.; Zhang, L.; Demir, H. V.; Sun, H. Ultrahigh Quality Microlasers from Controlled Self-Assembly of Ultrathin Colloidal Semiconductor Quantum Wells. *Laser Photonics Rev. n/a*, 2200849.

(142) Song, J.; Wang, O.; Shen, H.; Lin, Q.; Li, Z.; Wang, L.; Zhang, X.; Li, L. S. Over 30% External Quantum Efficiency Light-Emitting Diodes by Engineering Quantum Dot-Assisted Energy Level Match for Hole Transport Layer. *Adv. Funct. Mater.* **2019**, *29*, 1808377.

(143) Deng, Y.; Peng, F.; Lu, Y.; Zhu, X.; Jin, W.; Qiu, J.; Dong, J.; Hao, Y.; Di, D.; Gao, Y.; Sun, T.; Zhang, M.; Liu, F.; Wang, L.; Ying, L.; Huang, F.; Jin, Y. Solution-Processed Green and Blue Quantum-Dot Light-Emitting Diodes with Eliminated Charge Leakage. *Nat. Photonics* **2022**, *16*, 505–511.

(144) Bae, W. K.; Park, Y.-S.; Lim, J.; Lee, D.; Padilha, L. A.; McDaniel, H.; Robel, I.; Lee, C.; Pietryga, J. M.; Klimov, V. I. Controlling the Influence of Auger Recombination on the Performance of Quantum-Dot Light-Emitting Diodes. *Nat. Commun.* **2013**, *4*, 2661.

(145) Shirasaki, Y.; Supran, G. J.; Tisdale, W. A.; Bulović, V. Origin of Efficiency Roll-Off in Colloidal Quantum-Dot Light-Emitting Diodes. *Phys. Rev. Lett.* **2013**, *110*, 217403.

(146) Kim, W. D.; Kim, D.; Yoon, D.-E.; Lee, H.; Lim, J.; Bae, W. K.; Lee, D. C. Pushing the Efficiency Envelope for Semiconductor Nanocrystal-Based Electroluminescence Devices Using Anisotropic Nanocrystals. *Chem. Mater.* **2019**, *31*, 3066–3082.

(147) Baruj, H. D.; Bozkaya, I.; Canimkurbey, B.; Isik, A. T.; Shabani, F.; Delikanli, S.; Shendre, S.; Erdem, O.; Isik, F.; Demir, H. V. Highly-Directional, Highly-Efficient Solution-Processed Light-Emitting Diodes of All-Face-Down Oriented Colloidal Quantum Well Self-Assembly. *Small n/a*, 2206582.

(148) Bai, P.; Hu, A.; Liu, Y.; Jin, Y.; Gao, Y. Printing and In Situ Assembly of CdSe/CdS Nanoplatelets as Uniform Films with Unity In-Plane Transition Dipole Moment. *J. Phys. Chem. Lett.* **2020**, *11*, 4524–4529.

(149) Rodà, C.; Di Giacomo, A.; Tasende Rodríguez, L. C.; M, C. S.; Leemans, J.; Hens, Z.; Geiregat, P.; Moreels, I. Colloidal CdSe/CdS Core/Crown Nanoplatelets for Efficient Blue Light Emission and Optical Amplification. *Nano Lett.* **2023**, *23*, 3224–3230.

(150) Liu, B.; Altintas, Y.; Wang, L.; Shendre, S.; Sharma, M.; Sun, H.; Mutlugun, E.; Demir, H. V. Record High External Quantum Efficiency of 19.2% Achieved in Light-Emitting Diodes of Colloidal Quantum Wells Enabled by Hot-Injection Shell Growth. *Adv. Mater.* **2020**, *32*, 1905824.

(151) Kelestemur, Y.; Shynkarenko, Y.; Anni, M.; Yakunin, S.; De Giorgi, M. L.; Kovalenko, M. V. Colloidal CdSe Quantum Wells with Graded Shell Composition for Low-Threshold Amplified Spontaneous Emission and Highly Efficient Electroluminescence. *ACS Nano* **2019**, *13*, 13899–13909.

(152) Zhang, F.; Wang, S.; Wang, L.; Lin, Q.; Shen, H.; Cao, W.; Yang, C.; Wang, H.; Yu, L.; Du, Z.; Xue, J.; Li, L. S. Super Color Purity Green Quantum Dot Light-Emitting Diodes Fabricated by Using CdSe/CdS Nanoplatelets. *Nanoscale* **2016**, *8*, 12182–12188.

(153) Liu, B.; Delikanli, S.; Gao, Y.; Dede, D.; Gungor, K.; Demir, H. V. Nanocrystal Light-Emitting Diodes Based on Type II Nanoplatelets. *Nano Energy* **2018**, *47*, 115–122.

(154) Shabani, F.; Dehghanpour Baruj, H.; Yurdakul, I.; Delikanli, S.; Gheshlaghi, N.; Isik, F.; Liu, B.; Altintas, Y.; Canımkurbey, B.; Demir, H. V. Deep-Red-Emitting Colloidal Quantum Well Light-Emitting Diodes Enabled through a Complex Design of Core/Crown/Double Shell Heterostructure. *Small* **2022**, *18*, 2106115.

(155) Pu, C.; Dai, X.; Shu, Y.; Zhu, M.; Deng, Y.; Jin, Y.; Peng, X. Electrochemically-Stable Ligands Bridge the Photoluminescence-Electroluminescence Gap of Quantum Dots. *Nat. Commun.* **2020**, *11*, 937.

(156) Brovelli, S.; Bae, W. K.; Galland, C.; Giovanella, U.; Meinardi, F.; Klimov, V. I. Dual-Color Electroluminescence from Dot-in-Bulk Nanocrystals. *Nano Lett.* **2014**, *14*, 486–494.

(157) Galland, C.; Brovelli, S.; Bae, W. K.; Padilha, L. A.; Meinardi, F.; Klimov, V. I. Dynamic Hole Blockade Yields Two-Color Quantum and Classical Light from Dot-in-Bulk Nanocrystals. *Nano Lett.* **2013**, *13*, 321–328.
(158) Nizamoglu, S.; Mutlugun, E.; Özel, T.; Demir, H. V.; Sapra, S.; Gaponik, N.; Eychmüller, A. Dual-Color Emitting Quantum-Dot-Quantum-Well CdSe-ZnS Heteronanocrystals Hybridized on InGaN⁄GaN Light Emitting Diodes for High-Quality White Light Generation. *Appl. Phys. Lett.* **2008**, *92*, 113110.
(159) Sharma, M.; Gungor, K.; Yeltik, A.; Olutas, M.; Guzelturk, B.; Kelestemur, Y.; Erdem, T.; Delikanli, S.; McBride, J. R.; Demir, H. V. Near-Unity Emitting Copper-Doped Colloidal Semiconductor Quantum Wells for Luminescent Solar Concentrators. *Adv. Mater.* **2017**, *29*, 1700821.
(160) İzmir, M.; Durmusoglu, E. G.; Sharma, M.; Shabani, F.; Isik, F.; Delikanli, S.; Sharma, V. K.; Demir, H. V. Near-Infrared Emission from CdSe-Based Nanoplatelets Induced by Ytterbium Doping. *J. Phys. Chem. C* **2023**, *127*, 4210–4217.
(161) Benchamekh, R.; Gippius, N. A.; Even, J.; Nestoklon, M. O.; Jancu, J.-M.; Ithurria, S.; Dubertret, B.; Efros, Al. L.; Voisin, P. Tight-Binding Calculations of Image-Charge Effects in Colloidal Nanoscale Platelets of CdSe. *Phys. Rev. B* **2014**, *89*, 035307.
(162) Delikanli, S.; Canimkurbey, B.; Hernández-Martínez, P. L.; Shabani, F.; Isik, A. T.; Ozkan, I.; Bozkaya, I.; Bozkaya, T.; Isik, F.; Durmusoglu, E. G.; Izmir, M.; Akgun, H.; Demir, H. V. On the Rational Design of Core/(Multi)-Crown Type-II Heteronanoplatelets. *J. Am. Chem. Soc.* **2023**.
(163) Dede, D.; Taghipour, N.; Quliyeva, U.; Sak, M.; Kelestemur, Y.; Gungor, K.; Demir, H. V. Highly Stable Multicrown Heterostructures of Type-II Nanoplatelets for Ultralow Threshold Optical Gain. *Chem. Mater.* **2019**, *31*, 1818–1826.
(164) Philbin, J. P.; Brumberg, A.; Diroll, B. T.; Cho, W.; Talapin, D. V.; Schaller, R. D.; Rabani, E. Area and Thickness Dependence of Auger Recombination in Nanoplatelets. *J. Chem. Phys.* **2020**, *153*, 054104.
(165) Antanovich, A.; Yang, L.; Erwin, S. C.; Martín-García, B.; Hübner, R.; Steinbach, C.; Schwarz, D.; Gaponik, N.; Lesnyak, V. CdSexS1–x Alloyed Nanoplatelets with Continuously Tunable Blue-Green Emission. *Chem. Mater.* **2022**, *34*, 10361–10372.
(166) Cassette, E.; Pedetti, S.; Mahler, B.; Ithurria, S.; Dubertret, B.; Scholes, G. D. Ultrafast Exciton Dynamics in 2D In-Plane Hetero-Nanostructures: Delocalization and Charge Transfer. *Phys. Chem. Chem. Phys.* **2017**, *19*, 8373–8379.
(167) Galland, C.; Brovelli, S.; Bae, W. K.; Padilha, L. A.; Meinardi, F.; Klimov, V. I. Dynamic Hole Blockade Yields Two-Color Quantum and Classical Light from Dot-in-Bulk Nanocrystals. *Nano Lett.* **2013**, *13*, 321–328.
(168) Pinchetti, V.; Meinardi, F.; Camellini, A.; Sirigu, G.; Christodoulou, S.; Bae, W. K.; De Donato, F.; Manna, L.; Zavelani-Rossi, M.; Moreels, I.; Klimov, V. I.; Brovelli, S. Effect of Core/Shell Interface on Carrier Dynamics and Optical Gain Properties of Dual-Color Emitting CdSe/CdS Nanocrystals. *ACS Nano* **2016**, *10*, 6877–6887.
(169) Pelton, M.; Wang, Y.; Fedin, I.; Talapin, D. V.; O'Leary, S. K. Hot-Carrier Relaxation in CdSe/CdS Core/Shell Nanoplatelets. *J. Phys. Chem. C* **2020**, *124*, 1020–1026.
(170) Dennis, A. M.; Buck, M. R.; Wang, F.; Hartmann, N. F.; Majumder, S.; Casson, J. L.; Watt, J. D.; Doorn, S. K.; Htoon, H.; Sykora, M.; Hollingsworth, J. A. Role of Interface Chemistry in Opening New Radiative Pathways in InP/CdSe Giant Quantum Dots with Blinking-Suppressed Two-Color Emission. *Adv. Funct. Mater.* **2019**, *29*, 1809111.
(171) Inoshita, T.; Sakaki, H. Electron Relaxation in a Quantum Dot: Significance of Multiphonon Processes. *Phys. Rev. B* **1992**, *46*, 7260–7263.
(172) Valerini, D.; Cretí, A.; Lomascolo, M.; Manna, L.; Cingolani, R.; Anni, M. Temperature Dependence of the Photoluminescence Properties of Colloidal $\mathrm{Cd}\mathrm{Se}⁄\mathrm{Zn}\mathrm{S}$ Core/Shell Quantum Dots Embedded in a Polystyrene Matrix. *Phys. Rev. B* **2005**, *71*, 235409.
(173) Varshni, Y. P. Temperature Dependence of the Energy Gap in Semiconductors. *Physica* **1967**, *34*, 149–154.
(174) Ahn, N.; Livache, C.; Pinchetti, V.; Klimov, V. I. Colloidal Semiconductor Nanocrystal Lasers and Laser Diodes. *Chem. Rev.* **2023**.
(175) Grim, J. Q.; Christodoulou, S.; Di Stasio, F.; Krahne, R.; Cingolani, R.; Manna, L.; Moreels, I. Continuous-Wave Biexciton Lasing at Room Temperature Using Solution-Processed Quantum Wells. *Nat. Nanotechnol.* **2014**, *9*, 891–895.
(176) Gao, Y.; Li, M.; Delikanli, S.; Zheng, H.; Liu, B.; Dang, C.; Sum, T. C.; Demir, H. V. Low-Threshold Lasing from Colloidal CdSe/CdSeTe Core/Alloyed-Crown Type-II Heteronanoplatelets. *Nanoscale* **2018**, *10*, 9466–9475.
(177) Oron, D.; Kazes, M.; Banin, U. Multiexcitons in Type-II Colloidal Semiconductor Quantum Dots. *Phys. Rev. B* **2007**, *75*, 035330.
(178) Llusar, J.; Climente, J. I. Highly Charged Excitons and Biexcitons in Type-II Core/Crown Colloidal Nanoplatelets. *J. Phys. Chem. C* **2022**, *126*, 7152–7157.
(179) Geiregat, P.; Tomar, R.; Chen, K.; Singh, S.; Hodgkiss, J. M.; Hens, Z. Thermodynamic Equilibrium between Excitons and Excitonic Molecules Dictates Optical Gain in Colloidal CdSe Quantum Wells. *J. Phys. Chem. Lett.* **2019**, *10*, 3637–3644.
(180) Li, Q.; Lian, T. A Model for Optical Gain in Colloidal Nanoplatelets. *Chem. Sci.* **2018**, *9*, 728–734.
(181) Dang, C.; Lee, J.; Breen, C.; Steckel, J. S.; Coe-Sullivan, S.; Nurmikko, A. Red, Green and Blue Lasing Enabled by Single-Exciton Gain in Colloidal Quantum Dot Films. *Nat. Nanotechnol.* **2012**, *7*, 335–339.
(182) Li, Q.; Xu, Z.; McBride, J. R.; Lian, T. Low Threshold Multiexciton Optical Gain in Colloidal CdSe/CdTe Core/Crown Type-II Nanoplatelet Heterostructures. *ACS Nano* **2017**, *11*, 2545–2553.
(183) Taghipour, N.; Delikanli, S.; Shendre, S.; Sak, M.; Li, M.; Isik, F.; Tanriover, I.; Guzelturk, B.; Sum, T. C.; Demir, H. V. Sub-Single Exciton Optical Gain Threshold in Colloidal Semiconductor Quantum Wells with Gradient Alloy Shelling. *Nat. Commun.* **2020**, *11*, 3305.

(184) *Samsung Display | Products/Technology – QD-OLED*. Samsung Display. https://www.samsungdisplay.com/eng/tech/quantum-dot.jsp (accessed 2023-04-25).
(185) Wong, J. I.; Mishra, N.; Xing, G.; Li, M.; Chakrabortty, S.; Sum, T. C.; Shi, Y.; Chan, Y.; Yang, H. Y. Dual Wavelength Electroluminescence from CdSe/CdS Tetrapods. *ACS Nano* **2014**, *8*, 2873–2879.
(186) Liu, B.; Sharma, M.; Yu, J.; Wang, L.; Shendre, S.; Sharma, A.; Izmir, M.; Delikanli, S.; Altintas, Y.; Dang, C.; Sun, H.; Demir, H. V. Management of Electroluminescence from Silver-Doped Colloidal Quantum Well Light-Emitting Diodes. *Cell Rep. Phys. Sci.* **2022**, *3*, 100860.
(187) Liu, B.; Sharma, M.; Yu, J.; Shendre, S.; Hettiarachchi, C.; Sharma, A.; Yeltik, A.; Wang, L.; Sun, H.; Dang, C.; Demir, H. V. Light-Emitting Diodes with Cu-Doped Colloidal Quantum Wells: From Ultrapure Green, Tunable Dual-Emission to White Light. *Small* **2019**, *15*, 1901983.
(188) Durmusoglu, E. G.; Hu, S.; Hernandez-Martinez, P. L.; Izmir, M.; Shabani, F.; Guo, M.; Gao, H.; Isik, F.; Delikanli, S.; Sharma, V. K.; Liu, B.; Demir, H. V. High External Quantum Efficiency Light-Emitting Diodes Enabled by Advanced Heterostructures of Type-II Nanoplatelets. *ACS Nano* **2023**, *17*, 7636–7644.
(189) Dabard, C.; Guilloux, V.; Gréboval, C.; Po, H.; Makke, L.; Fu, N.; Xu, X. Z.; Silly, M. G.; Patriarche, G.; Lhuillier, E.; Barisien, T.; Climente, J. I.; Diroll, B. T.; Ithurria, S. Double-Crowned 2D Semiconductor Nanoplatelets with Bicolor Power-Tunable Emission. *Nat. Commun.* **2022**, *13*, 5094.
(190) Khoshkhoo, M. S.; Prudnikau, A.; Chashmejahanbin, M. R.; Helbig, R.; Lesnyak, V.; Cuniberti, G. Multicolor Patterning of 2D Semiconductor Nanoplatelets. *ACS Nano* **2021**.
(191) Riedinger, A.; Mule, A. S.; Knüsel, P. N.; Ott, F. D.; Rossinelli, A. A.; Norris, D. J. Identifying Reactive Organo-Selenium Precursors in the Synthesis of CdSe Nanoplatelets. *Chem. Commun.* **2018**, *54*, 11789–11792.
(192) Li, Q.; Lian, T. Area- and Thickness-Dependent Biexciton Auger Recombination in Colloidal CdSe Nanoplatelets: Breaking the "Universal Volume Scaling Law." *Nano Lett.* **2017**, *17*, 3152–3158.
(193) Pons, T.; Pic, E.; Lequeux, N.; Cassette, E.; Bezdetnaya, L.; Guillemin, F.; Marchal, F.; Dubertret, B. Cadmium-Free CuInS(2)/ZnS Quantum Dots for Sentinel Lymph Node Imaging with Reduced Toxicity. *ACS Nano* **2010**, *4*, 2531–2538.
(194) Li, L.; Pandey, A.; Werder, D. J.; Khanal, B. P.; Pietryga, J. M.; Klimov, V. I. Efficient Synthesis of Highly Luminescent Copper Indium Sulfide-Based Core/Shell Nanocrystals with Surprisingly Long-Lived Emission. *J. Am. Chem. Soc.* **2011**, *133*, 1176–1179.
(195) Coughlan, C.; Ibáñez, M.; Dobrozhan, O.; Singh, A.; Cabot, A.; Ryan, K. M. Compound Copper Chalcogenide Nanocrystals. *Chem. Rev.* **2017**, *117*, 5865–6109.
(196) Hendricks, M. P.; Campos, M. P.; Cleveland, G. T.; Jen-La Plante, I.; Owen, J. S. A Tunable Library of Substituted Thiourea Precursors to Metal Sulfide Nanocrystals. *Science* **2015**, *348*, 1226–1230.
(197) Keuleyan, S. E.; Guyot-Sionnest, P.; Delerue, C.; Allan, G. Mercury Telluride Colloidal Quantum Dots: Electronic Structure, Size-Dependent Spectra, and Photocurrent Detection up to 12 Mm. *ACS Nano* **2014**, *8*, 8676–8682.
(198) Kovalenko, M. V.; Kaufmann, E.; Pachinger, D.; Roither, J.; Huber, M.; Stangl, J.; Hesser, G.; Schäffler, F.; Heiss, W. Colloidal HgTe Nanocrystals with Widely Tunable Narrow Band Gap Energies: From Telecommunications to Molecular Vibrations. *J. Am. Chem. Soc.* **2006**, *128*, 3516–3517.
(199) Keuleyan, S.; Lhuillier, E.; Brajuskovic, V.; Guyot-Sionnest, P. Mid-Infrared HgTe Colloidal Quantum Dot Photodetectors. *Nat. Photonics* **2011**, *5*, 489–493.
(200) Lhuillier, E.; Scarafagio, M.; Hease, P.; Nadal, B.; Aubin, H.; Xu, X. Z.; Lequeux, N.; Patriarche, G.; Ithurria, S.; Dubertret, B. Infrared Photodetection Based on Colloidal Quantum-Dot Films with High Mobility and Optical Absorption up to THz. *Nano Lett.* **2016**, *16*, 1282–1286.
(201) Smith, A. M.; Nie, S. Bright and Compact Alloyed Quantum Dots with Broadly Tunable Near-Infrared Absorption and Fluorescence Spectra through Mercury Cation Exchange. *J. Am. Chem. Soc.* **2011**, *133*, 24–26.
(202) Po, H.; Dabard, C.; Roman, B.; Reyssat, E.; Bico, J.; Baptiste, B.; Lhuillier, E.; Ithurria, S. Chiral Helices Formation by Self-Assembled Molecules on Semiconductor Flexible Substrates. *ACS Nano* **2022**, *16*, 2901–2909.
(203) Tai, H.; Nakashima, S.; Hori, S. Optical Properties of (CdTe)1-x(CdSe)x and (CdTe)1-x(Cds)x Systems. *Phys. Status Solidi A* **1975**, *30*, K115–K119.
(204) Tenney, S. M.; Vilchez, V.; Sonnleitner, M. L.; Huang, C.; Friedman, H. C.; Shin, A. J.; Atallah, T. L.; Deshmukh, A. P.; Ithurria, S.; Caram, J. R. Mercury Chalcogenide Nanoplatelet–Quantum Dot Heterostructures as a New Class of Continuously Tunable Bright Shortwave Infrared Emitters. *J. Phys. Chem. Lett.* **2020**, *11*, 3473–3480.
(205) Lim, S. J.; Kim, W.; Shin, S. K. Surface-Dependent, Ligand-Mediated Photochemical Etching of CdSe Nanoplatelets. *J. Am. Chem. Soc.* **2012**, *134*, 7576–7579.
(206) Antanovich, A.; Achtstein, A. W.; Matsukovich, A.; Prudnikau, A.; Bhaskar, P.; Gurin, V.; Molinari, M.; Artemyev, M. A Strain-Induced Exciton Transition Energy Shift in CdSe Nanoplatelets: The Impact of an Organic Ligand Shell. *Nanoscale* **2017**, *9*, 18042–18053.
(207) Jagtap, A.; Martinez, B.; Goubet, N.; Chu, A.; Livache, C.; Gréboval, C.; Ramade, J.; Amelot, D.; Trousset, P.; Triboulin, A.; Ithurria, S.; Silly, M. G.; Dubertret, B.; Lhuillier, E. Design of a Unipolar Barrier for a Nanocrystal-Based Short-Wave Infrared Photodiode. *ACS Photonics* **2018**, *5*, 4569–4576.
(208) Gréboval, C.; Izquierdo, E.; Livache, C.; Martinez, B.; Dufour, M.; Goubet, N.; Moghaddam, N.; Qu, J.; Chu, A.; Ramade, J.; Aubin, H.; Cruguel, H.; Silly, M.; Lhuillier, E.; Ithurria, S. Impact of Dimensionality and Confinement on the Electronic Properties of Mercury Chalcogenide Nanocrystals. *Nanoscale* **2019**, *11*, 3905–3915.
(209) Spencer, B. F.; Leontiadou, M. A.; Clark, P. C. J.; Williamson, A. I.; Silly, M. G.; Sirotti, F.; Fairclough, S. M.; Tsang, S. C. E.; Neo, D. C. J.; Assender, H. E.; Watt, A. a. R.; Flavell, W. R. Charge Dynamics at Heterojunctions for PbS/ZnO Colloidal

Quantum Dot Solar Cells Probed with Time-Resolved Surface Photovoltage Spectroscopy. *Appl. Phys. Lett.* **2016**, *108*, 091603.

(210) Clark, P. C. J.; Lewis, N. K.; Ke, J. C.-R.; Ahumada-Lazo, R.; Chen, Q.; Neo, D. C. J.; Gaulding, E. A.; Pach, G. F.; Pis, I.; Silly, M. G.; Flavell, W. R. Surface Band Bending and Carrier Dynamics in Colloidal Quantum Dot Solids. *Nanoscale* **2021**, *13*, 17793–17806.

(211) Gréboval, C.; Rastogi, P.; Qu, J.; Chu, A.; Ramade, J.; Khalili, A.; Dabard, C.; Dang, T. H.; Cruguel, H.; Ouerghi, A.; Witkowski, N.; Silly, M. G.; Lhuillier, E. Time-Resolved Photoemission to Unveil Electronic Coupling between Absorbing and Transport Layers in a Quantum Dot-Based Solar Cell. *J. Phys. Chem. C* **2020**, *124*, 23400–23409.

(212) Amelot, D.; Rastogi, P.; Martinez, B.; Gréboval, C.; Livache, C.; Bresciani, F. A.; Qu, J.; Chu, A.; Goyal, M.; Chee, S.-S.; Casaretto, N.; Xu, X. Z.; Méthivier, C.; Cruguel, H.; Ouerghi, A.; Nag, A.; Silly, M. G.; Witkowski, N.; Lhuillier, E. Revealing the Band Structure of FAPI Quantum Dot Film and Its Interfaces with Electron and Hole Transport Layer Using Time Resolved Photoemission. *J. Phys. Chem. C* **2020**, *124*, 3873–3880.

(213) Bergeard, N.; Silly, M. G.; Krizmancic, D.; Chauvet, C.; Guzzo, M.; Ricaud, J. P.; Izquierdo, M.; Stebel, L.; Pittana, P.; Sergo, R.; Cautero, G.; Dufour, G.; Rochet, F.; Sirotti, F. Time-Resolved Photoelectron Spectroscopy Using Synchrotron Radiation Time Structure. *J. Synchrotron Radiat.* **2011**, *18*, 245–250.

(214) Hong, G.; Diao, S.; Chang, J.; Antaris, A. L.; Chen, C.; Zhang, B.; Zhao, S.; Atochin, D. N.; Huang, P. L.; Andreasson, K. I.; Kuo, C. J.; Dai, H. Through-Skull Fluorescence Imaging of the Brain in a New near-Infrared Window. *Nat. Photonics* **2014**, *8*, 723–730.

(215) Hansen, M. P.; Malchow, D. S. Overview of SWIR Detectors, Cameras, and Applications. In *Thermosense XXX*; SPIE, 2008; Vol. 6939, pp 94–104.

(216) Koktysh, D. S.; Gaponik, N.; Reufer, M.; Crewett, J.; Scherf, U.; Eychmüller, A.; Lupton, J. M.; Rogach, A. L.; Feldmann, J. Near-Infrared Electroluminescence from HgTe Nanocrystals. *ChemPhysChem* **2004**, *5*, 1435–1438.

(217) O'Connor, É.; O'Riordan, A.; Doyle, H.; Moynihan, S.; Cuddihy, A.; Redmond, G. Near-Infrared Electroluminescent Devices Based on Colloidal HgTe Quantum Dot Arrays. *Appl. Phys. Lett.* **2005**, *86*, 201114.

(218) Prado, Y.; Qu, J.; Gréboval, C.; Dabard, C.; Rastogi, P.; Chu, A.; Khalili, A.; Xu, X. Z.; Delerue, C.; Ithurria, S.; Lhuillier, E. Seeded Growth of HgTe Nanocrystals for Shape Control and Their Use in Narrow Infrared Electroluminescence. *Chem. Mater.* **2021**, *33*, 2054–2061.

(219) Bossavit, E.; Qu, J.; Abadie, C.; Dabard, C.; Dang, T.; Izquierdo, E.; Khalili, A.; Gréboval, C.; Chu, A.; Pierini, S.; Cavallo, M.; Prado, Y.; Parahyba, V.; Xu, X. Z.; Decamps-Mandine, A.; Silly, M.; Ithurria, S.; Lhuillier, E. Optimized Infrared LED and Its Use in an All-HgTe Nanocrystal-Based Active Imaging Setup. *Adv. Opt. Mater.* **2022**, *10*, 2101755.

(220) Qu, J.; Weis, M.; Izquierdo, E.; Mizrahi, S. G.; Chu, A.; Dabard, C.; Gréboval, C.; Bossavit, E.; Prado, Y.; Péronne, E.; Ithurria, S.; Patriarche, G.; Silly, M. G.; Vincent, G.; Boschetto, D.; Lhuillier, E. Electroluminescence from Nanocrystals above 2 Mm. *Nat. Photonics* **2022**, *16*, 38–44.

(221) Qu, J.; Rastogi, P.; Gréboval, C.; Lagarde, D.; Chu, A.; Dabard, C.; Khalili, A.; Cruguel, H.; Robert, C.; Xu, X. Z.; Ithurria, S.; Silly, M. G.; Ferré, S.; Marie, X.; Lhuillier, E. Electroluminescence from HgTe Nanocrystals and Its Use for Active Imaging. *Nano Lett.* **2020**, *20*, 6185–6190.

(222) Shen, X.; Peterson, J. C.; Guyot-Sionnest, P. Mid-Infrared HgTe Colloidal Quantum Dot LEDs. *ACS Nano* **2022**, *16*, 7301–7308.

(223) Rastogi, P.; Izquierdo, E.; Gréboval, C.; Cavallo, M.; Chu, A.; Dang, T. H.; Khalili, A.; Abadie, C.; Alchaar, R.; Pierini, S.; Cruguel, H.; Witkowski, N.; Utterback, J. K.; Brule, T.; Xu, X. Z.; Hollander, P.; Ouerghi, A.; Gallas, B.; Silly, M. G.; Lhuillier, E. Extended Short-Wave Photodiode Based on CdSe/HgTe/Ag2Te Stack with High Internal Efficiency. *J. Phys. Chem. C* **2022**, *126*, 13720–13728.

(224) Tian, Y.; Luo, H.; Chen, M.; Li, C.; Kershaw, S. V.; Zhang, R.; Rogach, A. L. Mercury Chalcogenide Colloidal Quantum Dots for Infrared Photodetection: From Synthesis to Device Applications. *Nanoscale* **2023**, *15*, 6476–6504.

(225) Greboval, C.; Ferre, S.; Noguier, V.; Chu, A.; Qu, J.; Chee, S.-S.; Vincent, G.; Lhuillier, E. Infrared Narrow Band Gap Nanocrystals: Recent Progresses Relative to Imaging and Active Detection. arXiv January 30, 2020. http://arxiv.org/abs/2001.11554 (accessed 2023-05-31).

(226) Ackerman, M. M.; Chen, M.; Guyot-Sionnest, P. HgTe Colloidal Quantum Dot Photodiodes for Extended Short-Wave Infrared Detection. *Appl. Phys. Lett.* **2020**, *116*, 083502.

(227) Geiregat, P.; Houtepen, A. J.; Sagar, L. K.; Infante, I.; Zapata, F.; Grigel, V.; Allan, G.; Delerue, C.; Van Thourhout, D.; Hens, Z. Continuous-Wave Infrared Optical Gain and Amplified Spontaneous Emission at Ultralow Threshold by Colloidal HgTe Quantum Dots. *Nat. Mater.* **2018**, *17*, 35–42.

(228) Sergeev, A. A.; Pavlov, D. V.; Kuchmizhak, A. A.; Lapine, M. V.; Yiu, W. K.; Dong, Y.; Ke, N.; Juodkazis, S.; Zhao, N.; Kershaw, S. V.; Rogach, A. L. Tailoring Spontaneous Infrared Emission of HgTe Quantum Dots with Laser-Printed Plasmonic Arrays. *Light Sci. Appl.* **2020**, *9*, 16.

(229) Anand, A.; Zaffalon, M. L.; Cova, F.; Pinchetti, V.; Khan, A. H.; Carulli, F.; Brescia, R.; Meinardi, F.; Moreels, I.; Brovelli, S. Optical and Scintillation Properties of Record-Efficiency CdTe Nanoplatelets toward Radiation Detection Applications. *Nano Lett.* **2022**, *22*, 8900–8907.

(230) Gupta, S.; Zhovtiuk, O.; Vaneski, A.; Lin, Y.-C.; Chou, W.-C.; Kershaw, S. V.; Rogach, A. L. CdxHg(1−x)Te Alloy Colloidal Quantum Dots: Tuning Optical Properties from the Visible to Near-Infrared by Ion Exchange. *Part. Part. Syst. Charact.* **2013**, *30*, 346–354.

(231) Sokolova, A. V.; Skurlov, I. D.; Babaev, A. A.; Perfenov, P. S.; Miropoltsev, M. A.; Danilov, D. V.; Baranov, M. A.; Kolesnikov, I. E.; Koroleva, A. V.; Zhizhin, E. V.; Litvin, A. P.; Fedorov, A. V.; Cherevkov, S. A. Near-Infrared Emission of HgTe Nanoplatelets Tuned by Pb-Doping. *Nanomaterials* **2022**, *12*, 4198.

(232) Dooley, C. J.; Dimitrov, S. D.; Fiebig, T. Ultrafast Electron Transfer Dynamics in CdSe/CdTe Donor−Acceptor Nanorods. *J. Phys. Chem. C* **2008**, *112*, 12074–12076.

(233) Williams, K. R.; Diroll, B. T.; Watkins, N. E.; Rui, X.; Brumberg, A.; Klie, R. F.; Schaller, R. D. Synthesis of Type I PbSe/CdSe Dot-on-Plate Heterostructures with Near-Infrared Emission. *J. Am. Chem. Soc.* **2019**, *141*, 5092–5096.

(234) Hildebrandt, N.; Spillmann, C. M.; Algar, W. R.; Pons, T.; Stewart, M. H.; Oh, E.; Susumu, K.; Díaz, S. A.; Delehanty, J. B.; Medintz, I. L. Energy Transfer with Semiconductor Quantum Dot Bioconjugates: A Versatile Platform for Biosensing, Energy Harvesting, and Other Developing Applications. *Chem. Rev.* **2017**, *117*, 536–711.

(235) Yao, Y.; Zhou, Y.; Sanderson, W. M.; Loomis, R. A.; Buhro, W. E. Metal-Halide-Ligated Cadmium Selenide Quantum Belts by Facile Surface Exchange. *Chem. Mater.* **2018**, *30*, 2848–2857.

(236) Momper, R.; Zhang, H.; Chen, S.; Halim, H.; Johannes, E.; Yordanov, S.; Braga, D.; Blülle, B.; Doblas, D.; Kraus, T.; Bonn, M.; Wang, H. I.; Riedinger, A. Kinetic Control over Self-Assembly of Semiconductor Nanoplatelets. *Nano Lett.* **2020**, *20*, 4102–4110.

(237) Chu, A.; Gréboval, C.; Goubet, N.; Martinez, B.; Livache, C.; Qu, J.; Rastogi, P.; Bresciani, F. A.; Prado, Y.; Suffit, S.; Ithurria, S.; Vincent, G.; Lhuillier, E. Near Unity Absorption in Nanocrystal Based Short Wave Infrared Photodetectors Using Guided Mode Resonators. *ACS Photonics* **2019**, *6*, 2553–2561.

(238) Bossavit, E. 2023.

(239) Prins, F.; Kim, D. K.; Cui, J.; De Leo, E.; Spiegel, L. L.; McPeak, K. M.; Norris, D. J. Direct Patterning of Colloidal Quantum-Dot Thin Films for Enhanced and Spectrally Selective Out-Coupling of Emission. *Nano Lett.* **2017**, *17*, 1319–1325.

(240) Rastogi, P.; Chu, A.; Gréboval, C.; Qu, J.; Noumbé, U. N.; Chee, S.-S.; Goyal, M.; Khalili, A.; Xu, X. Z.; Cruguel, H.; Ithurria, S.; Gallas, B.; Dayen, J.-F.; Dudy, L.; Silly, M. G.; Patriarche, G.; Degiron, A.; Vincent, G.; Lhuillier, E. Pushing Absorption of Perovskite Nanocrystals into the Infrared. *Nano Lett.* **2020**, *20*, 3999–4006.

(241) Zhao, J.; Cheng, Y.; Shen, H.; Hui, Y. Y.; Wen, T.; Chang, H.-C.; Gong, Q.; Lu, G. Light Emission from Plasmonic Nanostructures Enhanced with Fluorescent Nanodiamonds. *Sci. Rep.* **2018**, *8*, 3605.

(242) Curto, A. G.; Volpe, G.; Taminiau, T. H.; Kreuzer, M. P.; Quidant, R.; van Hulst, N. F. Unidirectional Emission of a Quantum Dot Coupled to a Nanoantenna. *Science* **2010**, *329*, 930–933.

(243) Chiu, N.-F.; Le Ster, M.; Yang, C.-D.; Tseng, M.-H.; Tsai, F.-Y. Interactions between Excitation and Extraction Modes in an Organic-Based Plasmon-Emitting Diode. *Appl. Surf. Sci.* **2015**, *332*, 97–104.

(244) Nien, S.-Y.; Chiu, N.-F.; Ho, Y.-H.; Lee, J.-H.; Lin, C.-W.; Wu, K.-C.; Lee, C.-K.; Lin, J.-R.; Wei, M.-K.; Chiu, T.-L. Directional Photoluminescence Enhancement of Organic Emitters via Surface Plasmon Coupling. *Appl. Phys. Lett.* **2009**, *94*, 103304.

(245) Dai, X.; Zhang, Z.; Jin, Y.; Niu, Y.; Cao, H.; Liang, X.; Chen, L.; Wang, J.; Peng, X. Solution-Processed, High-Performance Light-Emitting Diodes Based on Quantum Dots. *Nature* **2014**, *515*, 96–99.

Résumé

Les nanoplaquettes de chalcogénures de cadmium sont des semiconducteurs de la famille des II-VI présentant à la fois un confinement quantique unidimensionnel et une large extension latérale. Leurs synthèses, définies à la monocouche atomique près, confèrent à ces matériaux de fines propriétés optiques. Cette particularité justifie l'intérêt que j'ai porté à ces matériaux tout au long de ma thèse.

Dans un premier temps, des particules émettant deux couleurs différentes ont été synthétisées. La difficulté pour réaliser de telles particules réside dans la règle de Kasha. Pour surpasser cette contrainte, une hétérostructure cœur-couronne-couronne de CdSe-CdTe-CdSe a été synthétisée. Dans une telle particule, une large luminescence rouge (650 nm) est obtenue par recombinaison de l'exciton à l'interface CdSe/CdTe tandis qu'une fine luminescence verte (512 nm) est obtenue par la recombinaison de bord de bande dans le CdSe. En jouant sur les paramètres géométriques des différentes couronnes ainsi que sur la puissance d'excitation, une modulation du ratio vert-rouge est possible grâce au contrôle de la dynamique de recombinaison non-radiative Auger. L'incorporation de cette hétérostructure à l'intérieur d'un dispositif LED a également permis d'obtenir une électroluminescence bi couleur. Une stratégie similaire à ensuite été mise en place pour obtenir une particule émettant à la fois dans le bleu et dans le jaune.

Ces particules bidimensionnelles peuvent également être utiles pour obtenir des émetteurs fins dans le proche infra-rouge. Durant ma thèse, la synthèse d'une nouvelle classe de nanoplaquettes à base de chalcogénure de mercure ($HgSe_xTe_{1-x}$) a permis de sonder cette gamme optique. En particulier, l'optimisation du processus d'échange cationique a rendu possible l'obtention d'une modulation de la photoluminescence dans le proche infra-rouge. Le développement d'un processus de dépôt limitant la dégradation des propriétés optiques de nanoplaquettes de HgTe a également permis la fabrication du premier dispositif électroluminescent utilisant des nanoplaquettes à base de mercure ainsi que l'observation d'une émission orientée grâce au couplage d'un film de nanoplaquette de HgTe avec le plasmon généré par une nanostructure métallique.

Abstract

Cadmium chalcogenide nanoplatelets are II-VI semiconductors that exhibit both one-dimensional quantum confinement and a large lateral extension. Their syntheses, defined at the atomic monolayer scale, confer fine optical properties to these materials. This particularity justifies the interest I have had in these materials throughout my thesis.

First, particles emitting two different colors were synthesized. The challenge in creating such particles lies in Kasha's rule. To overcome this constraint, a core-crown-crown heterostructure of CdSe-CdTe-CdSe was synthesized. In such a particle, a broad red luminescence (650 nm) is obtained through exciton recombination at the CdSe/CdTe interface, while a narrow green luminescence (512 nm) is achieved through band edge recombination in CdSe. By adjusting the geometric parameters of the different crowns and the excitation power, modulation of the green-red ratio is possible thanks to the control of the dynamic of the non-radiative Auger recombination. Incorporating this heterostructure into an LED device allowed for the achievement of dual-color electroluminescence. A similar strategy was then implemented to obtain a particle emitting both blue and yellow lights.

These two-dimensional particles can also be useful for obtaining fine emitters in the near-infrared range. During my thesis, the synthesis of a new class of nanoplatelets based on mercury chalcogenide ($HgSe_xTe_{1-x}$) enabled exploration of this optical range. In particular, the optimization of the cation exchange process made it possible to achieve modulation of photoluminescence in the near-infrared. The development of a deposition process that limits the degradation of the optical properties of HgTe nanoplatelets also enabled the fabrication of the first electroluminescent device using mercury-based nanoplatelets. The plasmonic coupling of an HgTe nanoplatelet film with a metallic nanostructure allowed the achievement of directional emission.